Optimisation of Thermal Outputs from Shape Memory Alloy (SMA) Based Heat Pump

By

Mubarak Abdelrasoul Elnour Ismail

https://orcid.org/0009-0008-4264-8426

A thesis submitted in partial fulfilment of the requirements of the

London South Bank University

for the award of the degree of Doctor of Philosophy

April 2023

Supervisors

Prof. Issa Chaer

Dr Abas Hadawey

Dr Alex Paurine

Abstract

As countries transition to a low carbon economy, there are sizable environmental and economic benefits from developing and using efficient, innovative, low carbon heating and cooling technologies that have the potential to reduce energy use and carbon emissions. This thesis focuses on elastocaloric refrigeration technology and ways of enhancing the thermal outputs of Shape Memory Alloys (SMA), which are the core material of the technology.

The thesis includes an up-to-date and comprehensive critical review and evaluation of recent advances in emerging alternative heating and cooling technologies that have the potential to reduce the environmental impacts of the refrigeration, air-conditioning and heat-pumps (RACHP) sector.

The literature review on elastocaloric refrigeration showed that all the designed and manufactured prototypes to date either work under tension or under compression for pipes. The experiments also showed that using tension loading for a heat pump device is not practical despite its excellent heat transfer potential, as the material under tension tends to deform permanently much quicker, since the cracks on the surface of the material tend to grow and propagate and thus leading to failure; moreover, tension loading is limited to stress between 100 MPa to 200 MPa. On the other hand, although compressive loading requires specific geometric configurations to avoid failures such as buckling, it has a longer fatigue life, because the impurities and cracks do not grow and propagate; moreover, compression loading can exceed stresses of 1000 MPa allowing for better material performance.

To overcome the challenges as identified and stated in the literature, it was necessary to establish a thorough understanding of the designated material properties with the aid of COMSOL MULTIPHYSICS modelling. This included looking at methods of altering the material's characteristics by means of heat-treatment, as well as using material characterization equipment to achieve improved thermal outputs. Moreover, the research focused on proposing and studying a range of novel geometric designs and configurations for the material. The best performing configuration was established, and this led to designing the SMA-heat-pump stack and the fluid flow paths. Also, the research focused on modelling the

working fluids in COMSOL MULTIPHYSICS to establish the most appropriate means of enhancing their thermal properties. The first base-fluid to be tested was water, of which was followed by adding 1%, 2% and then 3% concentrations of Graphene Oxide nanoparticles to compose new nanofluids that had improved thermal properties.

The research included a study of the relationship between the stress and strain, the temperature lift, and the available latent heat. Since the potential design was to stack the plates and compress them, the results showed that applying a compressive loading of 500 MPa on an SMA specimen resulted in a 1.63% of material's deformation, a 10K temperature lift, and 1.46 $J.g^{-1}$ of latent heat. When the applied compressive loading was increased to 900 MPa, the material deformed by 5.4% and in so doing achieved a 19K temperature lift and 19 $J.g^{-1}$ of latent heat. On the plate design front, the results showed that the rectangular shape channels/fluid-path provided the highest Reynolds number which led to higher heat transfer coefficient; and as a result, it was possible to extract 98% of the available heat within the plate.

On the fluids front, the results showed that the channel/flow-path has different temperatures at different heights, and it was found that there is a lag between the increase of the material's temperature and that of the fluid. It was also found that water achieved a temperature span of 2.8K; however, when 1%, 2% and 3% concentrations of the nanoparticles were added to water, the newly formed nanofluids had better thermal properties, as their thermal conductivity increased by 52%, 59% and 65% respectively, and because of that the temperature lift increased by 25.9% and the loading cycle was shortened by 24% with the third nanofluid (water plus 3% of Graphene Oxide), which will have a positive impact on the compactness and the cost of the SMA core.

This research has contributed to knowledge through the following:

- ✓ Providing a roadmap for SMA modelling in CFD (COMSOL MULTIPHYSICS) and how SMA is susceptible to different applied stresses and cycle times.

- ✓ Providing a roadmap of how to design different SMA geometries that can withstand high stresses and thus could potentially be used as the core material for an SMA-based heat pump device without encountering material failure due to high stresses.
- ✓ Developing an innovative approach to enhance the heat transfer from SMA through using enhanced nanofluids.

Declaration

The research described in this thesis is the original work of the author except where otherwise specified or acknowledgement is made by references.

This research project was carried out at the school of the Built Environment and Architecture, London South Bank University, under the supervision of Professor Issa Chaer, Dr Abas Hadawey, and Dr Alex Paurine.

The work has not been submitted for another degree or award of another academic or professional institution during the research program.

Mubarak Abdelrasoul Elnour Ismail

To the soul of my beloved dad in heaven

إلى روح أبي الطاهرة في عليائها

Acknowledgements

I would like to thank Exergyn Ltd. and London South Bank University for sponsoring this match-funded PhD project.

I offer my heartfelt gratitude to my first supervisor and director of studies **Prof. Issa Chaer** for his supervision, mentoring, guidance and his unparalleled support during my PhD. His vast knowledge, his dedication and his words of encouragement always inspired me. I am also very grateful and appreciative to my second supervisor **Dr Abas Hadawey** for his continued support, kindness, and motivation. Special gratitude goes to my third supervisor **Dr Alex Paurine** for his unlimited support during my PhD, and for putting his valuable knowledge and precious time at my disposal.

Special thanks and appreciation also go to my industrial supervisors **Dr Kevin O’Toole** and **Mr Mike Langan** for their continued support and guidance, for the regular meetings and the invaluable advice, and for granting me access to their laboratories. I would also like to extend my sincere gratitude to **Mr Keith Warren** for his support in the modelling, and to **Dr Jan Pilch** and his team for their support and guidance during the laboratory experiments. I would also like to thank the rest of Exergyn’s team for making me feel so welcome during my industrial visits. I learned so much from Exergyn’s teams, and this thesis would not have been possible without you.

I would like to thank all my colleagues, the staff at the School of the Built Environment and Architecture, the visiting professor **Prof. Hamid Goshayeshi**, and everyone who helped directly or indirectly in creating an enjoyable working environment.

Last but not least, my deepest gratitude goes to my loving mum, kind siblings, my friends, and my family for their continuous support.

Table of Content

List of figures

List of tables

Nomenclature

Symbol	Description	Units
A_s	Austenite start temperature	℃
A_f	Martensite start temperature	℃
b^A	Polynomial Hardening for Austenite	J
b^M	Polynomial Hardening for Martensite	J
C_A	Stress influence coefficient for Austenite	$MPa.K^{-1}$
C_M	Stress influence coefficient for Martensite	$MPa.K^{-1}$
C_p	Specific heat capacity	$J.kg^{-1}.K^{-1}$
C_{pnf}	Specific heat capacity of the nanofluid	$J.kg^{-1}.K^{-1}$
C_{pf}	Specific heat capacity of the base fluid	$J.kg^{-1}.K^{-1}$
C_{pp}	Specific heat capacity of the nanoparticle	$J.kg^{-1}.K^{-1}$
CSA_{slot}	Cross-sectional area of one slot/channel	m^2
d	Material thickness	m
D_H	Hydraulic diameter	m
E_A	Young modulus of elasticity for Austenite	GPa
E_M	Young modulus of elasticity for Martensite	GPa
h	heat transfer coefficient	$W.m^{-2}.K^{-1}$
H	Maximum transformation strain	%
HT_{CSA}	Heat transfer's cross-sectional area	m^2
K_A	Thermal conductivity of Austenite	$W.m^{-1}.K^{-1}$
K_M	Thermal conductivity of Martensite	$W.m^{-1}.K^{-1}$
K_f	Fluid's thermal conductivity	$W.m^{-1}.K^{-1}$
LH	Available Latent Heat	kJ/kg
L_p	Channel's length	m
M_s	Martensitic start temperature	℃
M_f	Martensitic finish temperature	℃
m_{plate}	Mass of the plate	kg
$\dot{m}$	Mass flow rate	$kg.s^{-1}$
nr_{slot}	Number of slots/channels	-
Nu	Nusselt Number	-
Pr	Prandtl Number	-
Q	Volumetric flow rate	$m^3.s^{-1}$
q	Required heating load	kW
Re	Reynolds Number	-
S_A	Stress compliance Factor during Austenite Phase	GPa^{-1}
S_M	Stress compliance Factor during Martensite Phase	GPa^{-1}
T_s	Initial starting temperature	℃
u	Fluid velocity	$m.s^{-1}$
V_{plate}	The volume of the plate	m^3
V_{slot}	The volume of the slot/channel	m^3
x	Thickness between the slots/channels	mm
Y	Dynamic force needed for phase transformation	N

Greek Symbols

Symbol	Description	Units
ρ	Material density	$kg.m^{-3}$
ρ_f	Fluid’s density	$kg.m^{-3}$
ρ_p	Density of the nanoparticle	$kg.m^{-3}$
ρ_{nf}	Density of the nanofluid	$kg.m^{-3}$
α	Thermal Expansion	℃
α_A	Coefficient of expansion for Austenite	K^{-1}
α_M	Coefficient of expansion for Martensite	K^{-1}
ε^T	Macroscopic transformation strain	%
ε^{Tm}	Microscopic transformation strain	%
ξ_M	Martensitic volume fraction	%
μ	Dynamic Viscosity	$Pa.s$
μ_f	Dynamic viscosity of the base fluid	$Pa.s$
μ_{nf}	Dynamic viscosity of the nanofluid	$Pa.s$

List of Abbreviations

Abbreviation	Description
AMR	Active Magnetic Regenerative
BCE	Barocaloric Effect
CFC	Chlorofluorocarbons
CFD	Computational Fluid Dynamics
CO_2	Carbon Dioxide
CO_2e	Carbon Dioxide Equivalent
COP	Coefficient of Performance
DSC	Differential Scanning Calorimetry
ECE	Elastocaloric Effect
ECHA	European Chemical Agency
EMC	Electrocaloric Materials
EU	European Union
F-Gas	Fluorinated Gas
FOMT	First Order Magnetic Transition
GHGs	Greenhouse Gases
GWP	Global Warming Potential
HCFC	Hydrochlorofluorocarbons
HFC	Hydrofluorocarbons
HFO	Hydrofluoro-Olefins
HTF	Heat Transfer Fluid
HVAC	Heating, Ventilation, and Air Conditioning
kV	kilovolt
kW	Kilowatt
kWh	Kilowatt-hour
MCM	Magnetocaloric Materials
MCE	Magnetocaloric Effect
$MtCO_2e$	Million Tonnes of Carbon Dioxide Equivalent
MtOe	Million Tonnes of Oil Equivalent
NiTi	Nickel Titanium
NiTiX	Nickel Titanium X
NdFeB	Neodymium Iron Boron
nZEB	Nearly Zero-Emission Building
ODP	Ozone Depletion Potential
PFAS	Perfluoroalkyl and Polyfluoroalkyl Substances
RACHP	Refrigeration, Air Conditioning and Heat Pump
RHI	Renewable Heat Incentive
SMA	Shape Memory Alloys
SOMT	Second Order Magnetic Transition
UV	Ultraviolet
VCC	Vapour Compression Cycle

Chapter 1*:* Introduction

Chapter 1 Introduction

1.1 Overview

Heating and cooling accounts for almost half the energy demand in buildings and for nearly 40% of energy-related Carbon Dioxide CO_2 emissions in the European Union (Goodson, T. et al. 2022); and this is directly attributed to the systems used for heating and cooling. Table 1.1, shown below, outlines the quantity of CO_2 being released in the production of 1 kWh delivered heat through various sources as well as their efficiencies and Coefficient of Performance (COP) (Carbon Emissions Calculator, 2018).

Table 1.1: CO_2 released through different methods of heat production (Houses of Parliament. Carbon Footprint of Heat generation, 2016)

Heat production method	COP	Efficiency	Grams of CO_2 per kWh delivered heat
Ground Source Heat Pump	4		67
Air Source Heat Pump	3		83
Direct Electric heating		1	250
Gas Boiler		0.85	295
Oil Boiler		0.85	430
Coal		0.5	630

Heat pumps show significant reductions in CO_2 compared to other methods of generating heat. They release 3 to 4 times less CO_2 than direct electric heating and approximately 8 to 10 times less than coal. The main characteristic of a heat pump is its ability to generate greater heat energy than the energy needed to drive the cycle of the heat pump, hence they have high COPs. If the input energy to the heat pump is from a renewable source, it reduces the heat pump's carbon footprint further. Therefore, heat pumps would be vital in maintaining the current levels of heating while reducing the CO_2 produced in the process. However, in the UK for instance, only half of the electricity demand is generated from renewable resources (G.B. National Grid Status, 2023); moreover, heat pumps are relatively new systems and not yet well spread, therefore and according to Eurostat figure in 2019, 75% of heating and cooling is still generated from fossil fuels (Energy – European Commission, 2019).

Even if heat pumps were to replace other heating and cooling systems, it is known that heat pumps rely on refrigerants in their cycle, and these can be detrimental to the environment due to their Carbon Dioxide equivalent value (CO_2e). This value is a common unit for describing different greenhouse gases in relation to their Global Warming Potential (GWP) in terms of the equivalent amount of CO_2 to cause the same GWP. Due to this, the EU introduced the F-Gas Regulations, which is phasing down the quantities of F-gases used in the EU market by producers and importers. The number of F-gases allowed to market is based on their CO_2e (REGULATION (EU) No 517/2014 OF THE EUROPEAN PARLIAMENT AND OF THE COUNCIL, 2014). This regulation is beneficial to the environment, but detrimental to the cost of many refrigerants, which made two common refrigerants R404A and R134A increase in price by 500% and 200%, respectively, over a 3-year period (Supply and demand: why refrigerant costs are soaring, 2018). Moreover, The European Chemical Agency issued a proposal on the 8th of February 2023 scheduling a six-month plan for bans of perfluoroalkyl and polyfluoroalkyl substances PFAS. The agency proposed the ban of fluorinated refrigerants, namely HFOs and HFCs, where suitable alternatives exist; and that ban is because of the risks to the environment and human health associated with the use of PFAS (ECHA, Proposal for a Restriction, 2023). This fact places more strain on refrigerants and make the search for viable alternatives more insisting.

Peters et al. (2018) stated that there were 3.6 billion cooling appliances around the world and this number was expected to multiply by almost five folds by the year 2050, as the world might have around 14 billion cooling appliances. All these reasons combined instigated a need for alternative cooling and heating technologies that are energy efficient as well as environmentally friendly. Therefore, several researchers started looking at the possibility of using solid state material-based technologies to produce clean heating and cooling, hence why the development of alternative heat pump/refrigeration technologies have been researched extensively. However, limited products have been developed in terms of alternative cooling technologies. Table 1.2 provides a summary of alternative cooling and heating technologies that were reviewed in this thesis.

Table 1.2: Alternative cooling and heating technologies

1- Magnetic Refrigeration	2- Electro-caloric Refrigeration
3- Thermoelectric Refrigeration	4- Thermo-acoustic Refrigeration
5- Stirling Refrigeration	6- Barocaloric Refrigeration
7- Elastocaloric Refrigeration	

Despite its good potential, the elastocaloric refrigeration, commonly known as Shape Memory Alloy (SMA) Refrigeration technology, has not been progressed into real application as it is either still at a conceptual modelling stage or in small laboratory set-ups. Many different SMA materials have been developed and the most common material for heating and cooling applications is NiTi, which is a blend of Nickel (Ni) and Titanium (Ti), also named as NiTiNOL in honour of its discovery at the Naval Ordnance Laboratory (NOL). NiTi can be alloyed with many different chemical elements like Copper (Cu), Ferrum (Fe), Rhodium (Rh), Palladium (Pd), Cobalt (Co) and Gallium (Ga), and each blend has different properties.

This project researched the potentials of two different SMA materials, i.e., NiTiX and NiTi, with regards to their thermophysical properties and ways of enhancing the latent heat available within the material. This study was carried out by means of two components:

(a) laboratory experiments using a set of equipment which included: Micrometre, Differential Scanning Calorimetry, Furnace and inhouse built horizontal compression rigs.

(b) Modelling using Computational Fluid Dynamics (CFD) software, namely, COMSOL MULTIPHYSICS.

1.2 Outline of the Thesis

This thesis is composed of seven chapters, which are outlined as follows:

Chapter 1: Introduction

This chapter introduces the subject of the thesis and explains the reasons and motivation of carrying out this project. It also introduces the chapters of the thesis.

Chapter 2: Literature Review

This chapter covers a review of the current literature on the energy status in the UK with a focus on the energy consumed to provide heating. The chapter also provides a review of the current literature on six emerging technologies that are considered solid state and are being researched currently. The chapter reviews these technologies from the standpoint of their basic working principle, core material, challenges and state of development, applications, and advantages and disadvantages. Thereafter, this chapter covers a comprehensive review of Elastocaloric Refrigeration, which is the main topic of this thesis.

Chapter 3: Preposition

This chapter identifies the gap in knowledge and presents the strategies in which this thesis was carried out to fill the gap and how the contribution to knowledge was planned and drawn. It also presents the aim and objectives of the project.

Chapter 4: SMA Modelling

This chapter presents a mathematical explanation of SMA properties and behaviour using the Lagoudas Model, which is one of only two models in existence to date that explains SMA behaviours. The chapter also explains how COMSOL was used to conduct the modelling through explaining the effects of different factors on the performance of the material. It covers how the material reacts to applying different loads, the activation temperatures, and the stress triggering points, which are stresses at which each phase of the SMA two phases (Austenite and Martensite) start and finish.

Chapter 5: Material Experiments and Model Validation

This chapter presents the experiments carried out on the two SMA blends, NiTiX and NiTi. It goes through the process of preparing the samples and testing them on the DSC device. Then it shows how liquid nitrogen was added to the DSC device to expand the testing range to understand the material better, as some phase transformations take place below -60˚C which is the lowest temperature the DSC covers prior to adding liquid nitrogen. This chapter also presents a comparison between the results obtained from the modelling versus those obtained from the laboratory experiments.

Chapter 6: Heat Transfer and Fluid Flow

This chapter presents an in-depth study of how to enhance the thermal outputs from SMA material. It covers a comprehensive explanation of how to design a system using SMA that can produce 3 kW heating load. The chapter studies different designs and geometries for SMA plates and how to incorporate them into a stack that can be used as the source of heat and the heat exchanger for an SMA-based heat pump. The chapter also covers the usage of different fluids and the methods used to enhance the fluids capability of picking up the heat from a heat source. It also provides a comparison between water and three nanofluids, namely water graphene oxide, which were composed by using three different concentrations of graphene oxide nanoparticles.

Chapter 7: Conclusions and Recommendations for Future Work

This chapter summarises the finding of the research project and draws the conclusion taking into considerations all the processes included in the previous chapters, as briefly explained above. This chapter also highlights the main contribution to knowledge and the significance of this research and how it can be used as a pilot for future research, highlighting the avenues in which future research can be carried out, as well as presenting ideas that can be visited by researchers; ideas which were not studied thoroughly in this thesis because they were beyond the purpose of this project.

The methodology followed throughout the project in which the two components of the thesis (experiments and modelling) were carried out, is embedded within the chapters as every chapter describes different tasks and the methodology followed to achieve those tasks. The methodology covers the reasons why COMSOL MULTIPHYSICS was selected to carry out the task of modelling, and it presents all the equipment that was used, the steps of the modelling, as well as any assumptions that were made during the work.

Chapter 2: Literature review

Chapter 2 Literature Review

2.1 Introduction:

The world has changed holistically since the industrial revolution in the nineteenth century. People's lives have become much easier thanks to the development of technologies. However, this development has come at the expense of the environment's integrity, as the climate is significantly affected by the increasing emissions attributed to burning fossil fuels to produce energy. Those emissions include but are not limited to: Carbon dioxide (CO_2), methane (CH_4), nitrogen oxide (N_2O), hydrofluorocarbons (HFCs), perfluorocarbons (PFCs), sulphur hexafluoride (SF_6), and nitrogen trifluoride (NF_3); they are all called greenhouse gases (GHGs). The emission of GHGs is the main reason the earth is warming, a phenomenon known as global warming, which is the main contributor to climate change.

Climate change can be attributed to man-made emissions of greenhouse gases, and there are tangible evidence supports climate change. The United Nations has been holding conferences highlighting the potential consequences of not reducing greenhouse gas emissions. Many scientists, professors, academics, and activists have been exerting pressure on governments urging them to act. They believe climate change is one of the biggest current threats to Earth. Figure 2.1 shows that, as of 2020, the earth's temperature has increased by one degree Celsius, and all the current efforts are exerted to stop the temperature rise from reaching 2 degrees Celsius. If warming reaches 2 degrees Celsius, then more than 70% of Earth's coastlines will see sea-level rise of more than 0.66 feet (0.2 meters), resulting in increased coastal flooding, beach erosion, extreme weather, salinization of water supplies and another broad spectrum of impacts on humans and ecological systems (Climate change explained, 2014).

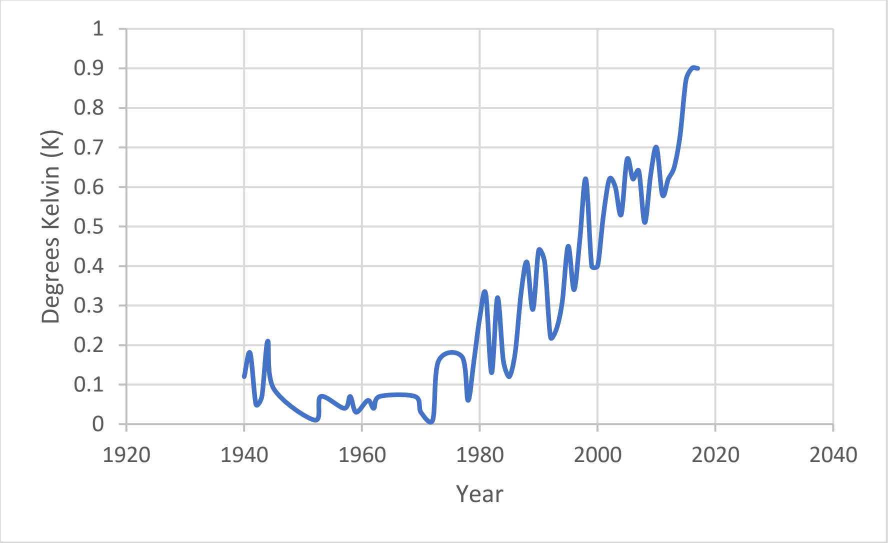

Figure 2.1: Earth warming in degrees Celsius (Nasa, vital signs of the plant, 2022)

The total UK emissions in 1990 were 605 million tonnes of carbon dioxide equivalent ($MtCO_2e$). Many sectors contributed to those emissions as follows: Electricity, gas, steam, and air conditioning supply had a total emission of 217 $MtCO_2e$, which represented 35.9% of the total emissions; Manufacturing contributed with 180 $MtCO_2e$, which represented 29.7% of the total emissions; Transport and storage emitted 66 $MtCO_2e$ which is 11% of the total emissions and households contributed with 142 $MtCO_2e$ which is 23.4% of the total emissions. The total GHG in the UK as of the year 2019 were over 550 $MtCO_2e$, which is 9% less than the emissions level in the year 1990. Comparing 2019 to the baseline (1990), we find that the emissions from electricity, gas, steam, and air conditioning decreased drastically to 88 $MtCO_2e$, and the manufacturing decreased significantly to 84 $MtCO_2e$. Households and transport increased to 148 $MtCO_2e$ and 80 $MtCO_2e$, respectively, as shown in figure 2.2. The emission as of 2021 dropped to 505 $MtCO_2e$ which is 16.5% less than the emissions in 1990; the new data for the emissions in 2022 will be released on Mar 30th, 2023 (UK Environmental Accounts - Office for National Statistics, 2022).

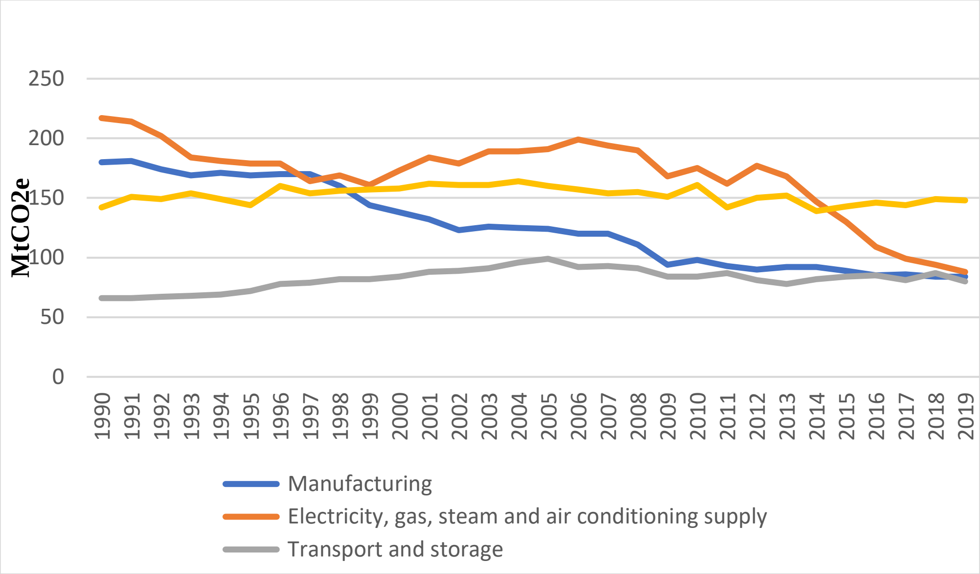

Figure 2.2: GHG emissions for the four highest-emitting sectors in the UK (UK Environmental Accounts - OFS, 2022).

GHGs emissions are directly attributed to energy use generated from burning fossil fuels. The UK's energy consumption in 2019 was 195 million tonnes of oil equivalent (MtOe), 88% of which was from fossil fuels. The four highest-emitting sectors, understandably, consumed the most energy; the energy use fell significantly for electricity generation because many renewable resources have come on board; and it as well fell for manufacturing as relatively cleaner resources such as natural gas has been used (UK Environmental Accounts - Office for National Statistics, 2022), as shown in figure 2.3.

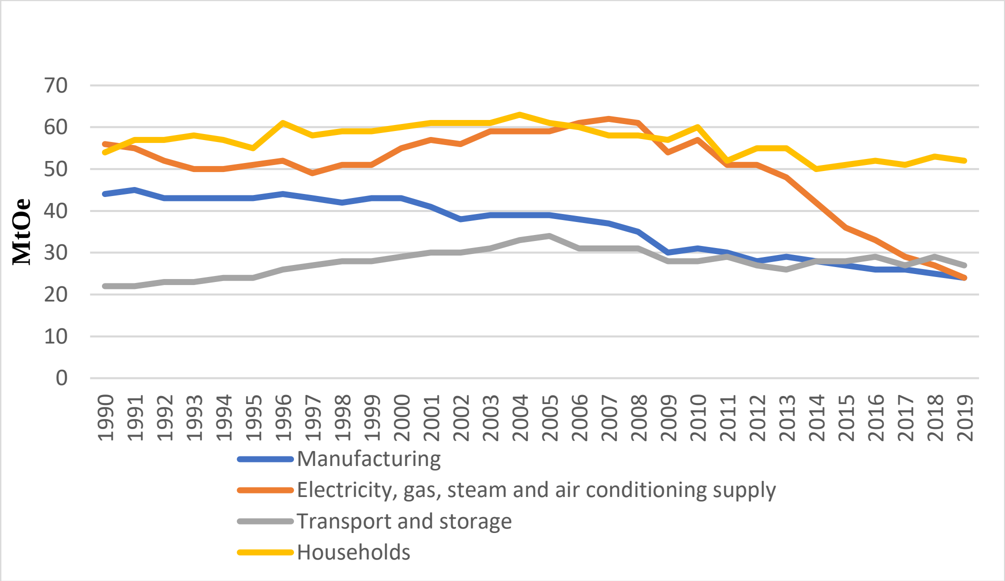

Figure 2.3: Energy use for the four highest-emitting sectors in the UK (UK Environmental Accounts - Office for National Statistics, 2022).

Electricity generation in recent years has become considerably cleaner compared to the electricity generation in 1990. In 1990, a high percentage of 72% of the electricity was generated from coal, one of the dirtiest fossil fuels, as carbon is the major component of coal. In contrast, there was no electricity generated from renewables. By looking at the electricity generation statistics for 2020, we find that renewables account for approximately 40% of the total electricity generation, (UK energy in brief 2021, 2022). However, the UK still largely depends on gas to cover its electricity demand, as gas covers more than 35% of the total electricity generated, as shown in figures 2.4 and 2.5 (UK energy in brief 2021, 2022).

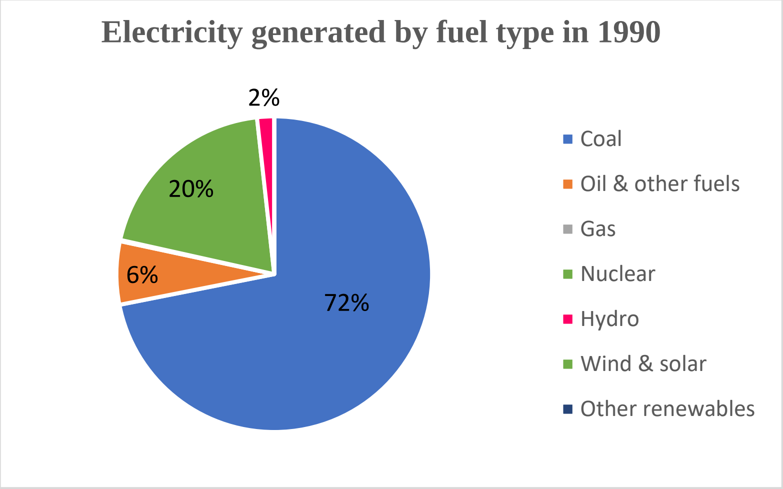

Figure 2.4: Electricity generated by fuel type in the UK in 1990 (UK energy in brief 2021, 2022)

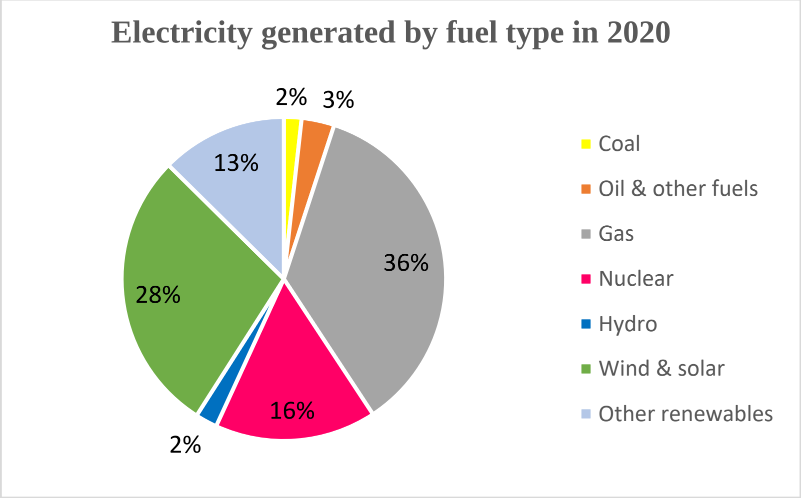

Figure 2.5: Electricity generated by fuel type in the UK in 2020 (UK energy in brief 2021, 2022)

Households' energy use refers to the energy consumed for space and water heating, space cooling or air conditioning, lighting, electrical appliances, and cooking; in other words, all the services that make the houses habitable, thus they are all called building services. The building services sector has the highest energy consumption, thus significantly impacting the climate. Buildings in the UK have direct and indirect emissions; the direct emissions are due to the leakage of the refrigerants used in the heating and cooling systems, whereas the indirect emissions are due to the electricity used by the systems in question. In 2019, the direct emissions from buildings were 85 $MtCO_2e$, 17% of the UK's GHG emissions; the residential on its own emitted 65.45 $MtCO_2e$, which is 77% of the direct emissions (The CCC – buildings, 2020). Whereas commercial buildings emitted 14% of the 85 $MtCO_2e$ and public buildings accounted for 9% of the direct emissions. The indirect emissions come from the electricity that buildings consume, which accounted for 59% of the electricity generated in the UK in 2019, as shown in figure 2.6.

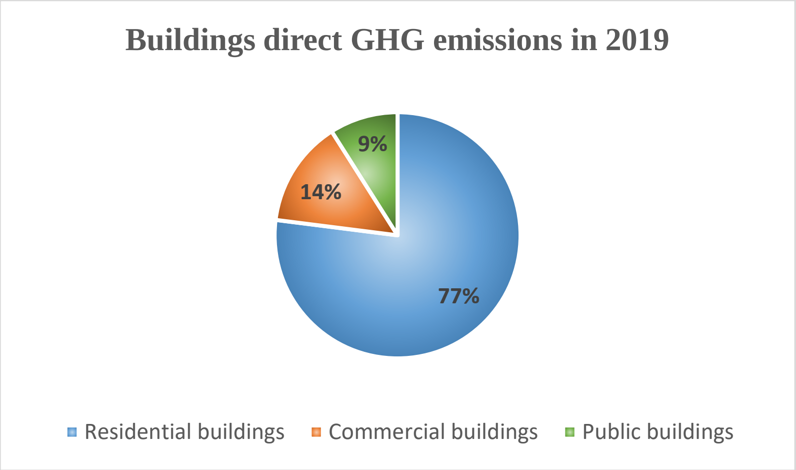

Figure 2.6: Buildings' direct GHG emissions in 2019 (The CCC – buildings, 2020)

Direct emissions from buildings are caused by burning fossil fuels for heating and the leakage of refrigerants. Almost 84% of the heating and hot water demand in the UK is dependent on natural gas and petroleum; the remaining 16% is covered by: 1- coal, which is not environmentally friendly; 2- biomass, around which there are many controversies 3- a small percentage covered by heat pumps. The old-fashioned methods of space and water heating that use fossil fuels have extremely high emissions; for instance, the CO_2 emitted per one kilowatt-hour (kWh) of delivered heat from an oil boiler is almost fivefold of those of a ground source heat pump. Figure 2.7 compares the emissions of different heating systems in gram of

CO_2 per kWh delivered heat (Amponsah et al., 2014; Houses of Parliament. Carbon Footprint of Heat generation 2016).

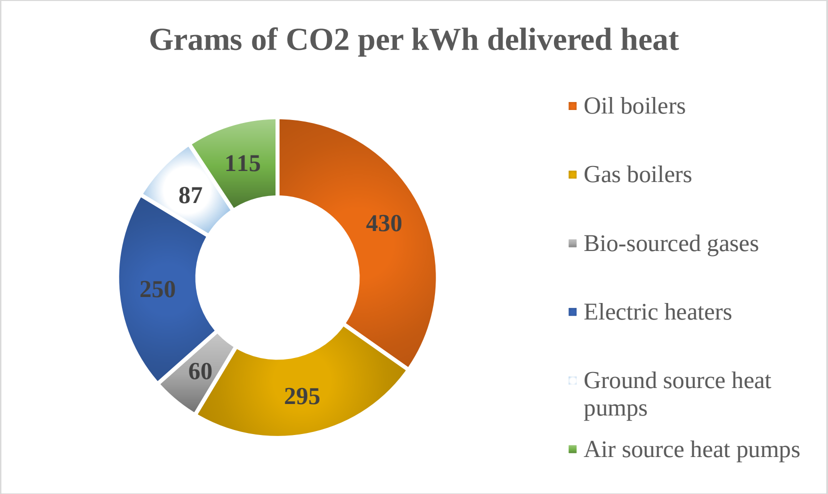

Figure 2.7: Grams of CO_2 per kWh delivered heat (Houses of Parliament. Carbon Footprint of Heat generation 2016).

Figure 2.7 shows that fossil fuels have significant CO_2 emissions, making them detrimental to the environment. Therefore, since heat pumps have very low CO_2 emissions when compared to their heating counterparts, they have recently gained wide popularity because they are considered an environmentally viable and economically attractive (in the long run) alternative to the old-fashioned heating, ventilation, and air conditioning (HVAC) systems.

The working mechanism of heat pumps depends on the vapour compression cycle (VCC). Heat pumps are composed of four main components: Evaporator, Compressor, Condenser and Expansion valve; and the medium that transfers the heat across the system is called the working fluid, which is a gas or liquid that moves the heat from a heat source to a heat sink. For better performance, the working fluid needs to possess a high thermal conductivity, a high latent heat of vaporisation, and low boiling and freezing points, so it can turn into a gas quickly and absorbs heat. Working fluids with those characteristics are called refrigerants, and there are many classifications for refrigerants.

2.2 Refrigerants:

Refrigerants are classified into different families which are Chlorofluorocarbons (CFCs), Hydrochlorofluorocarbons (HCFCs), Hydrofluorocarbons (HFCs) and Hydrofluoroolefin

(HFOs). These families are classified as per the substances they contain; for instance, CFCs and HCFCs families contain chlorine, as opposed to HFCs and HFOs, which are chlorine-free, and they are explained in subsequent sections. CFCs were the first refrigerants invented; they were found in the 1930s, and the first of the family was R12. Members of the CFC family, such as R11, R12, R114 and R502, and HCFC R22, have excellent thermodynamic properties and are non-toxic and non-flammable, making them very desirable and widely used equally in commercial and domestic refrigeration as well as in air conditioning. These refrigerants played a significant role in refrigeration and air conditioning; however, these refrigerants contain Chlorine which has a horrendous impact on the environment, as the existence of chlorine in the stratosphere depletes the Ozone layer, and a consequence for that they have been phased out **(**Hundy, Trott and Welch, 2016).

Over concerns about the environment, the Kyoto Protocol, and the Montreal Protocol, followed by F-Gas regulations, have instigated the change from CFCs and HCFCs into HFCs and HFOs with global warming potential (GWP). However, the direct emissions of these refrigerants still stand within the industry, which instigated the necessity of moving into lower GWP refrigerants.

F-gas regulations will limit the usage of R134a, R404A, R410A and R507A, which have GWPs of 1430, 3922, 2088 and 3985, respectively, and they are the most used refrigerants. From January 2022, all domestic refrigeration should not have a GWP of more than 150, and stationary refrigeration equipment should not have a GWP exceeding 2500, which means R134a, and R410A can continue to be used in stationary refrigeration equipment; however, their usage in domestic refrigeration has come to complete halt. R134a is replaced by R600a, whereas R404A is replaced by R407A/R407F from the HFC family and R448A/R449A from the HFO family. However, although these blends are only acceptable in commercial systems of 40 kW and more installed before January 2022, there was a ban, which came into effect in 2020, on servicing any system containing a refrigerant whose GWP is 2500 or more.

For domestic refrigeration, it was necessary to find alternatives for R134a and R404A, which have GWPs less than 150. Therefore it was found that HFC/HFO mixtures could provide viable options; R134a could be replaced by a wide variety of blends such as (AC5X, ARM-41a, D-4Y, N13, R450A, XP-10, AC5, R444A and ARM-42a), whereas R404A can be replaced by (ARM-30a, ARM-31a, ARM-32a, DR-33, N40, R448A, D2Y65, DR-7 and L40) and R410A can be replaced by (ARM-70a, D2Y60, DR-5, HPR1D, L41 and R447A) (Mota-Babiloni et al., 2015).

Ammonia and carbon dioxide are natural refrigerants with zero and one GWP, respectively. However, some of their properties make them inappropriate for all applications because Ammonia is toxic and flammable, and it corrodes copper, limiting its application in domestic refrigeration. At the same time, carbon dioxide requires very high pressures, which leads to a system with a low COP. Table 2.1 shows some of the currently in use refrigerants.

Table 2.1: Example of the currently in-use refrigerants (Mota-Babiloni et al., 2015; Jiang et al., 2021)

Refrigerant	GWP	Application	Status/ limitations
R134a	1430	Vehicle air conditioning, domestic refrigeration, and medium temperature commercial applications	150 < GWP < 2500, It cannot be used for domestic refrigeration since January 2022. It will continue to be used in stationary equipment.
R404A	3922	Medium to low-temperature commercial applications	GWP > 2500, It cannot be used for domestic refrigeration or large equipment
R410A	2088	Chillers and air conditioning systems	GWP < 2500, It will continue to be used in chillers and air conditioning systems (movable or stationary)
R32	705	Low evaporating temperature applications Boiling point: below -40℃	GWP < 2500, it can be used in stationary equipment where there is a necessity for a low boiling point
R125	3450	Low evaporating temperature applications Boiling point: below -40℃	GWP > 2500
R152a	148	Used in different fields of refrigeration and air conditioning as a replacement for the CFC R22	GWP < 150, this refrigerant can be used for domestic refrigeration
R1233zd	3.7	High-temperature heat pumps	HFO refrigerant that can replace R134a
R1234yf	<1	Proposed to replace R134a in vehicles air conditioning	HFO refrigerant that can replace R134a
R1234ze	<1	Proposed to replace R134a in water-cooled chillers and household refrigerators	HFO refrigerant that can replace R134a
R290	<1	Potential replacement of R22 in applications such as heat pumps	Flammable and achieves lower COP than R22
R717 (Ammonia)	0	Industrial refrigeration applications, food processing and storage	Toxicity, flammability, corrosivity, and high discharge temperature limit its application in domestic refrigeration

R744 (CO_2)	1	Commercial refrigeration	High operating pressures above 120 bar and low critical temperature lead to lower COP

2.3 Ozone Depletion Potential (ODP):

Earth’s atmosphere has five layers; the closest two layers to the earth's surface are Troposphere, which ranges between zero to ten miles; and the Stratosphere, which runs between 10 to 31 miles from the earth's surface. The ozone layer exists in the stratosphere, and its main job is to protect the planet from ultraviolet UV. Ozone (O_3) near the ground is a toxic gas that damages the lungs and causes asthma; however, when it is in the stratosphere, it forms layers that prevent two of the three types of ultraviolet radiation from getting into the earth. The importance of the Ozone layer comes from the fact that it absorbs UV-C and UV-B, which are highly harmful to living things, as depicted in figure 2.8. However, it was found that chlorine-containing substances such as CFCs and HCFCs, when they go into the stratosphere, get broken by ultraviolet radiation, and therefore they release chlorine atoms which break an ozone atom into an oxygen atom (O_2) and a chlorine monoxide molecule (ClO); any free oxygen atom would bump into the chlorine monoxide molecule setting the chlorine-free to attack another ozone atom, and thus the breaking of ozone atoms continues, as shown in figure 2.9. This process, in time, leads to ozone layer depletion and thus exposing earth to the horrendous ultraviolet radiation (The Ozone Layer | Centre for Science Education, 2022).

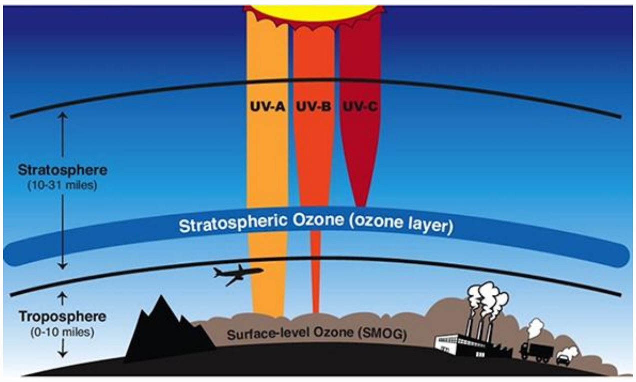

Figure 2.8: The different UV rays (The Ozone Layer | Centre for Science Education, 2022)

The Montreal treaty was held over concerns about the depletion of the Ozone Layer and its horrible consequences. The Montreal Protocol was signed on 16th September 1987; the participating parties agreed on phasing the substances that deplete the Ozone Layer by 1995. This new situation urged a significant necessity for the refrigeration industry to rapidly find alternatives to CFCs because they have an extremely high ozone depletion potential (ODP). The industry then decided to move to less ozone-depleting substances, so the industry found refuge in HCFCs, mainly R22. However, that relief did not last long, as a subsequent revision of the Montreal Protocol emphasised phasing out all ozone-depleting substances. Therefore, HCFCs usage will come to a complete halt by 2030. Moreover, the European Union in the year 2004 authorised a stricter regulation 2037/2000, which banned all the equipment that uses HCFCs, leaving the refrigeration industry in a new dilemma (Hundy, Trott and Welch, 2016; The Ozone Layer | Centre for Science Education, 2022).

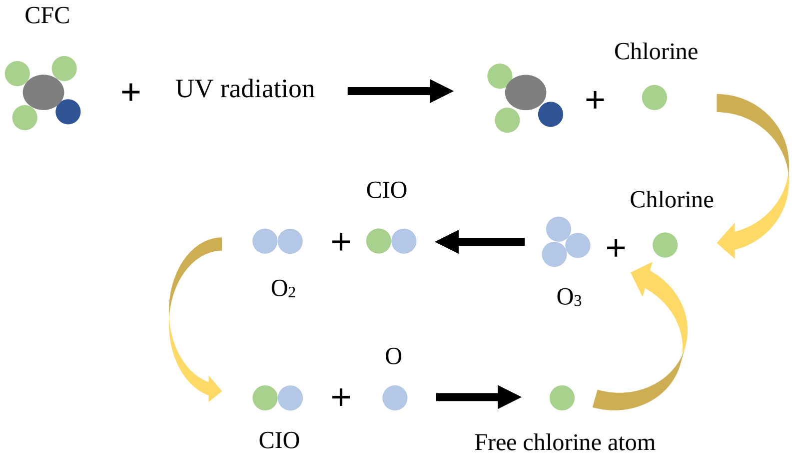

A free oxygen atom would break the CIO atom and set the chlorine free, allowing it to attack a new ozone atom; and the cycle continues.

Figure 2.9: The process of how chlorinated gases deplete the Ozone Layer (The Ozone Layer | Centre for Science Education, 2022)

After the refrigeration industry was faced with the fact that CFCs and HCFCs can no longer be used, the industry started looking for viable chlorine-free alternatives. HFCs were the answer to the industry's prayers; therefore, HFCs were developed and successfully applied in many applications. However, HFC substances have a high global warming potential (GWP), which makes their future nebulous, as they will eventually be phased out in the continuous endeavours to fight global warming (Hundy, Trott and Welch, 2016; The Ozone Layer | Centre for Science Education, 2022).

2.4 Global Warming Potential (GWP):

Global warming is the increase of earth's temperatures because of heat reflected onto the earth's surface due to the rise of greenhouse gases in the atmosphere. The most famous greenhouse gas is carbon dioxide CO_2, and thus it is used as a reference for measuring the global warming potential for different substances. Therefore, global warming potential (GWP) can be defined as an index that compares the impact of any chemical substance against the effect CO_2 has on the environment. For example, the refrigerant R134a, which belongs to the HFC family, has a GWP of 1430, which means one kilogram of R134a does the same damage to the environment as 1430 kilograms of carbon dioxide. This fact has brought concerns about the choice of refrigerant to be used in different HVAC applications because most HFCs have high global warming potential despite their zero-ozone depletion potential.

Despite the horrendous consequences refrigerants have, they are still do less damage when they are used in heat pumps compared to the old-fashioned systems that are used for heating building such as coal and gas. And since the direction is to phase out refrigerants, it was and still is of paramount significance to find viable alternatives that can deliver clean heating and cooling. This chapter reviews the use of heat pumps, as well as the recent advances in emerging alternative heating and cooling technology from basic working principle, challenges, state of development, applications, advantages, and disadvantages point of view; with a focus on Elastocaloric Refrigeration which is the main topic of this thesis.

2.5 Heat Pumps:

Heat pumps use refrigeration cycle to extract heat from a heat source and reject it into a heat sink; the four heat pumps are Air to Air, Air to Water, Ground Source and Open Loop. Heat pumps are expected to play a significant role in providing cleaner heating and cooling systems and thus reduce CO_2 and therefore participating in the Nearly Zero Energy Buildings (nZEB), which have become a requirement in Europe since 2020. Heat pumps are considered an effective low carbon heating solution because they use a small amount of electricity and achieve two to six folds of the electricity input as heating output.

The UK commits to achieving Net Zero by 2050. Therefore, the government plans to decarbonise the nation through the heat and buildings strategy. Decarbonising the UK is an ambitious plan that needs a lot of work and support, and hence the government introduced the Renewable Heat Incentive (RHI), as well as a grant of £5,000 that will be given to households to upgrade to low carbon technologies such as heat pumps; moreover, from April 2022, the government has scrapped the VAT on energy-efficient measures.

Heat pumps have a very high initial cost as follows: ground source heat pump (GSHP) costs between £20,000 to £40,000, air source heat pump costs between £8,000 to £18,000, and water source heat pump costs between £20,000 to £32,000. However, the running cost for heat pumps would be meagre compared to other heating means if electricity price was similar to gas price; and that because heat pumps achieve very high COPs (Heat Pumps: Types, Prices, Suppliers in 2022, 2022).

Heat pumps can be used for various applications, from water heating to space heating for residential and commercial buildings; they can also be used for large scale heating. Below table 2.2 shows some large-scale European projects in which heat pumps have been used successfully.

Table 2.2: Large scale heat pumps installed in European projects (Ehpa.org, 2022)

Project	Heating capacity	Refrigerant	Heating source	Supplied temperature	COP
Bergheim district heating system	865 kW	R744 (CO_2)	District heating water	90℃	3.1
Drammen district heating	13.2 MW	R717 (Ammonia)	River water	90℃	3
Skjern paper factory	5.3 MW	R717	Humid air	40℃	6.7
District heating in Fornebu/ Rolfsbukta	16 MW	HFP-1234ze	Water	75℃	4.4
Budapest Military Hospital	3.8 MW	R134a	Water	33℃	6.8
Budapest Military Hospital	3.8MW (cooling)	R134a	Water	6℃	7.3
Swiss Krono's chipboard factory	2 × 5 MW	R717	Ethylene glycol 34%	78℃	4.5

Table 2.2 shows how heat pumps can have a high performance in large scale applications; heating these projects using ordinary boilers or electric heating would incur a high running cost, whereas, with heat pumps, the running cost ranges between one-third to one-seventh of the heating capacity, depending on the COP. However, all these heat pumps use refrigerants, which means direct emissions are always possible. Thus, despite the considerable success these systems have achieved, they still threaten the environment due to refrigerant leakage. Moreover, there are already restrictions on using refrigerants with certain GWP, and these restrictions are getting tighter, hence many refrigerants are being

phased out. This has urged the necessity of developing heat pumps that do not use refrigerants as their working fluids; Therefore, research has been ongoing on this front in an insisting need of finding alternative heating and cooling technologies.

2.6 Emerging Heating and Cooling Technologies (Solid-state heat pumps):

Section 2.5 showed the current situation of heating and cooling systems and showed how the existing heat pumps, despite their good performance, will struggle to meet the future demand according to the Net Zero plan that has been put in place. This situation instigated the need to finding alternative technologies that are efficient and environmentally friendly. This section of the thesis explores the recent advances in emerging alternative heating and cooling technologies, with a focus on Elastocaloric Refrigeration Technology and the means of optimising the thermal output of Shape Memory Alloys (SMA), the core material of the technology.

2.6.1 Magnetic Refrigeration

2.6.1.1 Basic Working Principles for Magnetic Refrigeration

Magnetic refrigeration works on the principle of exposing paramagnetic materials to a magnetic field generated, preferably, by rare earth magnets as they have a stronger magnetic field. Paramagnetic materials have a high susceptibility to magnetic fields. They don’t retain the magnetic field when the external source is removed. They have paramagnetic properties due to the unpaired electrons, i.e., Magnesium, Lithium, Tantalum, etc.

Rare earth magnets are preferred over other magnets for their high magnetic anisotropy which gives the material high magnetic coercivity (resistance to being demagnetized), as well as for their high magnetic moment as they have many unpaired electrons which gives the material a high saturation magnetization. The maximum energy density is in a direct correlation with the saturation magnetization which means the magnetic field generated from a material like Neodymium is significantly high when compared to a magnetic field generated by a regular magnet (Peter C. Dent, 2012).

When a paramagnetic material is exposed to a magnetic field, the molecules in the material start to spin in one direction and align themselves in an orderly pattern. This process makes the material have a low specific heat capacity and expels heat. When the magnetic field is removed, the molecules go back to their original random pattern, causing the material to have a high specific heat capacity and therefore absorb heat. Figure 2.10 depicts the basic working principle of the technology (Gomez, J. et al., 2013).

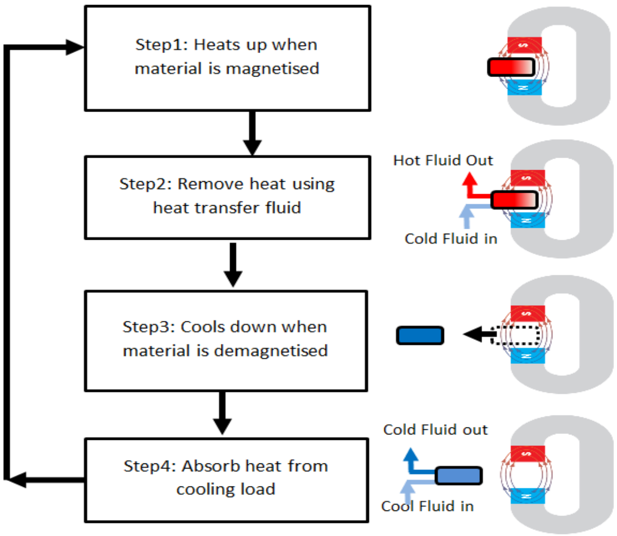

Figure 2.10: Schematic showing the basic working principle of Magnetic Refrigeration (Gomez, J. et al., 2013)

2.6.1.2 Working Materials

Magnetocaloric materials can generally be found in two main divisions which are: rare earth materials (containing crystalline and free crystalline) and Amorphous materials. The only pure rare-earth containing crystalline material is Gadolinium whose magnetocaloric effect can be improved by alloying it with other elements like Ferrum (*Fe*), Niobium (*Nb*) or Boron (*B*) and many other different chemical elements. Among all rare-earth containing materials, there are certain families whose good magnetocaloric effect attracted attention like: 1) A composition of Gadolinium (*Gd*) with Silicon (*Si*) and Germanium (*Ge*) with certain concentrations $(Gd_5Si_2Ge_2)$; 2) a composition of Lanthanum (*La*) with Ferrum (*Fe*), Silicon (*Si*) and Aluminum (Al) $La[Fe(SiAl)]_{13}$ and Rhenium (Re) containing compounds; 3) Laves phases materials, which are intermetallic compounds. The rare-earth free crystalline elements Ferrum (*Fe*), Cobalt (*Co*) and Nickel (*Ni*) showed a good Magnetocaloric Effect (MCE). In the other hand, the Amorphous materials which are classified into Gd-based and Fe-based show excellent properties in terms of their low hysteresis, low eddy currents, and their resistance to corrosion (Franco et al., 2018).

Magnetocaloric effect in materials can be enhanced by material processing such as hydrogenation, metal foam structuring and annealing at different temperatures to increase the grains size. Franco et al. (2018), through experiments, claimed that annealing at higher temperatures delivers better results. A high magnetocaloric effect is crucial in developing a magnetocaloric device, and so far, all the materials which have high MCE mainly depend on rare earth magnets, which 95% of their production is in China that has placed restrictions on rare earth magnets export.

2.6.1.3 Challenges and State of Development

Since the discovery of giant magnetocaloric effect by Pecharsky and Gscheidner in 1997, the research and development of this technology have been very active. Several (near room temperature) magnetic refrigeration prototypes were reported in many countries like the UK, USA, Japan, China, and several European countries.

Aprea et al. (2014) made a comparison between R134a refrigerant and two different geometries (porous and flat plate) of a 2 Tesla (T) active magnetic regenerator (AMR) using different rare earth magnets and water as heat transfer fluid (HTF). Aprea et al. used a mathematical model to calculate the COP and then made a comparison between (AMR) cycle, and the traditional vapor compression cycle (VCC), and the comparison was carried out in terms of ΔCOP, where:

$$\Delta COP = \frac{COP_{AMR} - COP_{VC}}{COP_{VC}} \tag{2.1}$$

where, COP_{VC} is the coefficient of performance for the vapour compression system and COP_{AMR} is the coefficient of performance of the active magnetic regenerator, which is calculated as the ratio between the cooling power the regenerator produces to the work input to the device (Eriksen, 2016).

Aprea et al. (2014) conducted experiments and their results showed first-order magnetic transition (FOMT) materials ($Gd_5Si_2Ge_2$, $MnAs_{0.9}Sb_{0.1}$, and $MnAs_{0.95}Sb_{0.05}$) have better energetic performances when compared to vapor compression systems, and they achieved $\Delta COP\ of + 1.69$. While the second-order magnetic transition (SOMT) materials (God, $Gd_{0.95}Dy_{0.05}$, and $Gd_{0.9}Tb_{0.1}$) achieved $\Delta COP\ of + 2.8$. The experiments also revealed that the geometry of the AMR plays an important role, and it was reported that the COP of the AMR cycle is better in the low mass flow rate when in a porous media regenerator, and the COP is better in the high mass flow rate in a flat plate regenerator (Aprea et al., 2014).

Olsen et al. (2014) published results from a numerical study on two active magnetic refrigeration models. The first model was designed utilizing, $500\ \mu m$ thick and 20 cm long, plates of graded Gd-like which achieved a maximum cooling power of 10 $kW.L^{-1}$, and the second model used thermal switch for controlling the heat flow in the magnetocaloric material (MCM) and the model achieved a maximum cooling power/volume of 34 $kW.L^{-1}$. In the same year, Gatti et al. 2014, introduced a hydraulic solution; the idea was implemented in a prototype with two linear stages with the ability to control the flow rate and heat transfer fluid's velocity. Gatti et al. 2014 achieved a temperature span of 33K at a volume flow rate of 6.6 $cm^3.s^{-1}$ and a frequency of 1 Hz; the test was run for a 1000 s and a heating load of 3.7 to 6.9 W was achieved. Then, by reducing the volume flow rate and the frequency to 4.55 $cm^3.s^{-1}$ and 0.55 Hz, respectively, a temperature span of 38K was achieved (Gatti et al., 2014).

Govindaraju et al. (2014) developed a time-dependent mathematical model of an AMR for large scale cooling (>1 kW). Govindaraju et al. (2014), through modelling, identified the characteristics required to achieve a cooling capacity as large as 50 kW. These characteristics are the diameter of Gd, room temperature, load temperature, utilization factor, frequency, the mass of MCM and magnetic field. They found that the cooling capacity is in direct relation with the mass of MCM, and the performance of AMR depends on the magnetic field as well as it could be improved by using a low viscosity and high heat capacity HTF. It was also found that the magnetic field and temperature span govern the COP and the utilization factor controls the temperature gradient.

Albertini et al. (2017) did some experiments on a prototype using Gadolinium as refrigerant and water as a medium for heat exchange. They carried out a preliminary investigation using a computational fluid dynamics analysis on a novel regenerator, and the results showed that the temperature distribution of Gadolinium decreased cycle by cycle which highlighted the effect of the regeneration.

Franco et al. (2018) carried out comprehensive research and studied magnetocaloric materials and their characteristics and directed the future research towards the discovery of new phases with a high magnetocaloric response. As well as looking at the microstructure of the material to achieve the engineering techniques of the refrigeration application.

The geometry of the material used could affect the performance of the AMR. Li et al. in 2019 assessed the performance of a gadolinium-based regenerator in a rotary type of magnetic refrigerator by altering the geometry of the gadolinium elements used in the AMR. They filled the AMR with three different shapes of Gadolinium pieces (Flakes, spheres, and plates). From experiments, they achieved 14.8K temperature span from flakes-filled AMR, and the temperature span dropped to 10.8K when the AMR was filled with sphere shape gadolinium pieces achieving a cooling power of 10 W. Huang et al. (2019) developed an experimental rotary magnetic refrigerator prototype named FAME cooler, and they used to assess how different MCM could affect the performance in a realistic environment. The AMR of their device was filled in with 1.18 kg sphere shape gadolinium pieces which produced 0.875 T. The FAME cooler achieved 162.4 W of cooling power at no temperature lift, and it achieved a temperature lift of 11.6K at zero cooling power. The maximum COP reached by the device was 1.85.

He et al. 2020 have constructed a device that allows testing three-cycle modes, which are series, parallel and cascade. The core MCM used is a 277 g of Gadolinium along with two Neodymium Iron Boron (NdFeB) permanent magnets which provide a magnetic field intensity of 1.5 T. From the study, they have found that the parallel mode improves the cooling power while the series mode increases the temperature lift. In contrast, the cascade mode has the highest temperature lift with a cooling capacity slightly less than the parallel mode's one. These results have been drawn as the temperature lifts achieved are 5.66K, 4.16K, and 7.35K in the series, parallel and cascade cycles, respectively; and the corresponding cooling powers are 29.02, 39.47, and 34.79 $W.kg^{-1}$. The study has not included the COP for each mode. Many other prototypes were reported, and the highest capacity reported was 844 W, and the COP ranged from 0.2 to 9.4 depending on the conditions under which the test was conducted. Therefore, this technology can be used only for a limited number of applications and in small-scale cooling/heating products.

The subject of magnetocaloric is vast, and the materials are not available yet as the existing materials are expensive and not abundant in the world (except in China), which makes the materials not suitable to be used for commercial devices. More focus should be put on machine design optimization using multidisciplinary support to achieve a design for Industrial applications. One of the critical factors that has not been researched is the materials ageing and its effect on the performance of the system and the device’s life span.

2.6.1.4 Applications for Magnetic Refrigeration

Magnetocaloric Refrigeration (MR) technology can be used for refrigerators working at room temperature as well as for cryogenic temperatures and in cooling and heating devices. Since 1953, there have been many attempts at building a working MR refrigerator. Still, none achieved an outcome which could be commercialized, for the highest cooling load achieved so far was less than one Kilowatt, and it was achieved by using an 890g Gd magnet which produced 1.5 Tesla (T). Which roughly means in the best scenario is one kilogram of rare earth magnet can produce one kW of cooling/heating, bearing in mind that the density of Gadolinium is $7900\ kg.m^{-3}$. This technology with its current state of development cannot be used for air conditioning in buildings.

2.6.1.5 Advantages and Disadvantages

This technology is still under research and its selling points when fully developed will be the fact that it is environmentally friendly, easy to switch between cooling and heating, run by the direct current which means less voltages, it does not require a chemical-based working fluid and water could be used as heat transfer fluid, high reliability, no moving part although this point is debatable because the magnet needs to rotate to alternatively expose the two plates to the magnetic field, and last but not least the technology is claimed to have unlimited life span which is also highly debatable, as there is no enough research on the material aging. On the other hand, this technology is extremely expensive, it has a bulky rotating magnet, requires rare earth metals, which are not easy to source, and it cannot be used for large scale with current fabrication technologies

2.6.2 Electrocaloric Refrigeration

2.6.2.1 Basic Working Principles for Electrocaloric Refrigeration

Correia and Zhang (2014) described the electrocaloric effect as “the isothermal entropy or adiabatic temperature change of a diaelectric material when an electric field is applied or removed”. Electrocaloric refrigeration works on the principle of applying an electric field on certain materials with certain dielectric properties. The applied electrical field makes the material change its temperature by changing the dipolar state, which results in a change in entropy which causes the material to expel heat. When the electric field is removed, the dipolar order returns to its original state, and thus the material absorbs heat, and this characteristic is called the electrocaloric effect (ECE), as depicted in figure 2.11. Kobeno and Kurtschatov in 1930 experimentally investigated the ECE for the first time. Despite this characteristic was discovered more than a hundred years ago, its microscopic physical picture is still not fully understood. However, on the macroscopic level, the ECE phenomenon can be described as entropy exchange between two entropy reservoirs (Kutnjak, 2015).

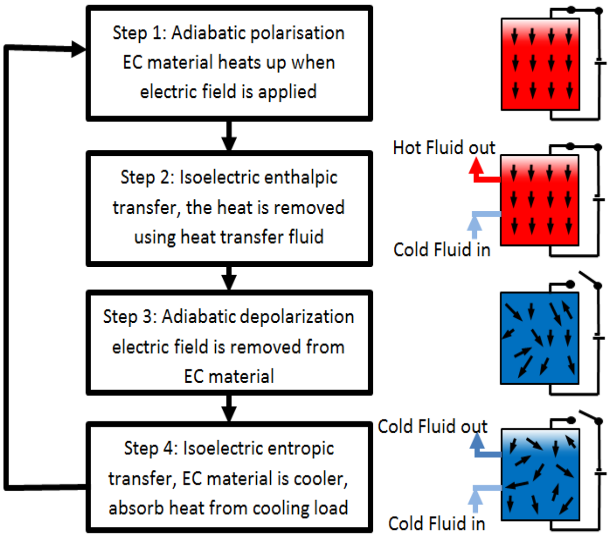

Figure 2.11: Schematics showing the basic working principle of Electrocaloric Refrigeration (Kutnjak et al., 2015)

2.6.2.2 Working Materials

ECE can be found in ferroelectrics, relaxor ferroelectrics (which are organic and inorganic disordered ferroelectrics) and Antiferroelectric. The lead-based relaxor ferroelectrics are the most studied materials, but due to environmental issues, the focus shifted to lead-free electrocaloric materials like $K_{0.5}Na_{0.5}NbO_3$–$SrTiO_3$ (KNN–STO) ceramics and $BaTiO_3$-based ferroelectrics (Kutnjak 2015). ECE has been known for too long, but it never drew the attention for commercial applications due to its small magnitude, until Mischenko et al. (2006) discovered the giant ECE. A giant ECE of ΔT = 12K was reported in Piezoelectric (PZT) thin films as well as in ferroelectric copolymer and terpolymer at near room temperature. Perovskites family showed high electrocaloric effect especially film relaxor perovskites $Pb_{0.8}Ba_{0.2}Zr_3$ as they achieved a temperature lift of 45K, which made this family among the most studied. There are many other different families who showed different levels of electrocaloric effects which include, but are not limited to, lithium niobate and lithium tantalite, hexagonal manganates, tungsten bronzes, pyrochlores, layered oxides, barium fluorides, molybdates, boracites, colemanite, halides, antimony sulfide iodides, triglycine sulphate, and ferroelectric polymers (Crossely S., 2013). Electrocaloric performance can be predicted by different measurements such as zero-field entropy change, pyroelectric coefficient, dielectric constant, and ferroelectric loops.

Among the above-mentioned families, Perovskites and ferroelectric polymers are promising for electrocaloric refrigeration for their high ECE, and they work at cure temperature of 83–763K and 350K respectively. However, all these families are lead-based materials which make their future use very nebulous, for lead is classified by European Chemical Agency (ECHA) as a very toxic material to aquatic life and can cause long-term damage in people like cancer, kidneys failure, anemia, or even death (Echa.europa.eu, 2019).

Since lead-based materials cannot have future in electromagnetic refrigeration, research has shifted focus onto finding less harmful and more environmentally friendly lead-free materials. Among the materials which have been studied is lead-free ferroelectric materials $Ba_{0.9}Sr_{0.1}Ti_{1-x}Sn_xO_3$ (with three different concentrations for Sn, x = 0.02, 0.05 & 0.10) which

is a composition of Barium, Strontium, Titanate, and Stannum. This composition showed ΔT = 0.188 K under an electric field of 7 $kV.cm^{-1}$ (Zaitouni et al., 2019).
Barium Strontium Titanate $Ba_{1-z}Sr_xTi\,O_3$ is widely studied, for it has an ECE potential. Zaitouni et al. (2019) conducted experiments and tested different compositions and concentrations, and they got the highest ECE with a temperature difference of ΔT = 0.34K under an electric field of 15 $kV.cm^{-1}$ while the highest ECE of Barium Strontium Titanate was ΔT = 0.207K under an electric field of 10 kV/cm. Which means to lift the temperature by 1K, an electric field of 44 $kV.cm^{-1}$ or 0.44 $kV.cm^{-1}$ is needed, provided the material used is BaSrTiSnO.

The density of Barium Strontium Titanate depends on Strontium's content, so if Sr increases from 0 to 0.5, the overall density of the compound drops from $5194\ to\ 4680\ kg.m^{-3}$(Abomostafa et al., 2018). Barium Strontium Titanate is available from different online suppliers for 12–23 US dollars per kg. And since the electrocaloric effect of any material is governed by the number of applied voltages which is challenging as it may be accompanied by the dielectric breakdown and current leakage. Therefore, if the required temperature difference (ΔT) is determined, then the required electric voltage can be determined, so can the size of the material and thereafter, the price could be determined as well.

2.6.2.3 Challenges and State of Development

Ozbalt et al. (2014) compared magnetocaloric and electrocaloric. To do so, they studied the effect of electric field and mass-flow on a thin-film electrocaloric ceramic refrigerator by applying three different electric fields of 32.9, 58.3 and 77.4 $MV.m^{-1}$, and by altering the water's mass-flow between 0.003 and 0.2 $kg.s^{-1}$under different frequencies. Whereas the magnetic field intensity in the Magnetocaloric regenerator was fixed at 1 Tesla. It was found that Electrocaloric refrigeration at higher temperature spans achieves higher theoretical COP; the COP drops with a higher electric field, but on the other hand, the cooling power increases. Whereas Magnetocaloric regenerator achieves higher cooling power with a smaller temperature span.

Aprea et al. (2016) used a 2D multi-physics model to test different ECMs working as refrigerants for an active electrocaloric refrigerator (AER) at room temperature under electric fields ranged between 0 to 100 $MV.m^{-1}$. They altered the mass flow rate of water to study the effect it can have on the performance. Their results showed that the best material for Electrocaloric refrigeration is PLZT ceramics, as it achieved a temperature span of 23K, a cooling load of 893 W and a maximum COP of 11.2. It was also found that there is a direct correlation between mass flow rate and cooling power.

Molin et al. (2016) tested two different multilayers ceramic (MLC) each of nine layers of $86\,\mu m$ and $39\,\mu m$ respectively, and they found that the electrocaloric response is independent of the layer's thickness. Molin et al. got an electrocaloric temperature change of 2.7K when applying an external electric field of $16\,kV.mm^{-1}$ and the result showed the significance of multilayer relaxor ferroelectrics.

Aprea et al. (2017) carried out a comparison between electrocaloric refrigerator working with an electrocaloric regeneration cycle (AER) using water as secondary fluid, and a commercial R134a refrigeration plant. The simulation showed that the COP is the highest when using thin films of PLZT materials and it also showed that using specific materials such as (PVDF n.s. 70 $MV.m^{-1}$, PST 77.4 $MV.m^{-1}$, PVDF n.s. 100 $MV.m^{-1}$) could produce higher greenhouse gas emissions compared to vapor compression system.

Following the restriction of lead-based materials by the European Union (due to their high toxicity), Shi et al. (2017) investigated lead-free ceramics (BCZT-Li) by citrate method which improved the electrical performance and made it possible to get a large electrocaloric effect.

Aprea et al. (2018) carried out a comparison between caloric materials operating in an active caloric regenerator using a numerical 2D model. The experiments were carried out on an AMR cycle with a frequency of 1.25 Hz, varying the mass flux between $150-250\ kg.sm^{-2}$. The experiments identified the most promising caloric materials for the four different technologies in question (Magneto, electro, elasto, and baro). The comparison was carried out using three main indexes which are COP, cooling power and temperature span. Aprea et al. concluded that the magnetocaloric materials (MCMs) including Gd (which is the best among its counterparts), have the weakest performance and that is due to the limited magnetic field produced by the permanent magnets. While the electrocaloric materials (ECMs), especially PLZT class, showed better performance as it achieved a temperature span of 40 K with a cooling load between 1 kW to 1.8 kW and a maximum COP of 15, which makes it applicable for a wider scope of applications.

Lu et al. (2019) studied the phenomenon of Joule heating, and they concluded that this phenomenon significantly reduces the refrigeration ability of electrocaloric materials at high electric field and temperature, as Joule heating is in direct relation with the electric field. Guvenc et al. (2019) looked at the influence aging has on electrocaloric effect on Lithium doped Barium Titanate ceramic ($Li\ doped\ BaTiO_3$) and they concluded that aging creates defect polarization, and its effect could be reduced by Li doping. Lu et al. synthesized the samples in question by using the conventional solid-state synthesis and found that aging changes the hysteresis loop and lowers the polarization. It was also found that aging has a negative and positive effect on polarization. Lu et al., through their work, concluded that it is possible to engineer the electrocaloric effect by using appropriate defect strategies. Planzik et al. (2019), on the other hand, studied the effect of the ECM's hysteresis and the electric energy recovery on the device's performance. They looked at these effects through a 2D numerical model that studies the characteristics of an AER's device. The results showed that the efficiency of the device is majorly affected by the degree of electric energy recovery and the hysteresis of the ECM used. Therefore, Planzik et al. highly recommended considering these two factors when designing an EC device. Based on the current situation, electrocaloric technology is considered a promising alternative to the vapor compression system, but it still needs a lot of research before it could achieve cooling and heating loads that will allow the technology to compete in the market.

2.6.2.4 Applications of Electrocaloric Refrigeration

All the Electrocaloric Refrigeration (ECR) prototypes and demonstrators designed and manufactured so far have not achieved high cooling/heating power nor a high-temperature span/difference. For instance, we found that Planzik et al. designed a cooling device using bulk ceramics, and they could achieve a temperature difference of 3.4 K at room temperature. While Zhang et al. achieved a temperature span of 5 K. The United Technology Research

Centre UTRC designed a gas-cooling electrocaloric device which reached a temperature difference of 14 K. Under the current state of development of ECR technology, it can be used in air conditioning of small size buildings as well as it can only be used in limited applications such as wearable coolers and cooling and heating vehicle seats (Shi et al., 2019).

2.6.2.5 Advantages and Disadvantages

Electrocaloric refrigeration technology depends on the electric field, which is easy and cheap to generate compared to the magnetic field. ECR has no moving parts (compressor free), which means less maintenance cost. In the other hand, the available EC materials are the lead-based materials which are toxic and can cause complicated health issues; therefore, more research into lead-free materials is needed; it was also proven that certain ECMs emit greenhouse gases. One of the issues with ECR is that the large electric field causes stress in the internal structure and that results in chemical degradation and electromechanical breakdown. Therefore, the fatigue life (aging) of the ECM needs more research and studying. It is not possible to apply a high electric field with low voltage on bulk materials unlike on thin films, but the energy that could be stored in thin films is very small, and that comes at the expense of the cooling power.

2.6.3 Thermoelectric Refrigeration

2.6.3.1 Basic Working Principles for Thermoelectric Refrigeration

Peltier first reported thermoelectric generator in 1834, and it is a solid-state semiconductor-based electronic device capable of converting a voltage input into a temperature difference which can be used for either heating or cooling. It also produces DC electrical current if a temperature difference is applied to the device.

The device contains ceramic substrates (Alumina, Beryllium oxide, or Aluminum nitride), p-type & n-type semiconductor elements, diffusion barrier (Ni) on the end of each element, and copper interconnects. The P & N semiconductors are wired electrically in series and thermally in parallel. When the current passes through the semiconductor, the lower side cools down, and the heat flows in reverse heating the top side of the thermoelectric cooler (TEC) (Yang et al., 2013). Figure 2.12 depicts the working principle of Thermoelectric Refrigeration.

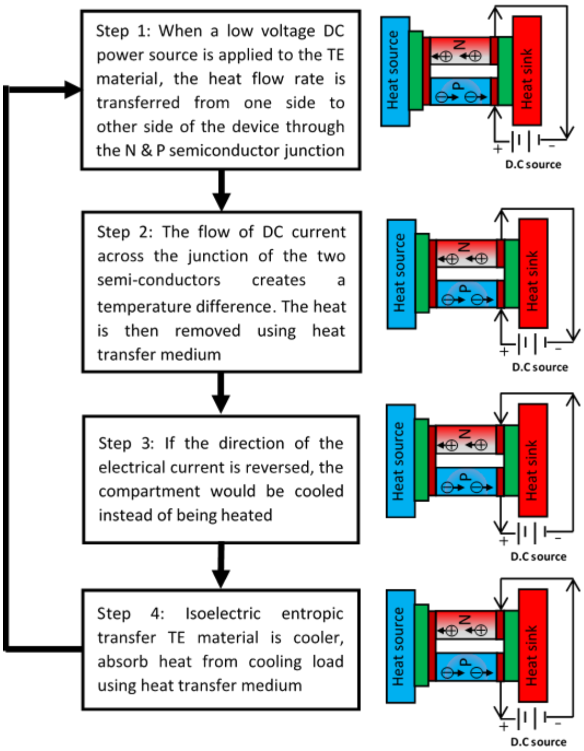

Step 1: When a low voltage DC power source is applied to the TE material, the heat flow rate is transferred from one side to other side of the device through the N & P semiconductor junction

Step 2: The flow of DC current across the junction of the two semi-conductors creates a temperature difference. The heat is then removed using heat transfer medium

Step 3: If the direction of the electrical current is reversed, the compartment would be cooled instead of being heated

Step 4: Isoelectric entropic transfer TE material is cooler, absorb heat from cooling load using heat transfer medium

Figure 2.12: Schematics showing the basic working principle of thermoelectric Refrigeration (Yang et al., 2013)

2.6.3.2 Working Materials

The classification of thermoelectric materials depends on their dimensions, as they are divided into low-dimensional thermoelectric materials and bulk thermoelectric materials. The performance of thermoelectric materials depends solely on the Seebeck coefficient (relation between thermoelectric voltage and temperature difference; best materials would have a Seebeck of 1.0), low thermal conductivity and high electrical conductivity. Thermoelectric materials come in chemical compounds of Bismuth Telluride(Bi_2Te_3), Lead Telluride ($PbTe$), Silicon Germanium ($SiGe$) and Cobalt Antimonite($CoSb_3$). Two of these families are not environmentally friendly, as $PbTe$ is lead-containing and therefore it is toxic; the other family $CoSb_3$ contains Antimonite which causes respiratory irritation as well as skin issues. It was also found that bulk materials of phonon-glass electron-crystal have a good thermoelectric potential as their electrons have high mobility (Zhao, 2014).

2.6.3.3 Challenges and State of Development

Thermoelectric generators (TEC) require a large DC current as well as an AC/DC converter which make them costly and have low energy efficiency. Because of that, they are mainly used in applications where reliability, silence and convenience are more important than the economic aspect. TEC has mainly been used in military, aerospace, industrial and scientific applications, but it was also introduced in small applications such as PC processors, car seats temperature control and portable food and beverage storages. TEC has low COPs of between 0.3 and 0.8 depending on the application as well as the ambient in which the application is operating (Zhao, 2014).

Navarro-Peris et al. (2015) ran experiments to investigate the energy output when the temperature difference is maintained by natural convention. The thermoelectric generator was tested by means of varying the hot and cold sides temperatures, and the results showed that the energy out is low. Therefore, this method was recommended not to be used.

Pietrzyk et al. (2016) presented a new factor for thermoelectric module design (B-factor) which is defined as the ratio of the area specified for thermoelectric material to the area of the module. Pietrzyk et al. developed a theoretical model and validated the model using three months' experimental data. They concluded that the module's performance is in a reverse relation with the contact resistance, and to ensure good performance, the leg's (P&N semiconductor pair) length should be increased.

Cao et al. (2017) designed a cooling helmet based on thermoelectric refrigeration. The helmet maintains a temperature of 24–30 °C when the ambient is below 40 °C, and the performance of the helmet drops noticeably when the ambient is above 40 °C. Xu et al. (2018) emphasized on the need of using synchrotron radiation in testing the thermoelectric materials, and they stated that the ideal TE materials should exhibit high electrical conductivity whereas the thermal conductivity should be low. Moria et al. (2019) took a different approach, as they studied a hybrid system where the TEC is energized by a solar cell. From the study, they achieved a COP of 4 at no temperature lift with a DC of less than 0.3 A.

Tian et al. (2020) have proposed, for the first time, changing the TEC from the ordinary flat shape into a tubular shape to design a thermoelectric air cooler. They have used a 3D numerical simulation in COMSOL multi-physics environment to study heat transfer rate, COP, and cooling power. The results have shown that the COP reduces significantly with increasing the DC voltage, whereas the cooling capacity increases with the increase of the DC voltage. The study also suggested that, to provide 2.5 kW of cooling capacity with a 100-litre per second of airflow, a greater number of tubular thermoelectric coolers are needed, which means more research into the tube-bundle arrangement is required. Shen et al. (2020) have also looked at thermoelectric technology from a design point of view as they have studied the thermoelectric element and they have concluded that the optimal number of segments for a thermoelectric cooler is two segments.

Cuce et al. (2020) have adopted a different approach, as they have studied the possibilities of improving the thermal output of a thermoelectric cooler through enhancing the properties of the heat transfer fluid by using different nanofluids. In this regard, they have studied three different nanoparticles (Al_2O_3, TiO_2, and SiO_2) with different particles sizes. The results have shown that when nanoparticles of Al_2O_3 are added to water, the temperature span of the system enhances as the cold side temperature dropped from −4.4 to −6.5˚C.

2.6.3.4 Applications of Thermoelectric Refrigeration

Thermoelectric devices have very low efficiencies and they cannot be produced economically at large scale with current fabrication technologies which limits the use of the technology to PC processors, car seats temperature control, and portable food and beverage storages.

2.6.3.5 Advantages and Disadvantages

This technology depends solely on electric current; therefore, it has no moving parts, which means less maintenance cost. Thermoelectric devices are light in weight, reliable and have an unlimited life span. On the other hand, all thermoelectric materials are costly and are less efficient than vapor compression technology except when the temperature lift is less than 5°C.

2.6.4 Thermoacoustic Refrigeration

2.6.4.1 Basic Working Principles for Thermoacoustic

The first time a theoretical study of thermoacoustic was carried out by Kramers in 1949 by generalizing the Kirchhoff theory of the attenuation of sounds waves. Thermoacoustic refrigerator has two main parts (driver and resonator), the driver houses the loudspeaker, and the resonator houses the gas, which is the medium in which the sound waves travel. The resonator houses two vital parts which are the stack and the cold and hot heat exchangers.

Thermoacoustic refrigerator (TAR) works on the principle of generating high amplitude sound waves (by the driver) in the resonator, which is a hollow tube filled with gas pressurized at several atmospheres (10 bar). The fluctuation of sound in the high pressure generates a high-temperature difference, which occurs across a stack of plates that are in between the two heat exchangers. The heat starts to flow from one side of the stack to the other, and therefore, one end heats up, and the other cools down, and this phenomenon is called the thermoacoustic effect, as shown in figure 2.13. The thermoacoustic effect is mainly based on Gay-Lussac's pressure-temperature law which states, "The pressure of a given amount of gas held at a constant volume is directly proportional to the Kelvin temperature" (Avent, A.W. and Bowen, C.R., 2015; Verma, 2014).

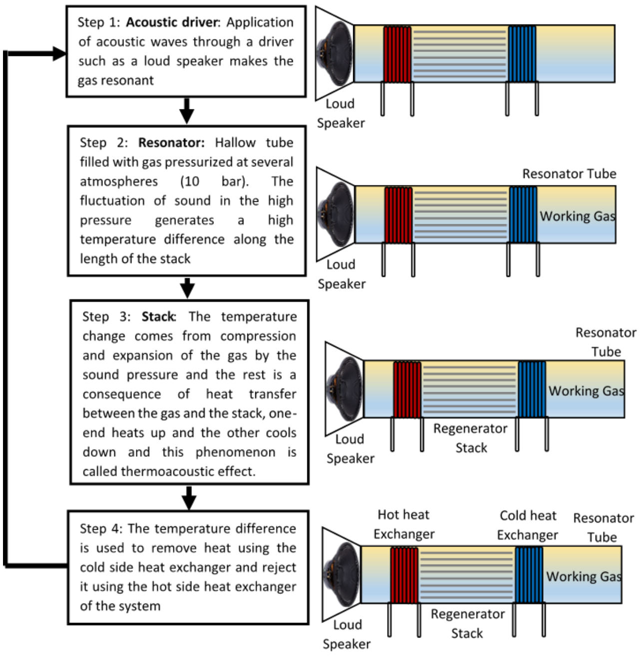

Step 1: **Acoustic driver**: Application of acoustic waves through a driver such as a loud speaker makes the gas resonant

Step 2: **Resonator:** Hallow tube filled with gas pressurized at several atmospheres (10 bar). The fluctuation of sound in the high pressure generates a high temperature difference along the length of the stack

Step 3: **Stack**: The temperature change comes from compression and expansion of the gas by the sound pressure and the rest is a consequence of heat transfer between the gas and the stack, one-end heats up and the other cools down and this phenomenon is called thermoacoustic effect.

Step 4: The temperature difference is used to remove heat using the cold side heat exchanger and reject it using the hot side heat exchanger of the system

Figure 2.13: Schematics showing the basic working principle of Thermoacoustic Refrigeration (Avent, A.W. and Bowen, C.R., 2015)

2.6.4.2 Working Materials

Thermoacoustic refrigerator does not have specific materials except those of the components of the device. The stack, for instance, needs to be made of a low thermal conductivity material, because otherwise, the performance of the stack will be affected. Many other factors affect the stack's performance, such as the spacing and the geometry (Bhansali, 2015). The thermoacoustic refrigerator also requires a medium in which the sound transfers to generate the cooling and heating, this medium needs to be an inert gas such as helium, helium-argon, helium-xenon, and helium-krypton, and they don't contain any toxic or injurious substances.

2.6.4.3 Challenges and State of Development

There have been many efforts in researching thermoacoustic refrigeration to develop an efficient Thermo-Acoustic Refrigerator (TAR). Nathad et al. (2018) designed and fabricated a TAR prototype (where helium pressurized at 1 bar was used as a medium gas) and tested it, and a temperature difference of 3 K was recorded in a one-hour test. The hot heat exchanger's temperature dropped 0.3 °C every 7.5 min, while the temperature of the cold heat exchanger rose 0.3 °C every 50 min. The output of the experiments was not satisfying to the authors as they designed the system to have a temperature difference of 30 K. This massive drop in the output was highly likely because of helium leakage, but it was difficult to test that as the gas was pressurized at atmospheric pressure. Nathad et al. concluded that to get a higher temperature difference, the following needs to be accounted for: 1) The stack holder should not be thick as this affects the heat transfer rate. 2) The loudspeaker used in the driver needs to be of a higher power. 3) The shape of the speaker has a significant effect, as if it does not fit properly into the tube, it might cause gas leakage and power loss which diminishes the Thermoacoustic effect.

Saechan et al. (2018) described delta modelling and fabricated a laboratory demonstrator which achieved a minimum temperature of −8.3 °C at a storage condition of +8 °C at a 7 W cooling power. Saechan et al. (2018) studied eight different locations for the cooler along the resonator at different frequencies (58.6 and 70.3 Hz) and found that the optimum cooler's location is 2.52 m away from the generator. In this respect, Mishra et al. (2017) after conducting experiments for high-temperature gradient, concluded that the best location for the stack was 1 cm from the top and it was also found, by hit and trial, that the optimum frequency is 369 Hz. Saechan et al. concluded that, to achieve higher cooling load, future research should include instance tuning of the acoustic network, which will result in reducing the phase difference between the regenerator and the volumetric velocity.

Wang et al. (2019) wanted to benefit from the wasted heat produced by the heavy-duty vehicles engines to cool down the cab and the sleeper; therefore, they proposed and simulated heat-driven thermoacoustic refrigerators and analyzed the simulation results. The concept of the idea is that the cooling power is secured by harnessing the acoustic work produced by the engine. The results showed that a cooling power of 3.1 kW could be obtained at a COP of 0.41. Xu et al. (2020) have done a similar study to what Wang's group did. Xu et al. have studied a thermoacoustically driven refrigerator for low-grade heat recovery using gas-liquid resonator. The study has considered the liquid volume ratio and the mean pressure, and the results have shown that a cooling power of 2.7 kW can be achieved with a system's efficiency of 67% when increasing the pressure as the overall performance is determined by high amplitude wave pressure and low working frequency.

Wang et al. (2020) have investigated and have numerically studied multi-stage travelling wave thermoacoustic refrigerator using SAGE software and have compared the results to a single-stage refrigerator. The results have shown that the cooling power of a single stage of 2.17 kW has increased to 6.42 kW achieving an increment of 195% for a seven-stage refrigerator, and the COP increased from 2.60 to 3.19. Thermoacoustic technology has seen some noticeable progress in recent years as better cooling loads were achieved. This technology may find a market within certain fields as vehicle cooling for the technology can benefit from acoustic work produced by vehicles engines.

2.6.4.4 Applications of Thermoacoustic Refrigeration

Thermoacoustic technology is not yet fully developed, and its efficiency in its present development state is lower than that of the vapor compression system. There is not a system working on Thermoacoustic principle commercially available yet. Thermoacoustic refrigeration, when fully researched and developed, can have the potential of covering a wide range of applications from cryogenic temperatures to food applications and domestic appliances.

There is room for development in structural design as well as enhancing heat transfer within the stack and between the heat exchangers and the stack. Also, different gases at different pressures need to be studied, e.g., nitrogen, argon, and different gas mixtures, such as helium-argon, helium-krypton, and helium-xenon.

2.6.4.5 Advantages and Disadvantages

Thermoacoustic refrigerators have no moving parts, and it is considered reliable, simple, and run at a very low cost. This technology can also be operated by converting waste heat into sound waves. Thermoacoustic technology is still under research, and currently, it has minimal efficiencies as well as small temperature spans.

2.6.5 Stirling Refrigeration

2.6.5.1 Basic Working Principles for Stirling Refrigeration

The Stirling cycle is one of the most famous thermodynamics cycles, and it can be used as a refrigerator, heat pump, and an engine. There are three types of Stirling engines:

1. Alpha engine: this type has two power pistons, and that makes it heavier than the other two types (beta and gamma). Both pistons are connected to a crankshaft, where the hot and cold pistons are 90 degrees apart, the crankshaft moves in and out within two cylinders. The alpha engine works on the following principle:

- Expansion: The gas heats up and expands and drives both pistons in the crankshaft.
- Transfer: Then the momentum of the flywheel carries the engine through the next 90 degrees, this causes most of the air to be transferred over to the cold cylinder.
- Contraction: The majority of the expanded gas shifts over to the cold cylinder, it cools and contracts which sucks both pistons outwards, away from the crankshaft.
- Transfer: The same transfer operation is repeated to transfer the air to the hot cylinder and thus complete the cycle.

2. Beta engine: this type has one cylinder, one piston and a displacer which shuttles the air back and forth with the cylinder. When the displacer moves away from the hot side, it

forces the air to go to the cold side, and thus the air heats up, expands, and the piston gets pushed outwards. Reversely, when the displacer moves towards the hot end, it causes the air to go to the cold side and cools down, contracts and the piston gets sucked inwards. In beta engine, the displacer and the piston are 90° apart.

3. Gamma (low-temperature differential): Gamma engine works by using the temperature difference between two metal plates, and this engine is complex as it has many components. Gamma engine is composed of two plates (bottom & top or hot & cold), displacer (contains a displacer cylinder and a rod), flywheel and a power piston with its supporting rod.

This engine works when the displacer moves up and down, causing the air within the cylinder to be in contact with either the hot or the cold plate. When the air is in contact with the hot plate, the air heats up, increases in volume and forces the power piston upwards. Similarly, when the air is in contact with the cold plate, it cools, contracts in volume, and creates a partial vacuum within the cylinder, the higher atmospheric pressure outside forces the power piston down in its cylinder. When the power piston is made to move by the changing pressures, it transfers this force through its connecting rod to the flywheel. This, in turn, forces the displacer rod to move as it is connected to the flywheel through the crankshaft, and so the cycle can continue, as shown in figure 2.14. The power piston must always be 90° behind the displacer on the crankshaft, and this allows the air inside the displacer cylinder to either expand or contract (Getie, M.Z. et al., 2020).

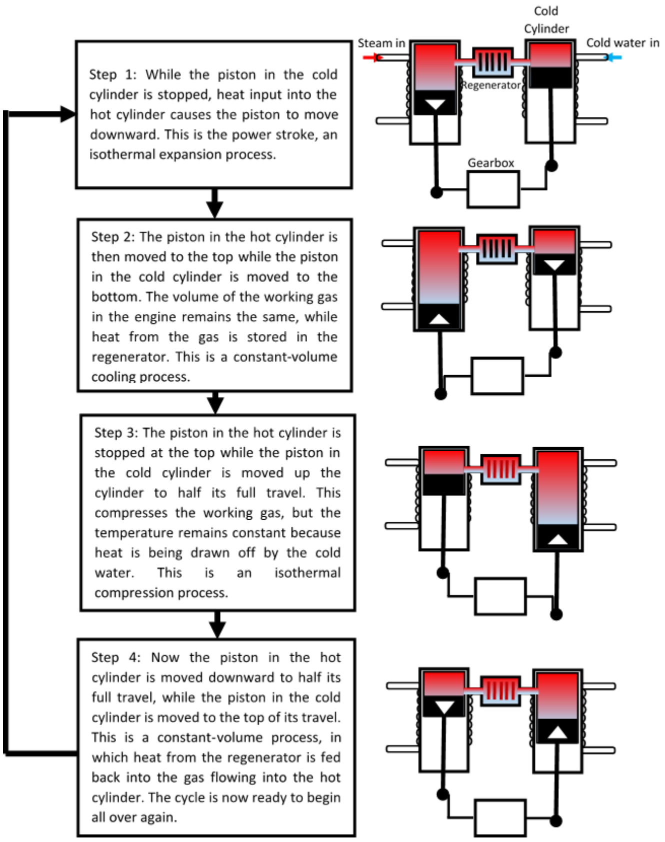

Step 1: While the piston in the cold cylinder is stopped, heat input into the hot cylinder causes the piston to move downward. This is the power stroke, an isothermal expansion process.

Step 2: The piston in the hot cylinder is then moved to the top while the piston in the cold cylinder is moved to the bottom. The volume of the working gas in the engine remains the same, while heat from the gas is stored in the regenerator. This is a constant-volume cooling process.

Step 3: The piston in the hot cylinder is stopped at the top while the piston in the cold cylinder is moved up the cylinder to half its full travel. This compresses the working gas, but the temperature remains constant because heat is being drawn off by the cold water. This is an isothermal compression process.

Step 4: Now the piston in the hot cylinder is moved downward to half its full travel, while the piston in the cold cylinder is moved to the top of its travel. This is a constant-volume process, in which heat from the regenerator is fed back into the gas flowing into the hot cylinder. The cycle is now ready to begin all over again.

Figure 2.14: Schematics showing the basic working principle of Stirling Refrigeration (Getie, M.Z. et al., 2021)

2.6.5.2 Working Materials

Stirling engines do not have specific materials other than the components mentioned in each one of the three types. However, Stirling engines use air, helium, nitrogen, and hydrogen as their working fluids, and all these gases are inert, and they do no harm to the environment.

2.6.5.3 Challenges and State of Development

The main barrier and challenge of commercializing this technology in its present state is the fact that it has low cooling/heating capacities as well as a low efficiency when compared to vapor compression systems, as well as the high cost for some of the gases used in the technology. However, besides the direct use of the Stirling engine in cooling and heating, it can also be used to improve the performance of other technologies. Gao et al. (2016) studied a hybrid refrigerator which combines magnetic refrigeration effect with Stirling cycle effect at room temperature. This hybrid refrigerator was built using sheets of Gadolinium (*Gd*) as the regenerator, and a rotating Halbach permanent magnet secured the magnetic field (0 to 1.4 T), all these components were placed in a helium-gas (heat transfer fluid) filled alpha type Stirling engine. The hybrid system achieved a cooling power of 40.3 W and 56.4 W over-temperature difference of 15K and 12K, respectively. Gao et al. concluded that the performance of the hybrid system improved by 28% when compared to the performance of a stand-alone Stirling cycle.

Ahmad et al. (2017) used COMSOL to develop a small-scale alpha Stirling Cryocooler and investigated the factors that affect the performance, such as operating speed, phase angle and heat exchanger length. The results showed that the best performance could be achieved with a phase angle of 90° and a heat exchanger length of 142 mm, and they also concluded that further length hinders the heat transfer. The Cryocooler achieved a cooling power of 455 W at a heat sink of 193 K with a COP of 0.57. Hachem et al. (2017) modelled an air-filled beta type Stirling refrigerator in terms of operations and geometrical parameters. The model was validated by experiments, and the results showed that the maximum COP could be achieved at a certain speed which is totally different to the speed at which the maximum cooling capacity could be achieved, which makes achieving maximum COP comes at the expense of attaining maximum cooling capacity and vice versa. The results also showed that the cold temperatures are reached by increasing the swept volume of the cold chamber. Hachem et al. concluded that the losses are in direct relation with the dimension of the engine and the optimal dimensions are a diameter of 22 mm and a length of 60 mm.

Gadalkareem et al. (2019) proposed a design for a hot and cold-water dispenser where the heat rejected by the engine was used to secure the hot water. Gadalkareem et al. developed a mathematical model and evaluated the device’s performance, and the results showed the Stirling cycle has a high potential in water coolers as a cold temperature of 10°C and hot of 95°C could be achieved. It was also proven that the cycle consumes the least electric power when used in water dispensers.

2.6.5.4 Applications of Stirling Refrigeration

Stirling refrigerators proved themselves successful in many applications, and that is due to their high reliability in terms of fast cool-down as well as their lightweight and low power consumption. Since Stirling refrigerators can achieve low temperatures, the demand for their use in Cryocoolers massively increased. Therefore, Stirling refrigerators are very efficient for water dispensers as well as they can be used in food applications such as small portable refrigerators and freezers, and in beverage vending machines. The literature showed no attempt of a large-scale cooling/heating device based on Stirling cycles.

2.6.5.5 Advantages and Disadvantages

Stirling engines, when used in refrigeration, are reliable and have a quick response in terms of cooling and heating as well as their lightweight, which makes them ideal for small portable applications. On the other hand, Stirling refrigeration so far has very low capacities and need more research before it could be commercially available for bigger scales. The system also has moving parts which means more maintenance will be required and therefore a higher running cost.

2.6.6 Barocaloric Refrigeration

2.6.6.1 Basic Working Principles for Barocaloric Refrigeration

The Barocaloric refrigeration cycle has four main processes: adiabatic compression where the Barocaloric material gets compressed and the second process is the heat transfer from the cold to the hot heat exchanger, the third process is the decompression which is followed by the fourth process where the heat transfers from the hot to the cold heat exchanger, as depicted in figure 2.15. The Barocaloric cooling is also known as active Barocaloric regenerative refrigeration cycle (ABR). The ABR has four main cycles which are: adiabatic compression, heat transfers from the cold heat exchanger (CHEX) to the hot heat exchanger (HHEX), adiabatic decompression, and heat transfers from HHEX to CHEX (De Oliviera, N.A., 2011).

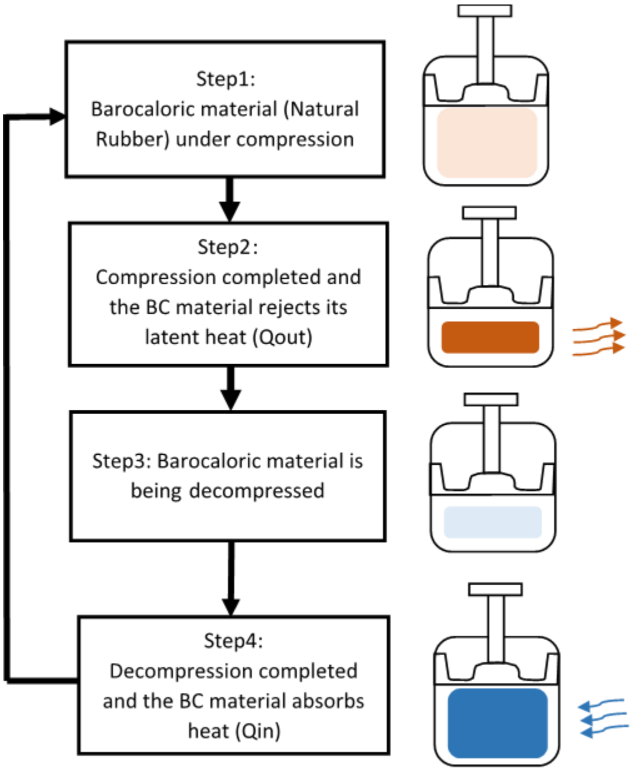

Figure 2.15: Schematic showing the basic working principle of Barocaloric Refrigeration (De Oliveira, N.A., 2011)

2.6.6.2 Working Materials

The main Barocaloric materials used in ABR are natural rubber and elastomers materials as they exhibit giant Barocaloric effect (BCE). The Barocaloric effect occurs when a Barocaloric material is put under pressure and therefore, the material response by expelling and absorbing heat because of the pressure. The most used heat transfer fluids in Barocaloric refrigeration are water and water-glycol mix as well as Nano-fluids.

2.6.6.3 Challenges and State of Development

Natural rubber heats up under stress and cools down when the stress is removed. This particular property is called the Barocaloric effect, and it was noticed for the first time by John Gough in 1805. Bom et al. (2017) studied the giant Barocaloric effect in natural rubber, which has higher entropy and temperature difference among its counterparts. Bom et al. through experiments found that a temperature difference of 25 K can be achieved at a stress of 390 MPa at 314 K, the results also showed that a change in entropy (ΔS_T) of 96 $J.kg^{-1}.K^{-1}$ can be achieved at a stress of 173 MPa at 290 K.

Aprea et al. (2019) investigated, via a two-dimensional model 2D, the effect on heat transfer in an ABR using vulcanizing rubber as core material and Nanofluid (ethylene glycol-water) as the working fluid. Vulcanized rubber is a treated rubber with sulfur and heat to exhibit high strength, elasticity, and durability. Aprea et al. studied the heat transfer between the ABR and the working fluid by varying the concentration of the fluid as well as adding Copper (Cu) to the mixture. The results showed that adding 10% Cu to the mixture enhances the heat transfer by 30%.

2.6.6.4 Application of Barocaloric Refrigeration

The literature on Barocaloric technology is very minimal, and there are no comprehensive studies and review nor experimental results, as it is still in the early stage of research.

2.6.7 Elastocaloric Refrigeration

2.6.7.1 Basic Working Principles for Elastocaloric Refrigeration

Since the discovery of NiTi in 1961, shape memory alloys (SMA) attracted a great deal of attention in many different applications due to their unique physical properties. SMA when experiencing external force, they change phase from martensite to austenite in what is called forward transformation, where the material undergoes a significant temperature change as they release latent heat (exothermic process). When the SMA is unloaded, they undergo a reverse transformation where the material changes phase from austenite to martensite absorbing heat from the surrounding (endothermic process), as shown in figure 2.16. This phenomenon is called Elastocaloric effect which can be used to generate heating and cooling and is considered one of the potential alternatives to vapour compression system. The performance of SMA is governed by many factors such as the composition of SMA, the percentages of the substances, the loading strategy (tensile, compression, torsion or bending) and the geometry of the pieces used as core materials (rods, tubes, plates… etc). Elastocaloric has two phases, Austenite and Martensite, and each phase has two activation temperatures at which each phase starts and finishes (Austenite start, Austenite finish, Martensite start, & Martensite finish). Each activation temperature happens at specific stress, depending on the material properties, as follows:

σ^{Ms}: Stress at which the Martensite phase is activated.

σ^{Mf}: Stress at which the Martensite phase ends.

σ^{As}: Stress at which the Austenite phase is activated.

σ^{Af}: Stress at which Austenite phase ends

The material starts rejecting heat when the martensite state is activated, and at σ^{Mf} the material rejects all its latent heat, and the material starts absorbing heat from the surrounding at σ^{As}.

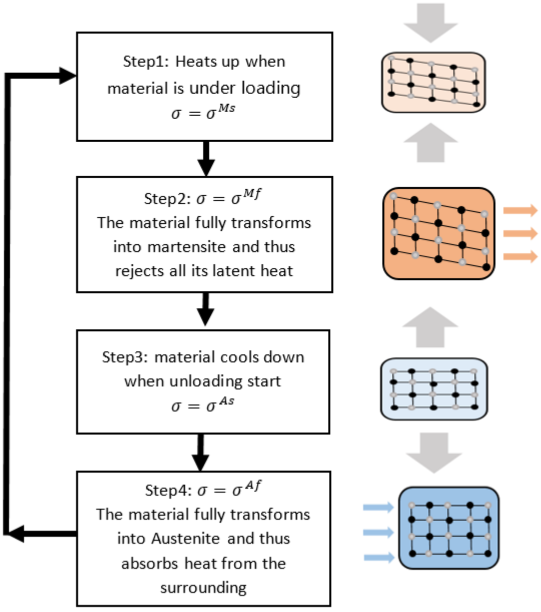

Figure 2.16: Schematics showing the basic working principle of Elastocaloric Refrigeration based on information obtained from Shape Memory Alloys by Lagoudas (Lagoudas, 2011)

2.6.7.2 Working Materials

The main Elastocaloric Material ECM is called Shape Memory Alloys. There are many different SMA materials and the most common material for heating and cooling applications is a blend of Nickel (Ni), and Titanium (Ti) and this blend (NiTi) is also named NiTiNOL in honor of its discovery at the Naval Ordnance Laboratory (NOL). NiTi is the most used in heating and cooling applications for its superior biocompatibility and fatigue behavior, as well as its high-temperature span and high entropy change. However, NiTi can be alloyed with many different chemical elements like Copper (Cu), Ferrum (Fe), Rhodium (Rh), Palladium (Pd), Cobalt (Co), and Gallium (Ga), and each blend has different properties with respect to adiabatic temperature, hysteresis, and fatigue life. For instance, when NiTi is doped with Cu, the blend will have a temperature difference of around 10 K as well as its fatigue life significantly enhances thus it can withstand millions of cycles; but on the other hand, copper reduces the latent heat. There are two other common groups of shape memory alloys, which are Cu-based alloys and Fe-based alloys. Cu-based blends like CuZnAl and CuAlNi have smaller hysteresis, which means less energy dissipation, and they as well require less stresses to fully transform from one phase to another (Tusek et al., 2016).

Since different blends have different properties, the loading strategy decides which blend is better for the application in question. There are four main loading methods, which are compression, tension, bending and torsion. In compression, we find that the Elastocaloric effect is sustained for a longer time and the potential for defects and cracks to grow and propagate is limited, therefore a better fatigue life. On the other hand, we find that loading in tension provides a rapid heat transfer and a higher temperature difference for smaller stress. However, the electrocaloric effect deteriorates in tension. Bending can be likened to compression, as the loading happens in the inner part of the bent piece, while the loading in tension occurs in the outer part. In bending mode, the stress-induced phase transformation remains incomplete due to the resulting strain profiles and the neutral axis. There’s no literature on using torsion for heating/cooling applications.

2.6.7.3 Challenges and State of Development

The literature revealed very limited research on this topic. Most of the literature is at the level of the material and not the application of the material in heating and cooling systems. The implementation and usage of SMA for cooling and heating are discussed below:

Qian Suxin (2015) carried out experimental research on SMA thermoelastic cooling system and evaluated the performance potential and limitations of this emerging new technology. A prototype was designed and fabricated at a maximum cooling capacity of 100 W, of which 65 W was achieved at a maximum temperature lift of 4.2 K. Qian’s design was based on Nitinol tubes arranged in a hexagonal layout in two conjugated beds under compression. Qian claimed that NiTi tube’s thermal mass does not allow heat transfer with high frequency, and that might be a limitation to increase the cycle’s frequency. To solve this issue, Qian used a thinner wall with smaller thermal mass per NiTi tube, and inserted plastic tubes inside the loading plate and the loading metal and that is to reduce the heat transfer between the heat transfer fluid (HTF) and the metal surfaces (Qian 2015).

Qian did not look at properties' losses, adiabatic compression losses and mechanical losses of the material. Qian only looked at minimizing heat transfer loss and cyclic loss and found that the cyclic losses are caused by the dead thermal masses (masses of the material used to support the tubes and to apply the loading, and those masses do not contribute in the efficiency of the system, in contrast, they reduce it) inside the system as the dead thermal mass of Heat Transfer Fluid (HTF) neutralizes the heat generated by the thin NiTi tubes and this case is exacerbated with high frequencies. Therefore, the performance of the system is limited by the parasitic loss caused by HTF heat dissipation, conduction to dead thermal mass and metal parts. Qian also concluded that the material level irreversibility causes performance degradation, which accounts to around more than 40% efficiency loss. Qian also observed that thermoelastic cooling works better in small to medium temperature lift applications (Qian 2015).

Hinnerk Ossmer was the second person to conduct research on the feasibility of using SMA to produce micro-cooling. The main two objectives for Ossmer's work were identifying suitable materials for elastocaloric micro-cooling after profoundly understanding their thermo-mechanical behaviours, as well as investigating the engineering tasks that would allow actual heat pumping for miniature scales. Ossmer explained the procedure of manufacturing different SMA blends and different ways of testing their properties such as differential scanning calorimetry, tensile test, infrared thermography, and digital image correlation. Ossmer also investigated different SMA geometries (films and foils) under different ways of loading (tensile, compression and bending) for elastocaloric micro-cooling. Ossmer found that the NiTi-based foils and films have the highest temperature changes as their self-cooling can get to −15 K and they could achieve a maximum temperature lift of 14 K and a COP of 6.7 for a temperature span of 6.3 K (Ossmer H., 2017).

Ossmer also found that thin SMA samples provide better cooling and heat pumping on a small scale, as they allow better heat transfer due to their large surface-to-volume ratio. Ossmer also stated that the highest COP is obtained for NiTiCuCo films as they have a low hysteresis comparing to their counterparts, whereas NiTi samples showed a strong functional degradation (Ossmer H., 2017).

Ossmer ran some experiments on a demonstrator that was built using NiTiFe foil bridges and the sink/source were fabricated from several copper segments. The experiments showed that decreasing the masses of sink and source did not result in increasing the temperature lift, which represents a challenge for small-scale applications (Ossmer H., 2017).

Kirsch et al. (2017) designed an SMA based air conditioning system. They used swash plates to convert rotary movement into linear movement as well as an inclination angle which allows loading (tensile) and adjusting the SMA strain during the rotation. This design allows for the use of a larger amount of SMA in a smaller assembly space. Through investigations, Kirsch et al. found that a combination of an adiabatic and an isothermal cycle shows the best performance. In this work, Kirsch et al. presented the concept of a continuously operating air-cooling device without having mentioned any information about COP and temperature lift.

Qian et al. (2019) proposed a heat-driven elastocaloric cycle using a high-temperature SMA. They built a 32 NiTi SMA wires with 1 mm diameter and divided the wires into four bundles; each bundle contains eight wires. This system showed a temperature difference of 26 K under no load, and it produced 0.64 $W.g^{-1}$ but under zero temperature difference. They also found that the prototype can be driven by a temperature below 80 °C.

Besides the studies mentioned above, many other studies on the implementation of SMA in cooling/heating systems were carried out without success in scaling up the output of the systems in question. In 2016, the Technical University of Denmark collaborated with the University of Ljubljana in an SMA device project, and they achieved a temperature span of 15.3 K at a COP of 3.5. The attempts continued, and Engelbrecht et al. (2017) designed an SMA device using 10 NiTi plates under tension, and they achieved a temperature span of 19.9 K and a heating power of 800 W per kg. Their device failed before completing 6000 of active elastocaloric regenerator (AER) cycles, which makes it impossible for the device to be commercialized. Kirsch et al. (2018) worked on a cooling device using NiTiCo-based alloys, and they achieved a cooling power of 250 W with a temperature span of 10 K and a COP of 9.5. Researchers at the University of Saarland in collaboration with Karlsruhe Institute of Technology designed a single-stage cooling/heat-pumping device using NiTi sheets under tension, and their device achieved a temperature span of 7 K (Kabirifar et al., 2019). There have also been attempts to achieve microscale cooling devices; the last attempt was carried out by Bruederkin et al. in 2018, where they presented a microscale system that achieved a temperature span of 14.8 K (Gerco 2019).

2.6.7.4 Applications of Elastocaloric Refrigeration

Elastocaloric refrigeration can cover a broad spectrum of applications thanks to the ability of adjusting the Austenite and Martensite activation temperatures. This technology can be used in domestic cooling and heating devices, large heat pumps for large scale cooling and heating as well as in heating and cooling vehicles.

2.6.7.5 Advantages and Disadvantages

This technology has been researched in different institutions and by other research groups in the last five years; and it is considered one of the most promising alternatives for vapor compression system, and that is because it doesn’t have the problems its counterparts have. The other emerging technologies either depend on toxic materials, incredibly expensive materials or have low efficiencies. Moreover, the Elastocaloric technology:

1- Is scalable, however, it is still unknown if it is economical at large scale.
2- Its core material is environmentally friendly, cheap, and abundant.
3- Theoretically, it has high efficiency and high COPs.

In the other hand, this technology is relatively new and still needs more research before it could be commercially available.

2.6.7.6 Heat Treatment on SMAs

Researchers also found that SMAs performance can be altered with heat-treatment processes. Elibol et al. (2015) studied the martensitic transformation in pseudoelastic Ni-rich NiTi bar whose diameter is 12.7mm, under tension, compression, and compression-shear. The specimens were hardened at 349.85 °C for an hour and were water-quenched at room temperature. Elibol et al. (2015) concluded that the transformation proceeds homogeneously with simple compression, whereas the transformation in compression-shear is inhomogeneous. However, the compression-shear requires less stresses.

Ossmer et al. (2013) studied the applicability of NiTi films for cooling; the films used in the experiments were 1.75mm wide and 35mm long with a thickness of 20 μm. The samples were annealed at 650 °C for 10 min and at 450 °C for another 10 min. The Differential Scanning Calorimetry (DSC) results showed that the Austenite finish (As) temperature is 20 °C which makes the films pseudoelastic at room temperature, hence the experiments were carried out at room temperature. Ossmer et al. (2013) started the experiments at a very small strain rate of $10^{-4}s^{-1}$ and no release of latent heat was recorded because the heat exchange with the environment was very fast. Then the strain rate was increased to $1.0\ s^{-1}$ and a decrease of temperature of 16K was recorded; providing that the specific heat capacity of the material used $C_p\ is\ 0.45\ Jg^{-1}K^{-1}$, and $\Delta T = L/C_p$, then the latent heat absorbed is $7.2\ J.g^{-1}$. Yang et al. studied NiTi wire under two different loading rates of 0.5 mm/min and 5 mm/min, and three different boundary condition; the experiments showed that the metallic grips work as a heat sink which leads to a smaller temperature variation when compared to the second boundary condition, in which the ends of the wires are insulted; therefore, there was no heat flux between the NiTi wire and the ambient.

Ben Faraj et al. (2017) studied the influence of heat-treatment on a Ni-rich NiTi bar under compressive behaviour. The specimens were annealed at various temperatures ranged from 500 °C to 700 °C for an hour, and thereafter they were water quenched. The compressive loading experiments were carried out at 37 °C. Ben Faraj et al. (2017) observed that the rhombohedral R-phase occurs when the sample are annealed at temperatures below 650°C; and it was also observed that the Austenite start, and finish temperatures (A_s & A_f)

significantly decrease with the increase of the heat-treatment temperatures (HTT). However, increasing the HTT creates Ni4Ti3 precipitates which reduce the concentration of Ni content, and as a result, the Martensite finish (Ms) temperature increases noticeably. It was also observed that the stress at which the martensite phase starts σ_s^M is significantly influenced by the HTT. Duerig et al. (2015) studied the R-phase on the superelastic behaviour of NiTi and concluded that R-phase requires very small stress comparing to Martensite phase; and the thermal hysteresis for Austenite to R-phase is around 1/6 to 1/10 the thermal hysteresis for Austenite to Martensite transformation. Khoo et al. (2018) after running heat-treatment experiments on NiTi, they found that annealing NiTi samples at 400°C for 5 min creates high density Ni4Ti3 precipitates and consequently enhances transformation strain. Xun Khoo et al. advised against heat-treating NiTi samples above 400°C, they claimed that annealing at higher temperatures degrades the material's properties. Li et al. compared between as-cast and heat-treated $Ni_{51}Ti_{49}$ and found that the as-cast specimen undergoes three stages transformation process (A→R→M1) and (R→M2) during cooling, and two stages (A→R→M) during heating; whereas the heat-treated specimens undergo two stages transformation process (M→R→A) during heating, and one stage (M→A) during heating. They also concluded that the sample heat-treated at 773°C and 823°C have stable strain energy and better superelastic properties. Kang et al. observed forward and reverse plateau when they increased the heat-treatment of a NiTi bar, with 55.8% at Ti%, from 400°C to 450°C; and they observed a decrease in Young Modulus. They also compared between two different samples heat-treated for 30 mins and 15 mins and found that the stress at which Austenite phase finishes reduced from 350 MPa to 170 MPa, respectively. Shen et al. investigated the effect of heat-treatment on Elastocaloric effect of a Ni-rich $Ni_{50.4}Ti_{49.6}$ rods under compression. The samples were annealed at 300 °C for an hour and thereafter aged at 275°C for 125 hours. The samples were trained under two different stresses of 1200 MPa and 1500 MPa, to stabilise the R-phase transformation. It was observed that the heat-treated samples showed less deformation and thus a better stability during the training. It was also noted that heat-treatment enhanced the energy dissipation.

Kato (2020) has studied SMA blends and has compared the latent heat in different NiTi composition with different concentrations of Nickel Ni content ranged between 48% to 51%

with an increment of 0.5% of the percentage of Nickel. The samples were prepared through solution treatment (oxidation layers) and were aged at 1100°C for 10h; thereafter, the samples were water-quenched at room temperature. The experiments showed that the peak temperature is in a reverse relationship with the Ni content, whereas the latent heat started at below 30 $J.g^{-1}$ for 48% at Ni% and increased until it reached a peak of 36.2 $J.g^{-1}$at 50% of Ni content in forward transformation; and - 38.6 $J.g^{-1}$ in reverse transformation.

2.7 Summary of the technologies reviewed.

Table 2.3 summarizes the seven technologies reviewed in this chapter.

Table 2.3: Summary of the emerging heating and cooling technologies

Technology	State of Development	Barriers	Presently Available Capacity	Technical Information				Efficiency/COP of Currently Available Systems	Current/Potential Area
				Key Material	**Material's Availability**	**Working Principle**	**Technology Readiness Levels (TRL)**		
Magnetocaloric	R&D focuses on MCM and machine design optimization	Materials are not available, and the technology can't be used for large scale with the available current fabrication technologies	>Up to 890 W >The technology doesn't store energy as the energy gets rejected under a specific circumstance	Rare earth magnets	95% of the global material production is in China	Rotating magnet to expose the paramagnetic materials to a magnetic field—moving part	3 to 4	Highest of 9.44 at 17.8 W (1.1 kg of Gd; HTF: water) Lowest of 0.7 at 0.46 W (70 g of GdEr/Gd; HTF: Helium)	Mobile refrigerators and cryogenic temperatures
Electrocaloric	>R&D shifted into lead-free materials as lead is classified as a toxic substance >Manufacturing of electrocaloric material and electrodes >Compact structures that offer high electric field	To produce high EC, large electric fields and required and they cause stress in the internal structure which results in chemical degradation and electromechanical breakdown	Few watts to 2 kW	Ferroelectrics, relaxor ferroelectrics & Antiferroelectric	Lead-based material available but more research into lead-free materials are required	Electric field	1 to 2	7 to 10	Wearable coolers and heating and cooling of vehicles seats
Thermoelectric	Current research focuses on: >Improvement of the intrinsic efficiencies of thermoelectric materials >Optimization of cooling system's thermal design	Thermoelectric devices have low energy efficiency; and they cannot be produced economically at large scale with current fabrication technologies	Few watts	Semiconductors	Available	DC current	4	0.3–0.8	PC processors, car seats temperature control and portable food and beverage storages
Thermoacoustic	>Structural and mechanical design	thermoacoustic prime mover generally requires a high-	Few watts to 6.5 kW	No special material except those	Available	Sound waves	4	up to 3.2	cryogenic temperatures, food applications, heavy-

	>Heat transfer within a stack and with heat exchangers > Different gases	temperature heat source to achieve effective acoustic power output, which is a huge barrier to utilizing the low-grade heat source		of the components					duty vehicles and domestic appliances
Stirling	studies on combining Stirling cycle with other novel technologies like magnetic refrigeration to generate higher cooling performance	Manufacturing cost and the challenges of differential expansion and linear generator design is a major barrier to the introduction of Stirling-cycle heat-pumps and refrigerators, particularly when competing against the very large-scale production of vapor compression technology	Few watts to 1 kW	No special material except those of the components	Available	Mechanical movement —moving parts	4	<1	Cryocoolers, water dispensers, portable refrigerators and freezers and beverages vending machines.
Barocaloric	Early R&D stage (materials and cycles)	Natural rubber has a very short fatigue life	Few watts on modeling	Natural Rubber	Available	Stress in tension or compression —moving parts	4	6	Miniature cryocoolers
Elastocaloric	Materials characterization, system engineering and stress strategies	System's complexity and many components	<1 kW	Shape Memory Alloys	Available	Stress in tension, torsion, or compression —moving parts	3 to 4	>9	Domestic cooling and heating devices, large heat pumps for large scale cooling and heating as well as in heating and cooling vehicles

2.8 Summary

Emerging alternative technologies are expected to play an important role in the transition into environmentally friendly cooling and heating systems. Many alternative systems have been and are still being researched vigorously by different research groups in different countries. None of the seven technologies which have been critically evaluated in this thesis has been commercialized yet. The literature showed that the magnetocaloric technology has a long way to go as the materials are still unavailable globally, and when found, they will need to be studied thoroughly from different perspectives, especially materials aging as this decides the life span of the magnetocaloric device. Similarly, electrocaloric technology has its materials challenge as the lead-based materials are toxic and detrimental to human's lives. Therefore, more research into lead-free materials is needed for this technology to compete. On the other hand, thermoelectric and thermoacoustic technologies have not yet achieved satisfactory efficiencies and COPs, and they are, so far, confined in small applications and for research purposes. There are two other technologies that work on the same principle which are Barocaloric and elastocaloric; the chances for Barocaloric to progress are very limited due to the short fatigue life of natural rubber which is the core material of the technology. Conversely, elastocaloric is the most promising technology among its alternative counterpart technologies, and that is for the abundance of its core material as well as the scalability, as this technology when fully developed can cover a wide spectrum of heating/cooling loads from a few kilowatts to a few hundreds of kilowatts.

Chapter 3: Preposition

Chapter 3 Preposition

3.1 Overview

The literature review on elastocaloric refrigeration showed that all the designed and manufactured prototypes to date either work under tension or under compression for pipes. The experiments also showed that deciding tension for a heat pump device is not practical despite its excellent heat transfer potential, as the material under tension tends to break a lot quicker, as any cracks on the surface of the material grow and propagate, and that leads to the failure of the material. On the other hand, compressive loading has a longer fatigue life, as the cracks and impurities do not grow and propagate. However, compressive loading requires certain geometries to avoid problems such as buckling. The literature showed that in one of the attempts, compression was used as the loading strategy for NiTi tubes, and in that project, the designer used plastic supports to restrain buckling, and that compromised the heat produced as well as the heat transfer, and thus the performance of the device. Therefore, if compressive loading were to be considered for an SMA heat-pump, special attention should be paid for the geometry, taking into account the effectiveness of the heat-transfer between the material and the heat transfer fluid (Qian S., 2015).

A few researchers attempted designing elastocaloric refrigeration systems; Qian, for instance, managed to get as little as 65 W of cooling with a temperature lift of 4.2K (Qian S., 2015). Other research groups faced different issues such as short fatigue life which halted their progress towards achieving a working system that could produce heating or cooling and will have a decent life span.

Most of the research in the field of elastocaloric is carried out from the material's point of view rather than from the system's point of view. That is where this project comes in to bridge the chasm, as it looks at the material from latent heat point of view; it looks at the amount of latent heat available within the material and how to extract that latent heat. It understands how the material behaves in relation to the activation temperatures under different heat treatments; and how it behaves under different amounts of applied mechanical loading. It looks at how the ambient temperature could potentially influence the material reactions and thus the overall system behavior.

The target of this project is to design a system that can produce 3 kW of heating load, and it considers compression as its loading strategy to avoid the material failure other researchers encountered in their projects. Therefore, after the material behavior has been understood, and the amount of available latent heat has been identified, the project moves onto looking at how to achieve the required heating load through designing different geometries. And since the loading strategy is compression, and to avoid buckling issues, the SMA material in this project is designed as plates. The plates are then stacked on top of each other to form a stack which acts as the heat source; to remove the heat from the heat source, the stack was provided with slots to allow the fluid to pass through the stack and thus expanding the heat transfer surface area and harvesting the most amount possible of heat by heat transfer fluids.

To achieve this vision, different geometries for the plates and for the slots were designed and simulated in COMSOL MULTIPHYSICS to understand the performance of the plate in relation to their ability of rejecting the most amount of latent heat onto a working fluid. The last section of this project covers how to enhance working fluids to pick up more heat from SMA material in shorter time; the importance of this step comes as the cycle time plays a significant role in enhancing the system’s overall COP. Figure 3.1 shows the sequence in which the work was carried out, as well as the tools used for every step.

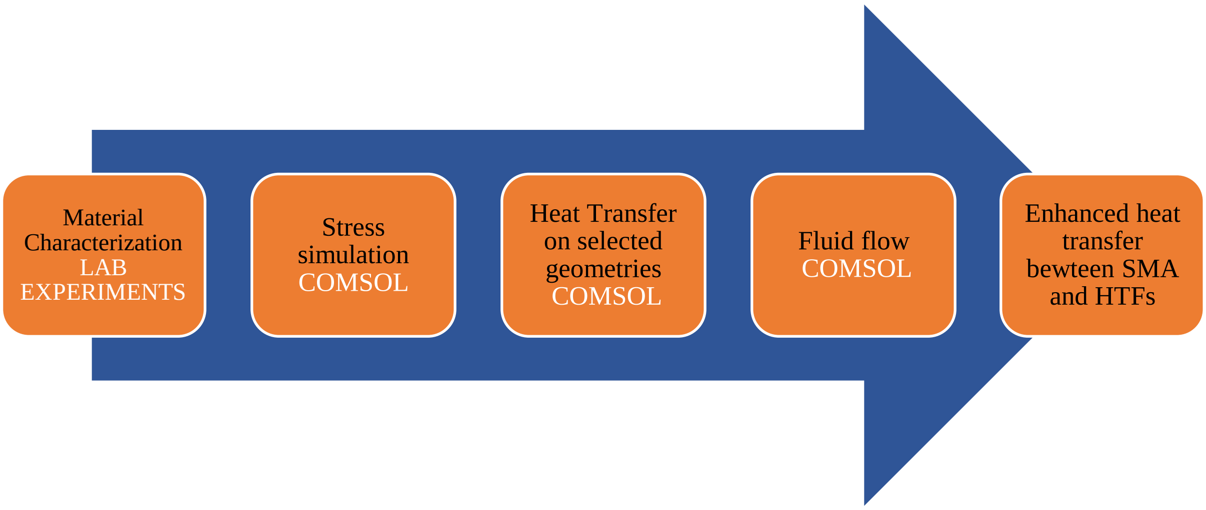

Figure 3.1: Project's workflow and tools used in each stage.

Figure 3.2 below, provides a roadmap for the steps need to be followed to design the system described above and shown in the workflow in figure 3.1. The design in the project, as shown in figure 3.2, followed nine steps as follows:

1- Decide the required application, as SMA material can cover a wide spectrum of applications from cryogenics to high temperature process heating.

2- Heat-treat the material to achieve the activation temperatures that will allow the SMA material to perform within the range of temperature decided beforehand when deciding the application.

3- Find out the available latent heat through experiments (mechanical DSC) or computer simulation (COMSOL MULTIPYSICS).

4- Decide the heating demand (3 kW in the case of this project, as 3 kW is the smallest commercial heat pump and suitable for other applications).

5- Based on heat demand, the user can decide whether they will achieve a reasonable design with the available latent heat; if not, they can go back to heat-treating the material to enhance its performance.

6- Design the plate and the slot geometry that will allow the best heat removal by the working fluid.

7- Design the stack.

8- Decide the flow type: one path, two paths, serpentine flow … etc. The flow type depends on the required heat transfer surface area.

9- Decide the fluid type: Water or nanofluids; if nanofluid, what sort of nanoparticles and what are the percentages?

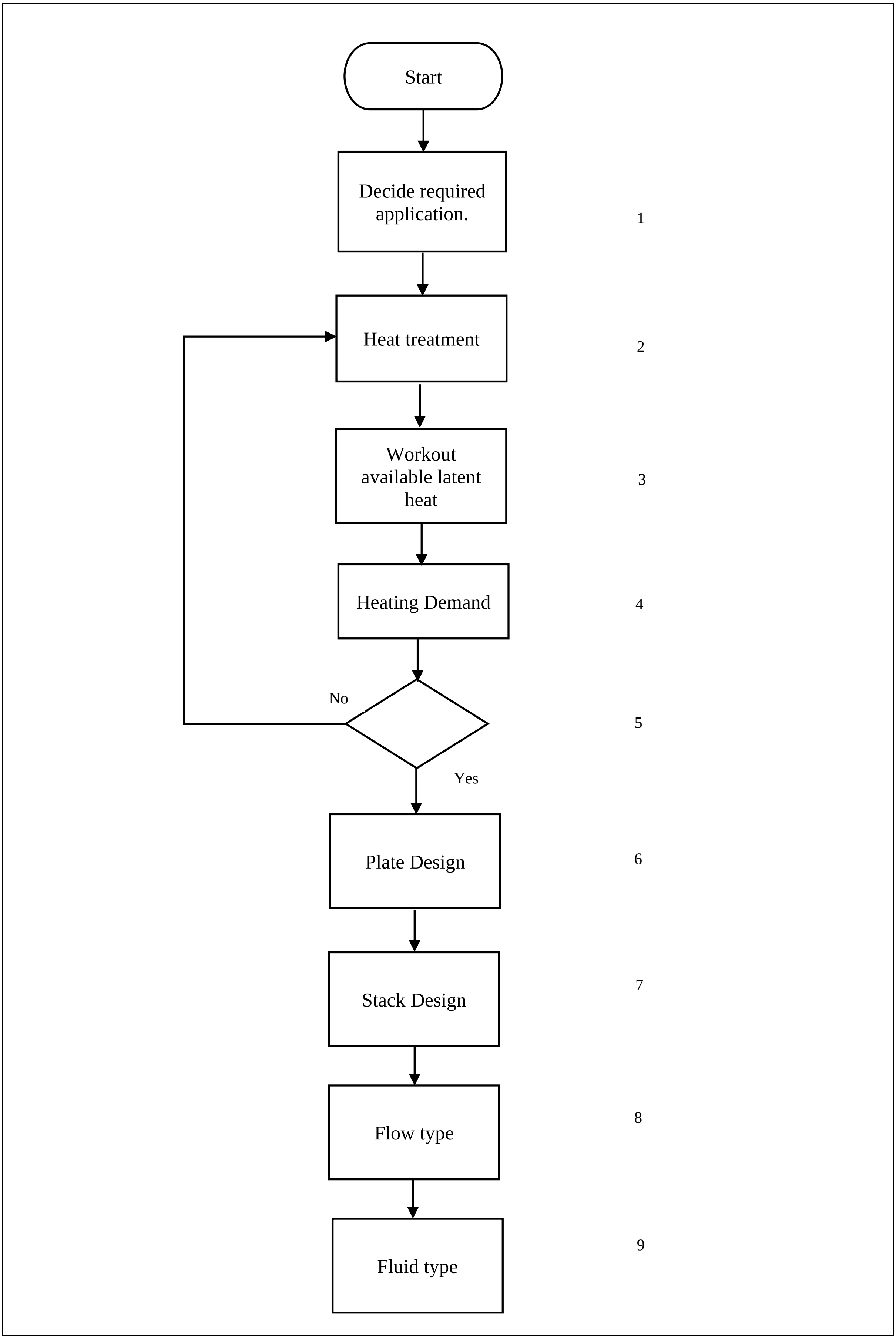

Figure 3.2: Flow chart for design steps

3.2 Summary

SMA material is being investigated in several fields from power generation, medical implants, aeronautical components, sports and even used in eyeglasses. Numerous research groups are examining these materials. All the previous works in Elastocaloric refrigeration field focused on using SMA for cooling purposes at small scale. However, this is the first attempt of utilising the material's behaviour for a big scale heat pump, and this where the importance of this project comes into play. Furthermore, this project provides an understanding of how the properties of SMA can be altered so the material could be used to cover a wider range of applications.

3.3 Aim

The aim of this project is to study different SMA blends and understand their thermophysical properties to enhance their thermal output, and thus incorporate them into a heat pump where they will work as the heat source, and then enhance the heat transfer between the heat source and working fluids.

3.4 Objectives

1- To complete and deliver a comprehensive literature review report on SMA and deliver a comparison review paper of alternative heating and cooling technologies.

2- To model SMAs in CFD to understand their behaviour under different loading conditions and cycle times, and then to validate the modelling results against data obtained from the test rigs being developed within the Exergyn's Laboratories.

3- To test different blends under different heat treatments which would lead to understanding the effect of heat treatment processes on SMA materials in terms of activation temperatures and available latent heat.

4- After the right blend for heat pump application has been decided, to test different geometries, using the model, to decide which geometry functions most efficiently with regards to heat transfer between the material and the HTFs.

5- Test different fluids (water and nanofluids) using different percentages of nanoparticles to enhance the fluids’ thermal properties and study the impact nanofluids will have on the overall performance. Compare between the fluids to decide which fluid is the best in relation to picking up heat from the SMA material.

Chapter 4: SMA modelling

Chapter 4 SMA modelling

4.1 Introduction:

Shape memory alloys have two phases; the grains in each phase have different orientation and crystal structure and therefore different properties. The first phase is Austenite which is called parent phase and it is the high temperature phase; the second is Martensite which is called the product phase and it is the low temperature phase. The SMA material changes between the two phases depending on the condition the material undergoes; in the absence of applied stress, the material changes from Austenite to twinned martensite, and this phase transition is called forward transformation. When the material is heated up when in Martensite phase, it transitions back to Austenite, and this transition is called reverse transformation. The other way of triggering the phase change is by applying load on the material when in Austenite shape, and that results in the material transitioning into detwinned Martensite (Lagoudas D., 2011).

Figures 4.1 and 4.2 show the phase transformation of SMA material between Austenite and the two case of martensite (twinned and detwinned), and the location of the four activation temperatures respectively. The transformation can also be initiated by applying certain amount of stress to the material when it is in Austenite phase which results in detwinned martensite; when the load is removed, the material fully recovers. This transformation is known as stress-induced transformation and the behaviour is called pseudoelastic effect, which is shown schematically in figure 4.3.

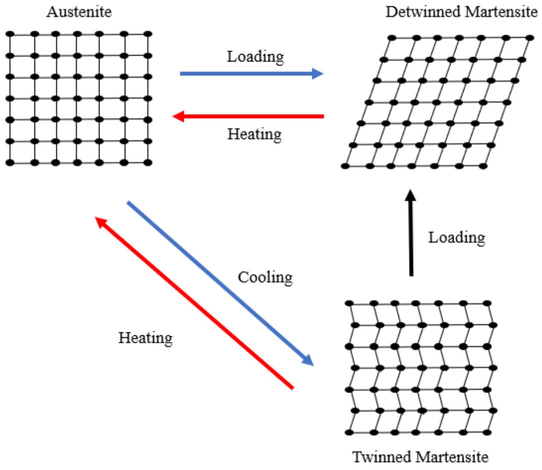

Figure 4.1: The two types of phase transformation in SMA material (Lagoudas D., 2011)

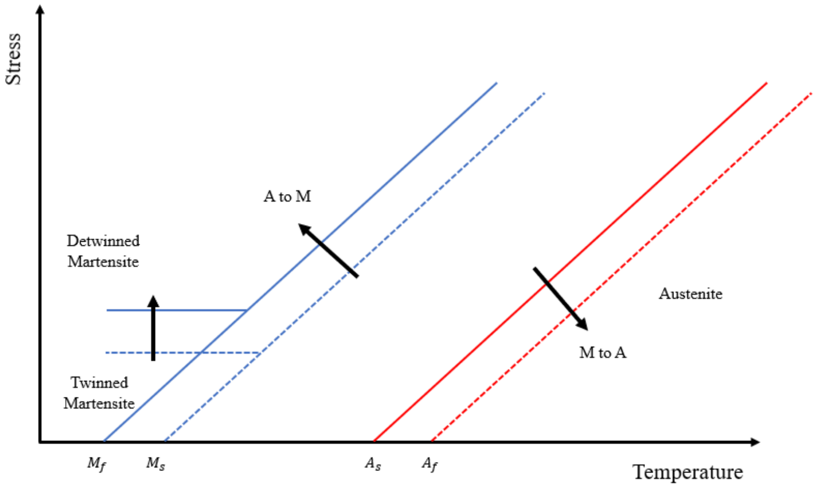

Figure 4.2: Stress-temperature diagram showing activation temperatures and transformation zones (Lagoudas D., 2011)

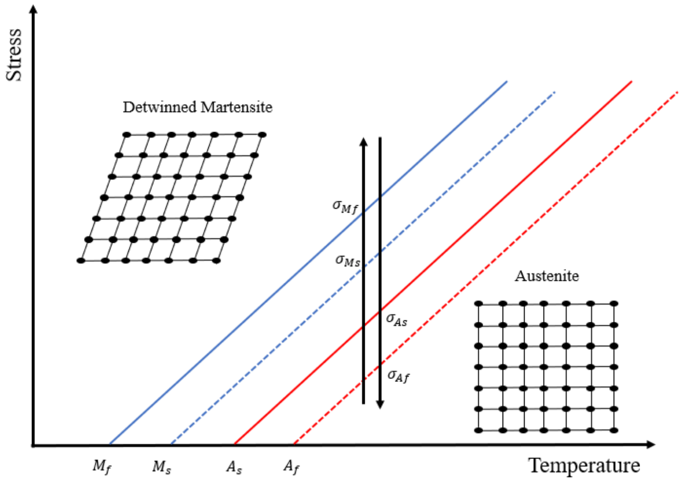

Figure 4.3: Pseudoelastic behaviour of Shape Memory Alloys (Lagoudas D., 2011)

Figure 4.3 also shows the triggering stresses, which are the stresses at which the activation temperatures are triggered; and it shows the amount of stress needed to transition the material between phases when the material is at certain temperatures. If the temperature of the material is below M_f, then detwinned martensite occurs upon loading at σ_{Mf}; on the other hand, a complete shape recovery of the material is noticed when the temperature is above A_f and when the stress applied is less than σ_{Af}.

4.2 Mathematical Model:

The mathematical model used in this research is obtained from the Lagoudas model, which was developed by Dimitri C. Lagoudas and his research team in the department of Aerospace Engineering at Texas University. The SMA behaviour is explained by Dimitri Lagoudas in his book where he wrote an SMA model using the thermomechanical coupled energy equation as follows (Lagoudas D., 2011):

$$\begin{aligned} T\alpha : \dot{\alpha} + \rho c\dot{T} + \left(-\pi + T\Delta\alpha : \sigma - \rho\Delta cT\ln\left(\frac{T}{T_\circ}\right) + \rho\Delta s_\circ T\right)\dot{\xi} \\ = -div\,(q) + \rho r \end{aligned} \tag{4.1}$$

Where:

Left hand side:

The first term ($T\alpha : \dot{\alpha}$): describes the material's temperature change due to the change in the material stress in three-dimensional setting, hence the double dot product.

The second term ($\rho c\dot{T}$): relates to the material heat capacity.

The third term $\left(-\pi + T\Delta\alpha : \sigma - \rho\Delta cT\ln\left(\frac{T}{T_\circ}\right) + \rho\Delta s_\circ T\right)\dot{\xi}$: expresses the material temperature change due to the variation of the Martensitic volume fraction with release/absorption of latent heat.

Right hand side:

The first term ($-\mathrm{div}\,(q)$): relates to the heat flux.

The second term (ρr): the heating source

To build up an SMA model, there are many parameters that the user needs to input. Some of these parameters are extracted from the physical testing through the Differential Scanning Calorimetry, and the remaining parameters are referenced from the manufacturer's material documentation. The parameters required are: (M_s, M_f, A_s, A_f, C_p, ρ, α_M, α_A, E_M, E_A, C_M, C_A, H, ε^T, ε^{Tm}, T_s, ξ_M, K_A & K_M).

The change in entropy for the two phases (Austenite and Martensite) can be calculated as follows:

Austenite

$$\Delta s_A = -\frac{C_A . \varepsilon^{Tm}}{\rho} \tag{4.2}$$

Martensite

$$\Delta s_M = -\frac{C_M . \varepsilon^{Tm}}{\rho} \tag{4.3}$$

The stress compliance factor is the inverse of the young's modulus of elasticity and therefore it is:

Austenite

$$S_A = 1/E_A \tag{4.4}$$

Martensite

$$S_M = 1/E_M \tag{4.5}$$

Therefore, the change between phases is:

$$\Delta S = S_M - S_A \tag{4.6}$$

To determine the thermodynamic boundary of the phase change, some polynomial hardening parameters need to be determined as follows:

Austenite

$$b^A = -\Delta s_A . (A_f - A_s) \tag{4.7}$$

Martensite

$$b^M = -\Delta s_M . (M_s - M_f) \tag{4.8}$$

The transformation temperatures at known stresses $A_s^\sigma, A_f^\sigma, M_s^\sigma \,\&\, M_f^\sigma$ can be found from the below formulas:

Austenite Start

$$\frac{1}{2}\Delta S \sigma^2 + \sigma H + \rho \Delta s_A . (A_s^\sigma - A_s) = 0 \tag{4.9}$$

Austenite Finish

$$\frac{1}{2}\Delta S \sigma^2 + \sigma H + \rho \Delta s_A . \left(A_f^\sigma - A_f\right) - \rho b^A = 0 \tag{4.10}$$

Martensite Start

$$\frac{1}{2}\Delta S\sigma^2 + \sigma H + \rho\Delta s_M.\left(M_s^\sigma - M_s\right) = 0 \tag{4.11}$$

Martensite Finish

$$\frac{1}{2}\Delta S\sigma^2 + \sigma H + \rho\Delta s_M.\left(M_f^\sigma - M_f\right) - \rho b^M = 0 \tag{4.12}$$

The thermomechanical response can be calculated as follows:

$$\varepsilon = S_A\sigma + \alpha_A(T - T_0) \tag{4.13}$$

Where: T is a starting temperature, and T_0 is a reference temperature.

The forward transformation occurs when the SMA temperature reaches to M_s^σ and it continues until the temperature of SMA reaches M_f^σ; this process is accompanied by temperature rise and material deformation (an increase in the total strain). Therefore, the increment of temperature ΔT that occurs as a result to an increment of stress $\Delta\sigma$ can be calculated as follows:

$$\Delta T = \frac{T\alpha - [\frac{(Hsgn(\sigma) + \Delta S\sigma)}{\rho\Delta s_0\left(M_s - M_f\right)}(-Y + \rho\Delta s_0 T)]}{[\rho c - \left(\frac{\rho\Delta s_0}{\rho\Delta s_0\left(M_s - M_f\right)}(-Y + \rho\Delta s_0 T)\right)]}\Delta\sigma \tag{4.14}$$

Where:

$\mathbf{sgn(\boldsymbol{\sigma})}$ determines the stress direction as it equals 1 when loading and -1 when unloading.

Y is the thermodynamic force needed for the phase transformation to take place, and it can be found from the below equation:

$$Y = 0.25\,\rho.\Delta s_M(M_s + M_f + A_f + A_s) \tag{4.15}$$

Then the martensitic volume fraction during the transformation can be calculated as follows:

$$\xi = \frac{1}{\rho b^M}[|\sigma|H + \frac{1}{2}\Delta S\sigma^2 + \rho\Delta s_0(T - M_s)] \tag{4.16}$$

Whereas the change in strain is calculated as follows:

$$\varepsilon = S(\xi)\sigma + \alpha(\xi)(T - T_0) + Hsgn(\sigma) \tag{4.17}$$

Stress compliance

$$S = S_A + \xi.(S_M - S_A) \tag{4.18}$$

Thermal expansion

$$\alpha = \alpha_A + \xi.(\alpha_M - \alpha_A) \tag{4.19}$$

4.3 Modelling Methodology

This chapter aims to investigate, through modelling, the thermophysical properties of Shape Memory Alloys; it aims at looking at how stress influences the material in relation to the amount of available latent heat, and whether it is affected by different external parameters. The chapter also goes through how the material is affected by different cycle times for one cycle and for multiple cycles.

4.3.1 Computational Fluid Dynamics:

The Computational Fluid Dynamics (CFD) software used in this project is COMSOL Multiphysics. After careful and extensive research into different CFD environments, COMSOL was chosen on the grounds of its ability to allow the user to define their physics as well as input their equations in the form of partial differential equations (PDEs) when needed, which allows a deeper investigation of the physics involved, despite the fact this deeper investigation comes at the expense of solution time, for it takes longer to solve a model in COMSOL. This feature is of paramount significance as this project required building nanofluids which are not included in the in-built library, which is explained in depth in chapter 6. One of the crucial aspects of COMSOL Multiphysics is that it is already being used in modelling SMA, and it has the two main SMA models (Lagoudas Model and Souza-Auricchio Model) built in it. However, that did not mean the project was carried out in COMSOL without any validation; the mathematical model in COMSOL was validated against results obtained from the experimental work, as explained later in the experiments and models validation chapter 5.

4.4 COMSOL modelling:

To conduct the modelling in COMSOL Multiphysics, the author needs to input the parameters mentioned in the previous section; as well as deciding the cycle time and the stain rate. This section explores COMSOL modelling step by step and it shows how the material behaves under different parameters, stresses and loading strategies.

The sample used for the different tests is a cube of $(h = 3mm; w = 3mm; d = 3mm)$; the sample is supported from the bottom with a roller and stressed on the top face using different stresses as explained later in this section (stress direction top to bottom). Figure 4.4 shows the sample and the loading arrangement.

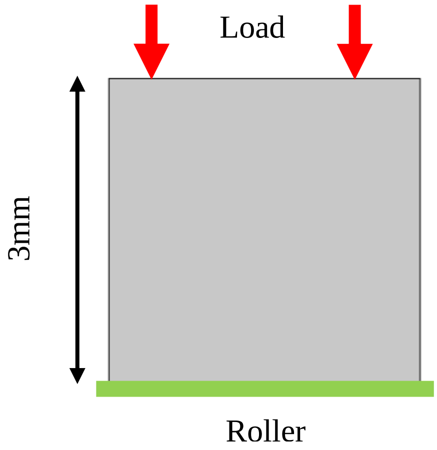

Figure 4.4: Sample used for COMSOL simulation and stress arrangement.

4.4.1 The effect of stress:

The parameters used for this simulation are in table 4.1.

Table 4.1: Parameters of the first NiTi sample used in the CFD modelling.

Parameter	Value	Parameter	Value
A_s	260 K	E_A	55 GPa
A_f	270 K	E_M	46 GPa
M_s	245 K	K_A	12 $W.m^{-1}.K^{-1}$
M_f	230 K	K_M	8 $W.m^{-1}.K^{-1}$
H	5.6 %	ρ	6450 $kg.m^{-3}$
C_A	$7.4 \times 10^6\ MPa.K^{-1}$	Poisson's ratio	0.33
C_M	$7.4 \times 10^6\ MPa.K^{-1}$	C_p at constant pressure	400 $J.kg^{-1}.K^{-1}$
SMA reference temp	25 ˚C		

Since the SMA material under compressive loading can withstand around 20 million cycles, as reported by Zhang et al., (2019); providing the SMA-based heat pump is designed to have a life span of 15 years, and if the device will operate for 8 hrs a day, that means the material can withstand between 6 to 8 cycles per minute. Therefore, the cycle time decided for this model is 8 seconds; 4 seconds for loading and 4 seconds for unloading, as shown in figure 4.5. The stress will be applied gradually starting at 500 MPa with an increment of 100 MPa, until the stress at which the material fully transforms from Austenite to Martensite is identified. Since the cycle time is fixed and there are different stresses, that means there will be different strain rate for each stress, which is explained later in this section.

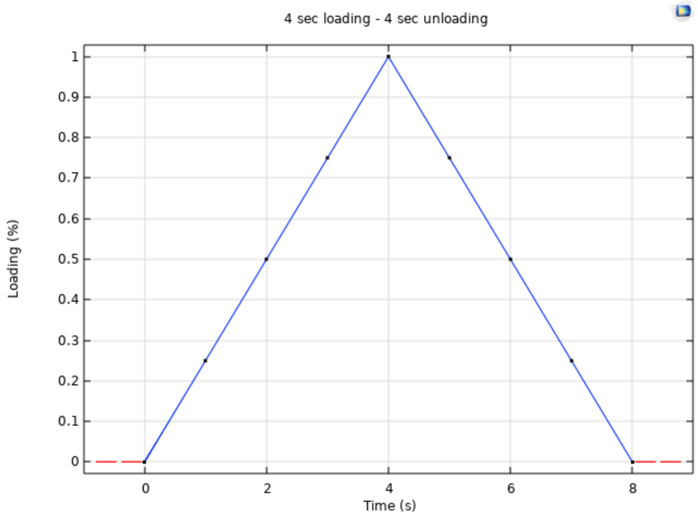

Figure 4.5: The loading cycle shows 4 seconds for loading and 4 seconds for unloading.

The second step in the set-up of the model is to set the heat transfer parameters, as the pressure applied on the material causes the material to rise in temperature; therefore, it is important to set the heat transfer interface to track the change in temperature as well as to know the amount of latent heat available within the material under every set of parameters. Figure 4.6 shows that the heat flux is set on the sides of the sample; and that is because the other two sides (bottom and top) of the sample are specified for the roller and the boundary loading, respectively. How the value of heat transfer coefficient was decided is explained thoroughly later in Chapter 6.

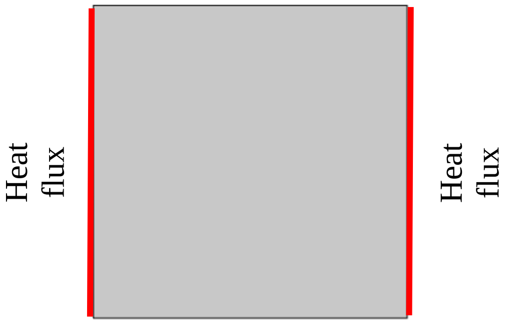

Figure 4.6: The sides of the geometry on which the heat flux was applied.

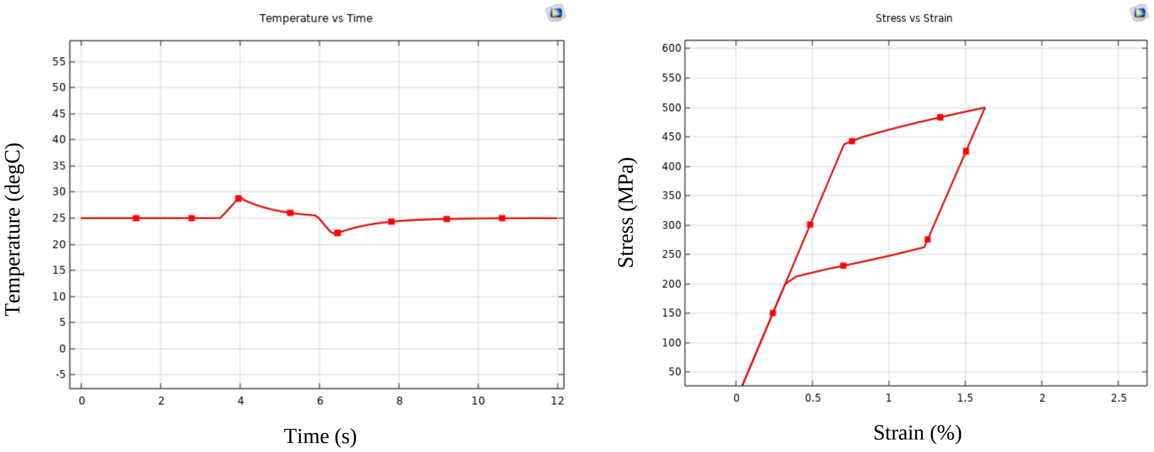

Figure 4.7: Temperature vs Time and Stress vs Strain curves for NiTi sample stressed at 500MPa.

Figure 4.7 shows a maximum transformation strain of 1.63%, and since the cycle time is 8 seconds split equally for loading and unloading, that means the strain rate for this scenario is 0.33% per second. From the temperature vs time graph, it is noticed that the temperature of the specimen at the end of the loading cycle increased from 25℃ to 29℃ achieving a temperature span of 4K rejecting a maximum latent heat of 2 $J.g^{-1}$. Whereas, during the unloading, the temperature of the specimen dropped to 22℃ accomplishing a temperature difference of 3K, and therefore harnessing a latent heat of 1.46 $J.g^{-1}$. Figure 4.8 shows the total internal energy versus time graph; the rejected latent heat can be found by applying integration and finding the area under the curve for loading. Similarly, the absorbed latent heat is found by applying the same process for the unloading.

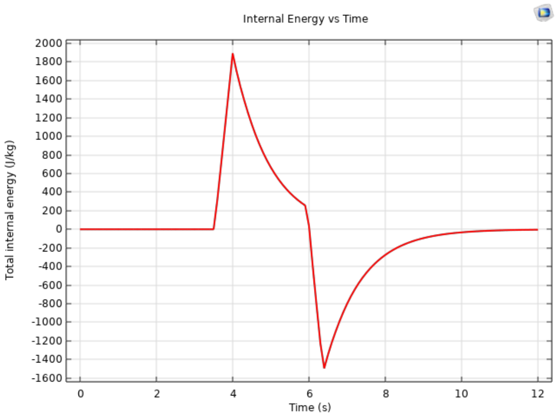

Figure 4.8: Total internal energy vs time graph for NiTi stressed at 500MPa; this graph is used to calculate the latent heat during loading and unloading.

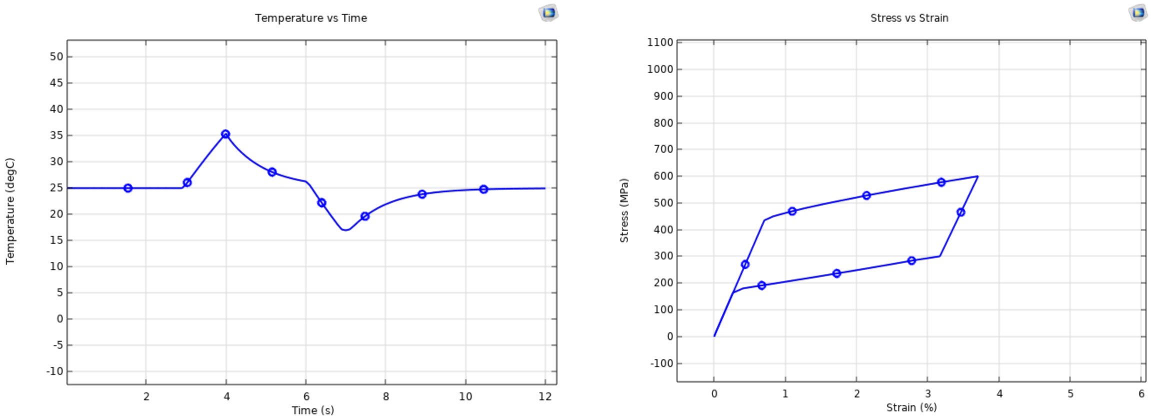

Figure 4.9: Temperature vs Time and Stress vs Strain curves for NiTi Sample Stressed at 600 MPa.

Figure 4.9 shows temperature vs time graph and stress vs strain graph for the same sample stressed at 600MPa. The results show that the temperature of the sample increases from 25℃ to 35℃ achieving a temperature lift of 10K during loading and the temperature of the sample during unloading drops to 16℃ to achieve a temperature span of 9K. The results show a maximum strain of 3.45% which means a strain rate of 0.86%. Figure 4.10, shows the total internal energy vs time graph, which, through integration, shows that the sample when stressed at 600MPa can reject latent heat of 7 $J.g^{-1}$, and it absorbs an amount of latent heat of 4.4 $J.g^{-1}$during the unloading.

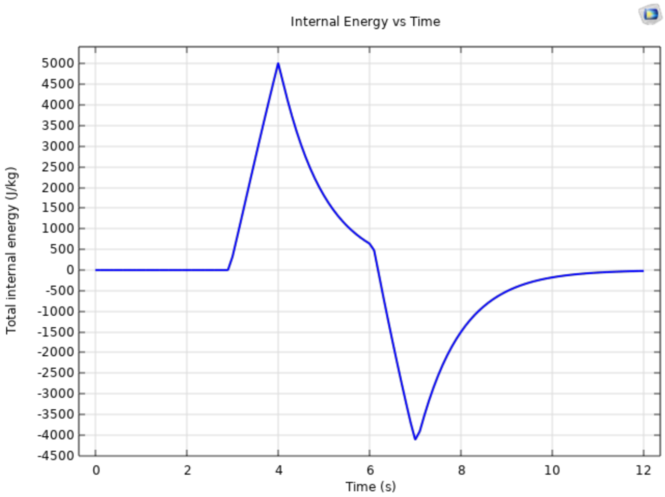

Figure 4.10: Total Internal Energy vs Time Graph for NiTi Stressed at 600MPa.

Figure 4.11 shows the behaviour of the NiTi specimen when stressed at three different stresses, 700 MPa, 800 MPa and 900 MPa. The figure shows the change in the specimen's temperature over time for the three stresses in question; as well as the deformation that happened with the specimen. This was also summarized in table 4.2 below.

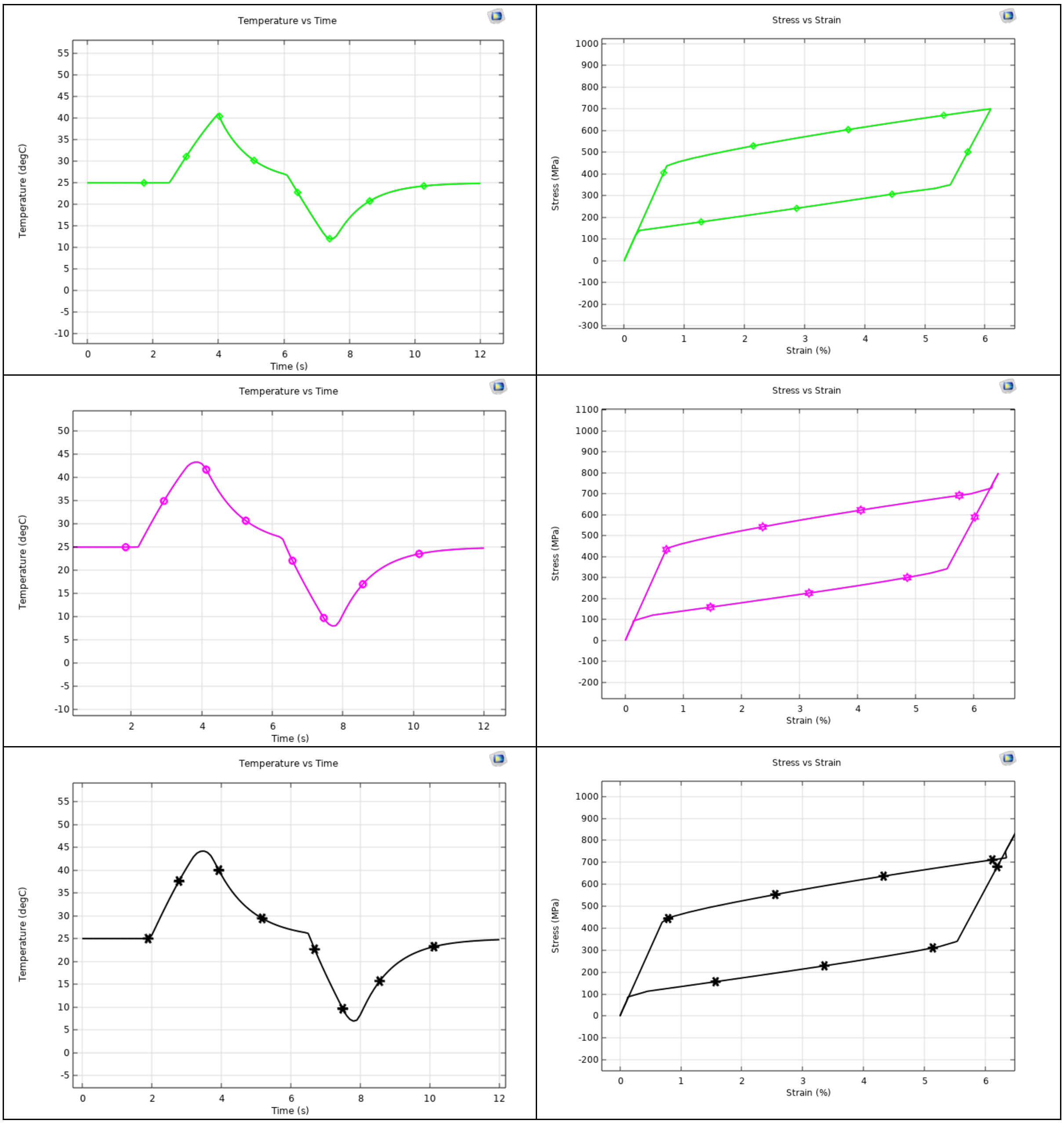

Figure 4.11: Temperature vs Time and Stress vs Strain curves for NiTi Stressed at 700MPa, 800MPa and 900MPa.

Table 4.2: Parameters of NiTi sample stressed at 500MPa, 600MPa, 700MPa, 800MPa and 900MPa.

Stress [MPa]	Strain rate [% per sec]	ΔT (heating) [K]	ΔT (cooling) [K]	Latent heat (heating) [J/g]	Latent heat (cooling) [J/g]
500	0.33	4	3	2	1.46
600	0.86	10	9	7	4.4
700	1.47	15	13	13.3	7
800	1.54	18	17	19.6	8.3
900	1.54	19	18	20.2	7.8

The summary table 4.2 shows how the stress influences how the material behaves, as it is directly linked to phase transition. When the material fully transforms from Austenite to martensite, it rejects all its latent heat during the transition between the two phases. However, when the material is fully transformed to Martensite, it stops rejecting latent heat into the surrounding. The bigger the stress applied the bigger the temperature span for heating and cooling and the bigger the rejected and absorbed latent heat is. Figure 4.12 shows the relationship between stress and the absorbed and rejected latent heat.

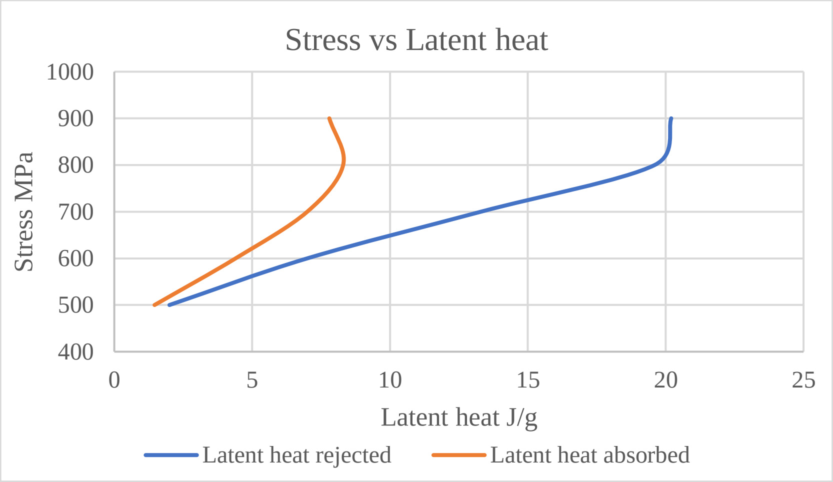

Figure 4.12: Latent Heat rejected and absorbed for NiTi sample stressed at 500 MPa, 600 MPa, 700 MPa, 800 MPa and 900 MPa.

As shown previously in figure 4.11, the material fully transforms at a stress higher than 700 MPa; therefore, any stress above the transformation stress does not affect the rejected latent heat as shown in figure 4.12. However, higher stresses lead to quicker heat rejection as the material transforms from Austenite to Martensite quicker because the stress at which the transformation occurs is reached faster due to the higher stress. To address this point, the strain rate needed to be uniform for all stresses and that to allow better judgement of the material reaction. Figure 4.13 shows the graphs for the same sample when stressed at 1500 MPa.

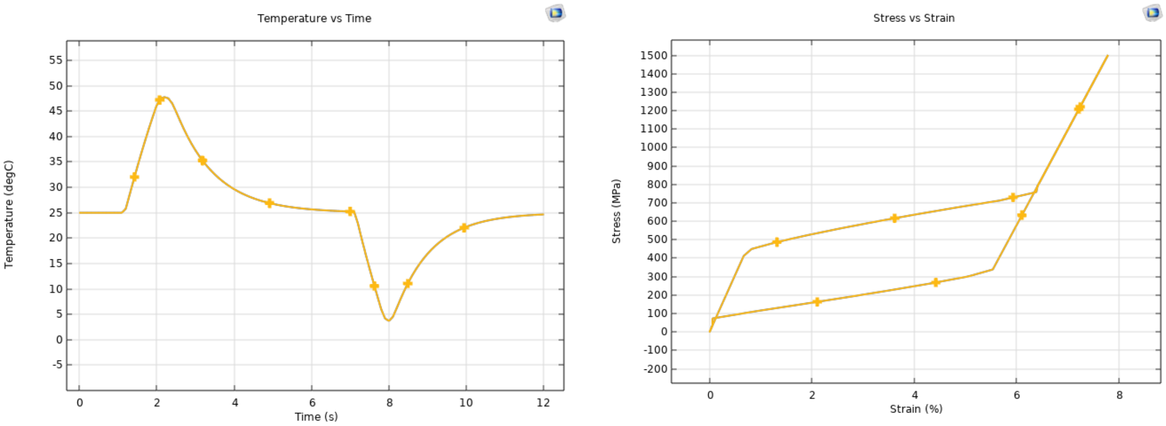

Figure 4.13: Temperature vs Time and Stress vs Strain curves for NiTi Sample Stressed at 1500 MPa.

It was noticed that applying a stress of 1500 MPa on a NiTi sample with the parameters shown previously in table 4.1, caused the sample to rise in temperature very fast, as it got to 47°C in 2 seconds; whereas it took three and a half second for the sample to reach the highest temperature when stressed at 900 MPa. On the cooling side, the sample stressed at 1500 MPa had more time to cool down before the unloading, which allowed the sample to cool down to less than 5°C.

Figures 4.14 and 4.15 show a comparison of stress vs strain and temperature vs time for six different stresses. It is noticeable that the bigger the stress applied the higher the temperature of the sample and the quicker it occurs. Figure 4.15, as well shows that the higher the stress the lower the temperature of the sample during unloading. Since the full transformation occurs at 800MPa, any stress less than that amount would lead to an incomplete transformation; and any stress above full transformation leads to an increase in Energy-in with no further benefit in Energy-out, which leads to smaller COP. Figure 4.14 shows a discrepancy in the hysteresis loops due to the incomplete transformation for 500 MPa, 600 MPa & 700 MPa.

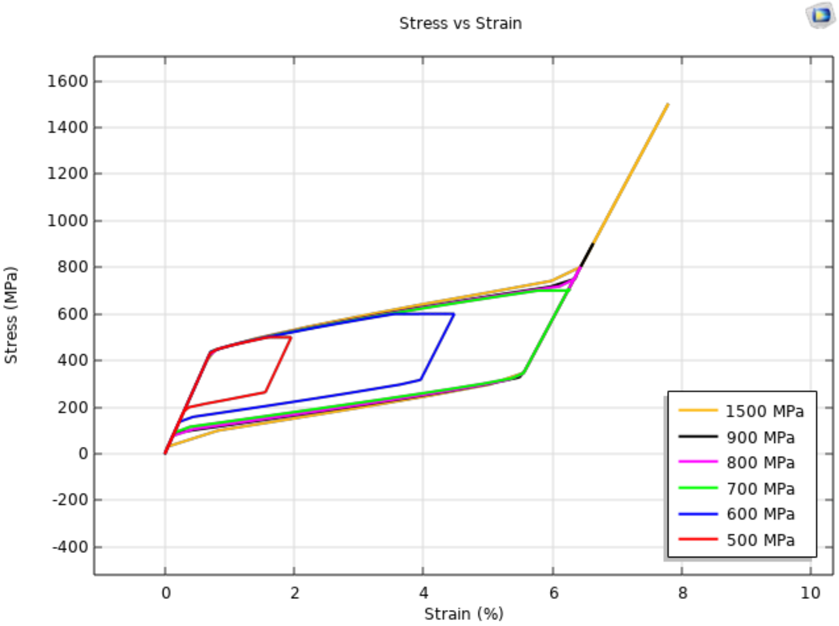

Figure 4.14: Comparison of Stress vs Strain graphs for NiTi Sample Stressed at 500, 600, 700, 800, 900 & 1500 MPa.

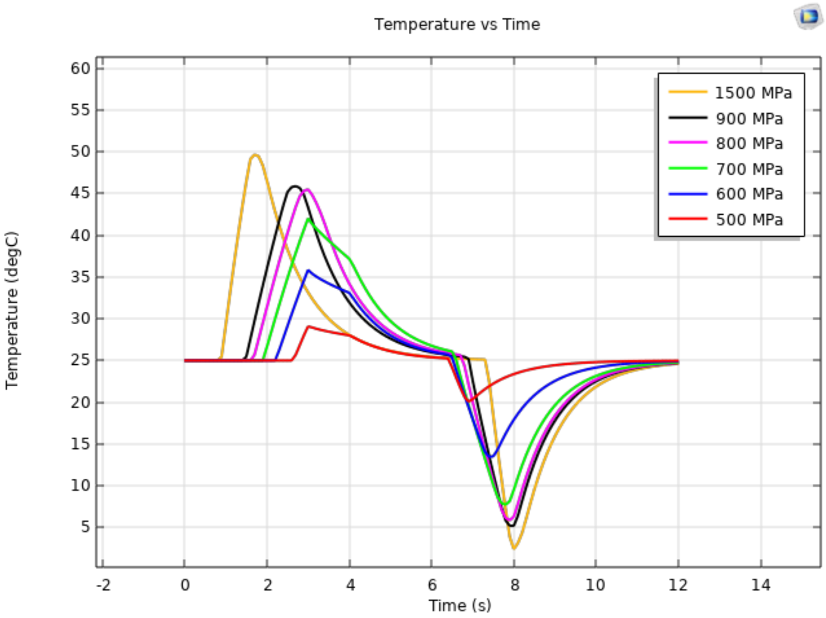

Figure 4.15: Comparison of Temperature vs Time graphs for NiTi Sample Stressed at 500, 600, 700, 800, 900 & 1500 MPa.

4.4.2 Cycle time:

The following modelling looked at cycle time (loading and unloading time) and what the implications of applying different cycle times are, and how the material's behaviour changes as the cycle time changes. To explore the effect of cycling, a NiTi sample with the parameters shown previously in table 4.1 was compressed at 900 MPa in two different cycle times. In the first cycle the loading was applied for 4 seconds and then unloading for 4 seconds; whereas in the second cycle the sample was compressed for 3 seconds, then the loading was paused for 2 seconds and then the load was removed gradually in 3 seconds. Figure 4.16 shows the two cycles.

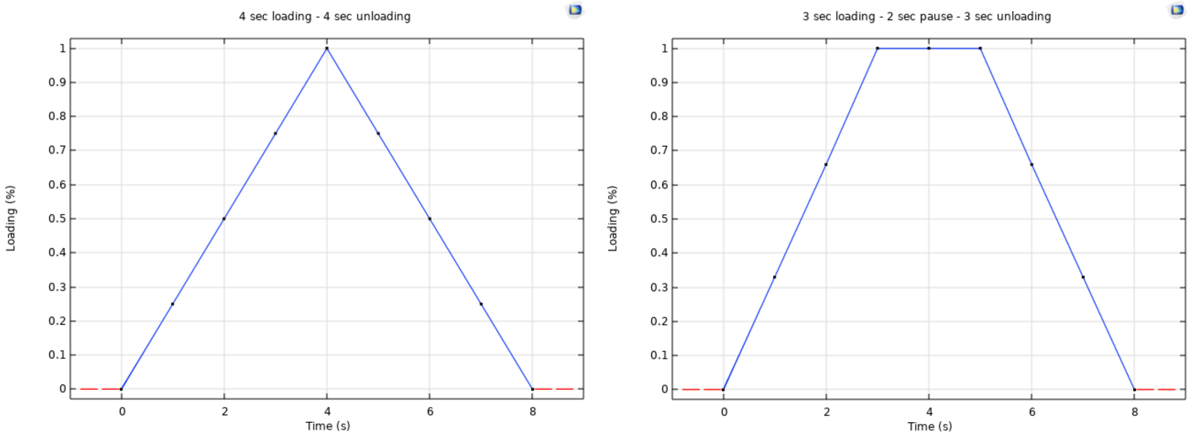

Figure 4.16: Two different cycling modes: 1) 4 seconds loading and 4 seconds unloading. 2) 3 seconds loading, 2 seconds pause and 3 seconds unloading.

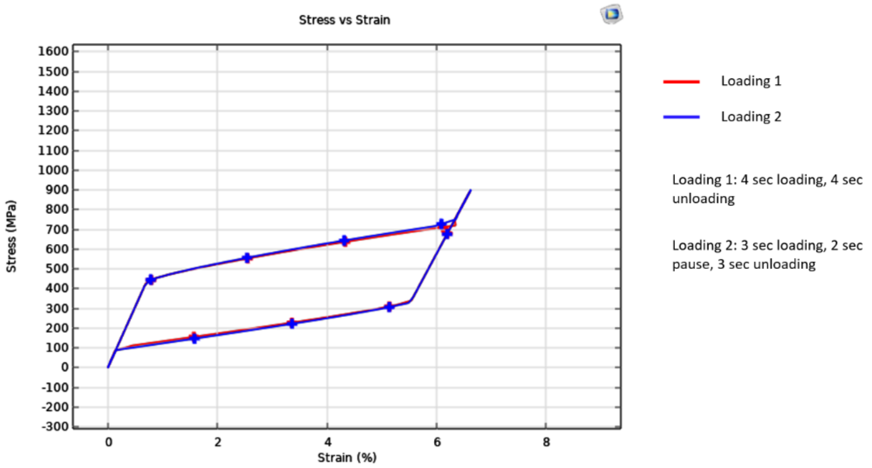

Figure 4.17: Stress vs Strain Curves for the same sample loaded at two different loading cycles

Figure 4.17 shows the stress vs strain curves of the NiTi sample loaded at the two above mentioned loading cycles. The graph shows that the stress-strain curve is not susceptible to the cycle time. However, Figure 4.18 shows that the sample loaded from 0 to 900 MPa in 3 seconds reached a higher temperature of 45.9℃ in 2.7 seconds and then the temperature of the sample started to decrease. Whereas the temperature of the sample loaded from 0 to 900 MPa in 4 seconds rose to 44.2℃ in 3.5 seconds.

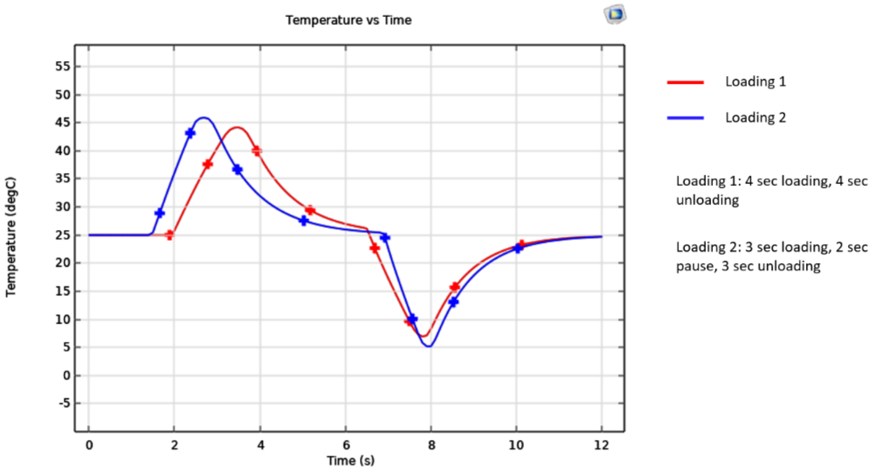

Figure 4.18: Temperature vs Time Curves for the same sample loaded at two different loading cycles.

Figure 4.19 shows the trajectory the latent heat within the sample followed in the loading and the unloading. The trajectory shows that when the sample was loaded quicker it rejected the latent heat quicker and the available latent heat was slightly more than the sample loaded slower; the graph shows that the rejected latent heat for the sample loaded in 3 seconds and the one loaded in 4 seconds are 20.5 $J.g^{-1}$ and 20.2 $J.g^{-1}$, respectively.

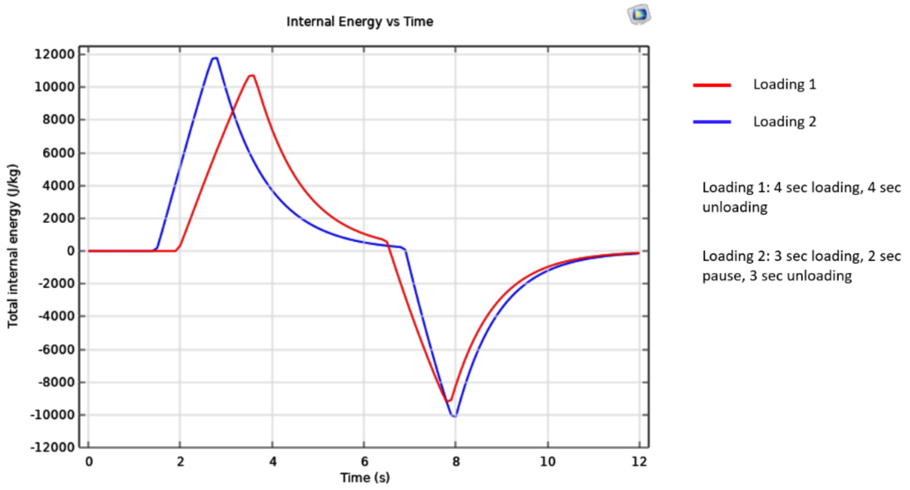

Figure 4.19: Rejected and Absorbed Latent Heat during the loading and unloading, respectively for two different loading strategies.

4.4.3 The effect of the activation temperatures:

The four activation temperatures play a vital role in determining the limits for stress-strain and temperature-time trajectories, as shown in figure 4.20; these activation temperatures were taken from the differential scanning calorimetry analysis results. The value of A_f, the temperature at which the Austenite phase finishes, determines the minimum temperature the sample can reach to during the unloading process.

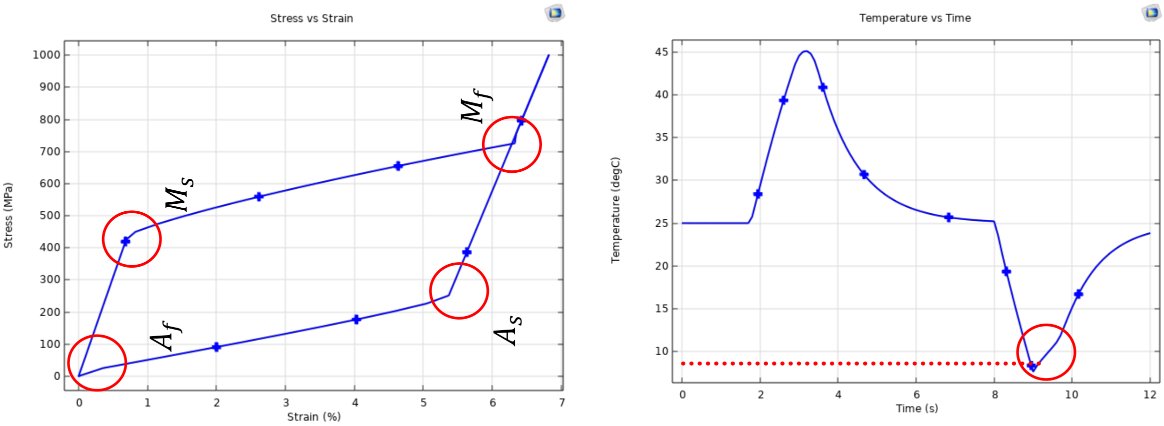

Figure 4.20: Rejected and Absorbed Latent Heat

The following study explored the behaviour of the material under different values for A_f. The loading cycle was set to follow the loading strategy shown previously in figure 4.5; the model was set so that the heat transfer kicked in when the temperature of the sample reached 35℃. Five different values of A_f were studied, and the material behaved as shown in table 4.3.

Table 4.3: NiTi sample reacting to five different values of the Austenite finish temperature A_f

A_f [K]	ΔT (heating) [K]	ΔT (cooling) [K]	Latent heat (heating) $[J.g^{-1}]$	Latent heat (cooling) $[J.g^{-1}]$
290	20.3	13.4	21.12	3.28
280	20.2	17.35	20.96	4.11
270	20	19.5	20.80	5.39
260	20	22.1	20.64	6.84
250	19.8	28	20.47	7.93

Table 4.3 shows that the temperature difference ΔT and the latent heat for the heating side are not influenced by the value of A_f; whereas ΔT and the latent heat for the cooling side are

significantly susceptible to the value of A_f; figure 4.21 shows the temperature-time and stress-strain curves for the five different values of A_f (290K, 280K, 270K, 260K and 250K). The temperature-time graph shows that the smaller the value of A_f the further the graph dips allowing the material to cool down more.

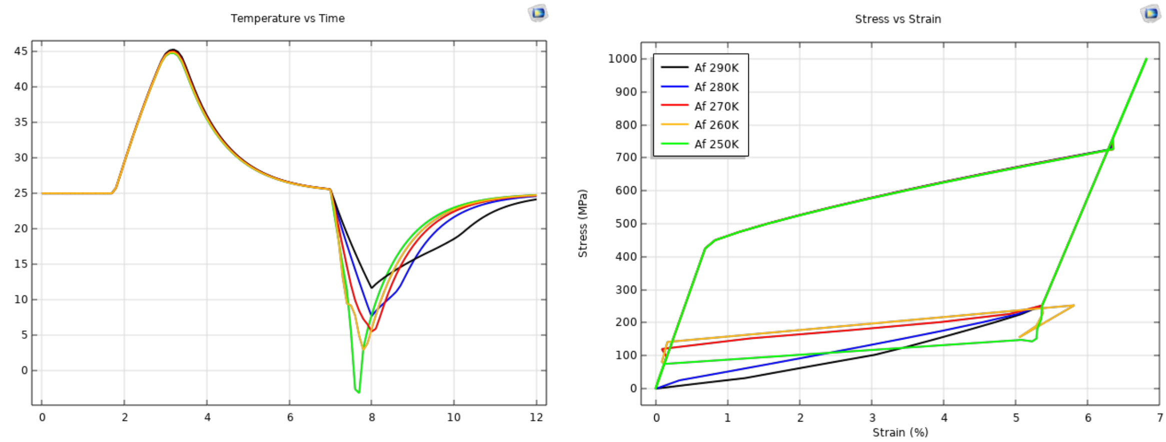

Figure 4.21: Temperature-Time and Stress-Strain curves for NiTi sample with five different values for Austenite finish temperature.

The stress-strain curve shown in figure 4.21 shows that the value of A_f influenced the hysteresis loop, the higher the A_f the bigger the hysteresis loop and therefore the bigger the required work input.

The value of A_f determines the cooling temperatures and it can be likened to the use of different refrigerants, as some refrigerants are used for cryogenics temperatures, other refrigerants are used for air conditioning for they evaporate at a temperature between 0°C and 6°C. Therefore, determining the value of A_f allows determining the cooling temperatures required for the specific application, be it sub-zero or above zero. By adjusting A_f temperature to 250K for the NiTi blend, with the parameters shown previously in table 4.1, it was found that the temperature of the sample at the end of the unloading dropped to 268.5K, which can be considered as evaporator temperature when compared to the vapour compression system. This temperature can be altered by changing the value of A_f; and the value of A_f can be altered through heat treating the blend as explained later in chapter 5.

Altering M_f, on the other hand, does not have an impact on the rejected or absorbed latent heat. However, different values of M_f affected the maximum temperature the sample can reach to, as shown in figure 4.22, which also shows that the value of M_f has an influence on the hysteresis loop; the smaller the M_f the bigger the stress required for the material to fully transform to the martensite phase, and that consequently negatively affects the overall COP. Therefore, and since the value of M_f does not influence the latent heat as shown in table 4.4, it is not recommended to set the material to have smaller values for the martensite finish temperatures M_f.

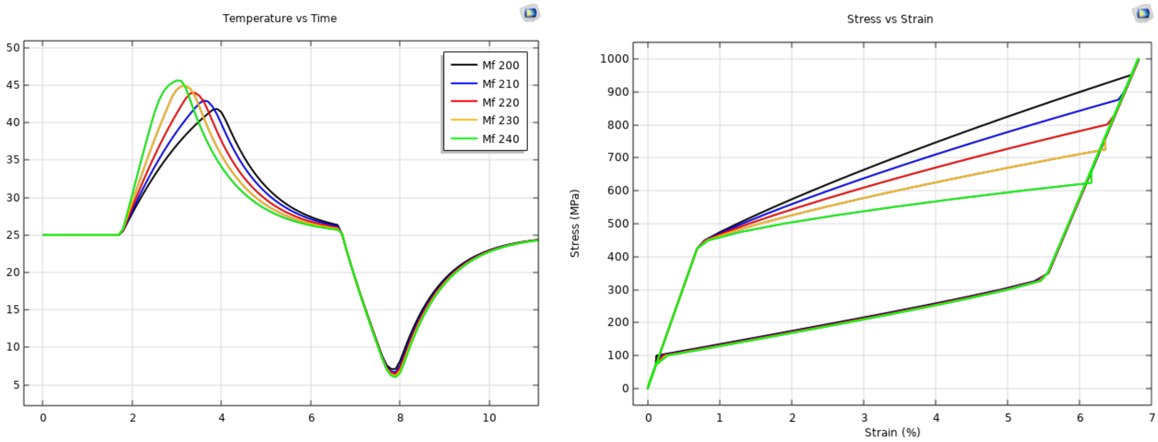

Figure 4.22: Temperature-Time and Stress-Strain Curves for NiTi sample with five different values for Martensite finish temperature.

Table 4.4: NiTi Sample reacting to five different values of the Martensite finish temperature M_f

M_f [K]	ΔT (heating) [K]	ΔT (cooling) [K]	Latent heat (heating) $[J.g^{-1}]$	Latent heat (cooling) $[J.g^{-1}]$
200	16.9	17.9	20.1	7
210	18	18.2	20.5	7.1
220	19	18.5	20.5	7.1
230	19.9	18.8	20.5	7.1
240	20.6	18.9	20.5	7.2

4.4.4 Cycles:

The following study was to test the material under more than one cycle to analyse the behaviour of the material. To achieve a cycle in COMSOL, the author used an analytic function that went from zero to full load in four seconds, then the load was held for one second, then the load was lifted gradually in four seconds, and thereafter there was a one second pause before the next cycle started. This process was repeated for three cycles as shown in figure 4.23.

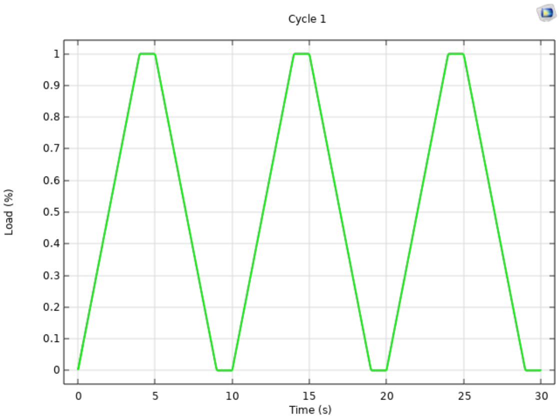

Figure 4.23: Loading cycles for cyclic loading.

The time for the study was set as 35 seconds to accommodate the three cycles and for the third cycle to fully take place. As shown in figure 4.24, it was noticed that the material's temperature in the first cycle spikes to 45.7°C and then the temperature stabilised at 41.7°C for the following two cycles; whereas in the cooling side, the temperature started at 9.4°C and stabilised at 9°C for the following two cycles. On the other hand, the stress vs strain graph showed that the material fully transformed to Martensite state in the first cycle at 760 MPa; and the full transformation in the following cycle took place at 720 MPa, as shown in figure 4.24 b.

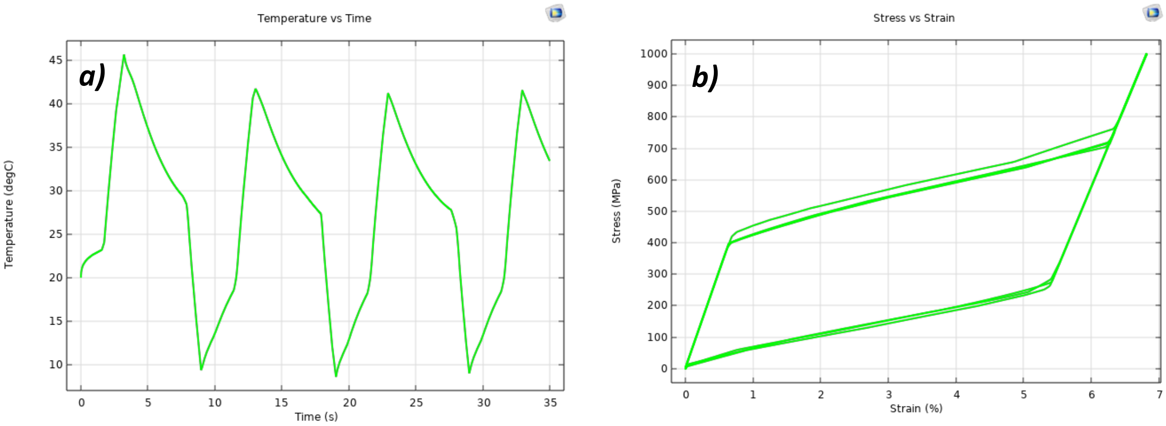

Figure 4.24: Temperature-Time and Stress-Strain Curves for cyclic loading.

The simulation also showed that the temperature of the sample in the first 1.5 second increased slightly from 20°C to 23°C and then in 1.7 second the temperature of the sample reached 45.7°C, that happened because the loading is set to take place gradually in 4 seconds which meant the load increaseed at a rate of 25% every one second; therefore, the temperature rose slightly in the first 1.5 second because the load applied on the material is 375 MPa which is below the point at which the material starts transforming from Austenite to Martensite which happens at stress equals σ_{Ms}; and the release of the latent heat started when the stress hit σ_{Ms}, as shown in figure 4.25.

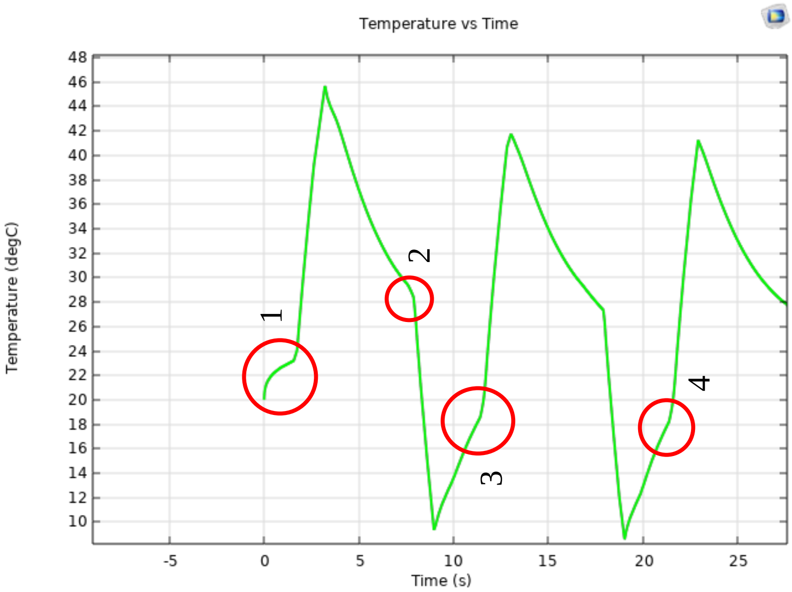

Figure 4.25: Temperature-Time for cyclic loading.

Figure 4.25 shows that the temperature of the sample reached the peak after 3.7 seconds of the loading, knowing that the loading is set to take place for 4 seconds. The figure shows that the material started losing its heat gradually even before the unloading started, until the temperature of the material reached 28°C after 7.9 seconds, which is shown in knee point 2. Thereafter, the temperature of the material dropped to 9.4°C at 8.96 seconds; this massive drop of temperature from 28°C to 9.4°C happened in one second; then the temperature of the material started increasing before the end of the unloading. Knee point (3) took place at 11.4 seconds, which is 0.4 seconds into the second cycle. At this point the temperature of the material started rising and it reached the peak of the second cycle at 13 seconds which is only 2 seconds after the second cycles started. This pattern repeated at knee point 4, as the material's temperature rose from 18°C to 41.7°C in less than 2 seconds. This similarity in the pattern leads to the fact that the material needs to be activated or trained in the first cycle before it could have a quicker response to loading and unloading.

The loading time plays a vital role in the performance of the material; the next study compared between the same cycle of 5 seconds loaded differently, in the first study, the material was loaded gradually from zero to full load in four seconds and the stress was held for one second and then the material was unloaded from full load to zero in four seconds, as shown in figure 4.20. Whereas in the second study, the material was loaded from zero to full load in one second and the stress was held for 4 seconds and then the load was removed from full load to zero in one second, and thereafter the next cycle started after 4 seconds. Figure 4.26 shows a comparison between the two different methods of cyclic loading.

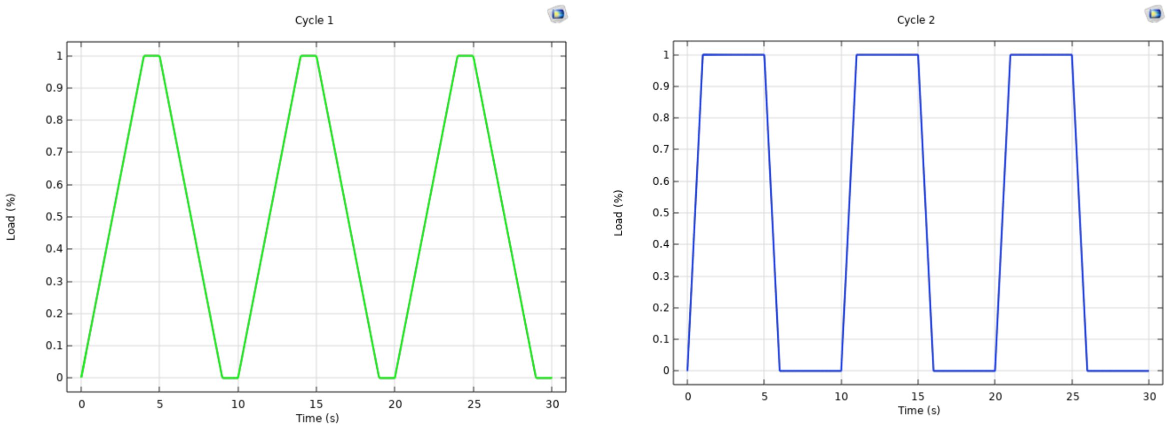

Figure 4.26: Loading cycles for two different ways of cyclic loading.

Figure 4.27 shows how the material reacted when loaded from zero to 1000 MPa in one second. The temperature vs time graph shows that the material temperature increased instantly from the reference temperature of 20°C to 56.5°C in one second achieving a temperature lift of 36.5K. The model is set so that the heat transfer kicked in when the temperature of the material reached 35°C and the heat transfer coefficient (*h*) is set to be $5000\ W.m^{-2}.K^{-1}$; The decision on the value of (*h*) was explained in more depth later in chapter 5. When the heat transfer kicked in, the temperature of the material dropped rapidly to 33.5°C at 5 seconds which was at the end of the loading; when the unloading started, the temperature of the material was already at 33.5°C and it dropped instantly to 6.5°C achieving a cooling temperature span of 13.5K.

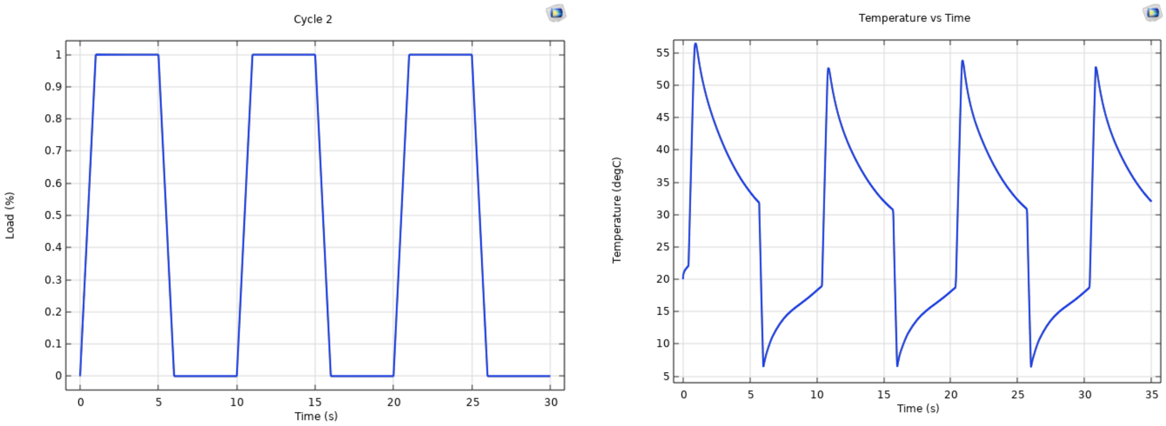

Figure 4.27: Temperature-Time for cycle 2 cyclic loading.

Figure 4.28 compares between the results of the two different cycles shown previously in figure 4.26, the results show that the quick loading resulted in a higher increase of the material temperature as the heat transfer fluid would not get enough time to remove the heat from the material despite the relatively high heat transfer coefficient (*h*); the temperature of the material reached to 56.5°C in the first cycle and then it stabilised at 53°C achieving an average temperature lift of 33K; and when the load was removed, the temperature of the material dropped rapidly to 6.5°C and stabilised at the same temperature. Whereas the temperature of the sample which was loaded slower got to 45°C and the stabilised at 41.7°C and it dropped to 9.4°C at the end of the unloading. This study showed that the loading strategy plays an important role, as through the loading one can decide the temperature they want to get as well as the speed of the heat transfer between the material and the heat transfer fluid.

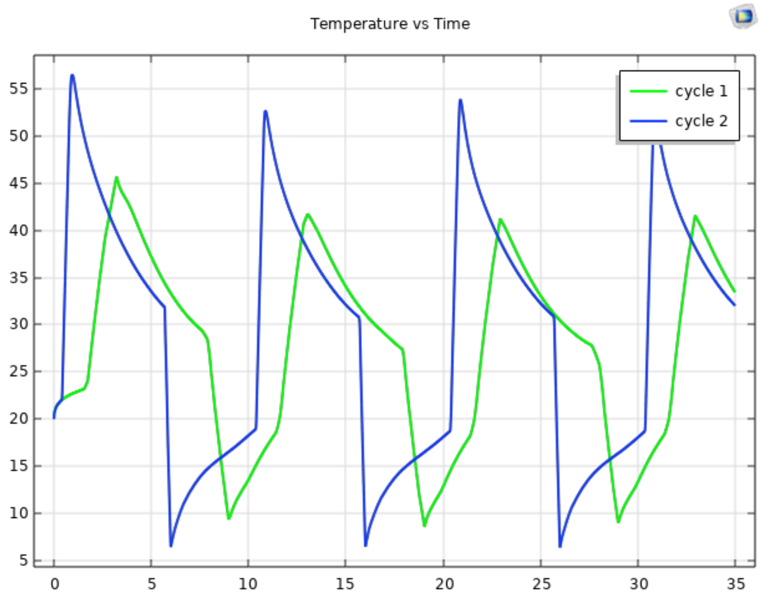

Figure 4.28: Comparison of temperature vs Time graphs for two different methods of loading (loading from zero to full load in four seconds and from zero to full load in one second)

Chapter 5: Material Experiments and Model Validation

Chapter 5 Material Experiments and Model validation

5.1 Introduction

Shape memory alloys have great thermophysical properties as discussed in chapter 2, and they have a great potential in several applications. The most important step in using SMAs in any design is to thoroughly understand their properties and characteristics; and this can be done through different processes one of which is Differential Scanning Calorimetry which gives a comprehensive analysis of heat flow and latent heat.

One of the most important procedures researchers are interested in for the vital role it plays in altering SMA's properties is heat treatment. There are many strategies to heat treating an SMA sample such as annealing and precipitation hardening or aging; the tough challenge in these processes is finding the suitable temperatures and treatment times that would lead to the desired output from the material (Rao et al., 2022). Rao et al. tested five SMA actuators for deflection at four different temperatures (450℃, 500℃, 550℃ and 600℃); two of the five specimens were tested at 450℃ for 30 mins and 60 mins, and they found that the deflection of the material increased with increasing the temperature and the heat treatment period. Resnina et al. studied the influence of annealing at different temperatures for different periods, and they found that annealing at 500℃ for 5 hours decreased the columnar grains and increased their width; they also found that increasing the annealing time made the columnar grain disappear, as they could not find the columnar grains in specimens annealed at 450℃ and 600℃ for 20 hours. They noticed a similar situation in a sample annealed at 900℃ for 2 hours, which made them conclude that higher temperatures have greater influence on columnar grain structure than the annealing time. Lu et al. studied the heat treatment of SMA at three different temperatures (500℃, 800℃ and 1000℃) and they concluded that annealing a specimen at 800℃ led to an obvious microstructure of the sample as the sample showed continuous long stripe shaped precipitates that were distributed in-homogeneously. To avoid the problems presented in the literature, the author of this research adopted a different strategy for heat treatment and that was by applying medium temperatures for shorter times as this chapter will reveal.

This chapter covers the experimental facility and the experimental procedure with highlights of the tests that were conducted, which include heat treatment test, tests conducted using DSC with and without liquid nitrogen, and test conducted in the mechanical testing rig. The results from the mechanical testing rig were compared to the modelling results and the comparison was carried out for activation temperatures, activation stresses, latent heat, and thermal conductivity.

5.2 Experiments Methodology and Test Facility

5.2.1 Differential Scanning Calorimetry:

Several thermal analysis methods are used to measure and analyse thermophysical properties such as specific heat, melting point and latent heat released because of a phase change. One of these methods is the DSC, which determines a sample's temperature and heat flow associated with phase change (Sanjay Kumar R., Srilakshmi R., 2019). DSC works by placing the sample into a chamber, and the DSC device raises the temperature of the chamber and then lowers it and measures the heat flow in both cases. For these tests, the DSC used was (Netzsch, DSC 214 Polyma, 99.54% similarity).

The DSC device has a temperature range of +80℃ to -60℃; however, since in some instances, the phase change occurs below -60℃, it was necessary to find a way and make the DSC cover very low temperatures. Therefore, the DSC device was provided with a liquid nitrogen system to allow for lower temperatures coverage; Figure 5.1 shows the DSC and the liquid nitrogen connected to it. The properties of liquid nitrogen are shown in table 5.1 below.

Figure 5.1: Differential Scanning Calorimetry Device (DSC) connected to a Liquid Nitrogen Vessel

Table 5.1: ***Physical and chemical properties of liquid nitrogen***

Chemical Formula	N_2
Molecular Weight	$28.01\ g.mol^{-1}$
Boiling point at 1 atm	-195.8 ℃
Freezing Point at 1 atm	-210.0 ℃
Critical temperature	-146.9 ℃
Critical pressure	33.5 atm
Density, Liquid at 1 atm	$808.5\ kg.m^{-3}$
Density, Gas at 1 atm	$1.16\ kg.m^{-3}$
Specific volume at 1 atm	$0.861\ m^3.kg^{-1}$
Latent heat of vaporization	$199.1\ kJ.kg^{-1}$
Expansion ratio, liquid to gas	1 to 694

This study assumed that the DSC delivered accurate readings and measurements, as scrutinising the accuracy of the measurement devices is not within the scope of this thesis.

5.2.2 Micrometre:

Prior to starting the experiments, samples of different SMA blends (manufactured in China) were cut and prepared in cubical shapes with the following dimensions: length = 3mm, width = 3mm and depth = 3mm, as shown in figures 5.2. After that, the dimensions of the samples were crossed-checked using a micrometre (with accuracy of 0.001 mm), as shown in figure 5.3. Thereafter, the samples were weighed with a calibrated scale (Radwag AS 60/220.R2), as shown in figure 5.4

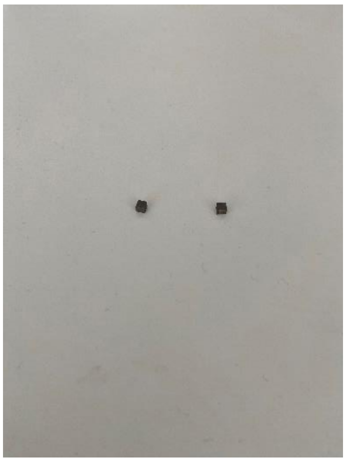

Figure 5.2: The SMA samples used for DSC testing and the mechanical loading.

Figure 5.3: a) Micrometre used for measuring samples dimensions b) Sample placed on the micrometre.

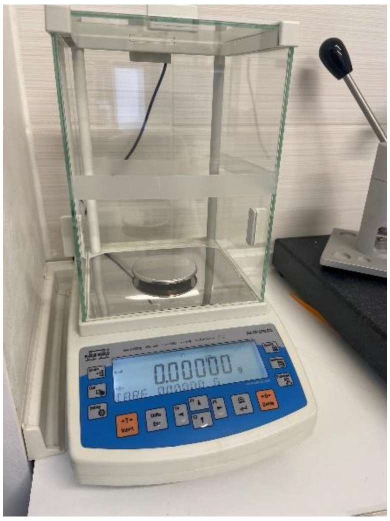

Figure 5.4: The scale device used to measure the weight of the samples.

5.2.3 Furnace:

- The temperature of the furnace was adjusted for the required annealing temperatures (450℃, 540℃ and 750℃) and the samples with the respective dimensions were put into the furnace. The samples were wrapped in an aluminium foil for security and to ensure no sample would be missing. See figure 5.5.

Figure 5.5: The electric Furnace used for heat-treating the SMA samples.

- All blend samples were left in the furnace for two different sets of times (8min and 10min).
- After the heat treatment, the samples were quenched using mains water at room temperature of 20°C.
- The samples were placed into the DSC and graphs were obtained for each sample and analysed.

5.2.4 Mechanical Loading (Testing Rig):

- Mechanical loading was carried out using an in-house built horizontal testing rig, as shown in figure 5.6.
- The test temperature (test condition) was set by a Peltier device built into the testing rig grips.

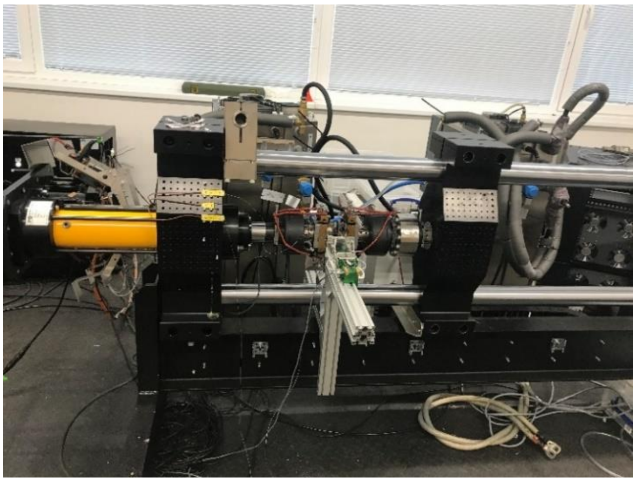

Figure 5.6; Mechanical loading testing rig (compression loading)

- The annealed samples were placed between the grips, and -5 MPa stress was applied to ensure the samples would not fall off prior to starting the loading.
- The calibrated extensometer (Epsilon 3549-01M-050-ST) was placed on the grips to read any deformation that would occur, as shown in figure 5.7; and the testing rig was set at different stresses depending on the application intended (1000 MPa for cycling and 2500 MPa for cold work); and the experiments were run for the number of cycles decided by the user.

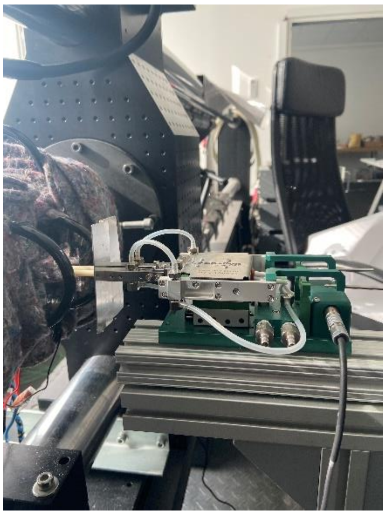

Figure 5.7: The extensometer placed on the grips of the compression rig.

5.3 Results and discussion:

5.3.1 DSC results and discussion

5.3.1.1 NiTiX

A specimen of an SMA blend of Nickel, Titanium and a third element referred to as X, for confidentiality, NiTiX was annealed at two different temperatures of 450℃ and 540℃. It was found that increasing the annealing temperature of NiTiX specimen from 450℃ to 540℃ moved the peaks to the left, as shown in figures 5.8 and 5.9, which means lower activation temperature and it was noticed that the peaks sizes changed, which means the available latent heat is significantly susceptible to the change in the annealing temperature.

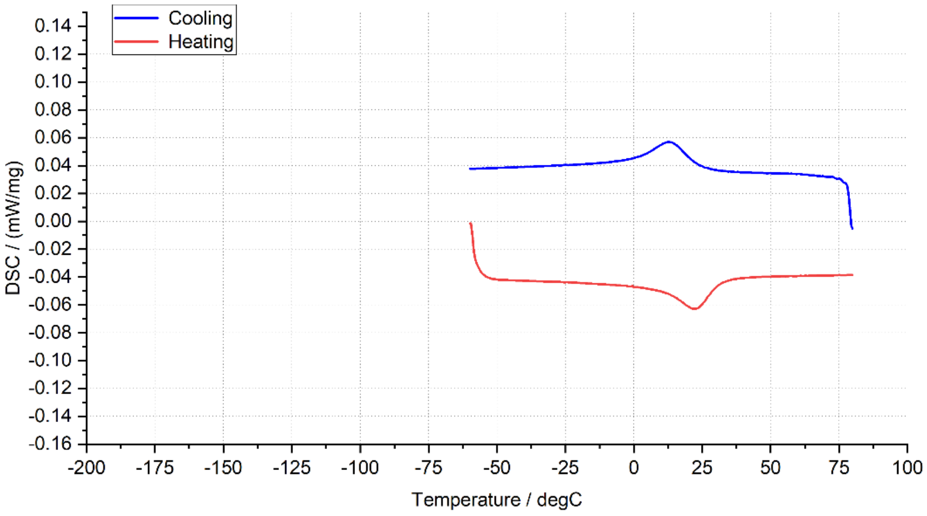

Figure 5.8: NiTiX annealed at 450℃ for 10min.

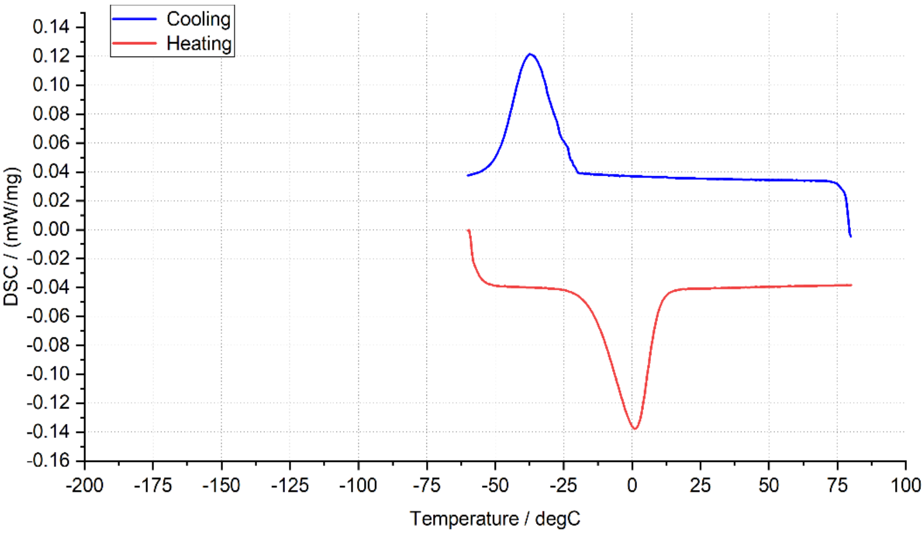

Figure 5.9: NiTiX annealed at 540℃ for 10min.

Figure 5.10 compares between the two cases in which the same blend was annealed at two different temperatures for the same amount of time. The graph shows that the activation temperatures took place at different areas, as the austenite start temperature A_s for the specimen annealed at 540℃ took place at -25℃, as the austenite finish temperature A_f occurred at 20℃. Whereas, for the specimen annealed at 450℃, A_s occured at 0℃ and A_f occured at 40℃. DSC analysis in figures 5.8 and 5.9 end at -60℃ which is before the Martensite transformation fully took place, therefore it was not possible to identify the Martensite activation temperatures.

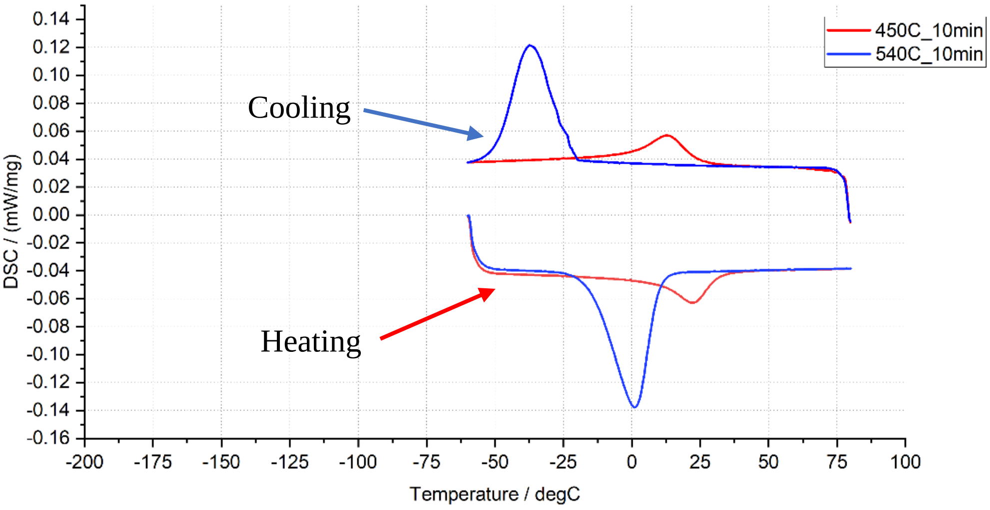

Figure 5.10: NiTiX annealed for 10min at 540℃ vs 450℃

During the testing, and in a pursuit of enhancing the material's output, it was decided to do coldwork process on one sample; the specimen was coldworked by compressing it at a high stress of 2500 MPa. Figure 5.11 compares between the same specimen of NiTiX processed as follows: NiTiX specimen annealed at 540°C for 10 minutes versus the same specimen cold-worked and then annealed at 540°C for 10 minutes. It was noticed that introducing cold-work to the specimen moved the peaks further to the left which means smaller activation temperatures and it was also noticed that the latent heat decreased noticeably with the addition of cold-work.

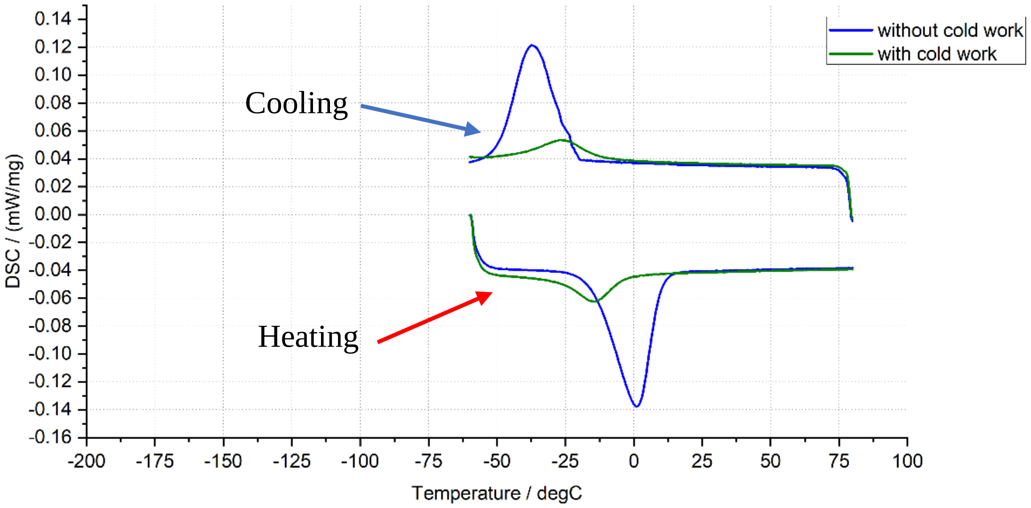

Figure 5.11: NiTiX annealed at 540°C for 10min before and after cold work.

All the above analysis could not reflect the Martensite transformation clearly, as Martensite phase took place below -60°C. Since the DSC range is between 80°C to -60°C, to solve this problem to make sure Martensite transformation is fully captured, a liquid nitrogen cylinder was installed and connected to the DSC device, as shown previously in the figure 5.1; and thus, the DSC's chamber in which the specimen was placed, could be cooled down to -170°C.

Figures 5.12 and 5.13 show the difference between the DSC reading with and without the addition of liquid nitrogen.

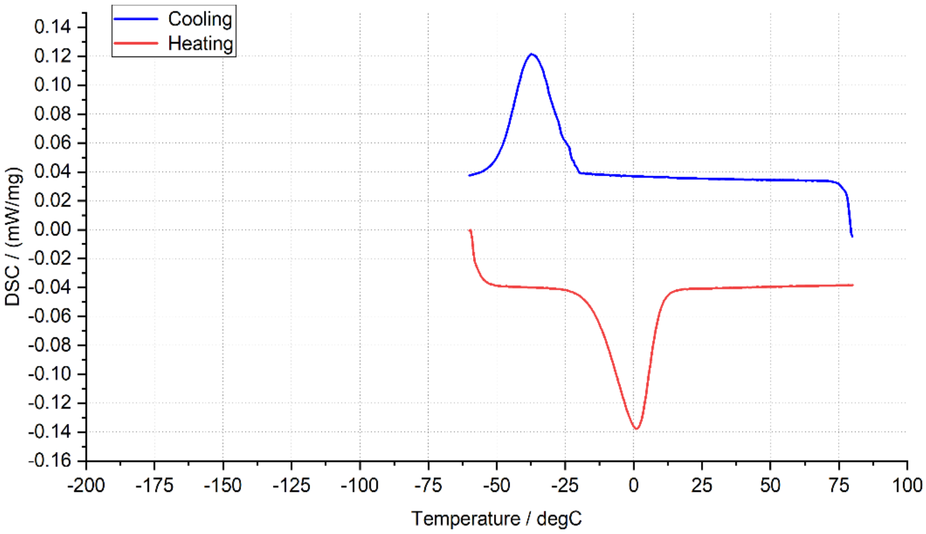

Figure 5.12: NiTiX annealed at 540℃ for 10min – Normal DSC analysis.

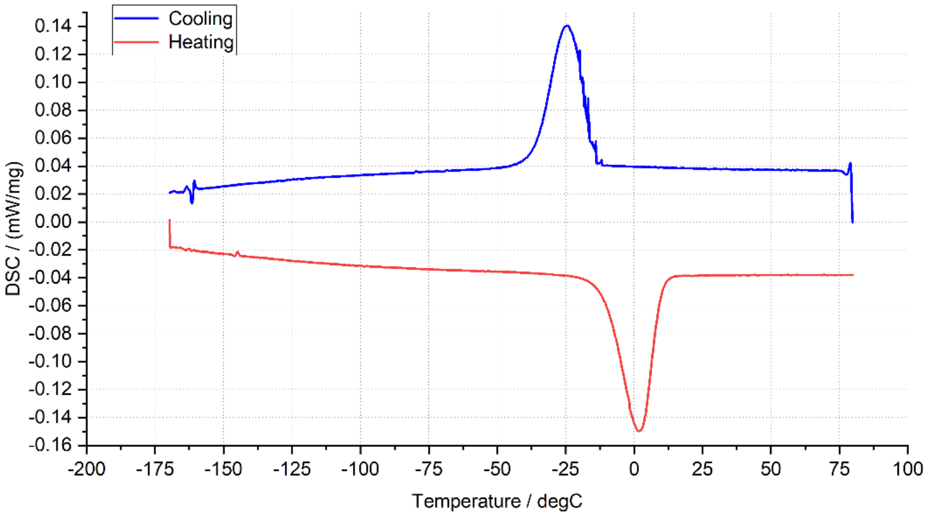

Figure 5.13: NiTiX annealed at 540℃ for 10min – After adding liquid nitrogen.

To better compare between the two different ranges of DSC analysis (-60℃ to 80℃ and -170℃ to 80℃), the two graphs were plotted on top of each other, as shown in figure 5.14. It was clearly shown that the Martensite finish temperature occurred at below -60℃, hence came the importance of adding liquid nitrogen to widen the range of the DSC analysis.

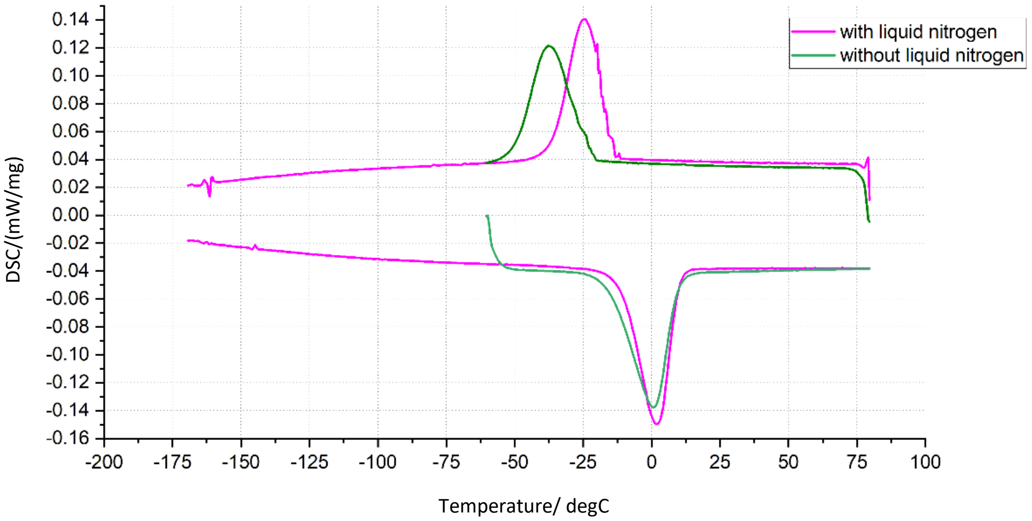

Figure 5.14: Comparison of DSC analysis with and without liquid nitrogen

Since the Austenite transformation was clear and was taking place between $\mathrm{A_s} = -25\ ^\circ\mathrm{C}$ and $\mathrm{A_f} = 20^\circ\mathrm{C}$ and there was no R-phase; then if the forward transformation curve was flipped and placed on top of the reverse transformation phase, the discrepancy between the two curves shows the range of the Martensite transformation. Figure 5.15 shows the heating curve flipped and placed on top of the cooling curve; the figure shows that the Martensite transformation started at $\mathrm{M_s} = -12.5^\circ\mathrm{C}$ and continued until $\mathrm{M_f} = -170^\circ\mathrm{C}$.

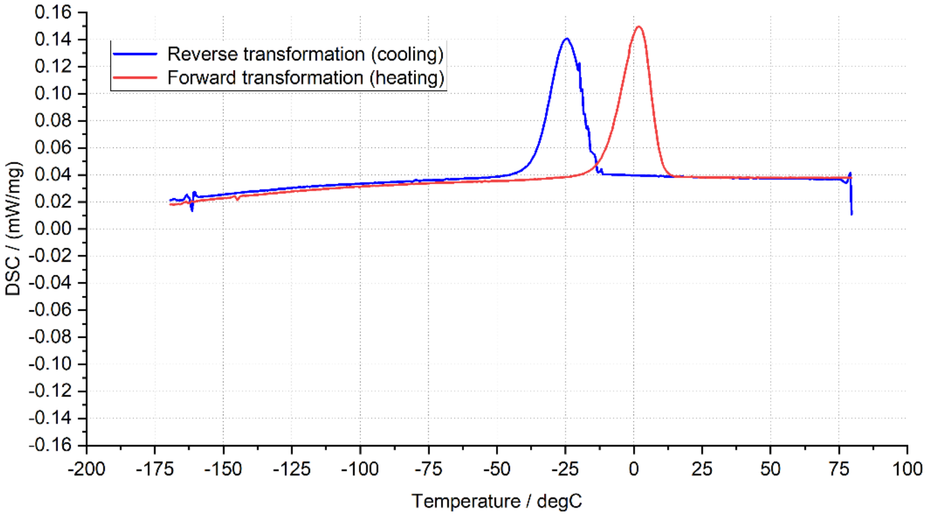

Figure 5.15: Heating curve flipped to showcase the Martensite transformation curve.

5.3.1.2 NiTi

The second sample was annealed at two different temperatures to showcase the behavioural change that occurs due to changing the annealing temperature. Firstly, the sample was annealed at 750℃ for 10 mins, and then the annealed sample was analysed in the DSC device. Figure 5.16 shows the DSC analysis for the annealed sample; the analysis showed that the Austenite transformation happened between $\mathrm{A_s}$= -75℃ and A_f= 0℃, and the Martensite transformation occured between $\mathrm{M_s}$= -25℃ and continued until $\mathrm{M_f}$=-100℃. Figure 5.17 shows a similar sample (same material and same dimensions) annealed at 450℃ for 8min; and the DSC analysis showed that the Austenite transformation happened between $\mathrm{A_s}$= -37.5℃ and $\mathrm{A_f}$= 40℃, and the Martensite transformation occured between $\mathrm{M_s}$= 0℃ and $\mathrm{M_f}$=-50℃.

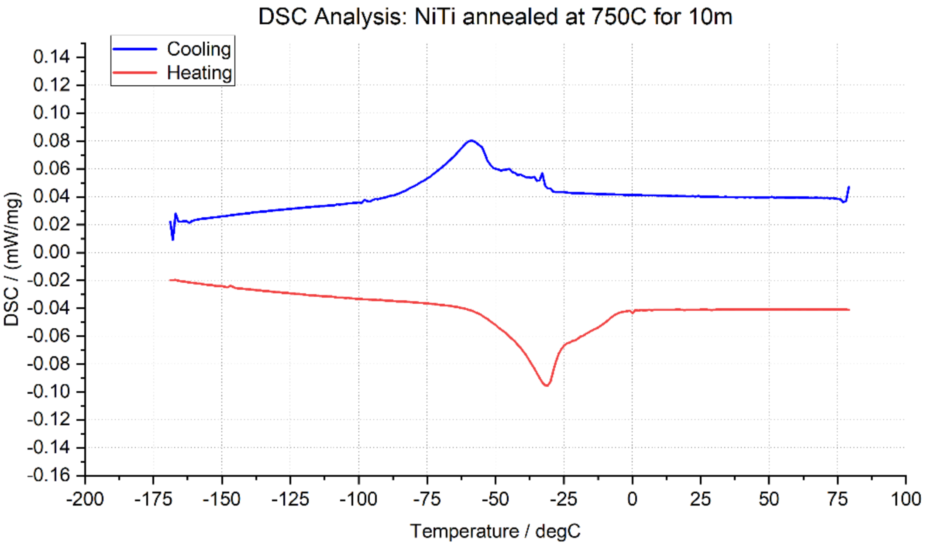

Figure 5.16: NiTi binary annealed at 750℃ for 10 min.

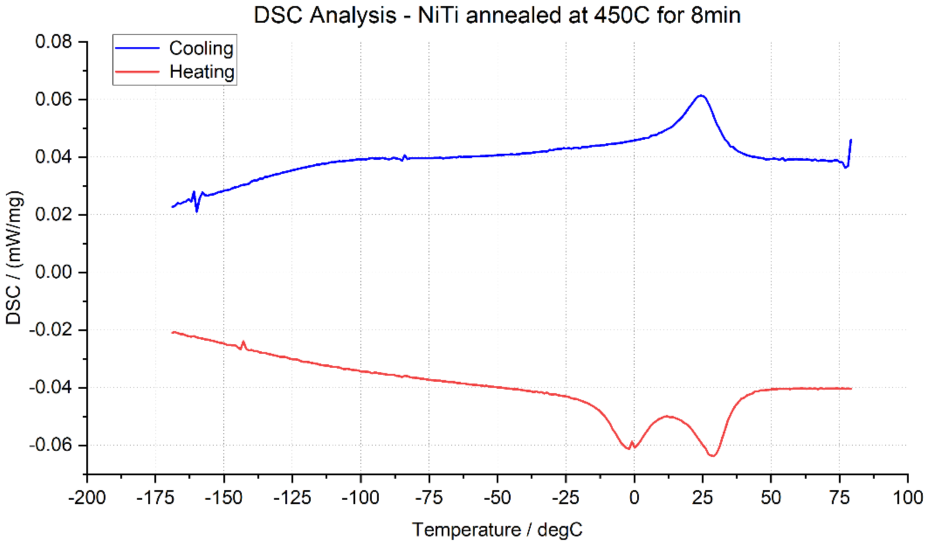

Figure 5.17: NiTi binary annealed at 450℃ for 8 min.

The tests conducted show clearly how different heat treatments change the material's properties and behaviour; and through thoroughly understanding the material's properties, it becomes possible to use the material for different applications as needed. And since the activation temperatures determine the operating range for the material, then by heat treating the material differently it possible to get different temperature ranges and thus different potential applications for any device that uses SMA material as its core heat source.

5.3.2 Mechanical testing results and discussion:

After the samples had been annealed and analysed in the DSC, they were tested for cycling in the mechanical loading testing rig. This step determined the available latent heat in the sample, transformation stresses and the maximum strain. The transformation stresses are the stresses at which each activation temperature occurs, the activation temperatures $\mathrm{A_s}$, $\mathrm{A_f}$, $\mathrm{M_s}$, & $\mathrm{M_f}$ occur at stresses σ^{As}, σ^{Af}, σ^{Ms}, & σ^{Mf} respectively.

The first sample tested for cycling was a cube of the following dimensions $(h = 3mm; w = 3mm;\ d = 3mm)$, of NiTi binary annealed at 450°C for 8 mins. The specimen was tested at three different test temperatures (15℃, 25℃ and 35℃). The mechanical loading testing rig produces stress-strain graphs as well as the available latent heat within the sample. The stress-strain graphs were used in understanding the behaviour of the material under stress, the hysteresis and the work required to achieve phase transformation; and thus, the COP of the system using SMA could eventually be calculated. The stress-strain curve through cycling gives an indication of the material robustness and its ability to withstand a certain number of cycles, which consequently decide the structural fatigue, and thus the life span of the device could be predicted as well. The figure 5.18 shows the stress-strain for the NiTi specimen tested under three different test temperatures.

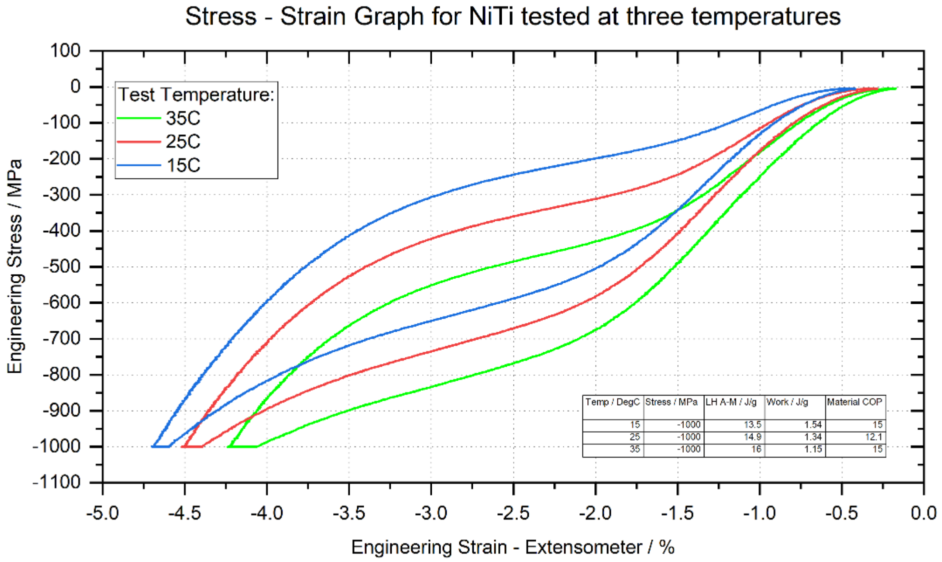

Temp / DegC	Stress / MPa	LH A-M / J/g	Work / J/g	Material COP
15	-1000	13.5	1.54	15
25	-1000	14.9	1.34	12.1
35	-1000	16	1.15	15

Figure 5.18: Stress-strain graph for NiTi tested at 15℃, 25℃ & 35℃

The graph in the figure 5.18 shows that the test temperature had a noticeable impact on the material's performance as well as the available latent heat. The graph shows that the latent heat increased with increasing the test temperature, as the material yielded 13.5 $J.g^{-1}$ at 15℃, 14.9 $J.g^{-1}$ at 25℃ and 16 $J.g^{-1}$ at 35℃. The graph shows that the higher the test temperature, the lower the work required which leads to a better material coefficient of performance. It was also noticed that the higher the test temperature, the lower the hysteresis loop and the lower the maximum transformation strain. When the test temperature was 15℃ the material had a transformation strain of 4.75% whereas the maximum transformation strain was 4.5% with 25℃ and a 4.25% with 35℃. However, since the strain in the three cases is not starting from the same point, when comparing between two graphs, it was necessary to shift one graph and place it on top of the other graph, as shown in the figure 5.19.

To compare between the hysteresis loop of the specimen when tested at 25°C versus 35°C, the two plots were plotted in COMSOL Multiphysics to simplify shifting the trajectory for one graph to plot it on top of the other graph. The graph for the sample tested at 35°C was plotted on top of the graph for the sample tested at 25°C; and to make the comparison possible, the starting point for the two graph was fixed, as shown in figure 5.19. Figure 5.19 shows the two graphs plotted on top of each other (for 35°C and 25°C) with the ending point for the strain fixed. In both cases, the hysteresis loop for the two samples did not follow the same trajectory, and the hysteresis loop for the sample tested at 35°C was smaller than the hysteresis loop for the one tested at 25°C, which means the sample tested at higher temperatures require less work.

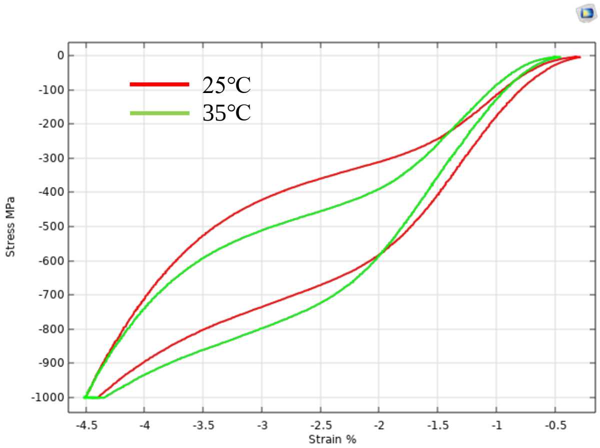

Figure 5.19: Stress-strain graph for NiTi tested at 25°C & 35°C.

5.3.3 Latent heat study:

To study the available latent heat in SMA under different conditions, two different blends (NiTiX and NiTi) were tested under compression. Each sample was stressed from 100MPa to 1000MPa with stress increment of 100MPa and the latent heat was calculated at each step. This procedure was repeated for four different test temperatures (10°C, 20°C, 30°C & 40°C). From the previous study shown in figure 5.18, it was established that the available latent heat increased with the increase of the test temperature. The current study, which is shown in figures 5.20 and 5.21, compares between the latent heat available in two different blends when tested under the similar test conditions. The NiTi blend in figure 5.20, shows that at the beginning of releasing latent heat, higher test temperatures required higher stresses; that continued to be true until the material reached a point where it released its entire latent heat, then the complete opposite happened, as the case became that the higher the test temperature the lower the required stress.

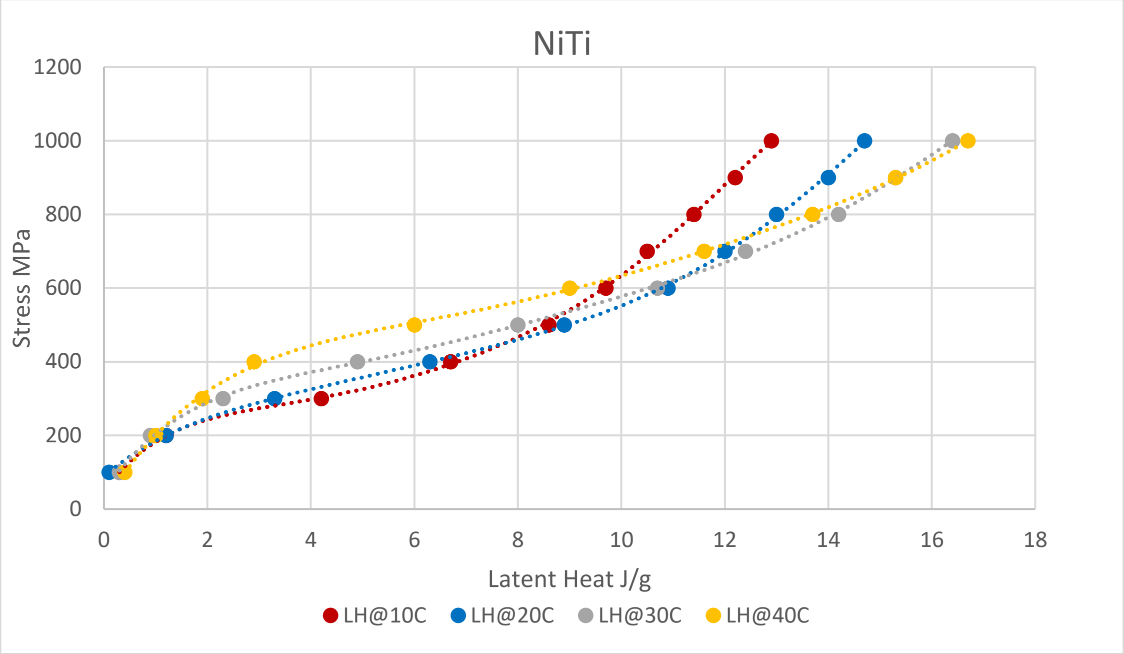

Figure 5.20: Latent heat available in NiTi blend tested at four different temperatures.

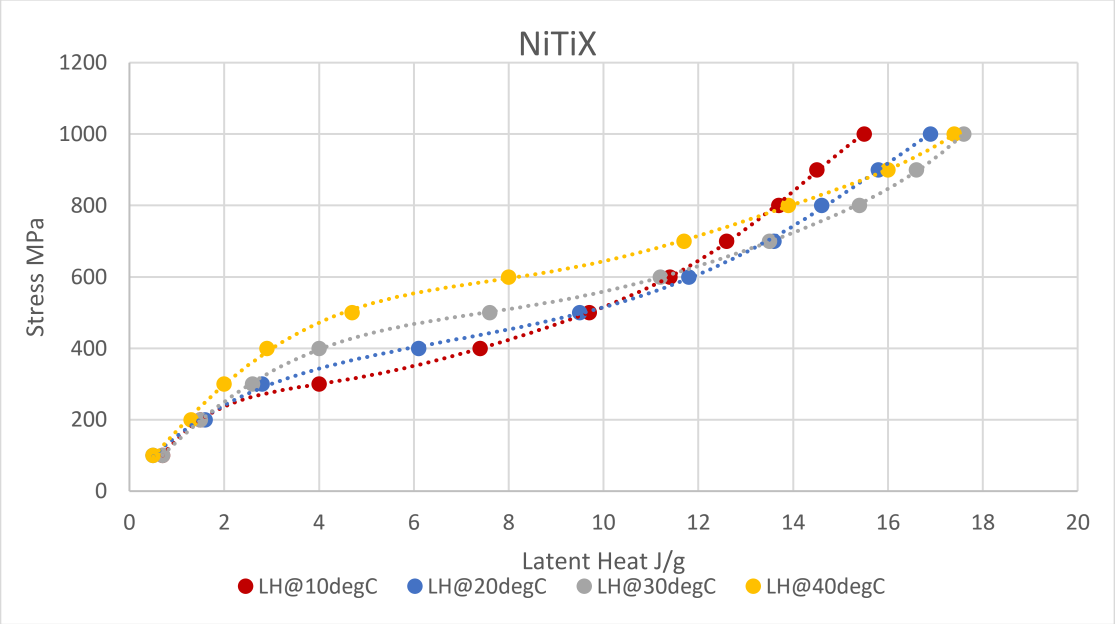

Figure 5.21: Latent heat available in NiTiX blend tested at four different temperatures.

Figure 5.21 shows the trajectories of latent heat at different test temperatures and different stresses for a NiTiX specimen. At the beginning of the test, it was noticed that higher test temperatures required higher stresses to release latent heat. NiTiX sample test results followed the same pattern as NiTi sample; the only difference between the two samples was that the latent heat available in NiTiX was more compared to NiTi.

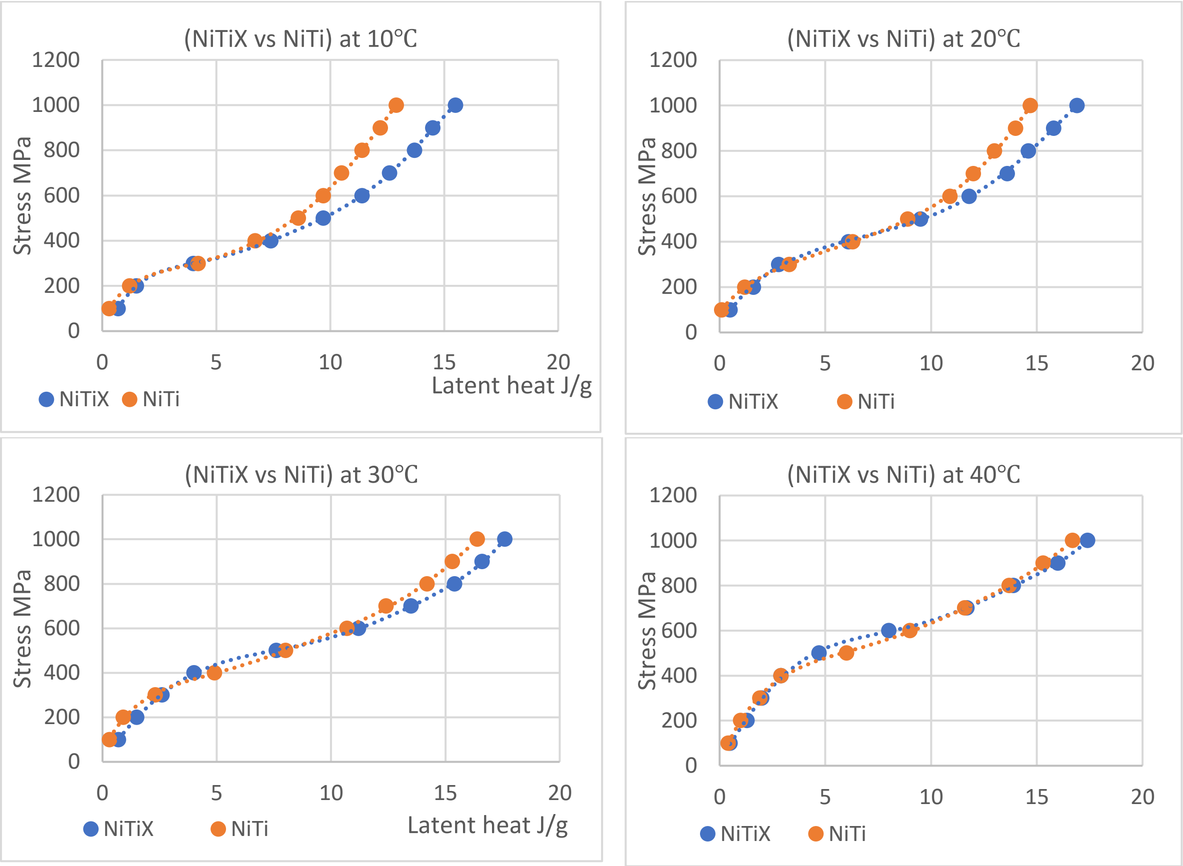

Figure 5.22: Comparison between latent heat available in NiTiX vs NiTi at each of the four test temperatures

The breakdown of the test results shown in figure 5.22, showed that at lower temperatures the latent heat available in the two tested blend followed different trajectories, and as the test temperature increased, the trajectories tended to move towards being on top of each other; the only difference was that the latent heat that could be released from a NiTiX blend was more than that of a NiTi blend. Through this test and these results, and given the ambient temperature was known, it becomes possible to predict an SMA's device performance through knowing the latent heat and the stress required to secure that latent heat in question.

5.4 Experimental results versus modelling results:

The testing rig was calibrated to deal with compression stress as a negative value, as it considers the direction of movement, see the figure 5.23. However, to validate the modelling results against the experimental results, the graph in figure 5.23 needed to be flipped and the trajectory needed to go from down to up to replicate the graph produced from the modelling, see the figure 5.24. The graphs shown in the below figures, show that a full martensitic transformation occurred at stress of 1000 MPa, and it shows that there was a continuous transformation. The maximum transformation strain was 4.5%; and the width of the hysteresis loop varied between 0 MPa and 300 MPa.

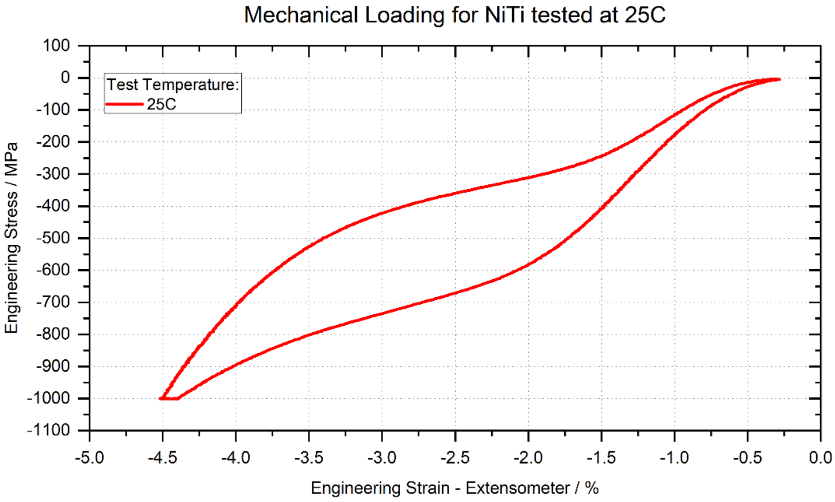

Figure 5.23: Testing rig stress-strain graph for NiTi tested 25℃

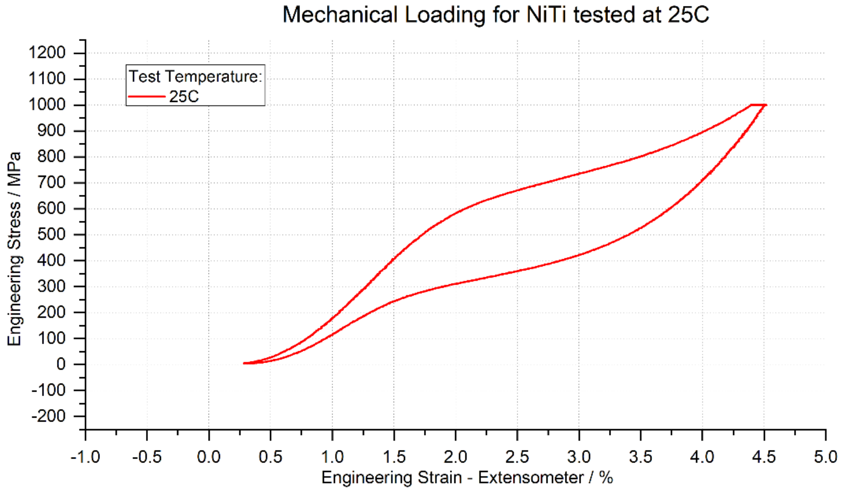

Figure 5.24: NiTi tested at 25℃ - Graph flipped to follow the modelling trajectory.

A similar sample with similar dimensions of $3mm \times 3mm \times 3mm$ SMA cube was used for modelling. As discussed in Chapter 4, SMA model in COMSOL Multiphysics requires the user to input many variables into the model, which includes: The activation temperatures, maximum transformation strain, material density, young modulus, stress influence coefficient for Martensite and Austenite, Poison's ratio, and heat capacity at constant pressure for Martensite and Austenite. The activation temperatures were taken off the DSC analysis for NiTi sample shown previously in figure 5.17. To better identify the location of the activation temperatures, The heating curve was flipped and was placed on top of the cooling curve; the discrepancy between the two curves showed the start and end of the Martensite phase, as shown in figure 5.25.

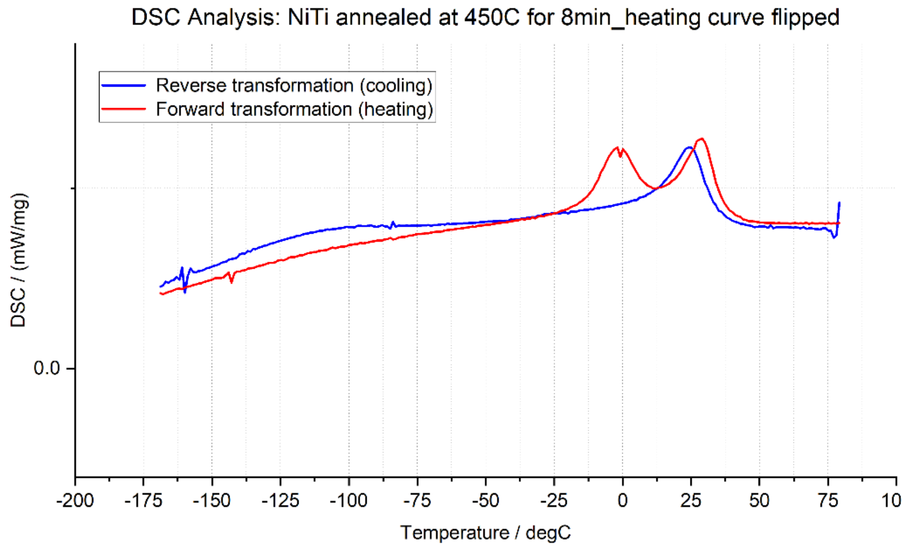

Figure 5.25: Heating curve flipped and placed on top of cooling curve to identify the Martensite activation temperatures for NiTi sample.

From figure 5.25, the point at which the red and blue curves first intersect represents the point at which the Martensite phase starts, which is $\mathrm{M_s}$ and it equals -25°C. It is hard to identify the Martensite finish point as the two curves go in parallel. However, through modelling different points for $\mathrm{M_f}$, the most accurate value for $\mathrm{M_f}$ can be predicted. Preliminarily, $\mathrm{M_f}$ was assumed to be -50°C, and then different values of $\mathrm{M_f}$ were tested in the pursuit of an optimised stress strain curve. The DSC analysis showed an R-phase in the heating curve, which made the activation temperatures for Austenite phase as follows: $\mathrm{A_s} = 13°\mathrm{C}$ and $\mathrm{A_f} = 50°\mathrm{C}$. However, when using these temperatures for Austenite transformation, the stress-strain curve did not fully transform back to Austenite, as shown in figure 5.26.

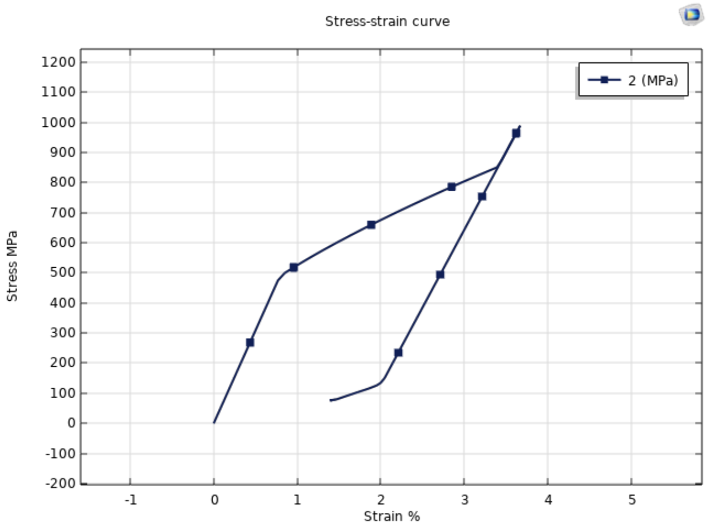

Figure 5.26: Stress-strain curve for NiTi sample modelled in COMSOL Multiphysics with A_s= 13℃ & A_f = 50℃

The relationships between R-phase to Austenite, Austenite to Martensite, and Martensite to R-phase have been studied extensively, and it was concluded that the kinetic barriers between R-phase and Austenite is very small compared to the kinetic barriers between Austenite and Martensite phases, which results in smaller hysteresis between R-phase and Austenite of (0℃ to 3℃) as opposed to (30℃ to 60℃) hysteresis between Austenite and Martensite (Bonsignore et al., 2019). Based on this fact, the author considered the temperatures at which R-phase started is -20℃ and finished is 10℃ and fed them into the model instead of $\mathrm{A_s}$ and $\mathrm{A_f}$; and the result is shown in figure 5.27.

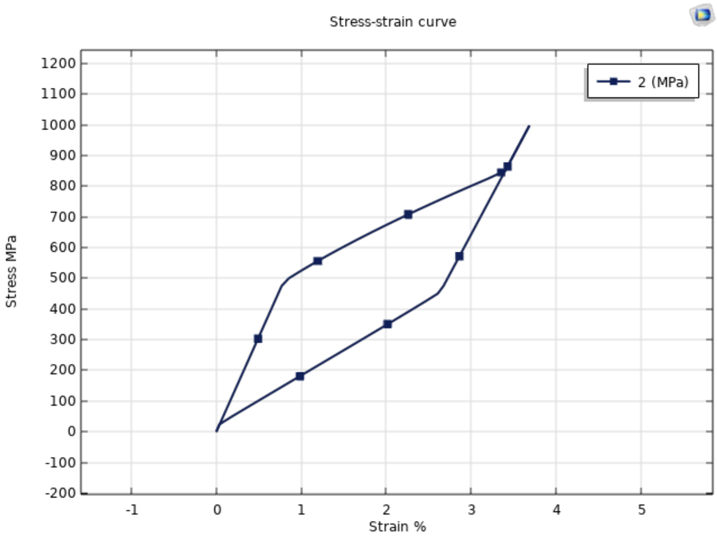

Figure 5.27: Stress-strain curve for NiTi sample modelled in COMSOL Multiphysics with R-phase temperatures considered as A_s & A_f

By adjusting the Austenite activation temperatures to equal the R-phase temperatures; it was noticed that the stress-strain curve showed a full transformation; and by comparing the curve produced by the modelling, shown in figure 5.28, to the curve produced by the testing rig, shown previously in figure 5.24, it was noticed that the two curves were following a similar pattern, as shown in figure 5.28.

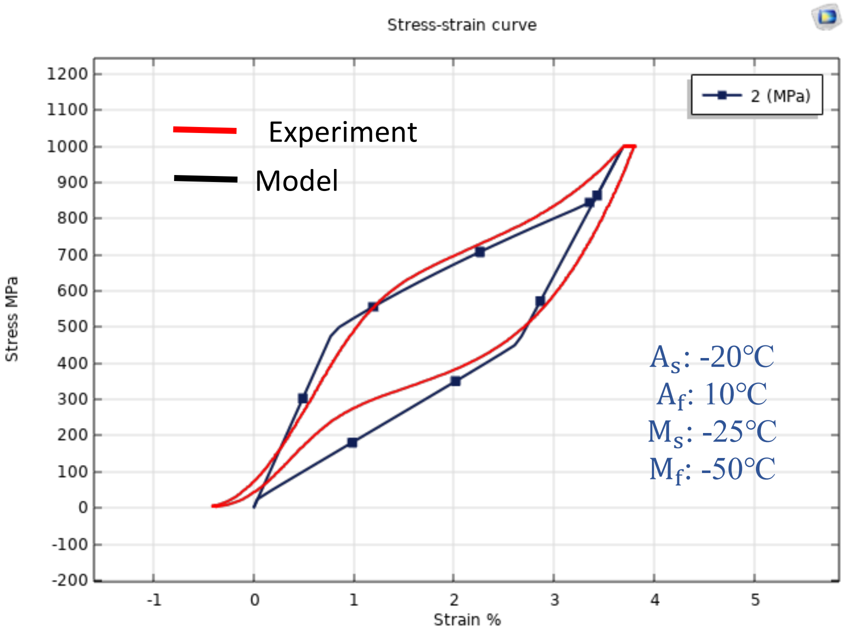

Figure 5.28: Comparison of stress-strain curve (COMSOL modelling vs testing rig)

The modelling graph in figure 5.28, did not fit the experiment graph properly; and this can be altered by changing the activation temperatures; as the stresses at which phase transformations occured can be explained by the Clausius Clapeyron relationship which specify the temperature dependence of stress, as per the below equation:

$$\frac{d\sigma}{dT} = \frac{\mathrm{Enthalpy}}{T \times \Delta v} \qquad (5.1)$$

Where T is the test temperature, and Δv is the change in volume. Therefore, since the Clausius Clapeyron ratio is a known variable that the user inputs into the system, then the resultant of every activation temperature and the test temperature can be multiplied by the Clausius Clapeyron ratio to obtain the different activation stresses. Figure 5.29 shows different sets of activation temperatures to optimise the curve produced by the modelling and make it fit the experiment curve.

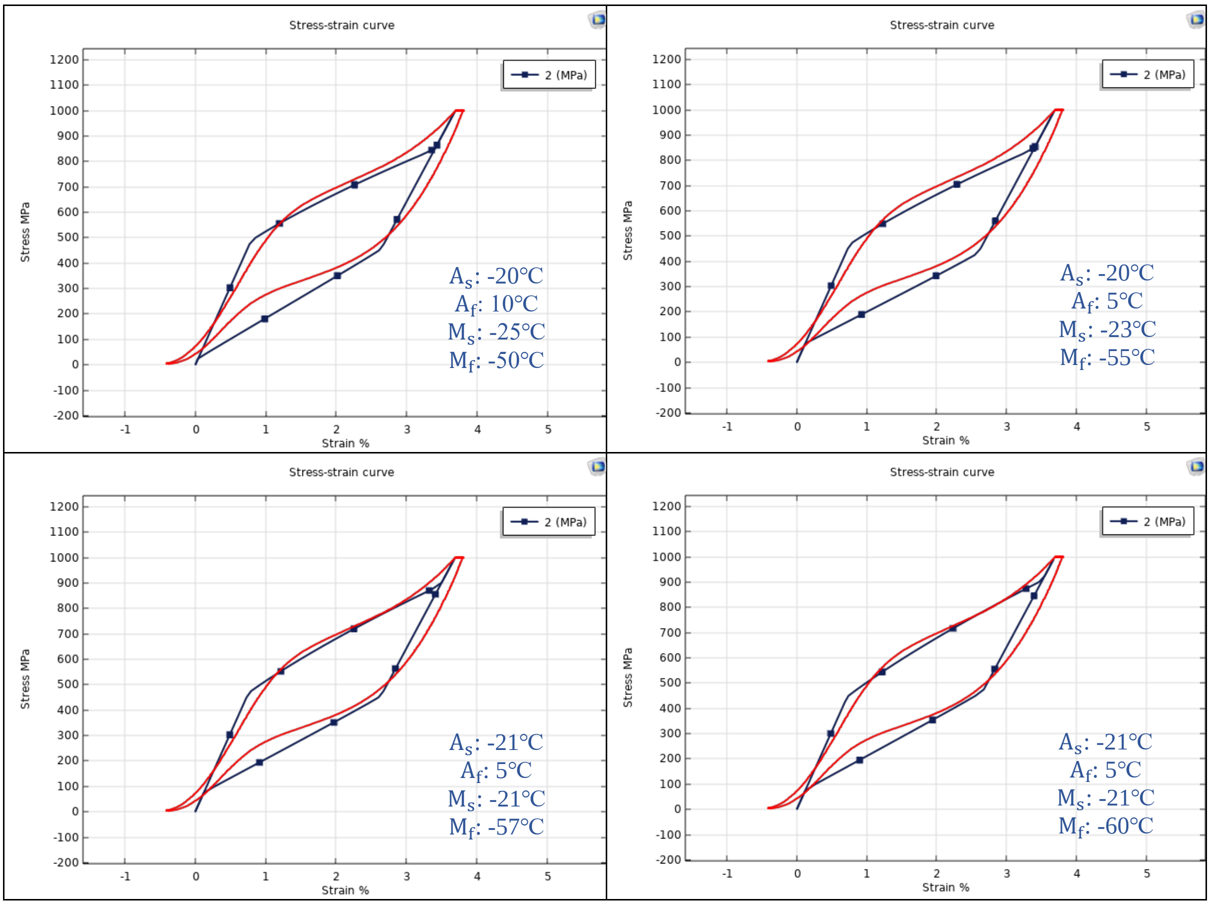

Figure 5.29: Curve optimisation through altering activation temperatures

Since the test temperature T was 25℃, and Clausius Clapeyron ratio was around 8.6 MPa; and since there was a range for each activation temperature, then the activation stresses can be found as follows:

$$\sigma^{\mathrm{As}} = |A_s + T| \times Clausius\ Clapeyron\ ratio \tag{5.2}$$

$$\sigma^{\mathrm{Af}} = |A_f + T| \times Clausius\ Clapeyron\ ratio \tag{5.3}$$

$$\sigma^{\mathrm{Ms}} = |M_s + T| \times Clausius\ Clapeyron\ ratio \tag{5.4}$$

$$\sigma^{\mathrm{Mf}} = |M_f + T| \times Clausius\ Clapeyron\ ratio \tag{5.5}$$

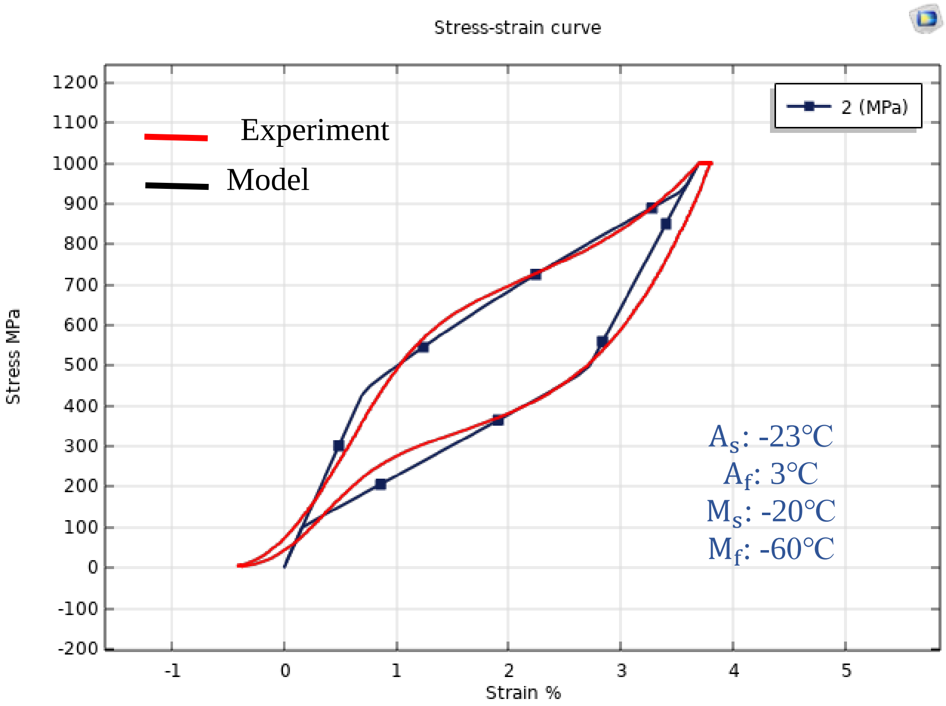

Figure 5.30: Comparison between the optimised modelling curve and the experiment curve

By choosing the set of temperatures shown in figure 5.30 ($A_s = -23$°C, $A_f = 3$°C, $M_s = -20$°C & $M_f = -60$°C), the graph produced by the model became the closest to the graph produced by the testing rig in terms of activation stresses as well as the width of the hysteresis loop, as shown in figure 5.30. This set of temperatures allowed the SMA specimen to have a temperature difference ΔT = 8K on the heating side, and a temperature difference ΔT = 7.5K on the cooling side, see below figure 5.31. The temperature of the specimen, in figure 5.31, increased under loading from 20°C to 28°C releasing a maximum internal energy of 6 $J.g^{-1}$at the end of the loading; then the temperature of the specimen falls to 12.5°C absorbing a maximum latent heat of 4.5 $J.g^{-1}$, see figure 5.32 below.

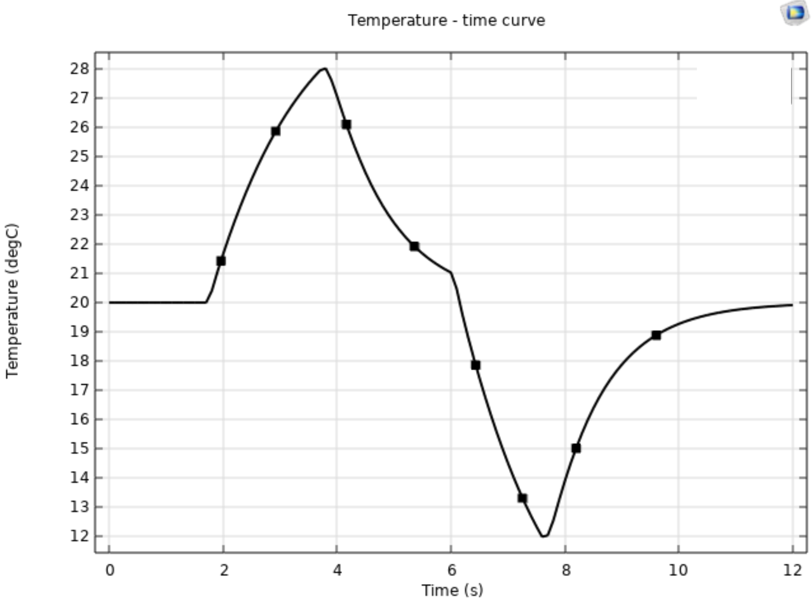

Figure 5.31: Temperature – time curve for SMA specimen modelled in COMSOL Multiphysics

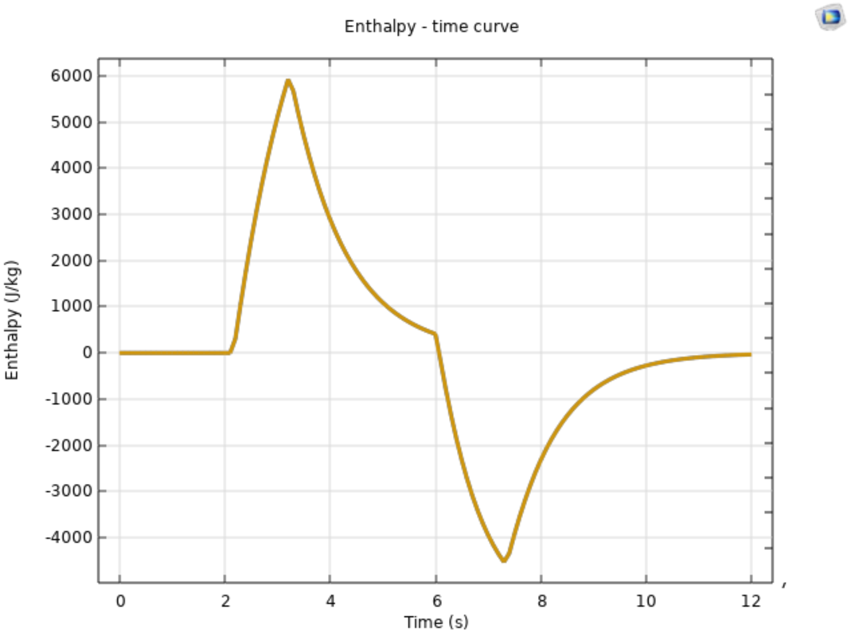

Figure 5.32: Enthalpy – time curve for SMA specimen modelled in COMSOL Multiphysics

Figure 5.32 shows the total enthalpy available within the sample (rejected into and absorbed from the surroundings) during loading and unloading. To find the total latent heat available within the specimen, the graph in the above figure needed to be divided into two graphs, one for loading and one for unloading and then the latent heat could be obtained by finding the integral area below the curve.

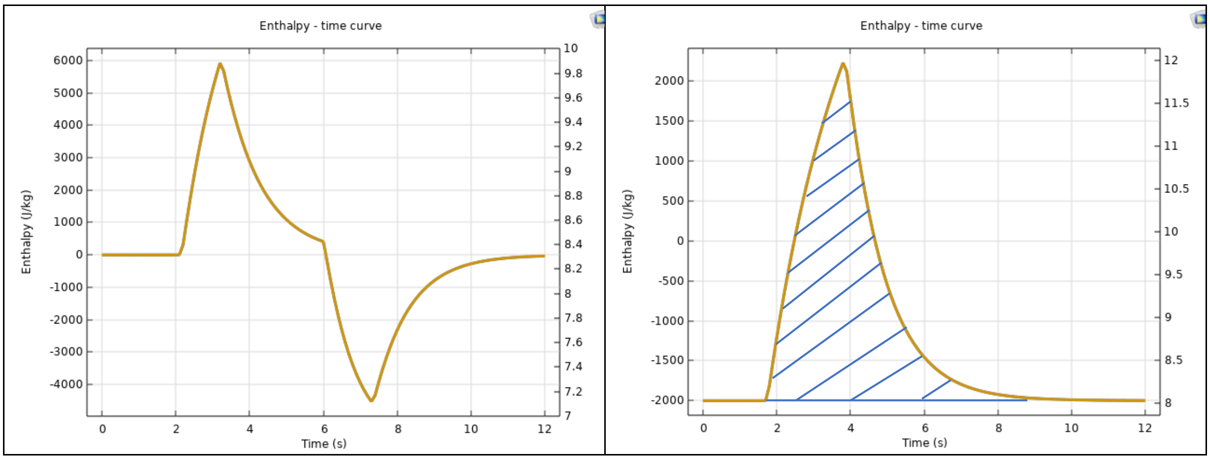

Figure 5.33: Enthalpy – time curve for loading only to allow latent heat calculation.

By integrating the hatched area in figure 5.33, and by taking the integral limits from 1.7 second, where the releasing of the internal energy started, to 10.5 seconds where all the energy was released, the latent heat found to be 13 $J.g^{-1}$which is slightly lower than the value calculated by the testing rig 14.9 $J.g^{-1}$.

Thermal conductivity K is an important factor that determines the heat transfer across the material and as consequence, determines the heat transfer between the material in question, and any working fluid. The thermal conductivity for NiTi is 12 $W.m^{-1}.K^{-1}$ when the material is Austenite phase and 8 $W.m^{-1}.K^{-1}$ in Martensite phase (Lagoudas D., 2007). COMSOL modelling allows the user to see the thermal conductivity at any given moment during the transition between the two SMA phases (Austenite and Martensite), as shown in figure 5.34.

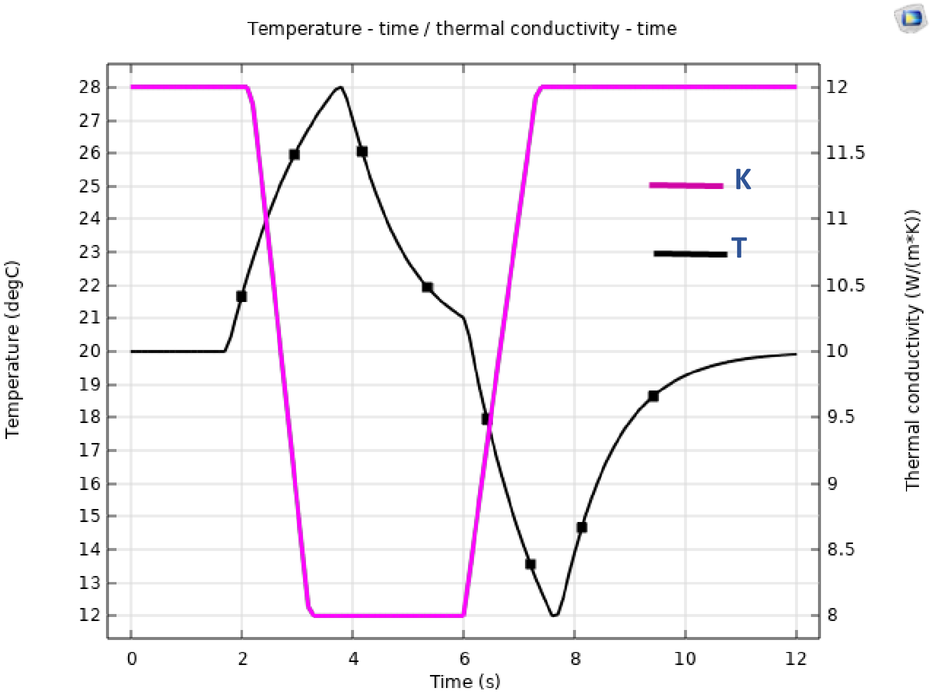

Figure 5.34: Temperature – time curve combined with thermal conductivity – time curve.

Figure 5.34 shows how the thermal conductivity changed as the material transitions between Austenite and Martensite. SMA material in Pseudoelasiticty started at Austenite whose thermal conductivity is 12 $W.m^{-1}.K^{-1}$, and then as the material started transitioning from Austenite to Martensite, the temperature of the material started rising and the thermal conductivity started decreasing. When the material fully transformed from Austenite to Martensite the thermal conductivity reached its lowest value which was 8 $W.m^{-1}.K^{-1}$, which meant despite the material's temperature was high, the material heat transfers capability was not optimum which explains why the temperature in the core of the material under loading is higher than the temperature around the edges.

5.5 Summary:

This chapter went through the material experiments and model validation. The chapter started by presenting the equipment used for the experiments; thereafter it went through the DSC analysis for two SMA blends heat-treated differently. The DSC results showed that increasing the annealing temperature shifted the activation temperatures to smaller values, which means if the material is intended to be used for low temperature applications, then it needs to be heat-treated at higher temperatures. The chapter also presented interesting results about how the material's latent heat is influenced by the ambient temperature as well as the applied stress; this study was conducted on two blends NiTi and NiTiX, and the results showed that the two blends behaved differently at lower temperature and similarly at higher temperatures. The last section in this chapter was validating the results of the mathematical model against the results obtained from the testing rig; the latent heat worked out from the model was 13 $J.g^{-1}$ and the one obtained from the testing rig was 14.9 $J.g^{-1}$. This discrepancy is due to the interaction between the testing rig's grips and the specimen which was not quantified in the modelling.

Chapter 6: Heat Transfer Analysis

Chapter 6 Heat Transfer and Fluid Flow Design

6.1 Introduction:

This project aims to produce 3 kW of heating with a temperature difference ΔT between the material and the working fluid of 5K. The SMA material was used as the heat source, and the value of the latent available in the material was taken from the analysis done in chapter 4. Since the stress method used was compression, to avoid buckling issues that are associated with wires and tubes, the SMA material in this project was designed into plates with different geometries with openings or slots of different geometries to allow the working fluid to pass through them and thus extract the heat generated. This chapter explores different geometries for the plates and for the slots and compares the performance of the different scenarios taking into consideration heat transfer calculations which include Hydraulic diameter, Mass flow rate, Volume flow rate, Reynolds number, Friction factor, Pressure drops, velocity, Nusselt number, Heat transfer coefficient and required surface area. Following designing the plate, the Computational Fluid Dynamics software (COMSOL Multiphysics) was used to simulate the design in question and work out the amount of heat that could be harnessed from each design.

6.2 Heat Transfer Analysis Methodology

6.2.1 Heat Transfer Study:

An in-depth heat transfer study was carried out on different plate geometries. The purpose of the study was to find the best geometry that would lead to the best heat transfer between the SMA material (heat source) and any working fluid that is meant to remove the heat from the source and reject it into a heat sink. To carry out such study, the user would decide the amount of heating load required from the system, the cycle time and the shape of the slots. The latent heat available within the material is extracted from testing a specimen under compression, and thereafter the value of the latent heat could be validated against the CFD model. These values (heating load, cycle time and latent heat) were used to calculate: Hydraulic diameter, velocity, Nusselt number, Reynolds number and heat transfer coefficient. The heat transfer coefficient was then used to decide the heat flux through the openings and thus deciding what geometry had better performance.

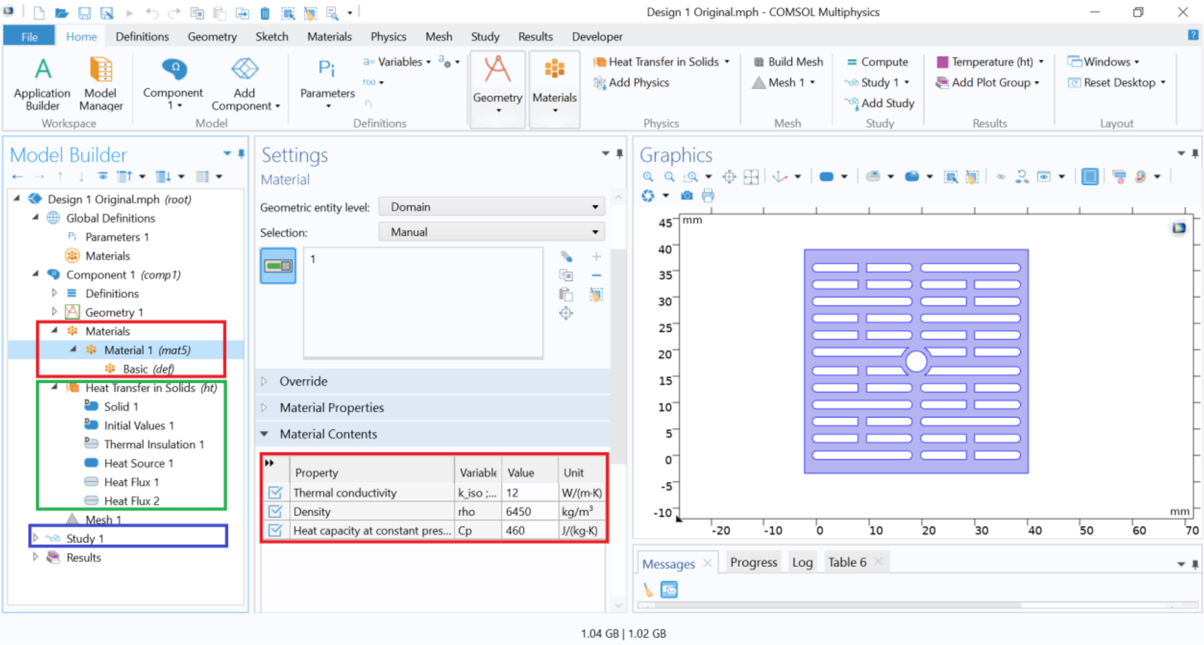

Geometric entity level: Domain

Selection: Manual

1

	Property	Variable	Value	Unit
☑	Thermal conductivity	k_iso ;...	12	W/(m·K)
☑	Density	rho	6450	kg/m³
☑	Heat capacity at constant pres...	Cp	460	J/(kg·K)

Figure 6.1: Main window of COMSOL software showing the model builder.

Figure 6.1 shows the set-up in COMSOL; the main five steps are:

i. Geometry: geometry is built as decided by the user. Different geometries were created and modelled, as explained in depth in the results section.

ii. Material: Since the SMA material used in the project is not included in COMSOL's library, it was necessary to build the material using the parameters and properties extracted from the literature review; it was assumed that all these properties are correct.

iii. Physics: This project involves three physics (Solid Mechanics, Heat Transfer and Fluid Flow). Each physics has a set of boundary conditions as explained in section 6.2.2.

iv. Mesh: There are two methods for meshing the geometry in question: physics-controlled, and user-controlled.

v. Study: There are two types of studies (Steady State and Time-Dependent). All the studies in this project are time dependent.

6.2.2 Multiphysics modelling (Solid Mechanics, Heat Transfer and Fluid Flow) Study:

The Multiphysics modelling combined the three physics mentioned in the above section; these physics work as follows:

i. Solid mechanics: The material (SMA) is selected in this section, and its thermophysical properties are input. This section allows the user to decide the location of any required support (roller) and the direction of the stress.

ii. Heat Transfer: This section allows the user to decide any boundary conditions that may be required to run the simulation (ambient temperature, temperature of the material before loading … etc); and to decide the temperature of the fluid entering the system, should there is any fluid at all.

iii. Fluid Flow: This physics allow the user to decide the fluid inlet and outlet as well as the velocity at which the fluid enters the stack. The type of flow and the velocity of the fluid are to be obtained from manual calculations using heat transfer equations as meticulously explained in the results section below. Figure 6.2 shows the setup of the three mentioned physics in COMSOL Multiphysics software.

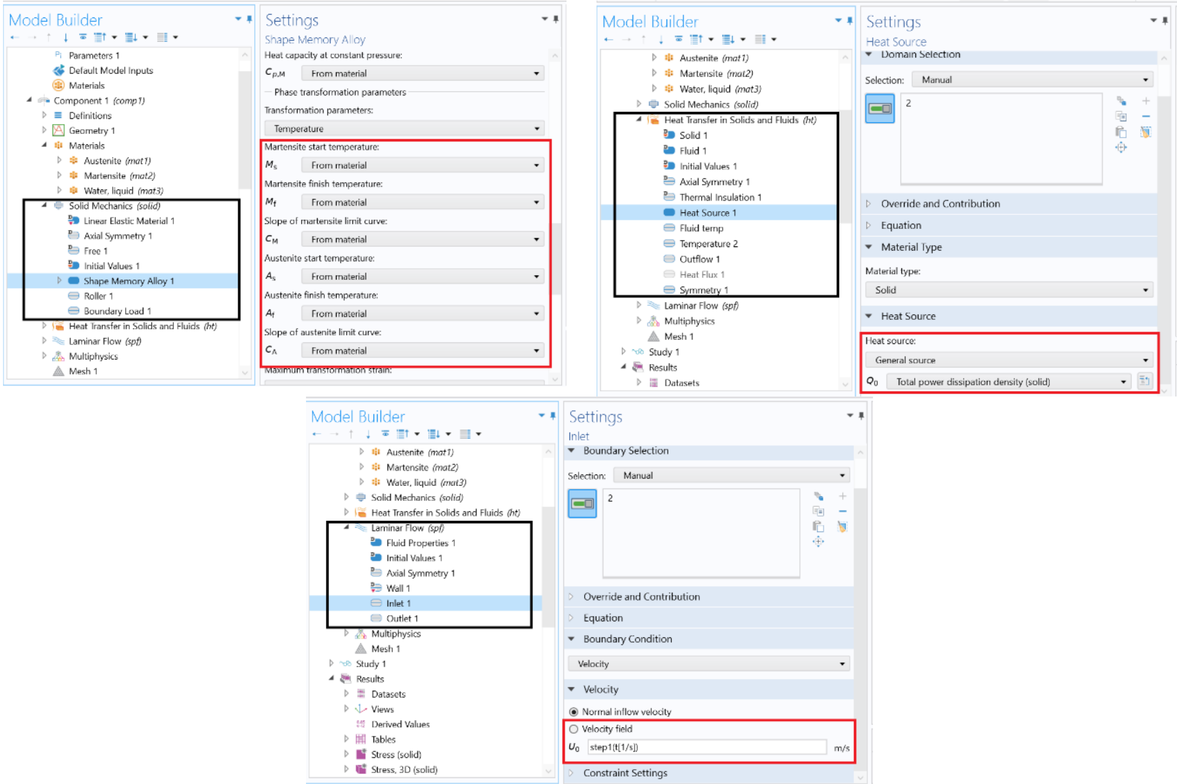

Shape Memory Alloy

Heat capacity at constant pressure:

$C_{p,M}$ From material

Phase transformation parameters

Transformation parameters:

Temperature

Martensite start temperature:

M_s From material

Martensite finish temperature:

M_f From material

Slope of martensite limit curve:

C_M From material

Austenite start temperature:

A_s From material

Austenite finish temperature:

A_f From material

Slope of austenite limit curve:

C_A From material

Maximum transformation strain:

Heat Source

Domain Selection

Selection: Manual

2

Override and Contribution

Equation

Material Type

Material type:

Solid

Heat Source

Heat source:

General source

Q_0 Total power dissipation density (solid)

Inlet

Boundary Selection

Selection: Manual

2

Override and Contribution

Equation

Boundary Condition

Velocity

Velocity

● Normal inflow velocity

○ Velocity field

U_0 step1(t[1/s]) m/s

Constraint Settings

Figure 6.2: The model builder for the three physics: Solid Mechanics, Heat Transfer and Fluid Flow

6.2.3 MATLAB:

MATLAB was used to validate COMSOL's heat transfer results by conduction as shown in the results section below. A code in MATLAB was written using transient conduction equations obtained from the seventh edition of Fundamentals of Heat and Mass Transfer by Frank P. Incropera. The code is annexed in the appendices (appendix A).

6.2.4 Actual Function of Excel sheets:

Excel sheets were used to calculate the different scenarios for the different slot geometries and plate dimensions. The goal of this study was to work out values that are needed as input for COMSOL modelling. After the modelling was complete, excel sheets were used once again to work out the percentage of heat removed by each of the different plates and the value was compared to the theoretical heat available within the plate to decide the efficiency of each plate. all the excel calculations are in appendix (B).

6.3 Heat Transfer Design Discussion

6.3.1 Parameters required for the design.

The SMA sample used for this study was a binary NiTi with the thermophysical properties mentioned previously in table 4.1 in chapter 4, which was brought into this chapter to smoothen the flow of information. The latent heat available within the material is 13 $J.g^{-1}$as calculated previously in figure 5.34 in Chapter 5; and the parameters of the specimen are as listed previously in table 4.1. Table 4.1 was brought into this chapter to make it easier for the reader to follow.

Table 4.1: Parameters of the first NiTi sample used in the CFD modelling.

Parameter	Value	Parameter	Value
A_s	260 K	E_A	55 GPa
A_f	270 K	E_M	46 GPa
M_s	245 K	K_A	12 $W.m^{-1}.K^{-1}$
M_f	230 K	K_M	8 $W.m^{-1}.K^{-1}$
H	5.6%	ρ	6450 $kg.m^{-3}$
C_A	7.4e6 $MPa.K^{-1}$	Poisson's ratio	0.33
C_M	7.4e6 $MPa.K^{-1}$	C_p at constant pressure	400 $J.kg^{-1}.K^{-1}$
SMA reference temp	25 K		

To complete the calculation and decide which geometry secures the optimum design, there were many factors that needed to be considered, in terms of the required input and the intended output, as well as the type of the fluid and its corresponding properties. The parameters that need to be considered are listed in table 6.1 below.

Table 6.1: Parameters required for SMA design and modelling.

Required Input Info	**Required Output**	**Fluid Parameters**
Austenite thermal conductivity $\boldsymbol{K_A}(W.m^{-1}.K^{-1})$	Required heating/cooling load $\boldsymbol{q}\ (kW)$	Dynamic viscosity $\mu\ (Pa.s)$
Martensite thermal conductivity $\boldsymbol{K_M}(W.m^{-1}.K^{-1})$	Cycle time $\boldsymbol{t}\ (s)$	Thermal conductivity $\boldsymbol{K_f}\ (W.m^{-1}.K^{-1})$
$\boldsymbol{\Delta T_{heating}}\ (K)$	Power $\boldsymbol{P}\ (kW)$	Specific heat capacity $\boldsymbol{C_p}(kJ.kg^{-1}.K^{-1})$
$\boldsymbol{\Delta T_{cooling}}\ (K)$	Heat Rejection time $\boldsymbol{HR_t}\ (s)$	Fluid density $\boldsymbol{\rho_f}\ (kg.m^{-3})$
Material density $\boldsymbol{\rho_m}\ (kg.m^{-3})$		Prandtl number $\boldsymbol{Pr}$
Material thickness $\boldsymbol{d}\ (m)$		Channel length $\boldsymbol{L_p}\ (m)$
Latent heat $\boldsymbol{LH}\ (J.kg^{-1})$		
Thickness between slots $\boldsymbol{x}\ (m)$		

The design calculations go through the following steps:

- Plate parameters
- Slots parameters
- Plate parameters after slots
- Stack parameters
- Heat transfer and fluid flow calculations

The length (l), width (w) and depth (d) of the plate are required to calculate the plate's volume (V), mass (m) and the available amount of latent heat within the plate.

$$V_{plate}\ (m^3) = l \times w \times d \tag{6.1}$$

$$m_{plate}\ (kg) = V \times \rho_m \tag{6.2}$$

The mass of the plate is determined from equation (6.2), and since the required heating/cooling load (q) is decided by the user, then by benefitting from the value of the latent heat available within the material, it becomes possible to work out the mass required to deliver the required (q), as follows:

$$overall\ Mass\ \boldsymbol{m_{overall}}\ (kg) = q \times t/LH \tag{6.3}$$

The number of plates required to deliver specific (q), can be calculated through dividing the overall mass required obtained from equation (6.3) by the mass of a single plate obtained from equation (6.2), therefore:

$$Number\ of\ uncut\ plates\ \boldsymbol{nr} = m_{overall}/m_{plate} \tag{6.4}$$

The equations 6.1 to 6.4 decide the mass required to produce specific amount of heating/cooling load (q), and the number of plates to achieve (q) in question. However, since the material is the heat source and there will be a working fluid pumped through the material to pick up that (q), then there is a need of designing openings/slots through which the fluid is to be pumped. The design of the slots depends on the selected geometries.

6.3.2 Slots calculation

The author of this research started by assuming a preliminarily number for the slots (nr_{slot}); thereafter the geometry of the slots needs to be decided, then the cross-sectional area of one slot (CSA_{slot}) is calculated followed by calculating the volume of one slot. The volume of one slot (V_{slot}) when multiplied by the number of slots represents the volume of the material that is lost from the original uncut plate; and since the mass of the plate required to achieve the desired (q) is known, then the number of plates will need to be updated to secure the required overall mass $(m_{overall})$ and consequently to achieve (q). The heat transfer surface area (HT_{CSA}) can be calculated as well by multiplying the cross-sectional of one slot (CSA_{slot}) by number of slots (nr_{slot}).

$$V_{slot}(m^3)\ = CSA_{slot} \times d \tag{6.5}$$

$$m_{\ slot}(kg) = V_{slot} \times \rho_m \times\ nr_{slot} \tag{6.6}$$

The mass of the plate after the slots have been cut $(\boldsymbol{m}_{\ \boldsymbol{cut}})$ equals the original mass of the plate minus the mass of the slots which is calculated by equation (6.6)

$$m_{\,cut}(kg) \;=\; m_{overall} - \; m_{\,slot} \tag{6.7}$$

From equation (6.7), the new number of plates after the slots can be derived as follows:

$$Number\ of cut\ plates\ \boldsymbol{nr_{cut}} = m_{overall}/m_{cut} \tag{6.8}$$

It is now possible to calculate the percentage of mass loss and the percentage gain over loss for heat transfer, as follows.

$$\%m_{loss} = (m_{\,slot}/m_{overall}) \times 100 \tag{6.9}$$

$$\%HT_{gain/loss} = (HT_{CSA}/CSA_{slot}) \times 100 \tag{6.10}$$

Equations (6.1) to (6.10) calculate the parameters of the plate which will be used in the designing the stack; the following step is using the plate with the specifications obtained from the above equations and using it in heat transfer calculations.

6.3.3 Heat transfer calculations

Performing heat transfer calculations on the selected plate geometries is a paramount step, through which the user can decide whether the final output is desirable and whether the final device is good enough to compete in the market in terms of size, efficiency, and coefficient of performance. There are many parameters that need to be calculated before deciding about the viability of the design; these parameters are:

1- Hydraulic diameters:

$$D_H = \frac{4 \times CSA_{slot}}{P_{slot}} \tag{6.11}$$

Where P_{slot} is the perimeter of one slot

2- Mass flow rate $\boldsymbol{\dot{m}}$ (kg/s)

$$\dot{m} = \frac{q}{C_p \Delta T} \tag{6.12}$$

3- Volumetric flow rate $\boldsymbol{Q}$ (m^3/s)

$$Q = \frac{\dot{m}}{\rho_m} \tag{6.13}$$

4- Reynolds number $\boldsymbol{Re}$

$$Re = \frac{\rho_f \times \, u \times \, D_H}{\mu} \tag{6.14}$$

Where u is the velocity of the fluid. And since u is known, then Reynolds number could be calculated as follows:

$$Re = \frac{\dot{m} \times \, D_H}{\mu \, \times CSA_{slot} \times (nr_{slot}/nr_{path})} \tag{6.15}$$

Where (nr_{path}) is the number of flow path for the fluid through the plate. The value of Re determines the type of flow as follows:

$$Re < 2300 \quad Laminar\ flow$$
$$2300 < Re < 10000 \quad Turbulent\ flow$$
$$Re \geq 10000 \quad Fully\ developped\ turbulent\ flow$$

5- Fluid velocity $\boldsymbol{u}$ (m/s)

The fluid velocity can be worked out by shuffling equation (6.14), since Reynolds number was obtained from equation (6.15). Therefore, the fluid's velocity can be obtained by:

$$u = \frac{Re \times \, \mu}{\rho_f \times \, D_H} \tag{6.16}$$

6- Pressure-drop $\boldsymbol{\Delta P}$ (kPa)

To calculate the pressure-drop, the friction factor (f) needs to be calculated as follows:

$$f = (0.79 \times \ln{(Re)} - 1.64)^{-2} \qquad 3000 \leq Re \leq 5 \times 10^6 \tag{6.17}$$

Above equation (6.17) is valid for internal flow with smooth surfaces. Therefore, the pressure-drop can be calculated as follows:

$$\varDelta P = \frac{f \times u^2 \times \rho_f}{2 \times L_p} \tag{6.18}$$

7- Nusselt number $\boldsymbol{Nu}$

There are many factors that play a vital role on deciding which equation should be used to calculate the value of Nusselt number such as: the type of flow, whether it is internal or external flow and whether it is laminar or turbulent, and the geometry of the fluid path. These equations are classified as follows:

For internal flow in a channel with smooth surfaces, Nusselt number can be obtained from the below equation:

$$Nu = 0.023 \times Re^{4/5} \times Pr^{1/3} \tag{6.19}$$

Above equation (6.19) is correct for $2 \times 10^4 < Re < 10^6$

A review of above equation (6.19) was published by Dittus and Boelter to cater for smaller Reynolds numbers $(2500 < Re < 1.24 \times 10^5)$ and a different range of Prandtl number $(0.7 \leq Pr \leq 120)$

$$Nu = 0.023 \times Re^{4/5} \times Pr^{n} \tag{6.20}$$

The Prandtl number exponent *(n)* is 0.4 when the fluid is being heated, and 0.3 when the fluid is being cooled. (Bergman, T.L. and Lavine, A.S., 2019)

Equations (6.19) and (6.20) were fine-tuned and made more accurate by Gnielinski who came up with the below formula for calculating Nusselt number when $(2300 < Re < 5 \times 10^6)$ and $(0.5 < Pr < 10^6)$

$$Nu = \frac{(f/2)(Re - 10^3)Pr}{1 + 12.7(f/2)^{1/2}(Pr^{2/3} - 1)} \tag{6.21}$$

Above equation (6.21) was simplified as follows

$$Nu = \begin{cases} 0.0214(Re^{0.8} - 100)Pr^{0.4}\ for\ (0.5 \leq Pr \leq 1.5\ ;\ 10^4 \leq Re \leq 5 \times 10^6) \\ 0.012(Re^{0.87} - 280)Pr^{0.4}\ for\ (1.5 \leq Pr \leq 500\ ;\ 3 \times 10^3 \leq Re \leq 10^6) \end{cases} \tag{6.22}$$

Taler D., (2018) investigated Nusselt number for turbulent flow in a pipe when Reynolds number is between three thousand and one million ($3 \times 10^3 < Re < 10^6$) for three different ranges of Prandtl number. The formulas are as follow:

$$Nu = 0.02155 \times Re^{0.8018} \times Pr^{0.7095} \quad for\ 0.1 \leq Pr \leq 1 \tag{6.23}$$

$$Nu = 0.01253 \times Re^{0.8413} \times Pr^{0.6179} \quad for\ 1 \leq Pr \leq 3 \tag{6.24}$$

$$Nu = 0.00881 \times Re^{0.8991} \times Pr^{0.3911} \quad for\ 3 \leq Pr \leq 1000 \tag{6.25}$$

Equation (6.19) to (6.25) are all used to obtain the value of Nusselt number; they need to be used very carefully as per the situation in question. Therefore, it is always a good practice to identify the fluid in use and subsequently its Prandtl number and then calculate Reynolds number, and accordingly the user can decide on which equation is most suitable for the scenario in hand.

8- Heat transfer coefficient $\boldsymbol{h}$ $(W/m^2.K)$

Heat transfer coefficient is defined as the rate of heat transfer between a solid surface and a fluid per unit surface area per unit temperature difference. The value of (*h*) is influenced by the surface geometry, the nature of the fluid and its properties. Therefore, (*h*) plays an important role, as it determines the ability of a fluid to pick up heat from a solid surface; and it is significant to calculate the value of (*h*), as it is one of the variables the user needs to input into the CFD software to run design enhancement models.

$$h = \frac{k_f \times Nu}{D_H} \tag{6.26}$$

9- Overall heat transfer surface area $\boldsymbol{A_{HT}}$ (m^2)

After all the above parameters have been calculated, the overall stack surface area that is required to deliver the required (q) need to be calculated from below equation:

$$q = U \times A_{HT} \times \Delta T \tag{6.27}$$

Since (q) is an input, then by shuffling equation (6.27), the heat transfer surface area can be obtained as shown below:

$$A_{HT} = \frac{q}{U \times \Delta T} \tag{6.28}$$

Where (U) is the overall heat transfer coefficient, which is the inverse of the total thermal resistance of the material (R_{total}). Therefore, (R_{total}) needs to be calculated; and since SMA is a phase change material and has different values for thermal conductivity, then this fact must be considered when calculating R_{total} to ensure accurate values for (U) and thereafter accurate values for heat transfer surface area (A_{HT}).

$$\boldsymbol{R_{total}} = \frac{1}{h} + \frac{x/2}{k_A} \quad For\ Austenite \tag{6.29}$$

$$\boldsymbol{R_{total}} = \frac{1}{h} + \frac{x/2}{k_M} \quad For\ Martensite \tag{6.30}$$

From equations (6.29) and (6.30) the value of the total thermal resistance is obtained; the overall heat transfer coefficient (U) is the inverse of (R_{total}) which means there will be two values for (U). By substituting the value of (U) in equations (6.28), the required surface area (A_{HT}) to achieve certain (q) can be acquired. Since there are two different values for (U), that will lead to two different values for (A_{HT}), therefore, the decision will be based on the purpose of the design; if the design is to deliver heating, then the selection of (A_{HT}) will be based on the value obtained from using the thermal conductivity of the material at Austenite.

6.4 Plate and Stack design

6.4.1 Plate design

The required output of this project was a system that generates 3 kW of heating. The task was to design a heat exchanger that could secure the transfer of 3 kW between the heat source (The SMA material) and the working fluid. This section explores different plate designs/geometries and different cycle times and compares between them. Table 6.2 shows the parameters used for the design, and table 6.3 shows the first plate and its dimensions.

Table 6.2: SMA – NiTi parameters and user's assumptions

$\boldsymbol{K_A}$	12	$(W.m^{-1}.K^{-1})$
$\boldsymbol{K_M}$	8.6	$(W.m^{-1}.K^{-1})$
Latent Heat	13	$(kJ.kg^{-1})$
Required Power [per Core]	3	(kW)
Cycle Time	9	(s)
Heat Rejection Time	4	(s)

Table 6.3: Plate 1 design and dimensions

Name: Plate 1 **Plate dimensions:** 37 mm × 37 mm **Plate thickness:** *d*: 3 mm **Slot dimensions:** *w*:1.5 mm; *l*:10 mm **Number of slots** (nr_{slot})**:** 40 **Thickness between slots:** 1 mm **Radius of stiffener-opening:** *r:* 3 mm **Mass of uncut plate:** 26.49 g	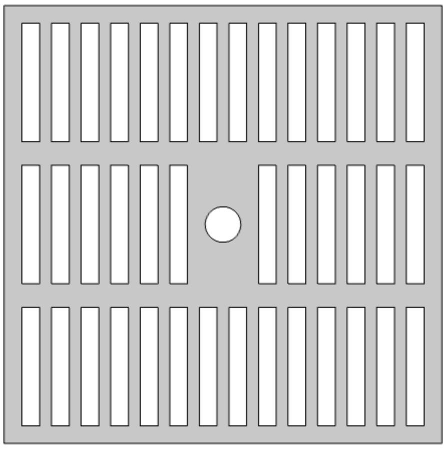

To know how many of plate 1 will be required to deliver 3 kW, the author started by calculating the overall mass required from equation (6.3), $\boldsymbol{m_{overall}}\ (kg) = q \times t/LH$; since all the variable in equation (6.3) were known as shown in tables 6.2 and 6.3, therefore:

$$\boldsymbol{m_{overall}}\ (kg) = 3 \times 4/13 = 0.92kg$$

Since the plate mass was worked out as mentioned in table 6.3, therefore, the number of plates required was:

$$\boldsymbol{nr} = m_{overall}/m_{plate} = 920/26.4 = 35\ plates$$

To achieve 3 kW, there should be 35 plates of plate 1 design. However, this was the plate before cutting the slots which would lead to material loss and therefore the number of plates required would increase, the calculation for that started with calculating the volume of the cut material, which was determined by calculating the volume of one slot and multiplying it by the number of slots, and adding to that the volume of the stiffener opening which was designed for stack support purposes; thereafter the mass of the cut material could be obtained, and by using equation (6.8) the new number of plates required could be obtained.

$$Volume\ of\ cut\ material = (1.5 \times 10 \times 3) \times 40 + \pi \times 1.5^2 \times 3 = 1821mm^3$$
$$= 18.21 \times 10^{-9}m^3$$

$$Mass\ of\ cut\ material = volume\ of\ cut\ material\ \times material\ density$$
$$= 18.21 \times 10^{-9}m^3 \times 6450\ kg/m^3 = 0.01175kg\ or\ 11.75g$$

After cutting the slots on the plate, the mass of the plates dropped from $26.49g\ to\ 26.49g - 11.75g = 14.74g$ which meant the plate lost 44.35% of its weight. Therefore, the new number of plates required was $0.92/0.01474 = 63\ plates$. Which meant the number of plates required to deliver 3kW has increased from 35 plates to 63 plates due to the material loss resulted from cutting slots on the original plate.

One of the important parameters was finding the percentage of gained heat transfer surface area after making slots on the plate. This percentage can be found by working out the heat transfer surface area for the slots divided by the cross-sectional area of the slots as follows:

$$\%gain/loss\ for\ HT\ surface\ area = \frac{slots\ HT\ surface\ area}{slots\ CSA} \tag{6.31}$$

This percentage for plate 1 design is:

$$\%\frac{gain}{loss} for\ HT\ surface\ area = \frac{(w+l) \times 2d \times nr_{slot}}{w \times l \times nr_{slot}} = \frac{(1.5+10) \times 2 \times 3 \times 40}{1.5 \times 10 \times 40}$$
$$= 460\%$$

Note: the volume of the stiffener opening was neglected in calculating the above percentage as it had a negligible impact. Which meant even though the plate lost 43.9% of its weight, it multiplied its heat transfer surface area by 4.6 folds thanks to the slots which have been made on it.

The next step in the design manual calculation was to find the heat transfer parameters through using equations (6.11) to (6.30); through these equations the value of the heat transfer coefficient (h) was obtained. This value was needed to perform modelling in COMSOL Multiphysics, as it was one of the required inputs. The values of heat transfer parameters were calculated and were summarised in table 6.4 below.

Table 6.4: Heat transfer calculated parameters for plate 1.

$D_h\ (mm)$	$\dot{m}\ (kg.s^{-1})$	Re	$u\ (m.s^{-1})$	Nu	$h\ (W.m^{-2}.K^{-1})$
2.61	0.144	3500	1.2	25.5	5850

From the heat transfer calculation and as shown in table 6.4, the heat transfer coefficient for the current design (Plate 1) was $5850\ W.m^{-2}.K^{-1}$; this was the value which was used in COMSOL simulation to test the average temperature on the plate as well as the percentage of heat that could be picked up from this design. Considering the goal here was to study the heat transfer, then the SMA physics was not included at this stage of simulation; however, it will be included in the coming section when all the physics were to be incorporated in one model. Figure 6.3 shows the setup of the model in COMSOL.

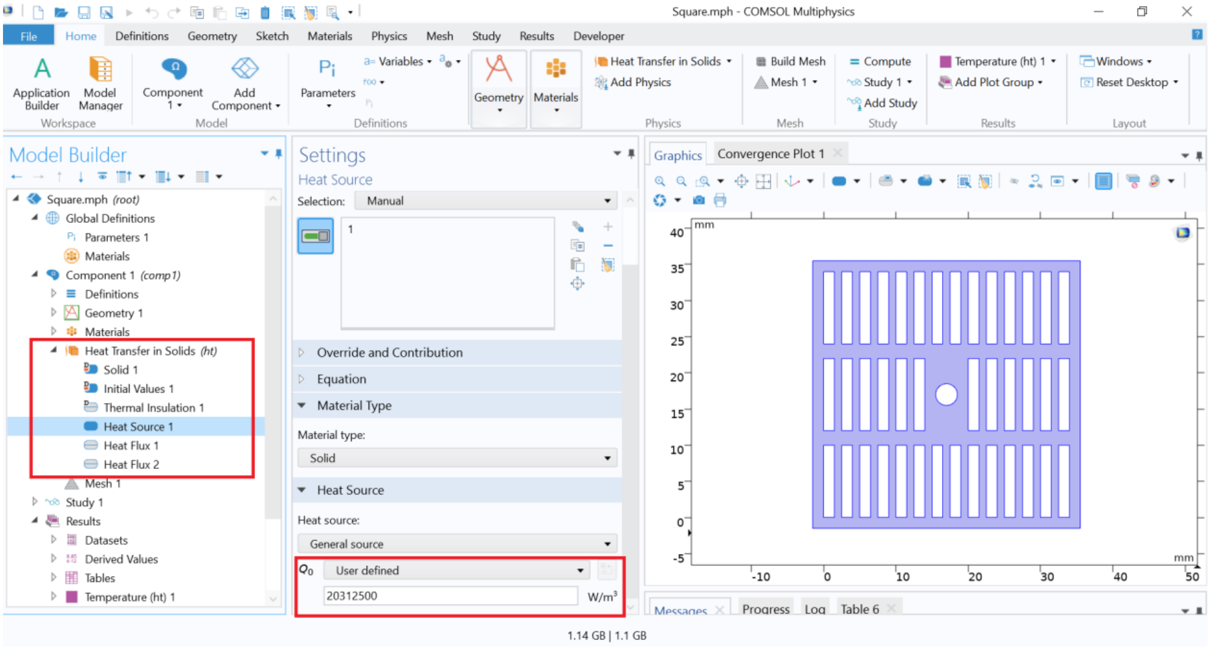

Selection: Manual

1

Material type: Solid

Heat source: General source

Q_0 User defined

20312500 W/m³

Figure 6.3: Heat transfer physics set-up in COMSOL Multiphysics

Due to the fact that the SMA physics was not included as mentioned earlier, therefore the amount of energy available within the material needed to be calculated manually from the equation below (6.32):

$$Q_0 = \frac{Q_{material}(W)}{V_{plate}(m^3)} \tag{6.32}$$

And $Q_{material}$ could be obtained from the material's latent heat and the cycle time; and V_{plate} is the volume of the plate after the slots have been cut. Therefore,

$$Q_0 = \frac{70\ W}{2307 \times 10^{-9}(m^3)} = 21125000\ W.m^{-3}$$

Figure 6.4 shows the setup of the heat flux around the slots, seeing that the fluid is to be pumped through the slots. The value of the heat transfer coefficient was entered as calculated and shown previously in table 6.4.

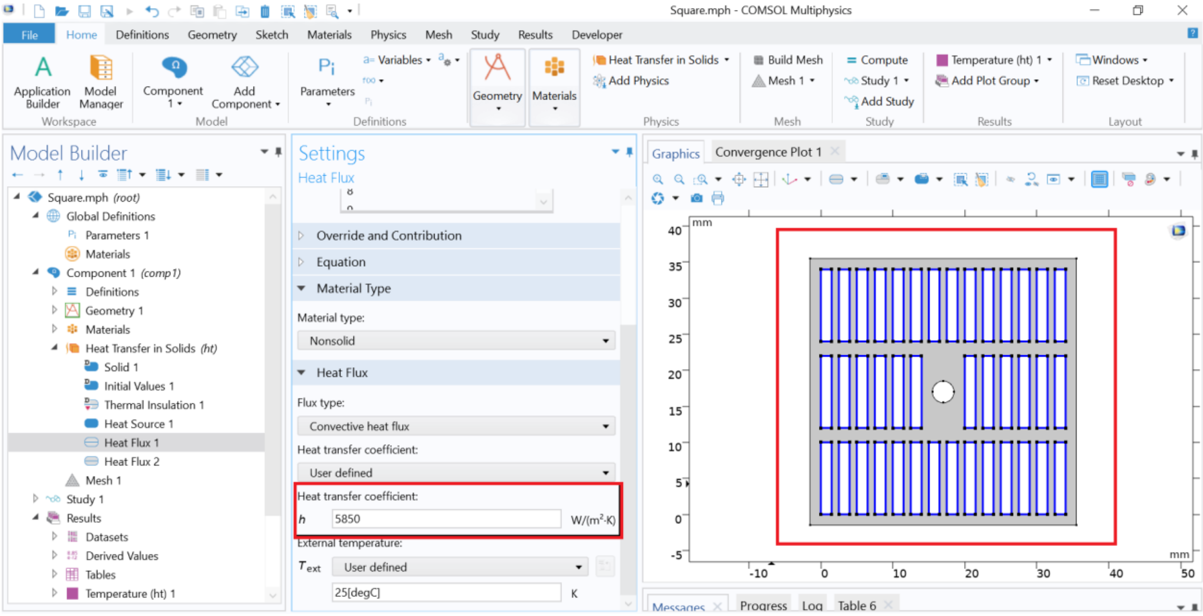

Settings
Heat Flux

Override and Contribution

Equation

Material Type

Material type: Nonsolid

Heat Flux

Flux type: Convective heat flux

Heat transfer coefficient: User defined

Heat transfer coefficient:

h 5850 W/(m²·K)

External temperature:

T_{ext} User defined

25[degC] K

Figure 6.4: Heat flux location and set-up in COMSOL Multiphysics

The reference temperature of the plate was set at the room temperature of 25°C; figure 6.5 shows the temperature distribution across the plate after the model has been run and solved. The figure shows that after 4 seconds of loading, there was still high temperature around the stiffener opening that was not picked up by the heat transfer fluid, relative to the temperature around the slots. From COMSOL modelling the heat rate could be obtained which was then used to compare between the theoretical heat removed and the practical heat removed from the plate. The theoretical heat-removed/heat-out could be calculated from the equation below (6.33)

$$Heat\ out\ (J) = Plate\ net\ CSA \times stack\ height \times \rho_m \times LH \qquad (6.33)$$

The plate's net cross-sectional area is the area of plate taken off it the cross-sectional area of the slots and the stiffener opening and that can be calculated as follows:

$$Plate\ net\ CSA = 37^2 - (1.5 \times 10 \times 40) - \pi \times 1.5^2 = 761.93mm^2$$

The stack height is the number of plates required multiplied by the thickness of the plate; and since the design requires *63 plates* each of *3mm* depth, then the height of the stack required to achieve 3kW is $63 \times 3 = 189\ mm$. Therefore, the theoretical heat out is:

$$Heat\ out\ (J) = 761.93 \times 10^{-6}(m) \times 0.189(m) \times 6450(kg/m^3) \times 13(kJ/kg) \times 1000$$
$$\approx 12100\ J$$

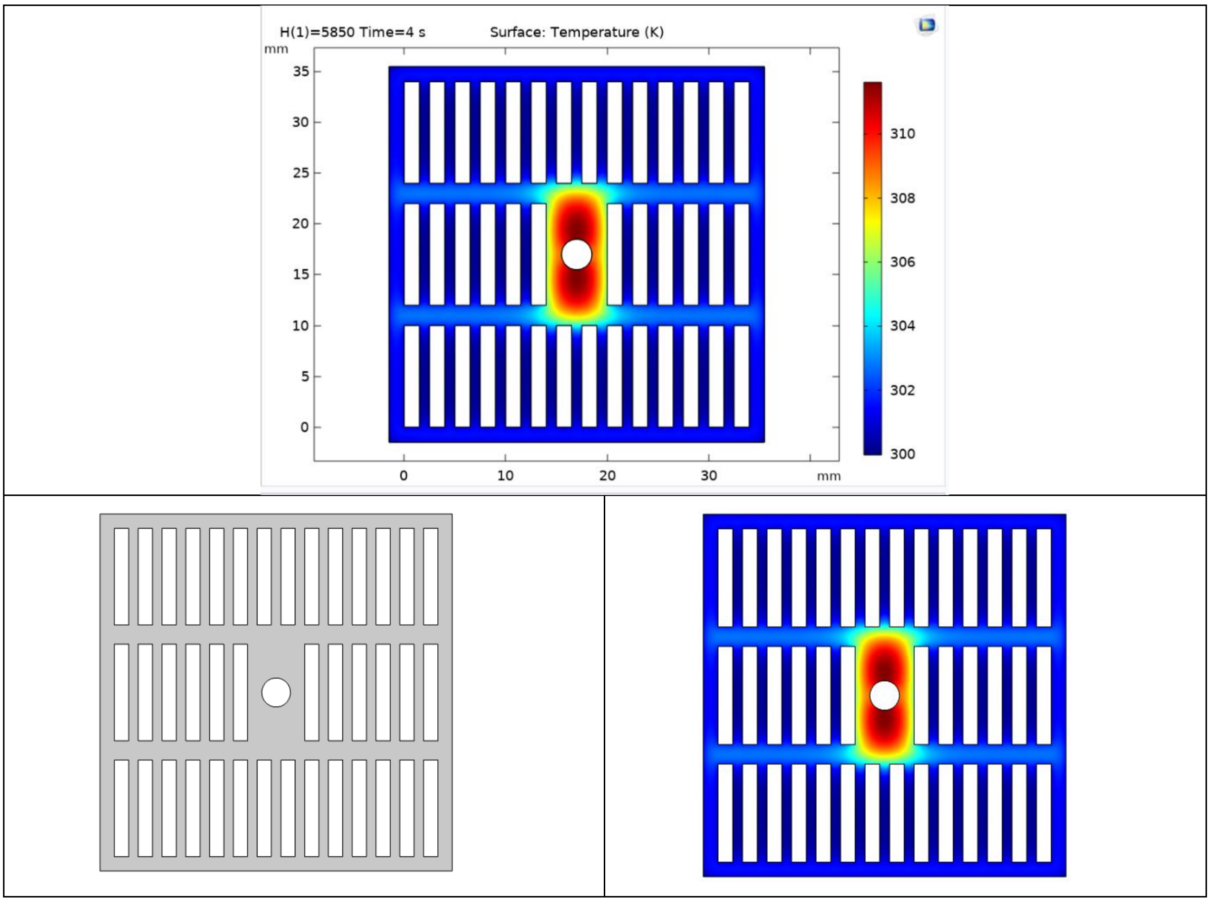

Figure 6.5: COMSOL modelling solution for plate 1

From the results of the modelling, the amount of heat that was removed after 4 seconds of loading was 11708.65 J which is 96.9% of the total theoretical heat available within the plate; and the maximum temperature of the plate was 30°C and the average temperature from the start of loading until the end is 27.7°C. Table 6.5 summarises the results of plate 1 performance.

Table 6.5: Summary of the results of plate 1 performance in COMSOL

Plate cross-sectional area (mm^2)	1369	**Theoretical heat out (J)**	12074.82
Holes cross-sectional area (mm^2)	600	**Practical heat out (J)**	11708.65
Stiffener cross-sectional area (mm^2)	7.07	**Percentage of heat removed %**	96.9
Plate net cross-sectional area (mm^2)	761.93	**Maximum temperature (°C)**	30
Plate net mass (g)	14.74	**Average temperature (°C)**	27.7
SMA removed (%)	44.35		

Table 6.6: Plate 2 design and dimensions

Name: Plate 2 (Ellipse) **Plate dimensions:** 31.5 mm × 11 mm **Plate thickness:** *d*: 3 mm **Slot dimensions:** *r*:1.5 mm; *a*: 4 mm  **Number of slots (nr_{slot}):** 10 **Thickness between slots:** 6.5 mm **Mass of uncut plate:** 21.06 g	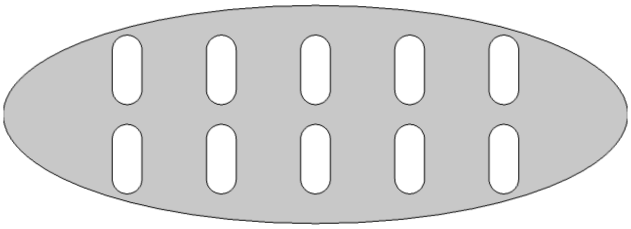

The second design which was denoted (plate 2), as shown in table 6.6, had a weight of 21.06 g; by following the set of equations (6.1) to (6.10), it was found that the stack would need 44 plates to deliver the required (q) before cutting the slots. The mass of slots was 3.68 g which led to a net plate weight of 17.37 g, which meant the number of plates required jumped to 53 plates, which consequently meant the stack height was 159 mm. By using the heat transfer equation, the heat transfer parameters of the plates were obtained, and their values are shown in table 6.7. The fluid used to obtain the heat transfer parameters for plate 1 and 2 was water. More fluids were tested, and their results were shown later in this chapter.

Table 6.7: Heat transfer calculated parameters for plate 2.

$D_h\ (mm)$	$\dot{m}\ (kg.s^{-1})$	Re	$u\ (m.s^{-1})$	Nu	$h\ (W.m^{-2}.K^{-1})$
4.38	0.144	3697	0.75	26.78	3659

After calculating the heat transfer coefficient (h) from the manual design calculations and obtaining its value as shown in table 6.7, this value along with the stack height were taken and input into COMSOL module; the module was run for 4 seconds, and the temperature rise and distribution across the plate are shown in figure 6.6. From COMSOL results, it was noticed that the temperature of the plates rose to above 40℃ and, there were hot points at the corners of the plate at the end of the loading cycle; that meant the plate was retaining the heat and it was not transferring it into the working fluid, which contradicts the purpose of the design, given that the idea was for the working fluid to pick as much heat as possible. The summary of the plate's performance is shown in table 6.8.

Table 6.8: Summary of the results of plate 2 performance in COMSOL

Plate cross-sectional area (mm^2)	1088.56	**Theoretical heat out (J)**	9555.65
Holes cross-sectional area (mm^2)	190.69	**Practical heat out (J)**	5261.63
Stiffener cross-sectional area (mm^2)	NA	**Percentage of heat removed %**	55
Plate net cross-sectional area (mm^2)	897.8	**Maximum temperature (°C)**	45.7
Plate net mass (g)	17.37	**Average temperature (°C)**	38.9
SMA removed (%)	17.52		

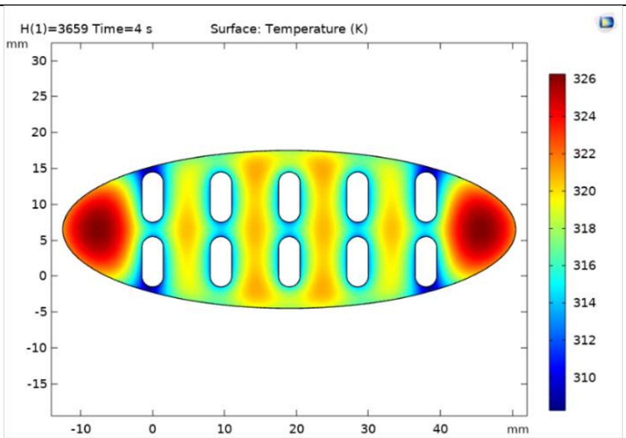

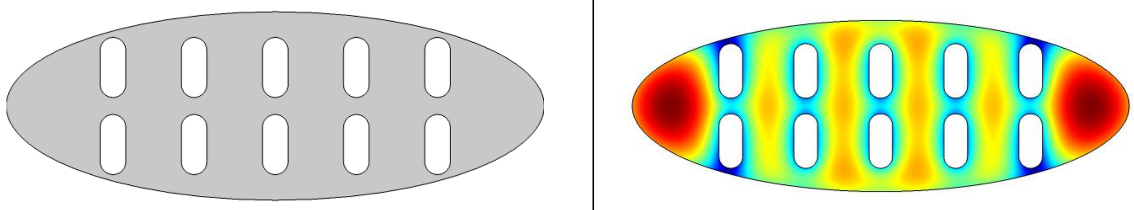

Figure 6.6: COMSOL modelling solution for plate 2.

Following the set of equations illustrated above, plate 1 and 2 were designed and their performances were analysed through running their models in COMSOL Multiphysics. The following plates 3 to 9 were designed at Exergyn's labs and the results of the CFD simulations were shown in figure 6.7 below:

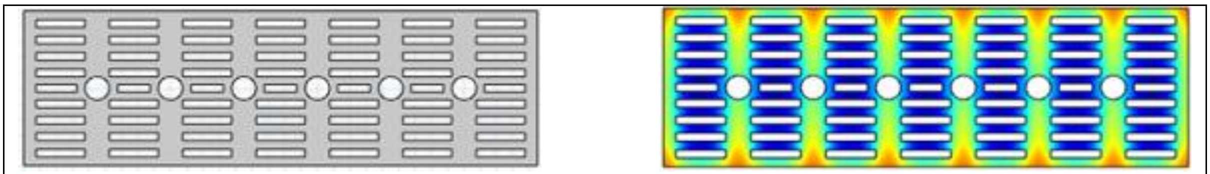

Plate 3:

Weight (g)	SMA removed (%)	Theoretical heat out (J)	Practical heat out (J)	Percentage heat out (%)	Max temp (°C)	Average temp (°C)
16.5	32.4	9425.5	9208.7	97.7	30.5	26.7

Plate 4:

Weight (g)	SMA removed (%)	Theoretical heat out (J)	Practical heat out (J)	Percentage heat out (%)	Max temp (°C)	Average temp (°C)
19.1	21.9	10898.07	10058.9	92.3	31.8	28.1

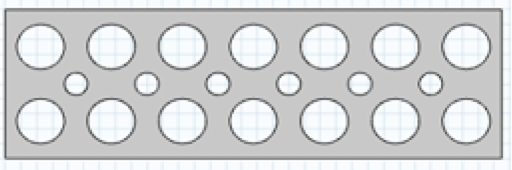

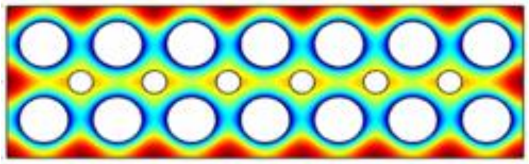

Plate 5:

Weight (g)	SMA removed (%)	Theoretical heat out (J)	Practical heat out (J)	Percentage heat out (%)	Max temp (℃)	Average temp (℃)
15.9	34.8	9095.27	7048.8	77.5	33.3	29

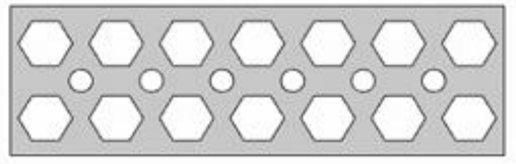

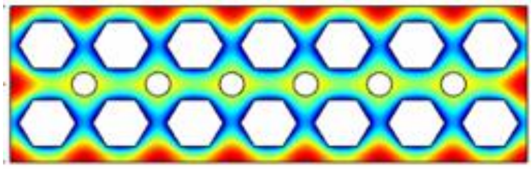

Plate 6:

Weight (g)	SMA removed (%)	Theoretical heat out (J)	Practical heat out (J)	Percentage heat out (%)	Max temp (℃)	Average temp (℃)
15.1	37.9	8656.93	7791.24	90	32.5	28.5

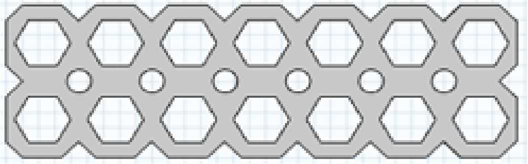

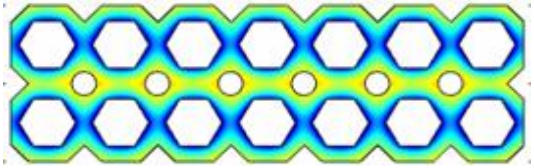

Plate 7:

Weight (g)	SMA removed (%)	Theoretical heat out (J)	Practical heat out (J)	Percentage heat out (%)	Max temp (℃)	Average temp (℃)
13.7	43.6	7860.02	7270.51	92.5	30.1	27.8

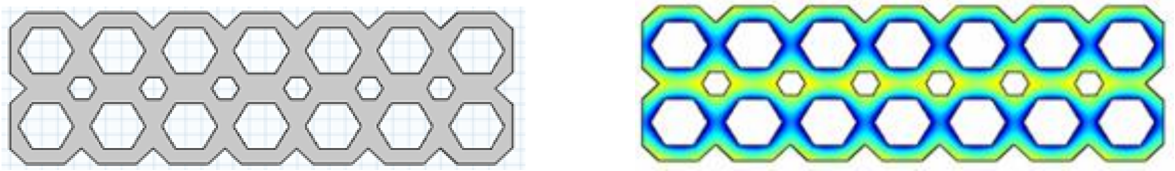

Plate 8:

Weight (g)	SMA removed (%)	Theoretical heat out (J)	Practical heat out (J)	Percentage heat out (%)	Max temp (℃)	Average temp (℃)
13.7	44	7813.06	7234.89	92.6	29.9	27.7

Plate 9:

Weight (g)	SMA removed (%)	Theoretical heat out (J)	Practical heat out (J)	Percentage heat out (%)	Max temp (℃)	Average temp (℃)
14.9	39	8511.32	7796.36	91.6	30.6	28

Figure 6.7: COMSOL modelling solution and performance results for plates 3 to 9

The above analysis showed that all the different geometries of the plates, except the circle slots, delivered more than 90% of the available heat within the plates; with the horizontal rectangular geometry of plate 3 achieving the best performance of 97.7%. Therefore, this set up was used for the rest of the designs. Generally, all the above designs (plate 1 and plate 3 to plate 9) had good performances in terms of the amount of heat that could be harvested relative to the theoretical heat that was available within the plate. However, since the heat transfer surface area is paramount in achieving the required heating load (q), therefore it is required to maximize the heat transfer surface area to ensure using less material and subsequently producing a cost-efficient device. That can be achieved by increasing the number of flow paths; which means instead of letting the fluid to flow through one channel, the fluid will be made to go through more than one channel in a serpentine flow; so, the fluid will go up the stack then down through a different set of slots and then up again before it exists the stack. The method of working out the fluid paths and design the fluid flow along with the type of fluid which can provide the best heat transfer were all explained later in this chapter.

The next plate is designed to allow for 3 paths fluid flow, where the fluid get pumped into the stack at the bottom of the stack and goes in a serpentine flow path before it exits the stack at the top of it. The approach triples the heat transfer surface area and allows more time for the heat transfer between the material and the working fluid. See table 6.9.

Table 6.9: Plate 10 design and dimensions

Name: Plate 10 **Plate dimensions:** 42.5 mm × 42.5 mm **Plate thickness:** *d*: 3 mm **Slot dimensions (stadium shape):** 1- *r*: 0.8 mm; *a*:17.35 mm 2- *r*: 0.8 mm; *a*:7.87 mm **Number of slots (nr_{slot}):** 40 **Thickness between slots:** 1.6 mm **Radius of stiffener-opening:** *r:* 2 mm **Mass of uncut plate:** 34.95 g **Mass of net plate:** 20.8 g	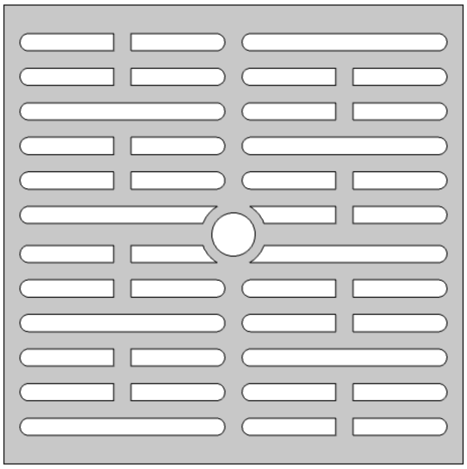

When removing the cut mass of the slots from the plate, the net weight of the plate dropped to 20.8 g, losing 40% of its mass; therefore, the number of plates needed for the stack jumps from *27 plates* to *44 plates* making the stack height 132 mm. These worked-out figures were used to calculate the heat transfer parameters of the design which are summarised in table 6.10.

Table 6.10: Heat transfer calculated parameters for plate 10.

$D_h\ (mm)$	$\dot{m}\ (kg.s^{-1})$	Re	$u\ (m.s^{-1})$	Nu	$h\ (W.m^{-2}.K^{-1})$
2.91	0.144	3877	1.2	27.94	5941

The COMSOL results showed that Plate 10 design had a high performance in terms of the amount of heat removed relative to the theoretical heat available within the plate, as the results showed that 98% of the heat was picked up by the working fluid, which was water in that instance.

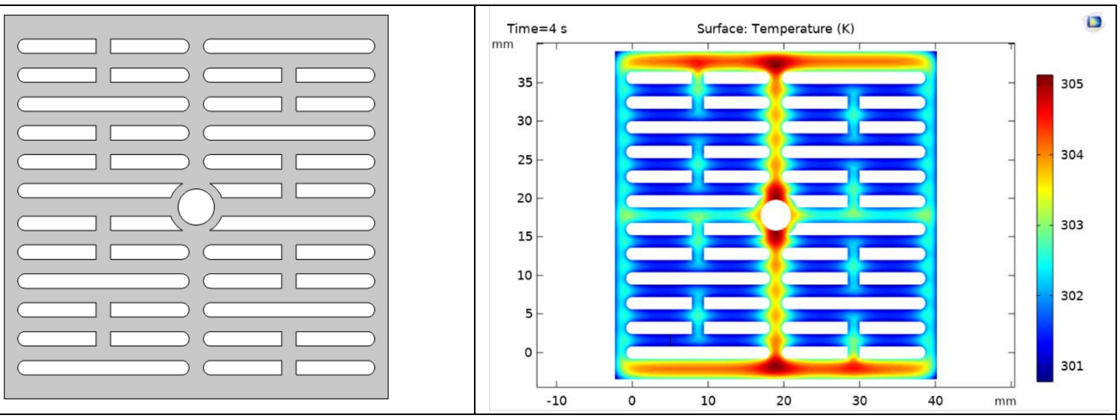

Plate 10:

Weight (g)	SMA removed (%)	Theoretical heat out (J)	Practical heat out (J)	Percentage heat out (%)	Max temp (℃)	Average temp (℃)
20.8	40	12486	12332.72	98.7	30	29.3

Figure 6.8: COMSOL modelling solution and performance results for plate 10.

Figure 6.8 shows the plate after the model was solved; the plate achieved high performance, however there were still hot points at the top and bottom ends of the plate, as well as around the stiffener opening. These hot points meant the working fluid did not manage to pick up the heat from those edges. To tackle this issue, the next design was like the design of above plate 10 with smaller dimensions for the slots; the big slots were reduced by 1 mm and the small slots were reduced by 0.5 mm as shown in table 6.11.

Table 6.11: Plate 11 design and dimensions

Name: Plate 11
Plate dimensions: 42.5 mm × 42.5 mm
Plate thickness: *d*: 3 mm
Slot dimensions (stadium shape):

1- *r*: 0.8 mm; *a*:16.35 mm
2- *r*: 0.8 mm; *a*:7.37 mm

Number of slots (nr_{slot}): 40
Thickness between slots: 1.6 mm
Radius of stiffener-opening: *r:* 2 mm
Mass of uncut plate: 34.95 g
Mass of net plate: 21.55 g

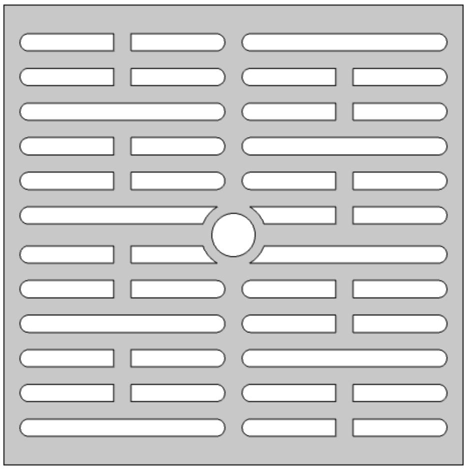

The new design of plate 11 solved the issue of the hot points on the bottom and top edges of the plate. However, it created new hot points in the middle of the plate, around the stiffener opening and along the entire middle part, and that was because there was a wider space in the middle of the plate compared to the previous design, which meant the fluid could not pick up the heat from those point because it did not pass adjacent to them.

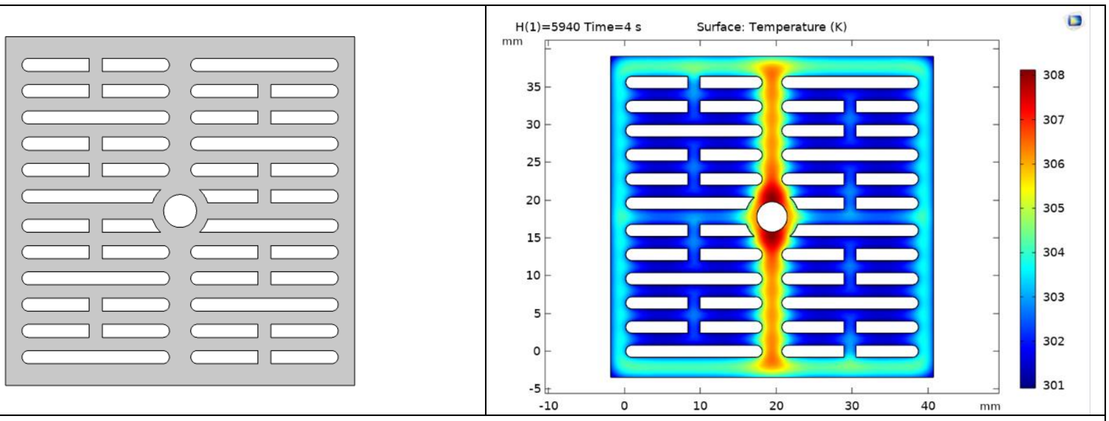

Plate 11:

Weight (g)	SMA removed (%)	Theoretical heat out (J)	Practical heat out (J)	Percentage heat out (%)	Max temp (℃)	Average temp (℃)
21.55	38.3	12902.23	12668.64	98.2	30	29.7

Figure 6.9: COMSOL modelling solution and performance results for plate 11.

Since the new hot spots on the plate were created in the middle and around the stiffener opening, the author needed to change the approach and put the stiffener on the side;

therefore, instead of one stiffener in the middle, the new design had two stiffeners on the sides. Plates 12 and 13 were redesigned following this approach, and they were tested in COMSOL, and the results are shown in figures 6.10 and 6.11.

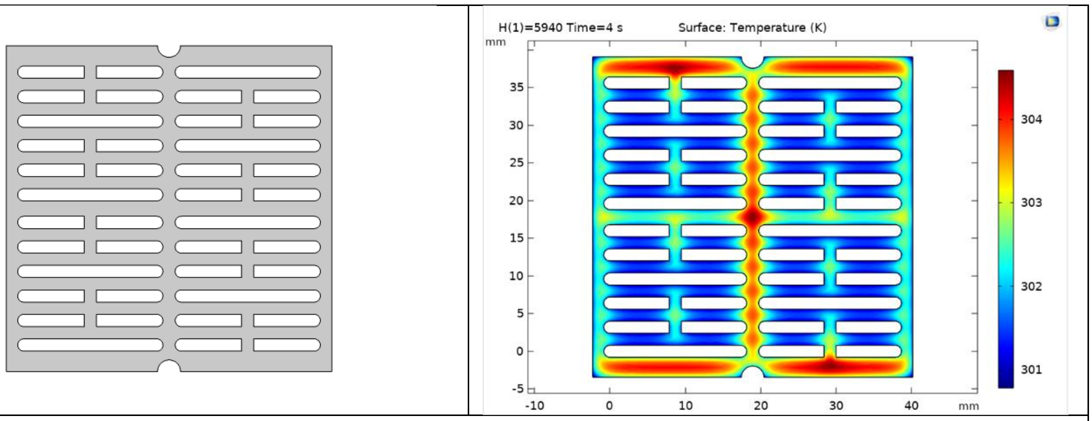

Plate 12: Has the same dimensions of plate 10, the only difference is that the stiffener in plate 12 is on two sides of the plate (bottom and top)

Weight (g)	SMA removed (%)	Theoretical heat out (J)	Practical heat out (J)	Percentage heat out (%)	Max temp (℃)	Average temp (℃)
21.78	37.67	12460.76	12339.57	99.03	30	29.3

Figure 6.10: COMSOL modelling solution and performance results for plate 12.

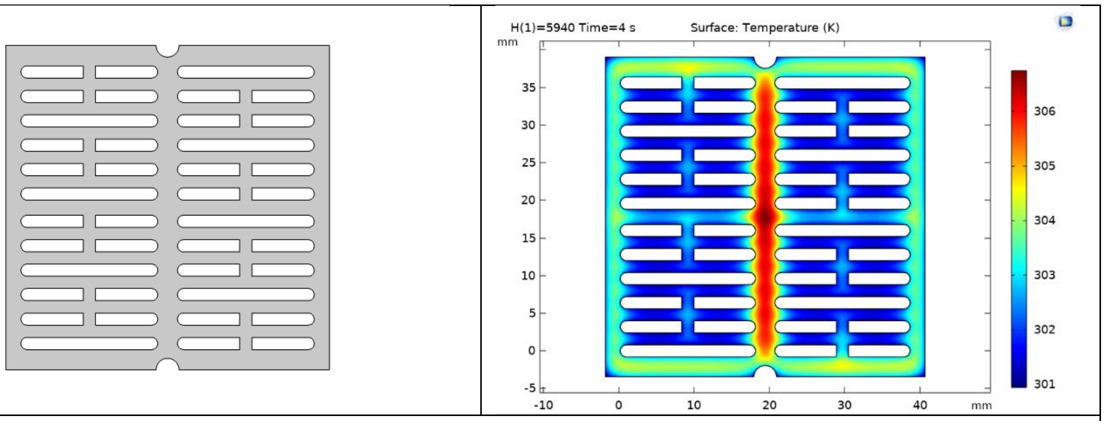

Plate 13: Has the same dimensions of plate 11, the only difference is that the stiffener in plate 13 is on two sides of the plate (bottom and top)

Weight (g)	SMA removed (%)	Theoretical heat out (J)	Practical heat out (J)	Percentage heat out (%)	Max temp (℃)	Average temp (℃)

21.91	37.32	12530.67	12492	99.7	30	29.7

Figure 6.11: COMSOL modelling solution and performance results for plate 13.

The analysis above showed that moving the stiffener from the middle of the plate to two sides of the plate resulted in better performance and better heat distribution across the plate. The only concern with this design was that it required two rods to support the stack which would add to the dead mass within the stack which would end up compromising the amount of heat transferred between the material (heat source) and the working fluid, as a percentage of the heat generated would be absorbed by the dead mass. Therefore, and after taking all the above points into consideration, it was concluded that the best design for the purpose of achieving 3kW was the plate designed denoted (plate 10); and therefore, the final stack was built using the selected plate as is shown later in this chapter.

6.4.2 Heat transfer validation in MATLAB:

Before moving onto the next step of designing the stack and the fluid flow, the results from COMSOL needed to be validated. Therefore, in collaboration with Exergyn’s team, a MATLAB code was written to work out the conductive heat transfer across the plate and the convective heat transfer between the plate and the working fluid. To carry out this validation exercise, a small strip on the plate was taken and its temperature was plotted on COMSOL, as shown in figure 6.12; a similar strip of the plate was taken and modelled in MATLAB with the code developed, see appendix (a). The following equations were used to develop the code and to obtain results which were compared to COMSOL results to make sure the two sets of results were in line with each other. The strip taken, as shown in figure 6.12, was divided into five nodes; nodes 1 to 4 affect each other with conduction heat transfer, and the fifth node is where the convection heat transfer took place between the material and the fluid.

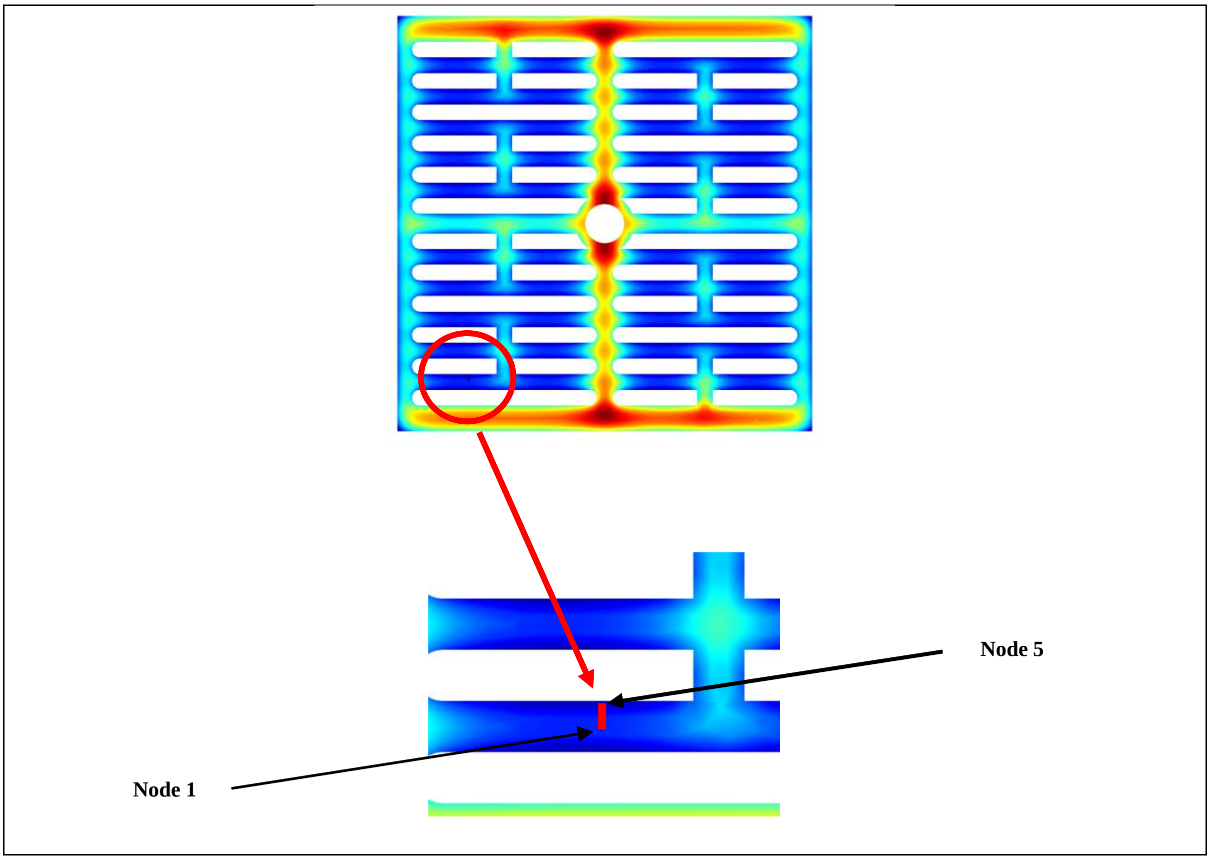

Figure 6.12: A strip taken between two slots to validate COMSOL heat transfer results with manual calculation.

There are two ways of finite difference method for solving the conduction and convective heat transfer for nodes (explicit and implicit); where the solution is obtained for the current time step for the implicit method, and for the next time step for the explicit method. The equations used are as follows:

1- Energy balance equation:

$$E_{st} = E_{in} + E_g \tag{6.34}$$

Where:

E_{st}: rate of change of energy content:

$$E_{st} = m.c.dT/dt \tag{6.35}$$

E_{in}: rate of energy conduction at all surfaces:

$$q_{cond.} = k.A.\Delta T/L \tag{6.36}$$

$$q_{conv.} = h.A.\Delta T \tag{6.37}$$

E_g: rate of energy generated within the element:

$$E_g = q.A.L \tag{6.38}$$

Explicit method: Solve for the next time step (p+1)

Implicit method: Solve for the current time step (p)

Equations for three cases:

1- Node with one insulated end

$$m.c.\frac{dT}{dt} = \frac{kA}{\Delta x}.\left(T_{n+1}^{p} - T_{n}^{p}\right) + q.A.\Delta x \tag{6.39}$$

Where $\boldsymbol{m} = \boldsymbol{\rho V} = \boldsymbol{\rho}.\Delta\boldsymbol{x}.\boldsymbol{A}$; $\Delta\boldsymbol{x}$ is the distance between the nodes, $\mathbf{n}$ is node number, therefore equation (6.39) becomes as follows:

$$\rho c\Delta x.A.\frac{T_{n}^{p+1} - T_{n}^{p}}{\Delta t} = \frac{kA}{\Delta x}.\left(T_{n+1}^{p} - T_{n}^{p}\right) + q.A.\Delta x \tag{6.40}$$

2- Centre Nodes

$$\rho c\Delta x.A.\frac{T_{n}^{p+1} - T_{n}^{p}}{\Delta t} = \frac{kA}{\Delta x}.\left(T_{n+1}^{p} - T_{n}^{p}\right) + \frac{kA}{\Delta x}.\left(T_{n-1}^{p} - T_{n}^{p}\right) + q.A.\Delta x \tag{6.41}$$

3- Node with conduction from one side and convection from the other side

$$\rho c\Delta x.A.\frac{T_{n}^{p+1} - T_{n}^{p}}{\Delta t} = \frac{kA}{\Delta x}.\left(T_{n-1}^{p} - T_{n}^{p}\right) + hA\left(T_{\infty} - T_{n}^{p}\right) + q.A.\Delta x \tag{6.42}$$

Multiply all terms in all three equations by $\frac{\Delta x}{KA}$ and consider that:

$Fo = \alpha\Delta t/\Delta x^2$ where α is the thermal diffusivity.

$Bi = h\Delta x/k$ where Bi is Biot number.

$\Delta t = \Delta x^2/2\alpha$

For explicit, shuffle the equations for T_{n}^{p+1} ; and for implicit, shuffle the equations for T_{n}^{p}

By using the above equations as illustrated in the attached MATLAB code in appendix (a), a graph that represents the nodes temperature was produced; this graph was compared with the graph produced by COMSOL to ensure that COMSOL results were accurate and were in line with manual calculations, as shown in figure 6.13.

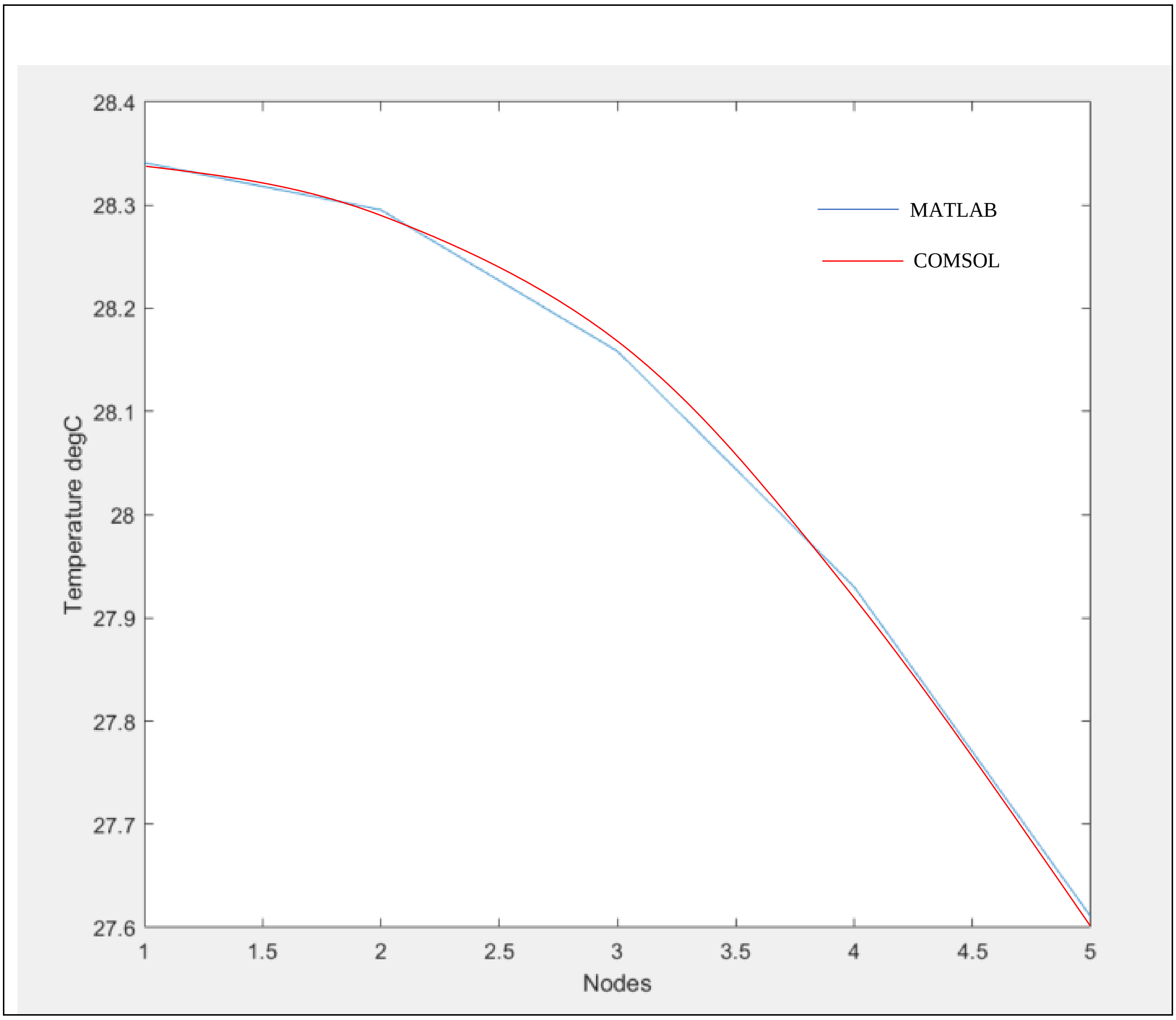

Figure 6.13: COMSOL results against MATLAB results.

Figure 6.13 shows the temperature vs nodes graphs produced in COMSOL and MATLAB; both graphs were following the exact same trajectory except there is a small variation of less than 0.2℃ at the fifth node where the convective heat transfer took place. Therefore, it safe to say that COMSOL modelling has a high accuracy calculating conductive and convective heat transfer and thus it can be used in continuing the analysis with great confidence.

6.4.3 Stack Design:

The above plates analysis showed that the plate design, namely plate 10, had the best performance in terms of rejecting its latent heat onto the working fluid passing through the slots. Therefore, this plate was used in designing the stack which is meant to work as the heat source for the SMA-based heat pump. It was determined that (R_e) would need to be greater than 3800 to achieve the required heat transfer assuming flow was passed in parallel through all slots. As a 5K temperature lift was desired, this indicated an ideal mass flowrate of 0.69 $kg.s^{-1}$. This flowrate was outside of the spec of 0.3-0.5 $kg.s^{-1}$. Also, at 0.69 $l.s^{-1}$the (R_e) would only be 3200 assuming parallel flow across all slots. Reducing the flowrate to 0.5 $kg.s^{-1}$ would increase the (ΔT) to 6K however the (R_e) at this point would reduce to 2600 which would result in a Laminar/transitional flow and a certain decrease in the heat transfer performance.

To solve the above issue, the team at Exergyn did a Simulink and COMSOL analysis and decided that the solution required had to increase the fluid velocity without increasing the mass flowrate or to decrease the temperature lift below 5K. If the number of slots was decreased but the mass flowrate remained the same, then the channel velocity could be increased. However, reducing the slot number would increase the thickness between channels and increasing the stack length was not an option. The chosen solution was to cascade the flow through the existing stack to achieve this, the manifold plates were designed so the number of inlet ports were reduced from 24 to 8. As the fluid reached the end of the slot rather than exiting the stack it was redirected over the neighbouring slot where it would flow back down through the stack. Due to the layout of the core, the inlets needed to be kept at the bottom and outlets at the top of the stack, so the fluid would need to be redirected back up a neighbouring slot to exit. Therefore, the same portion of fluid flows in series through 3 slots per stack. The proposed stack assembly is shown in figure 6.14.

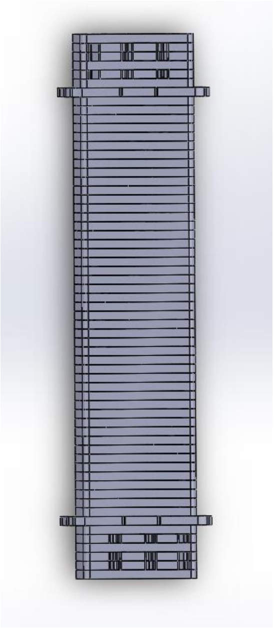

Figure 6.14: Assembly of full stack using plate 10.

Based on the stack structure shown in figure 6.14, the stack is designed to allow for three paths flow; where the fluid circulates within the stack in a serpentine flow arrangement, as it enters the stack at the bottom, goes up, down and up again before it leaves at the top of the stack. Figure 6.15 shows the flow direction within the stack.

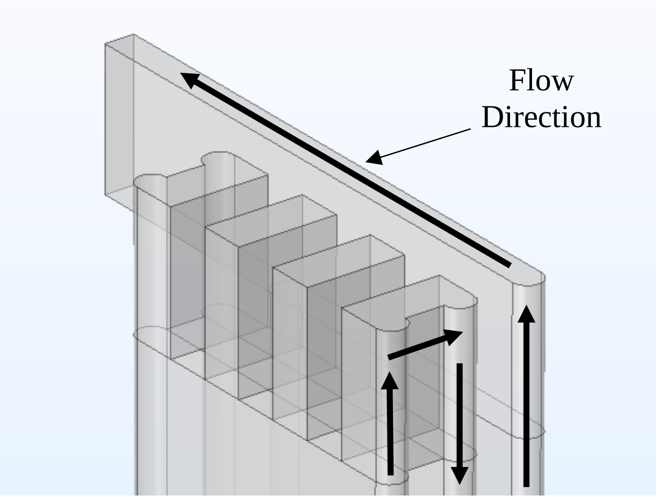

Figure 6.15: Section of the stack to show the direction of the fluid flow.

To understand the capability of the SMA material of rejecting its heat onto a working fluid, one path of the stack was taken, and different analysis were carried out to decide what is the best arrangement to pick up the heat from the stack. These arrangements included studying different working fluids that are environmentally friendly, namely, water and then mixtures of water and different percentages of nanoparticles to compose nanofluids. The analysis as well include changing the path's length and the thickness between the slots to have a comprehensive picture of the different scenarios that can be used in the future projects. The single path was considered a channel through which the fluid passes; the analysis was done in COMSOL Multiphysics combining three physics that are solid mechanics, heat transfer and fluid flow. The solid mechanics physics was set up to cater for the changes happened within the SMA material when it was put under stress and to calculate the dissipated energy because of that, as explained in Chapter 4 and validated in Chapter 5.

The first analysis was run on a NiTi channel of 30 mm length, 3 mm inner diameter and 2.5 mm wall thickness. The NiTi material used to construct the channel had the same properties mentioned previously in table 4.1 in Chapter 4; the cycle chosen was 4 seconds loading, one second pause and four seconds unloading as shown in figure 6.16. The NiTi channel was stressed at 1000 MPa and the fluid was pumped through the channel at a velocity of 1 $m.s^{-1}$.

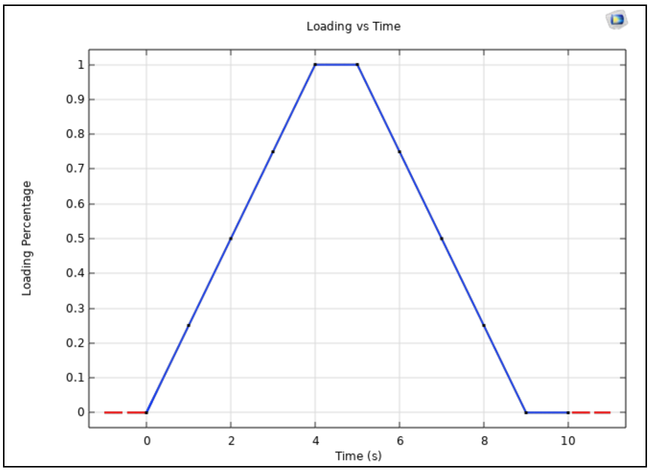

Figure 6.16: Cycle of (4 seconds loading, 1 second pause and 4 second unloading) used to study the transfer between SMA and working fluids.

6.5 Fluid Analysis

Four different fluids were used separately and a comparison between the four fluid was carried out to decide which fluid was the best in picking the heat from the channel. The first fluid used was water and then different concentrations of graphene oxide were added to water in the pursuit of enhancing the thermal properties of the fluid.

6.5.1 Water

The four main properties that determine the thermal performance of a fluid are the thermal conductivity, specific heat capacity, density, and dynamic viscosity. These parameters change as the temperature of the fluid changes; therefore, it is very important to ensure that the change of these properties is captured and taken into consideration when carrying out any analysis. Figure 6.17 shows how these four properties change with temperature in case of water. Later in this chapter, these properties were obtained using different percentages of nanoparticles to compose different nanofluids and then their performance in relation to picking heat from an SMA channel was analysed.

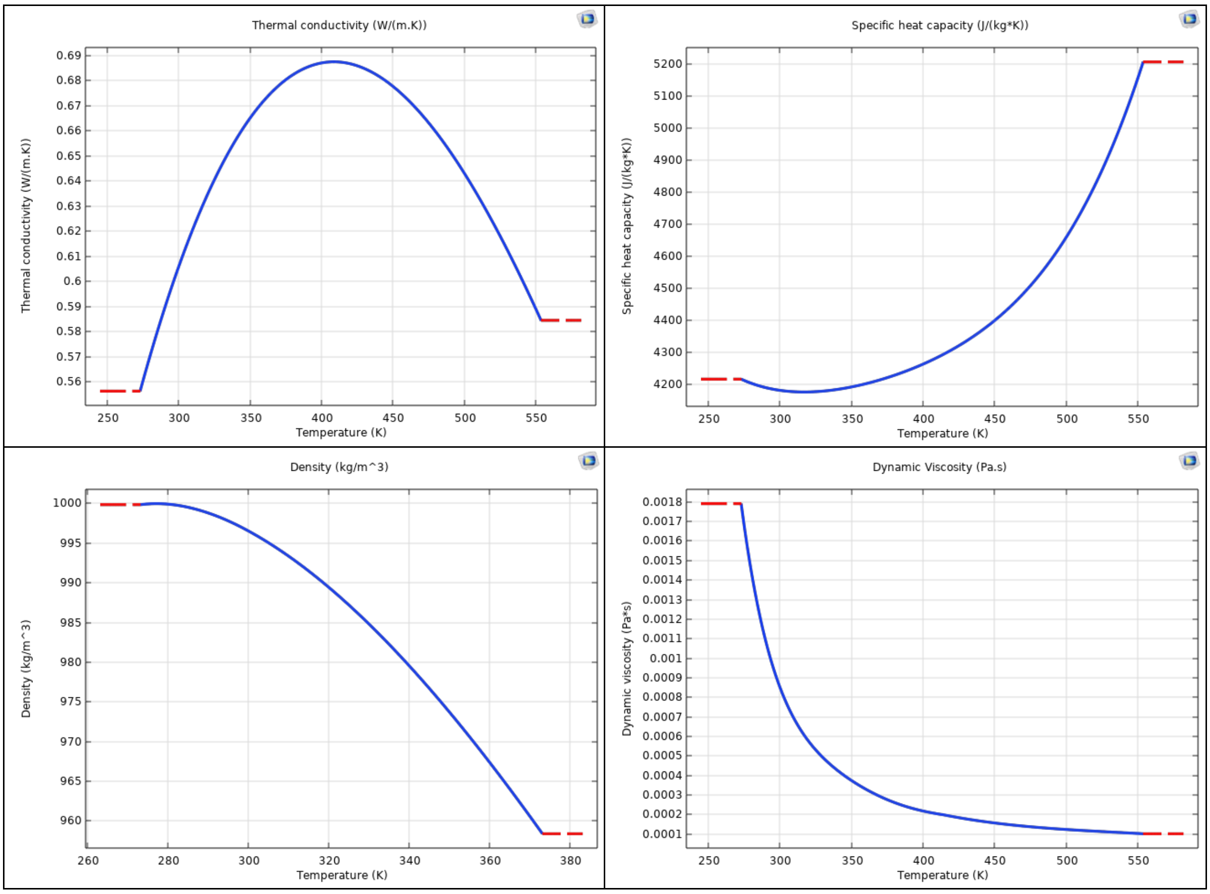

Figure 6.17: The change of the four thermal properties of water with the change of temperature

As shown in figure 6.18 below, the SMA channel was loaded for 4 seconds, then one second pause before the unloading took place for 4 seconds; when the loading started, the fluid (water) was pumped at a velocity of 1 $m.s^{-1}$. The channel's temperature rose during the loading to 44℃ and started gradually dropping, and by the end of the unloading at 8 seconds, the channel's temperature dropped to the base line which was 25℃, see figure 6.18. However, this was the case only in the middle of the channel, for the edges of the pipe behaved differently. The temperature of the material drops during the unloading because the material absorbed latent heat as explained in chapters 4 and 5; therefore, the temperature of the channel dropped during the unloading. However, this drop in temperature did not show in the middle of the channel as the cycle was very short and it did not allow for heat recovery to bring the temperature of the channel to base line before unloading, and subsequently allowing the material to cool down through absorbing latent heat from the surrounding.

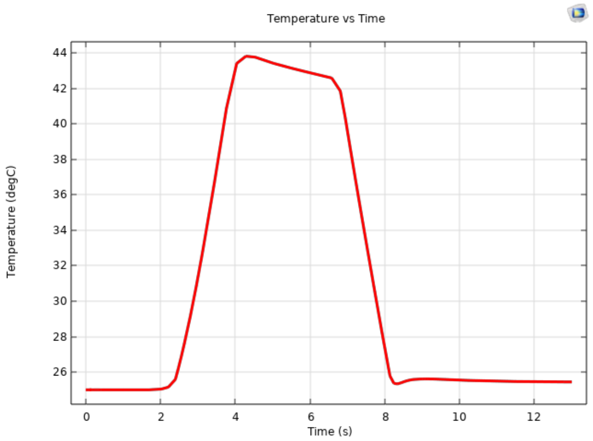

Figure 6.18: The temperature of the SMA channel at 15mm height during the loading and unloading.

The temperature of the channel was different across the height of the channel during the cycle. The edges of the channel cooled quicker with a cooling temperature span of 7K at 1 mm height and 3.5K at the top of the channel. Whereas the middle of the channel remained hot throughout the cycle, and its temperature did not drop below the baseline of 25℃. Figure 6.19 shows the temperature of the channel at four different heights (1 mm, 7 mm, 15 mm, and 29.5 mm).

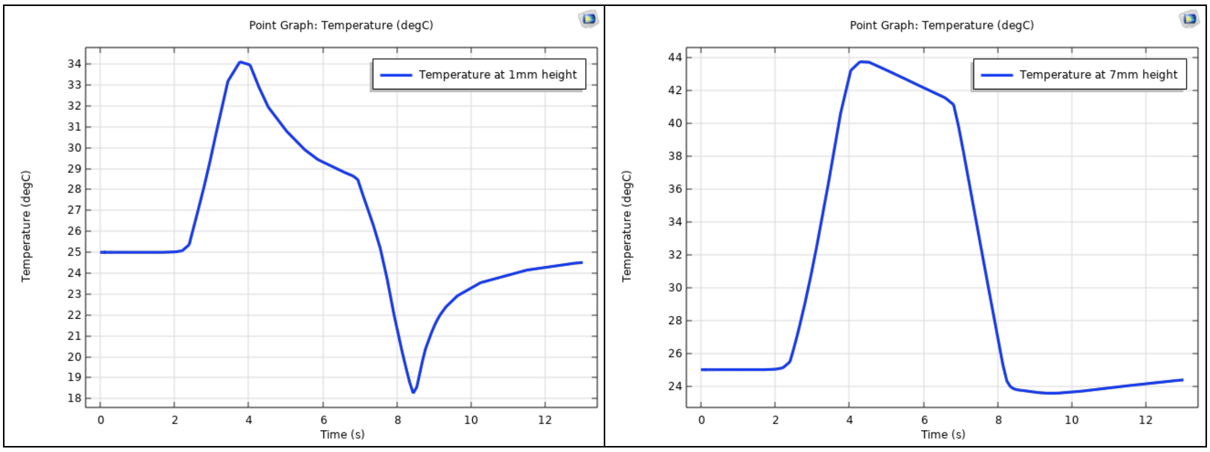

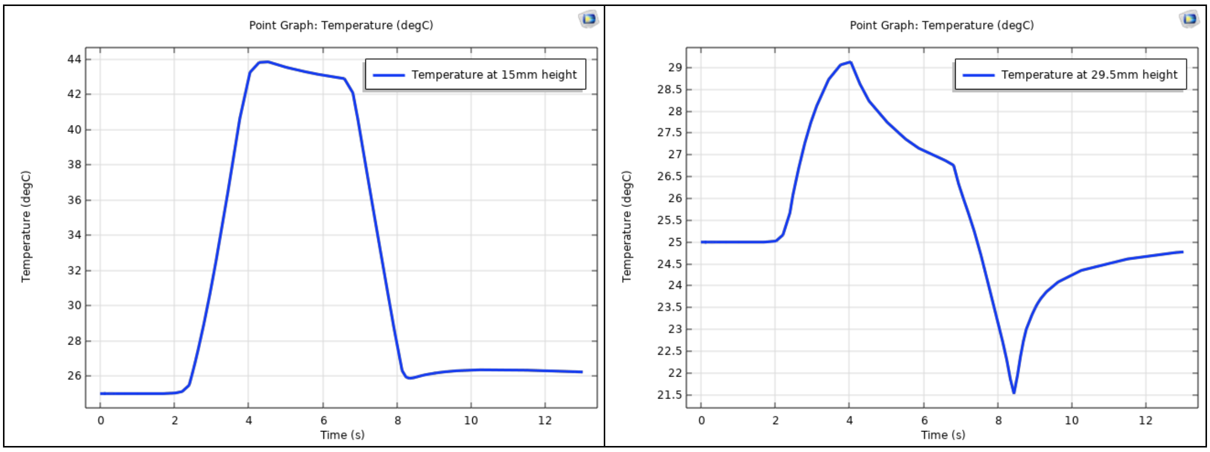

Figure 6.19: The temperature of the SMA channel at four different heights during the loading and unloading.

The different temperature across the channel affected the temperature of the fluid (water). It was noticed that the temperature of the fluid in the middle of the channel was much higher than the temperature exiting the channel. That was understandable because there were different temperatures across the channel, as well as the heat rejection took place in the first four seconds, and it was followed by heat absorption, as the material cooled down during the unloading. And that resulted in the fluid picking less heat when it exited the channel; the temperature of water at the middle of the channel rose to 38°C after 7 seconds of the cycle, which meant there was a 4 second delay between the peak temperature of the channel and the peak temperature of water, as shown in figure 6.20. Figure 6.20 as well shows the temperature of the fluid in the middle of the channel and when it exited the channel; the figure shows that the temperature of the channel rose to 29°C after 4 second of loading and then dropped to 21.5°C after 8.4 second. Whereas, the temperature of the fluid followed a different trajectory, as it rose to 27.8°C after 7 second of loading and then dropped to baseline of 25°C at the end of the 9 second cycle.

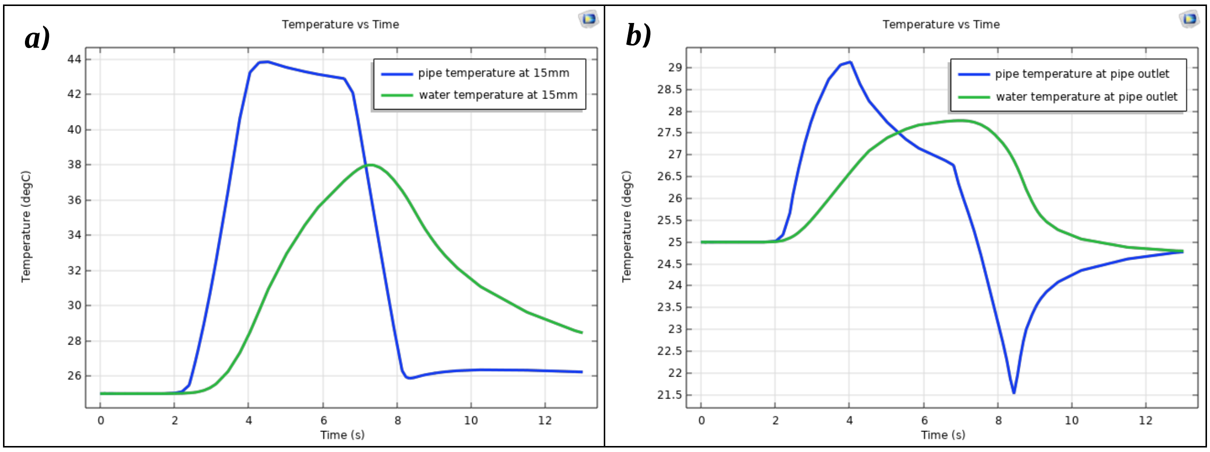

Figure 6.20: a) Channel and water temperature at 15mm b) Channel and water temperature at the channel outlet

Figure 6.21 shows a cross-section of the channel at 0 second, 4 seconds and 9 seconds respectively. It was noticed that at start of the cycle, the channel, and the fluid temperatures were at the reference temperature of 25℃; then at the end of loading at 4 seconds, it was noticed that the temperature of the middle of the channel reached 44℃ as shown in the graph in figure 6.20. Whereas the temperature of the fluid was still low relative to the temperature of the channel. However, at the end of the cycle (at 9 seconds) the temperature of the channel dropped, and the temperature of the fluid increased relative to the channel's temperature.

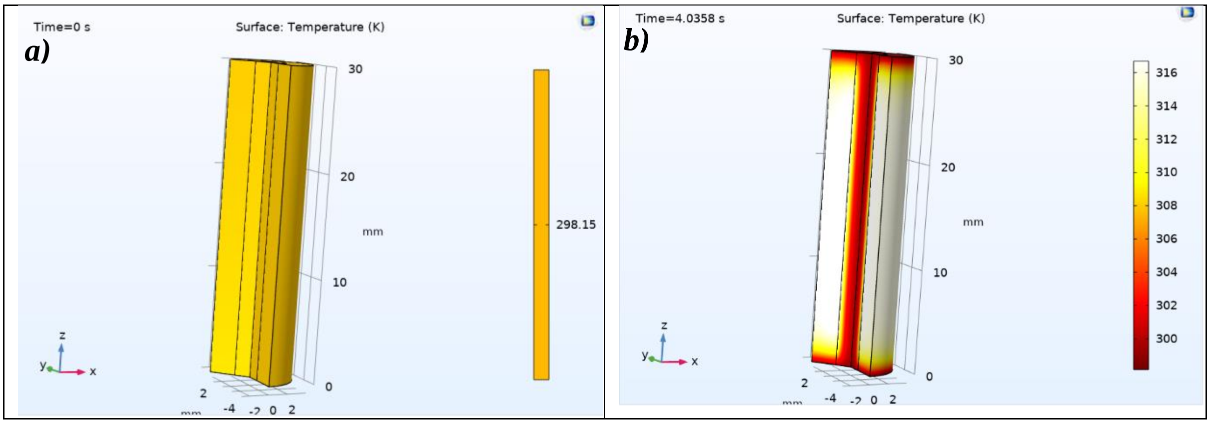

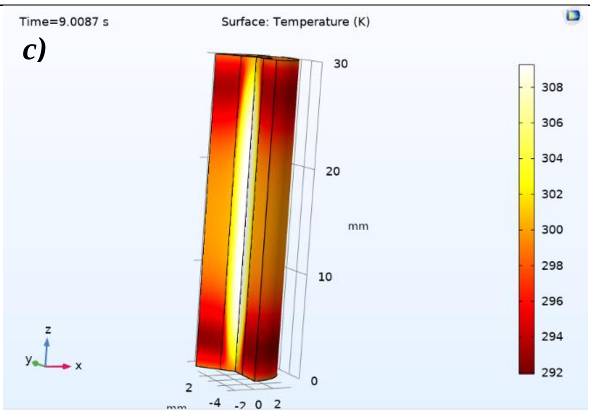

Figure 6.21: Cut section of the channel to show the change in temperature at a) start of the cycle b) end of loading and c) end of the entire cycle.

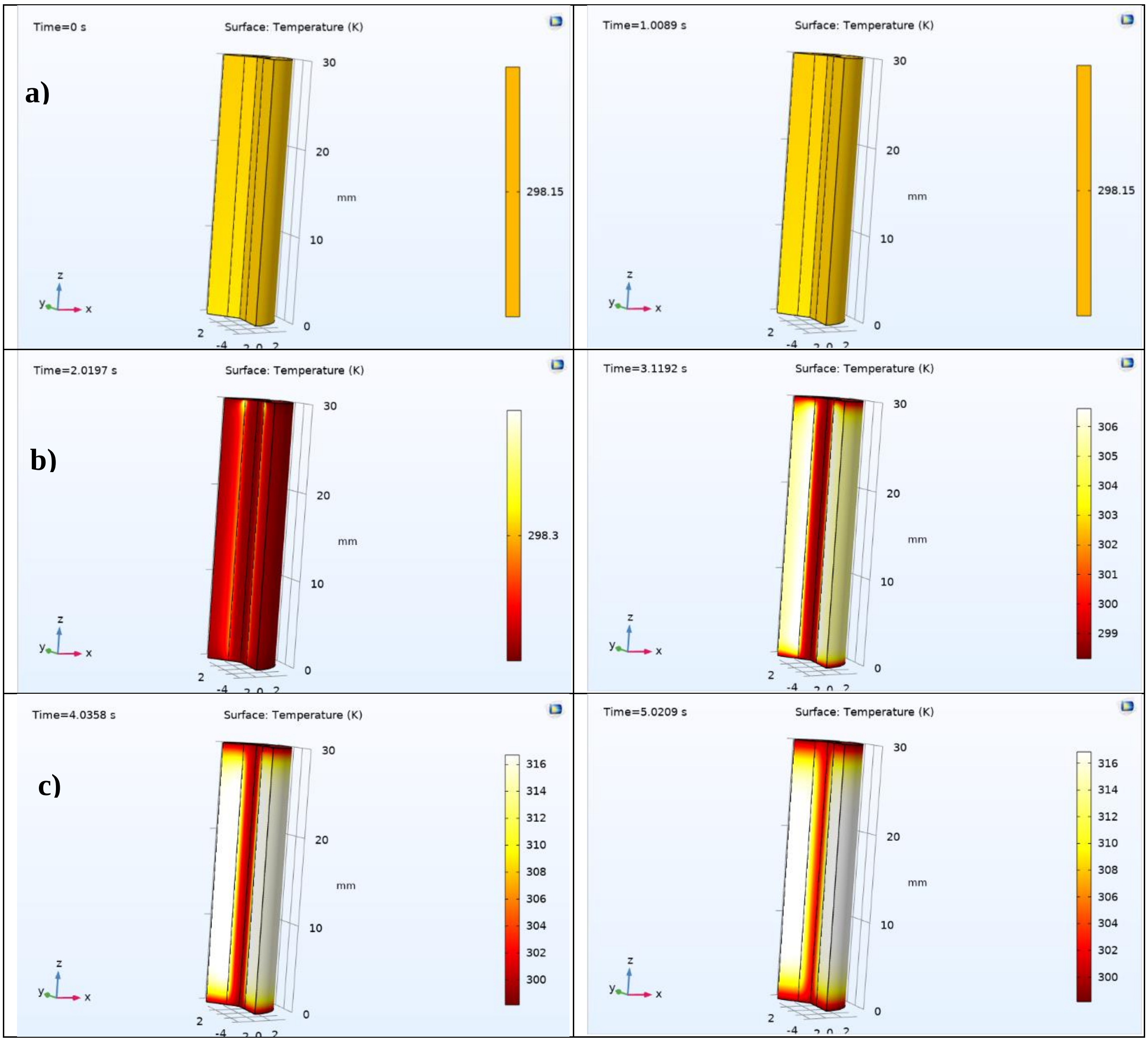

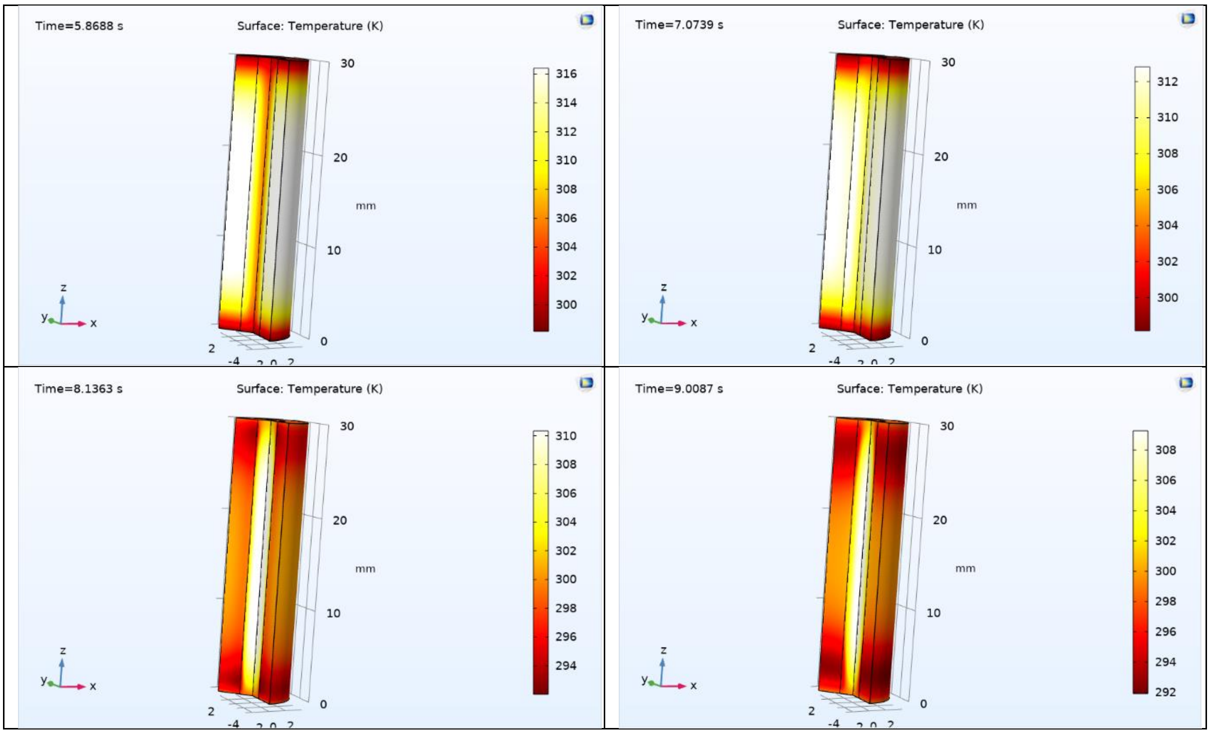

Figure 6.22: Cut section of the channel to show the change in temperature throughout the cycle 0 sec to 9 second.

Figure 6.22 shows a section of the channel at every second of the 9 seconds loading cycle. The figure shows the channel started heating up after two seconds of loading, and it shows that the temperature of the fluid towards the end of the cycle was higher than the temperature of the channel.

Water is considered a good heat transfer fluid, as it has high thermal capacity and low viscosity. However, it is possible to enhance water’s thermal performance by adding nanoparticles which have higher thermal conductivity and thus forming nanofluids. By adding nanoparticles to a base fluid, the density and viscosity of the fluid increase and the nanoparticles contact larger area than a conventional fluid by itself; hence achieving a better heat transfer.

6.6 Nanofluids Analysis

Water is an in-built fluid in COMSOL MULTIPHYSICS with the thermal properties shown previously in figure 6.17. However, when mixing water with nanoparticles and forming nanofluids, the thermal properties of the nanofluids in question need to be calculated and then input into COMSOL software to simulate the performance of the newly formed nanofluids. The nanoparticle chosen for this study was Graphene Oxide (GO), for its high thermal conductivity and good thermal properties, as shown in table 6.12 below.

The four main thermal properties (Density, Dynamic viscosity, Specific heat capacity and Thermal conductivity) for nanofluids can be calculated from the below equations (Chabok N. et al. 2020):

$$\rho_{nf} = (1 - \Phi)\rho_f + \Phi\rho_p \qquad (6.43)$$

Where:

ρ_{nf} is the density of the nanofluid.

ρ_f is the density of the base fluid.

ρ_p is the density of the nanoparticle.

Φ is the percentage of the nanoparticle added to the base fluid.

$$\mu_{nf} = \frac{1}{(1 - \Phi)^{2.5}} \times \mu_f \times \frac{\rho_f}{\rho_{nf}} \qquad (6.44)$$

Where:

μ_{nf} is the dynamic viscosity of the nanofluid.

μ_f is the dynamic viscosity of the base fluid.

$$C_{pnf} = \frac{(1 - \Phi)\rho_f C_{pf} + \Phi\rho_p C_{pp}}{\rho_{nf}} \qquad (6.45)$$

Where:

C_{pnf} is the specific heat capacity of the nanofluid.

C_{pf} is the specific heat capacity of the base fluid.

C_{pp} is the specific heat capacity of the nanoparticle.

$$k_{nf} = \frac{k_p + 2k_f + 2(k_p - k_f)\Phi}{k_p + 2k_f - 2(k_p - k_f)\Phi} \qquad (6.46)$$

Where:

k_{nf} is the thermal conductivity of the nanofluid.

k_f is the thermal conductivity of the base fluid.

k_p is the thermal conductivity of the nanoparticle.

By using the above equations (6.43) to (6.46), the four thermal properties were obtained for three different nanofluids with three concentrations of the GO nanoparticles as follows (1%, 2% and 3%). These three new nanofluids concentration were used in COMSOL software with the SMA channel to compare between the thermal performance of the nanofluids and the base fluid (water).

Table 6.12: Thermal properties of Graphene Oxide

Graphene Oxide (GO)	
$k(W.m^{-1}.K^{-1})$	3000
$\rho(kg.m^{-3})$	3600
µ $(Pa.s)$	NA
$C_p\ (J.kg^{-1}.K^{-1})$	765

When calculating the four thermal properties of the newly formed nanofluids, the change in temperature and how it influenced the properties was considered; and since the temperature targeted for this project is between 20°C to 40°C, the change in the four properties was studied and observed for temperatures between 0°C to 50°C, and that was to make sure every change in temperature was captured in the pursuit of accuracy.

6.6.1 Preparation of Nanofluids

The right preparation of nanofluids plays a significant role in enhancing the overall performance of the system in which the nanofluid is to be used, as it is of paramount significance to avoid phenomena like precipitation which compromises the quality of the nanofluid. Generally, there are two methods of preparing nanofluids, single-step method and two-step method. In the single-step method, the nanoparticles are prepared by the process of physical vapour deposition (PVD), and then dispersed inside the base fluid. Whereas in the two-step method, the nanoparticles are prepared with different techniques before they have been dispersed inside the base fluid. In collaboration with Mashhad university, the author worked on nanofluids using Graphene Oxide as the nanoparticle, and the nanofluid was prepared by using a 22 kHz ultrasonic device for 4 hours, thereafter the Zeta potential test was used to examine the stability of the prepared nanofluid.

Moghadam et al., 2022, used graphene oxide nanoparticles to prepare nanofluids and they sonicated the nanoparticles in water for 90 mins and then added Arabic Gum to the mixture to increase dispersity. They also used surfactants to separate bubbles form the boiling surface and thus they managed to increase heat transfer coefficient. The step Moghadam et al. followed to prepare their nanofluid are shown in figure 6.23.

Figure 6.23: Preparation steps for water graphene oxide nanofluid (Moghadam et al.,2022)

6.6.2 Water plus (1%, 2%, and 3%) of Graphene Oxide Nanoparticles

The second fluid studied was a mixture of water and 1% of graphene oxide nanoparticle. The first step was obtaining the thermal properties of the newly formed nanofluid through using the equations (6.43) to (6.46). It was found that the change in the thermal conductivity for the new nanofluid for temperatures 0 to 50 is very small and hence it was neglected and thus it was considered constant at $1.0408\ W.m^{-1}.K^{-1}$ for the range of temperature in question. The rest of the thermal properties changed as the temperature of the fluid changed; that change of the properties was captured as shown in figure 6.24.

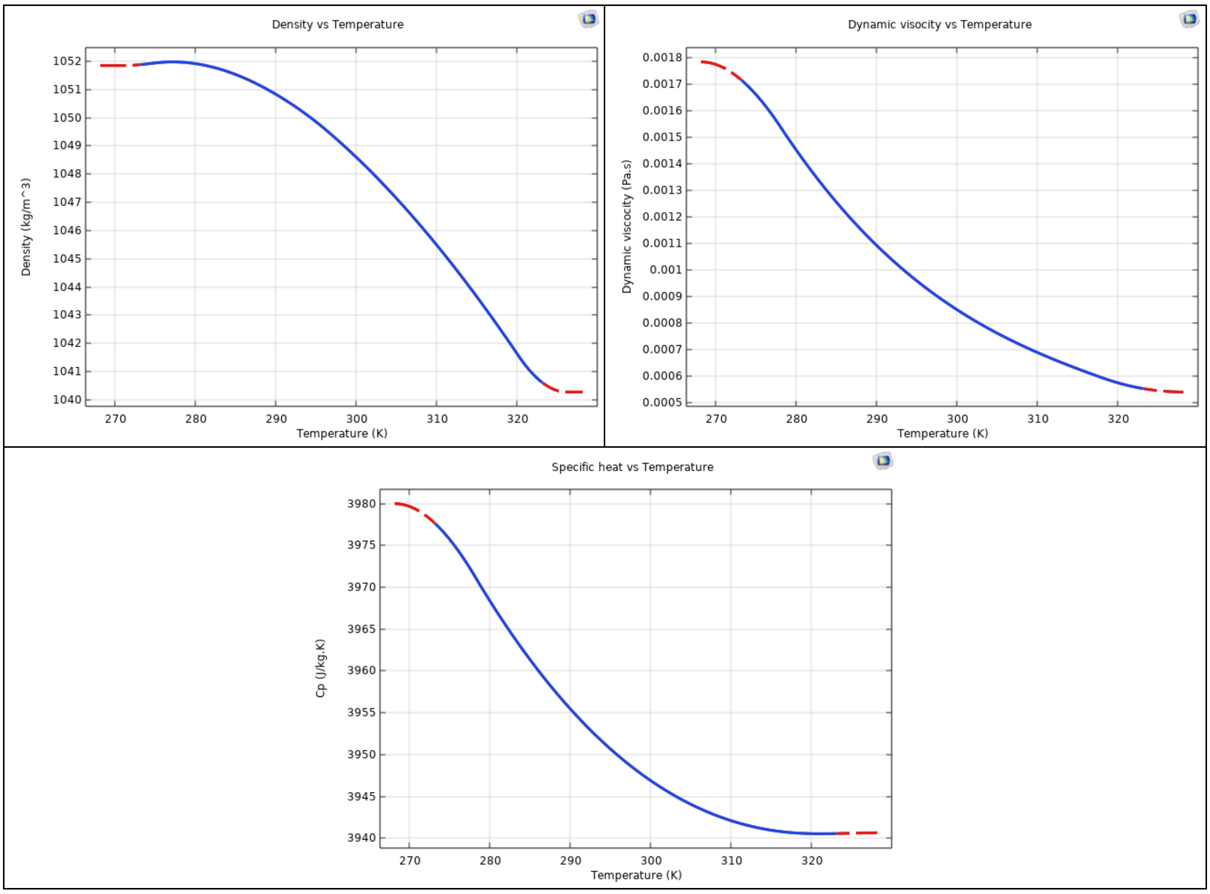

Figure 6.24: Thermal properties (Density, Dynamic Viscosity & Specific Heat) for nanofluid of water plus 1% of graphene oxide nanoparticles

The above procedure was repeated for water plus two more concentrations of graphene oxide nano particles (2% and 3%), and the thermal properties of the three nanofluids were compared to those of water; it was found that the change in thermal conductivity for the nanofluids of water plus 1% GO, water plus 2% GO and water plus 3% GO was negligible and therefore the values used for simulations were $1.0408\, W.m^{-1}.K^{-1}$, $1.0833\, W.m^{-1}.K^{-1}$ and $1.1276\, W.m^{-1}.K^{-1}$ resepectively. Figure 6.25 showed how the thermal properties of the four fluids changed when the temperature of the fluid changed. These three fluids were pumped separately through the SMA channel with the dimensions mentioned earlier in this section. The performances of the four fluids were plotted in one graph to showcase the behaviour of each fluid during the loading and the unloading of the SMA channel, as shown in figure 6.26 below.

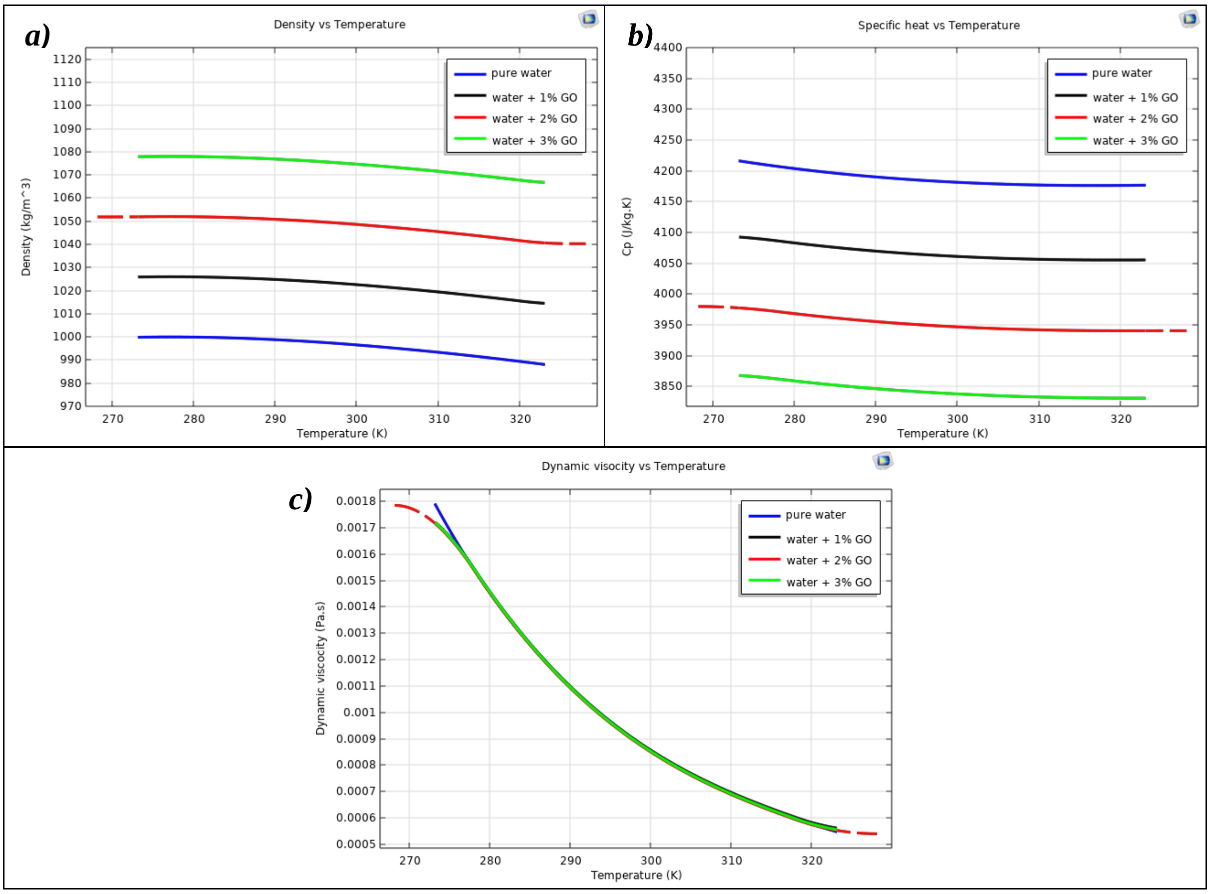

Figure 6.25: Comparison between the thermal properties versus temperature for water and the three nanofluids (water plus 1%, 2% and 3% of GO nanoparticles) a) Density b) Specific heat capacity c) Dynamic viscosity.

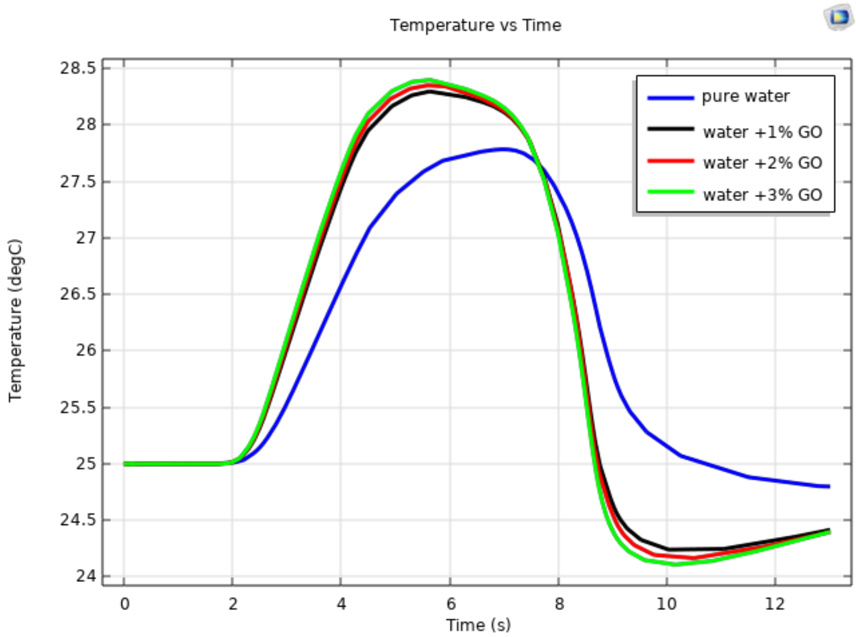

Figure 6.26: Comparison between the four fluids performance when pumped through an SMA channel.

Figure 6.26 shows the results of the simulation for the four fluids. The temperature of water started rising gradually after 2.2 seconds from the start of the cycle; and after 7 seconds, the temperature of water reached its maximum of 27.7℃ and then started dropping to baseline temperature at the end of the unloading. Whereas the temperature of the nanofluids started rising at 2.1 seconds and reached 28.3℃, 28.34℃ and 28.4℃ for water plus 1%, 2% and 3% graphene oxide nanoparticles respectively. The temperature of the three nanofluids started dropping one second before the end of unloading and it dropped to below the baseline temperature and reached 24℃ achieving a 1K temperature difference in the cooling side. This analysis showed that adding graphene oxide nanoparticles to water enhanced the thermal properties of water and subsequently enhanced the thermal performance of the newly formed fluid, which allowed for a better and quicker heat transfer between the SMA material (heat source) and the working fluid. The newly formed nanofluid also showed a better performance in rejecting their heat as the SMA channel cooled down because of unloading the channel and thus absorbing latent heat from the surrounding.

6.7 Flow Path Analysis

6.7.1 Flow Path Thickness

The previous analysis was done on a channel with wall thickness of 2.5mm. The current analysis was a comparison between three thicknesses of 2.5mm, 3.5mm and 4.5mm to understand which channel thickness leads to a better heat transfer between the SMA pipe (heat source) and the working fluid. The analysis showed that the smaller the thickness of the channel the better the heat transfer between the channel and the material, as shown in figure 6.27. Figure 6.27 (a) shows that the temperature of the fluid rose to 27.8℃ with a channel thickness of 2.5mm, which is 0.8℃ higher than that of a 4.5mm thickness. The temperature across the thickness of the channel changes changed as well; as the analysis showed that the temperature of the channel was highest on the internal wall of the channel and it dropped gradually as through the channel until it was the lowest on the external wall of the channel, as shown in figure 6.27 (b).

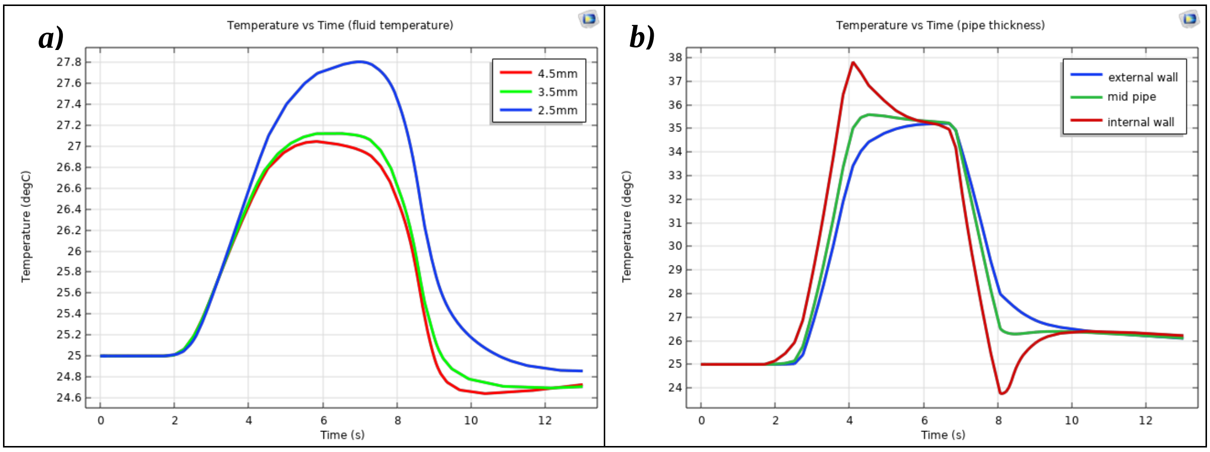

Figure 6.27: a) Comparison between the three channel thicknesses b) Temperature at three different point of the channel thickness 4.5mm at a height of 15mm

Figure 6.28 shows a section of the channel for the three tested thicknesses of 2.5 mm, 3.5 mm, and 4.5 mm.

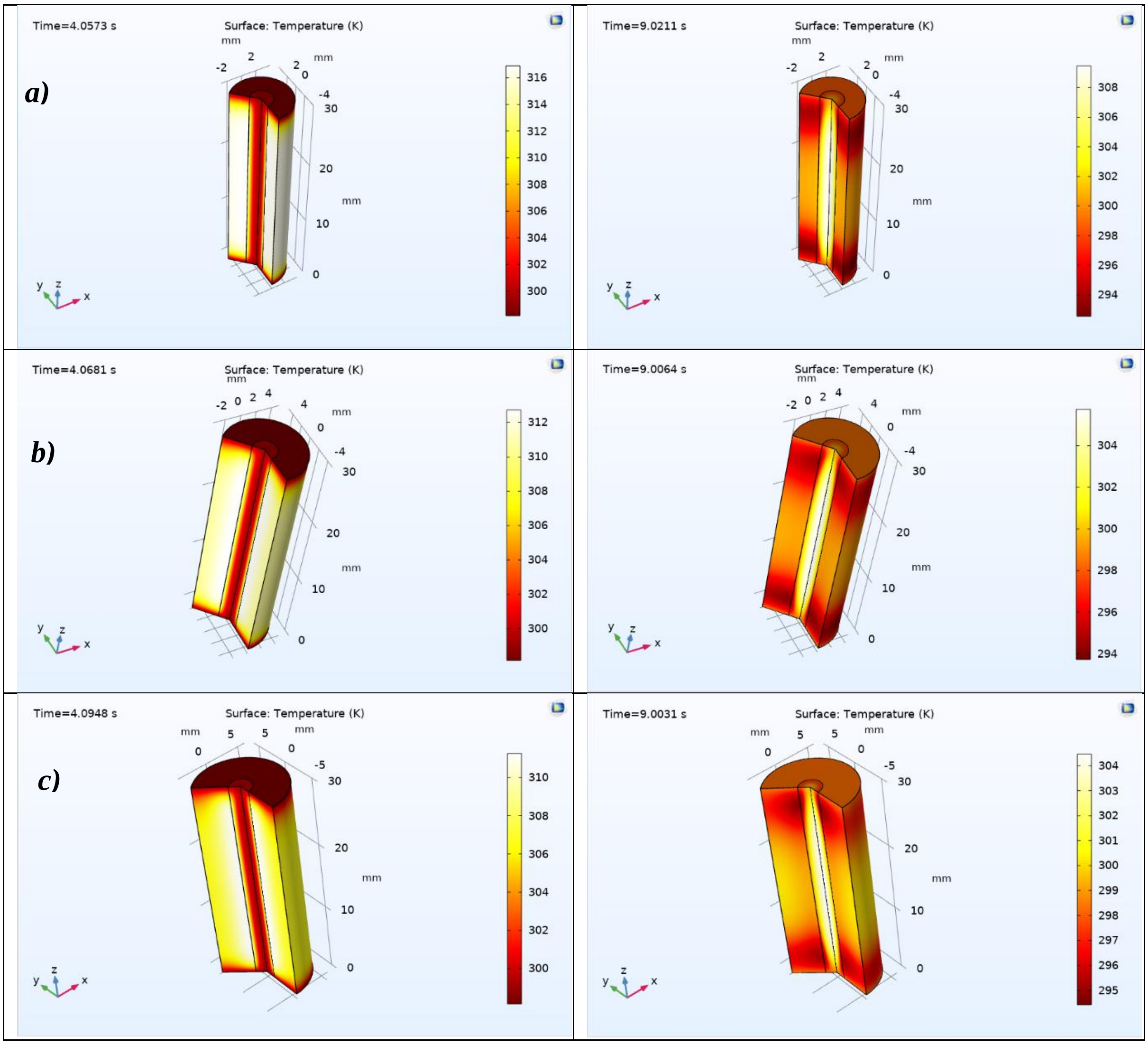

Figure 6.28: Cross-section of the channel to show the change in temperature at the end of loading and end of cycle for three different channel thicknesses of a) 2.5mm b) 3.5mm and c) 4.5mm respectively.

6.7.2 Flow Path Length

The previous analysis shown in figures 6.27 and 6.28, showed the effect the channel thickness had on the heat transfer across the channel and onto the fluid. This section explored the effect the channel's length had on heat transfer. Three different lengths of the channel (25mm, 30mm and 35mm) were studied and their results were compared. Figure 6.29 shows the results of pumping water through three SMA channels with different lengths of 25mm, 30mm and 35mm. The results showed that the channel length does not have big of an impact on the temperature of the fluid exiting the channel/flow-path; as the temperature of the fluid for the channel of 25 mm length was 27.6℃ and when increasing the channel's length to 35 mm, the temperature of the fluid was 27.7℃. Therefore, 10mm difference between the two channels resulted in les 0.1℃.

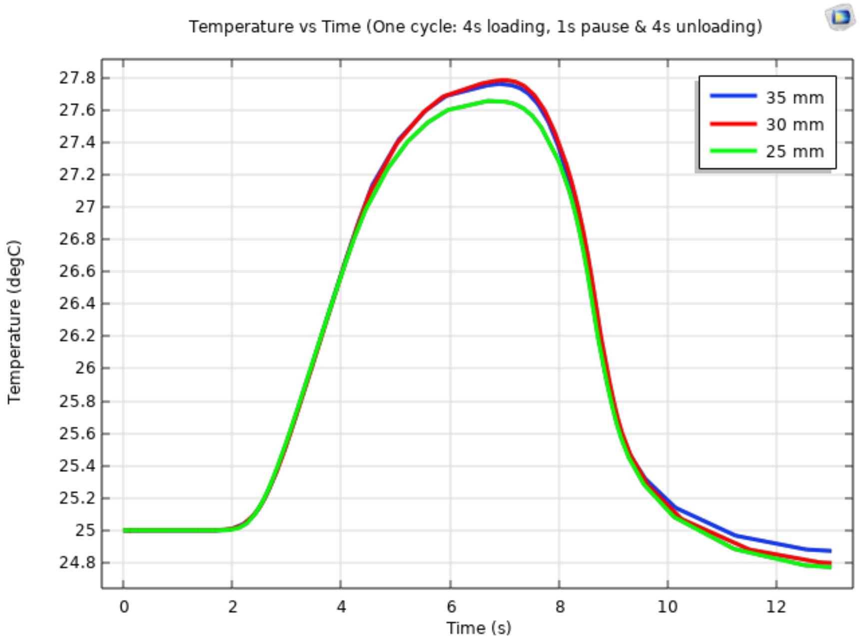

Figure 6.29: Comparison between heat transfer between three channel lengths of with 25mm, 30mm and 35mm and the working fluid. The results are for the fluid's temperature at the exit of the channel.

6.8 Summary:

This chapter went through the design steps for the plates, the stack, the fluid flow, and the type of the fluid that secured the best heat transfer between the material and the working fluid. The chapter started by looking at different geometries for the plates and for the channels through which the working fluid was to pass. The results showed that the best geometry for the channels is rectangular shape, as it provided higher Reynolds number, higher heat transfer coefficient and thus better performance. Since better heat transfer requires more surface area, the stack was designed to allow for three-paths serpentine flow, which meant that the fluid entered the stack at the bottom, went up, down and up again before it exited the stack having harvested the maximum amount of heat possible from the material. The last component that this chapter covered was the fluid used to pick the heat up from the material. The chapter started by looking at water as the working fluid which achieved 2.8K temperature difference; however, after introducing different percentages (1%, 2% and 3%) of Graphene Oxide nanoparticles for their high thermal properties, it was found that thermal properties of the newly formed fluids were enhanced noticeably, especially the thermal conductivity. When these nanofluids were pushed through the SMA channel, they achieved nearly 25.9% enhancement on the temperature difference, and they shortened the loading cycle by one second which is 24% of the original cycle. These two facts of increasing the temperature difference and shortening the cycle time will make a significant difference in terms of the device’s overall efficiency, device’s compactness, and costs of SMA core. The higher cost of nanofluids could be offset by lower cost of the system.

Chapter 7: Conclusions and Recommendations for Future Research

Chapter 7 Conclusions and Recommendations for Future Research

7.1 Introduction

Since its discovery in 1965, Shape Memory Alloys (SMA) have been researched extensively and have been used in many different fields, one of which is Refrigeration and Air Conditioning. Elastocaloric refrigeration is considered one of the most promising emerging cooling and heating technologies, and it is expected to play a great role in the transition from vapor compression refrigeration into cleaner refrigeration. This technology is based on using SMAs as the core material, for their unique thermophysical properties; the SMA material changes phase from Austenite to Martensite when it is subjected to uniaxial stress. Due to this phase change, the structure of the crystals changes which results in increasing the temperature of the material; when the load is removed, the structure of the crystals reverts to its original orientation, and this process is accompanied with a significant drop in the temperature of the material.

The literature review carried out in this project showed that all the efforts in Elastocaloric refrigeration research faced different obstacles; the common bottleneck problem for most of the previous projects was enhancing the heat transfer between the material and any working fluid to have an efficient device that can achieve a reasonable COP. One of the other issues that faced a few researchers was the fatigue life of the material, as in some projects the material failed after less than ten thousand cycles, because the geometries used were not robust enough to withstand the large stress that needed to be applied to the material to trigger the phase change. This project addressed these issues, from how to enhance the performance of the material through different technique of heat treatment, to exploring different designs and geometries for the material to enhance its robustness to finally looking at different ways of enhancing heat transfer between the heat source and the heat transfer fluid. The work in the project was carried out by means of laboratory experiments as well as computer simulation; the laboratory experiments were mainly focused on the material, from looking at how heat treatment influences the material's behavior to looking at how different blends of SMA can have different available latent heat depending on the amount of stress applied to the specimens and the temperature in which the test is conducted, alternatively known as the test condition. The other component is the computer simulation which was carried out in COMSOL MULTIPHYSICS; the simulations targeted understanding the material behavior through altering the amount of stress applied as well as the cycle time. Then the simulation was carried out to understand the amount of latent heat available within the material. Thereafter, the SMA model was validated against the results obtained from the laboratory experiments.

The experiments results showed that the activation temperatures of SMA can be moved through heat treating the material differently; which means through heat treatment, it is possible to make the SMA material cater for different applications from cryogenic to space heating. The results also showed that the Martensite phase transformation sometimes takes place at temperatures lower than -60℃, hence it was necessary to provide the DSC with liquid nitrogen to ensure capturing the Martensite transformation; and that was true in the NiTi specimen, which was annealed at 450℃ for 8 minutes, as the Martensite transformation continued to take place up to -150℃, as shown in figure 5.17 in Chapter 5.

7.2 Achieving the Project's Objectives

The aim of the project is to study different SMA blends and understand their thermophysical properties to enhance their thermal outputs and thus incorporate them into a heat pump where they work as the heat source, and then enhance the heat transfer between the heat source and working fluids. To achieve this aim, five objectives were set at the beginning of this project and are highlighted in Chapter 3. This section explains how each objective was accomplished.

1- **To complete and deliver a comprehensive literature review report on SMA and deliver a comparison review paper of alternative heating and cooling technologies.**

Chapter 2 provided a comprehensive review on seven emerging heating and cooling technologies highlighting the basic working principle of operation, its main applications, the challenges, and opportunities in penetrating the market. The literature also highlighted further research and development needed to accelerate the development and adoption of these alternative refrigeration technologies by the sector. Most of the technologies reviewed have a Technology Readiness Level (TRL) of 3–4, except electrocaloric technology which is less ready compared to its counterparts with a TRL of 1–2 at this stage. Furthermore, most of the technologies have capacities ranging between a few watts to a maximum of 7 kW with a coefficient of performance COP between 1 and 10 reported in the literature. The literature review carried out in the project bred a review paper which was published in the reputable journal “energies” with the title: “A Review of Recent Advances in Emerging Alternative Heating and Cooling Technologies”.

2- To model SMAs in CFD to understand their behaviour under different loading conditions and cycle times, and then to validate the modelling results against data obtained from the test rigs being developed within the Exergyn’s Laboratories.

Understanding the behaviour of SMAs and how their thermophysical properties change under different circumstance is of paramount significance in incorporating them into any design. Chapter 4, via means of CFD simulations, examined applying different stresses on an SMA specimen to understand the amount of stress needed to trigger phase change. The results showed that applying a compressive loading of 500 MPa resulted in a deformation/strain of 1.63%, a temperature lift of 4K, and a latent heat release of 1.46 $J.g^{-1}$. These values increased to 3.45%, 10K, and 7 $J.g^{-1}$ respectively when the applied stress was increased from 500 MPa to 600 MPa. The results also showed that the maximum stress needed for the material’s specimen tested to achieve full transformation was 900 MPa, where the material achieved a strain of 5.4%, temperature lift of 19 K, and a latent heat release of 19 $J.g^{-1}$, see table 4.2.

The second component in understanding SMA behaviour was to understand how the material behaves under different cycling strategies. The results showed that the quicker the loading the quicker the material reached a higher temperature; the results showed that the temperature of the material reached 44℃ when the specimen was loaded for 4 seconds; whereas the temperature of the material reached 46℃ when the material was loaded for 3 seconds achieving a 4.5% increase. The latent heat also increased with the decrease of the loading time from 20.2 $J.g^{-1}$ to 20.5 $J.g^{-1}$achieving 1.48% increase. The results from the

CFD modelling were then validated against the results obtained from the testing rig as shown in Chapter 5 section 5.4.

3- **To test different blends under different heat treatments which would lead to understanding the effect of heat treatment processes on SMA materials in terms of activation temperatures and available latent.**

Chapter 5, section 5.3 provided a detailed description of the heat treatment processes that were carried out on two blends NiTi and NiTiX. The results showed that changing the annealing temperature for the NiTiX specimen from 450℃ to 540℃, the activation temperatures A_s, A_f, M_s, M_f moved from 12.5℃, 37.5℃, 25℃, -20℃ to -25℃, 10℃, -20℃, -60℃ respectively, see figure 5.10 in Chapter 5.

Chapter 5 also provided a validation for CFD modelling as shown in figures 5.23 through 5.28; and it provided validation for the latent heat obtained in CFD and the one obtained from the testing rig, there was a slight discrepancy of 14.6% between the two, as the latent heat obtained from the modelling was 13 $J.g^{-1}$and the one obtained from the testing rig was 14.9 $J.g^{-1}$; however, the model is more accurate because the testing rig did not take into account the heat transfer between the specimen and the rig's grips.

On the front of the latent heat, Chapter 5 provided a study carried out on the effect of the amount of stress applied and the ambient temperature in which the SMA material in question is to function. The results, shown in figures 5.20 through 5.22, showed that the higher the ambient temperature (test temperature), the lower the required stress.

4- **After the right blend for heat pump application has been decided, to test different geometries, using the model, to decide which geometry functions most efficiently with regards to heat transfer onto the heat transfer fluids (HTFs).**

As shown in the material experiments section and summarised in above objective 3, the activation temperatures can be moved through heat treating the material differently. Moving the activation temperatures results in the material being functioning in different ranges, from cryogenics to space heating. Since the target of this project is a heat pump that can provide a heating load of 3 kW with a temperature lift of 5K, the blend used was NiTi whose activation temperatures A_s, A_f, M_s, M_f were -20℃, 10℃, -25℃, -50℃ respectively, as shown in figure 5.28 in Chapter 5.

Chapter 6 then provided an in-depth study of geometries design for the plate and the slots through which the fluid flows. This analysis was carried out through studying and designing 13 different plates. The design depends on many parameters which were divided into three groups: required input, required output and fluid parameters, as shown in table 6.1. The first plate design was a square plate with rectangular slots; the rectangular shape was preferred over the other shape because it secured the highest Reynolds number which is paramount in enhancing the heat transfer. The first design which was named plate 1, achieved an average temperature lift of 2.7K and an efficiency of 96.6%, as shown in table 6.5. The second design was for an elliptic shape which had a poor performance achieving an efficiency of 55%, as shown in table 6.8. The analysis then continued to study a rectangular shape for the plate with different shapes for the slots and plates 3 to 9 achieved different efficiencies between 70% to 97%, as shown in figure 6.5. These designs were not considered for the final heat pump design because they did not allow for different flow types for the fluid; being able to change the flow of the fluid has a significant importance as there was a necessity to expand the heat transfer surface area to the maximum, and that was not possible without allowing for different fluid flow types such as serpentine flow. Therefore, the design of plate 10 shown in table 6.8, came about because when the plates are stacked on top of each other, with the help of manifolds, they will force the fluid to move into the stack in a serpentine flow and thus expanding the heat transfer surface area to the maximum, as shown in figure 6.14 and 6.15.

Then the design moved on reducing slots dimensions for plate 10 which bred plate 11, shown in table 6.11; when the two plates were simulated in COMSOL, the results showed that plate 11 whose slots were smaller by 1 mm achieved a temperature lift of 4.7K whereas plate 10 achieved 4.3K. However, when it came to the efficiency, plate 10 achieved 98.7% against 98.2% achieved by plate 11, which meant by reducing the slots' dimensions, there was more material which resulted in higher temperature, however, reducing the slots also resulted in less heat transfer area which resulted in slightly less efficiency. That goes to tell the reader that they need to decide what they want to achieve from their design, and then they can take the decision that will meet their criteria. Since the goal of the project was to design a core stack that would have a better efficiency, plate 10 was selected to design the stack, as shown in figure 6.14 in Chapter 6.

5- Test different fluids (nanofluids) using different percentages of nanoparticles to enhance the fluids' thermal properties and study the impact nanofluids will have on the overall performance. Compare between the fluids to decide which nanofluid is the best in relation to picking up heat from SMA material.

As part of the stack's design, this project provided an in-depth study on how best to remove the heat from an SMA stack using different fluids. To carry out this study, one fluid path was selected and treated as a channel, and then four different fluids (water and three different concentrations of Graphene Oxide nanoparticles added to the base fluid to compose three nanofluids), were pumped through the channel and the performance of the different fluids was analysed. The study focused on the four main properties that govern the heat transfer within fluids, which are: thermal conductivity, specific heat capacity, density, and dynamic viscosity. It was also found that these properties change as the temperature of the fluid changes. The analysis started by looking at water, whose thermal properties change as the temperature of water changes, as shown in figure 6.17 in Chapter 6. The performance of the four fluids was as follows:

- Water: The results showed that the channel had different temperatures at different heights; the results showed that at the bottom and the top of the channel, the temperature of channel/material oscillated between 34℃ at the end of loading and 18℃ at the end of the unloading; whereas, at the middle of the channel, the temperature reached 44℃ at the end of the loading and it went back to baseline temperature of 25℃ at the end of the unloading, as shown in figure 6.20. The results showed that at the end of the channel (channel outlet), the temperature of the channel reached 29℃ in 4 seconds which was the end of the loading, then the temperature started dropping gradually until it got to 21.5℃ at 9 seconds which was at the end of the unloading. However, the fluid's temperature followed a different trajectory, as the fluid started picking up the heat from the channel after 3 seconds, and the temperature of the fluid continued rising until it reached its maximum of 27.7°C after 7 seconds which is two seconds before the end of the unloading, as shown in figure 6.20, achieving a temperature lift of 2.7K.

- Nanofluids: The project in Chapter 6, discussed how three different nanofluids using water as the base fluid were composed. The main reason of adding nanoparticles to the base fluid (water) was to enhance the thermal properties of the working fluid; the nanoparticles chosen were Graphene Oxide for their high thermal properties that are shown in table 6.12. Since the thermal properties of the base fluid (water) are not constant, then the nanofluids were built based on the change of the thermal properties. The three fluids that were built were water plus three different concentrations (1%, 2% and 3%) of Graphene Oxide nanoparticles. Using the equations 6.43 to 6.46 it was found that the change in thermal conductivity of the nanofluids as their temperature change is negligible; however, the three other properties changed as shown in figure 6.25. The results of using the three nanofluids showed an increase in the fluid temperature as the percentage of the nanoparticle increased. The nanofluids started picking up the heat at slightly more than two seconds and the maximum temperature reached was 28.4°C at 5.8 seconds of the cycle; these results showed that using nanofluids improved the temperature lift of the fluid from 27.7°C to 28.4°C increasing the temperature lift from 2.7K to 3.4K which is an increase of 25.9% in the temperature lift. Since the nanofluids reached their maximum temperature in 5.8 seconds compared to 7 seconds compared to using water, that meant the nanofluids shortened the cycle by 1.2 second which is 24%, as shown in figure 6.26.

The analysis also included how the channel’s thickness and length could potentially influence the heat transfer between the SMA and the working fluid. The results showed that the channel’s thicknesses of 2.5mm, 3.5mm and 4.5mm resulted in fluid temperatures of 27.7°C, 27.1°C and 27°C respectively, which goes to show that the smaller the channel’s thickness the better the heat transfer onto the fluid.

7.3 Contribution to the Knowledge

This section highlights the novelty of this project and its original contribution to knowledge. This project makes contributions by:

- ✓ Providing a roadmap for SMA modelling in CFD (COMSOL MULTIPHYSICS) and how SMA is susceptible to different applied stresses and cycle times.
- ✓ Providing a roadmap of how to design different SMA geometries that can withstand high stresses and thus could potentially be used as the core material for an SMA-based heat pump device without encountering material failure due to high stresses.
- ✓ Developing an innovative approach to enhance the heat transfer from SMA through using enhanced nanofluids.

7.4 Recommendations for Future Work

Based on the conclusions drawn in this research, further work is required to investigate the following:

1- Look into the possibility of coating the SMA material with materials that have higher conductivity such as copper, to enhance the heat transfer between the SMA material and working fluids.
2- Look into whether adding percentages of Graphene Oxide to water and using it as a working fluid will have chemical reaction with the SMA material.
3- Consider a study on the embodied carbon for an SMA heat pump versus an ordinary heat pump.
4- Consider a cost study and life cycle assessment of an SMA based heat pump versus a conventional heat pump.

References

Abomostafa, H.; Ellamey, M. Studying the mechanical properties of Barium Strontium Titanate ceramics by an ultrasonic pulse-echo technology. *J. Ovonic Res.* 2018, *14*, 307–316.

Albertini, F.; Bennati, C.; Bianchi, M.; Branchini, L.; Cugini, F.; De Pascale, A. 2017; Fabbrici, S.; Melino, F.; Ottaviano, S.; Peretto, A.; et al. Preliminary Investigation on a Rotary Magnetocaloric Refrigerator Prototype. *Energy Procedia*, *142*, 1288–1293.

Ammar, O., Dieng, L. and Haddar, N., 2018. Modeling of strain rate effect on the pseudoelastic behavior of NiTi SMA using a simple thermomechanical coupling model. Mechanics of Materials, 124, pp.7-17. (Ammar, Dieng and Haddar, 2018)

Amponsah, N., Troldborg, M., Kington, B., Aalders, I. and Hough, R., 2014. Greenhouse gas emissions from renewable energy sources: A review of lifecycle considerations. Renewable and Sustainable Energy Reviews, 39, pp.461-475.

Aprea, C.; Greco, A.; Maioriono, A.; Masselli, C. Enhancing the Heat Transfer in an Active Barocaloric Cooling System Using Ethylene-Glycol Based Nanofluids as Secondary Medium. *Energies* 2019, *12*, 2902.

Aprea, C.; Greco, A.; Maiorino, A., 2014 Magnetic refrigeration: A promising new technology for energy saving. *Int. J. Ambient. Energy* 2014, *37*, 294–313

Aprea, C.; Greco, A. 2014; Maiorino, A. Magnetic refrigeration: A promising new technology for energy saving. *Int. J. Ambient. Energy*, *37*, 294–313.

Aprea, C.; Greco, A.; Maiorino, A.; Masselli, C. 2016, A comparison between different materials in an active electrocaloric regenerative cycle with a 2D numerical model. *Int. J. Refrig.*, *69*, 369–382.

Aprea, C.; Greco, A.; Maiorino, A.; Masselli, C. 2018Solid-state refrigeration: A comparison of the energy performances of caloric materials operating in an active caloric regenerator. *Energy*, *165*, 439–455.

Aprea, C.; Greco, A.; Maiorino, A.; Masselli, C. Electrocaloric refrigeration: an innovative, emerging, eco-friendly refrigeration technique. *J. Phys. Conf. Ser.* 2017, *796*, 12019.

Avent, A.W. and Bowen, C.R. (2015) “Principles of Thermoacoustic Energy Harvesting,” *The European Physical Journal Special Topics*, 224(14-15), pp. 2967–2992. Available at: https://doi.org/10.1140/epjst/e2015-02601-x.

Ahmed, H.; Almajri, A.K.; Mahmoud, S.; Al-Dadah, R.; Ahmad, A. CFD modelling and parametric study of small scale Alpha type Stirling Cryocooler. *Energy Procedia* 2017, *142*, 1668–1673.

Ben Fraj, B., Gahbiche, A., Zghal, S. and Tourki, Z., 2017. On the Influence of the Heat Treatment Temperature on the Superelastic Compressive Behavior of the Ni-Rich NiTi Shape Memory Alloy. *Journal of Materials Engineering and Performance*, 26(11), pp.5660-5668.

Bhansali, P.S.; Patunkar, P.P.; Gorade, S.V.; Adhav, S.S.; Botre, S.S. An Overview Of Stack Design For A Thermoacoustic Refrigerator. *Int. J. Res. Eng. Technol.* 2015, *4*, 68–72.

Bom, N.M.; Imamura, W.; Usuda, E.O.; Paixao, L.S.; Carcalho AM, G. Giant barocaloric effects in natural rubber: A relevant step toward solid-state cooling. *ASC Macro Lett.* 2017, *7*, 470–471.

Bonsignore, C., Shamini, A. and Duerig, T., 2019. The Role of Parent Phase Compliance on the Fatigue Lifetime of Ni–Ti. Shape Memory and Superelasticity, 5(4), pp.407-414.

Choudhari, C. and Sapali, S., 2017. Performance Investigation of Natural Refrigerant R290 as a Substitute to R22 in Refrigeration Systems. Energy Procedia, vol . 109, pp.346-352

Climate Change: Vital Signs of the Planet. 2022. Graphic: Temperature vs Solar Activity – Climate Change: Vital Signs of the Planet. [online] Available at: <https://climate.nasa.gov/climate_resources/189/graphic-temperature-vs-solar-activity/> [Accessed 30 May 2022].

Climate change: an archaeological study: how our prehistoric ancestors responded to global warming / John D. Grainger you need the year.

Correia, T., Zhang, Q. (2014). Electrocaloric Effect: An Introduction. In: Correia, T., Zhang, Q. (eds) Electrocaloric Materials. Engineering Materials, vol 34. Springer, Berlin, Heidelberg. https://doi.org/10.1007/978-3-642-40264-7_1

Crossley, S. 2013, Electrocaloric Materials and Devices. Ph.D. Thesis, University of Cambridge, Cambridge, UK,.

Cuce, E.; Guclu, T.; Cuce, P.M. Improving thermal performance of thermoelectric coolers (TECs) through a nanofluid driven water to air heat exchanger design: Experimental research. *Energy Convers. Manag.* 2020, *214*, 112893.

Duerig, T. and Bhattacharya, K., 2015. The Influence of the R-Phase on the Superelastic Behavior of NiTi. *Shape Memory and Superelasticity*, 1(2), pp.153-161.

De Oliveira, N.A. (2011) “Barocaloric effect and the pressure induced solid state refrigerator,” *Journal of Applied Physics*, 109(5), p. 053515. Available at: https://doi.org/10.1063/1.3556740.

Echa.europa.eu. Lead-Substance Information-ECHA. 2019. Available online: https://echa.europa.eu/substance-information/-/substanceinfo/100.028.273 (accessed on 19 December 2019).

Ehpa.org. 2022. [online] Available at: <https://www.ehpa.org/fileadmin/documents/Large_heat_pumps_in_Europe_final.pdf> [Accessed 27 May 2022].

Elibol, C. and Wagner, M., 2015. Investigation of the stress-induced martensitic transformation in pseudoelastic NiTi under uniaxial tension, compression and compression–shear. *Materials Science and Engineering: A*, 621, pp.76-81.

Eriksed, D. 2016, Active Magnetic Regenerator Refrigeration with Rotary Multi-Bed Technology. Ph.D. Thesis, Technical University of Denmark, Lyngby, Denmark,

Espenson, T., n.d. 2018. Heat pump. Electric heating; Ground source heat pump system

Franco, V.; Blázquez, J.; Ipus, J.; Law, J.; Moreno-Ramírez, L.; Conde, A. Magnetocaloric effect: From materials research to refrigeration devices. *Prog. Mater. Sci.* 2018, *93*, 112–232.

Gadelkareem, M.T.; EldeinHussin, A.; Hennes, G.M.; El-Ehwany, A.A. Stirling cycle for hot and cold drinking water dispenser. *Int. J. Refrig.* 2019, *99*, 126–137.

Gao, X.Q.; Shen, J.; He, X.N.; Tang, C.C.; Li, K.; Dai, W.; Li, Z.X.; Jia, J.C.; Gong, M.Q.; Wu, J.F. Improvements of a room-temperature magnetic refrigerator combined with Stirling cycle refrigeration effect. *Int. J. Refrig.* 2016, *67*, 330–335.

Gatti, J.; Muller, C.; Vasile, C.; Brumpter, G.; Haegel, P.; Lorkin, T. 2014, Magnetic heat pumps–Configurable hydraulic distribution for a magnetic cooling system. *Int. J. Refrig. 37*, 165–175.

Getie, M.Z. *et al.* (2020) "Reversed Regenerative Stirling cycle machine for refrigeration application: A Review," *International Journal of Refrigeration*, 118, pp. 173–187. Available at: https://doi.org/10.1016/j.ijrefrig.2020.06.007.

Goodson, T. et al. (2022) Heating, IEA. International Energy Agency. Available at: https://www.iea.org/reports/heating (Accessed: February 2023).

GOV.UK. 2022. UK energy in brief 2021. [online] Available at: <https://www.gov.uk/government/statistics/uk-energy-in-brief-2021> [Accessed 17 March 2022].

Govindaraju, V.; Vilathgamuwa, D.M. 2014; Ramanujan, R. Modelling of a magnetocaloric system for cooling in the kilowatt range. *Int. J. Refrig.*, *43*, 143–153.

Grandi, D. and Stefanelli, U., 2015. The Souza-Auricchio model for shape-memory alloys. Discrete & Continuous Dynamical Systems - S, 8(4), pp.723-747. (Grandi and Stefanelli, 2015)

Grassi, E., Chagnon, G., de Oliveira, H. and Favier, D., 2020. Anisotropy and Clausius-Clapeyron relation for forward and reverse stress-induced martensitic transformations in polycrystalline NiTi thin-walled tubes. Mechanics of Materials, 146, p.103392. (Grassi, Chagnon, de Oliveira and Favier, 2020)

Greco, A.; Aprea, C.; Maiorino, A.; Masselli, C. A review of the state of the art of solid-state caloric cooling processes at room-temperature before 2019. *Int. J. Refrig.* 2019, *106*, 66–88.

Greenmatch, 2022. Heat Pumps: Types, Prices, Suppliers in 2022. [online] Available at: <https://www.greenmatch.co.uk/heat-pump> [Accessed 27 May 2022].

Guvenc, C.M.; Adem, U. Influence of aging on electrocaloric effect in Li+ doped BaTiO3 ceramics. *J. Alloy. Compd.* 2019, *791*, 674–680.

Hachem, H.; Gheith, R.; Aloui, F.; Ben Nasrallah, S. Optimisation of an air-filled Beta type Stirling refrigerator. *Int. J. Refrig.* 2017, *76*, 296–312.

He, J.; Wu, J.; Lu, B.; Liu, C. Comparative study on the series, parallel and cascade cycles of a multi-mode room temperature magnetic refrigeration system. *Int. J. Refrig.* 2020, *117*, 94–103.

Houses of Parliament. Carbon Footprint of Heat generation 2016

Huang, B.; Lai, J.; Zeng, D.; Zheng, Z.; Harrison, B.; Oort, A.; Van Dijk, N.; Brück, E. Development of an experimental rotary magnetic refrigerator prototype. *Int. J. Refrig.* 2019, *104*, 42–50.

Jiang, J., Hu, B., Wang, R., Liu, H., Zhang, Z. and Li, H., 2021. Theoretical performance assessment of low-GWP refrigerant R1233zd(E) applied in high temperature heat pump system. International Journal of Refrigeration, vol 131, pp.897-908.

Kang, L., Qian, H., Guo, Y., Ye, C. and Li, Z., 2020. Investigation of Mechanical Properties of Large Shape Memory Alloy Bars under Different Heat Treatments. *Materials*, 13(17), p.3729.

Kato, H., 2021. Latent heat storage capacity of NiTi shape memory alloy. *Journal of Materials Science*.

Kirsch, Su.; Schmidt, M.; Welsch, F.; Michaelis, N.; Schütze, A.; Seelecke, S. Development of a shape memory-based air conditioning system. In Proceedings of the 59th Ilmenau Scientific Colloquium, Ilmenau, Germany, 11-15 Septembe 2017.

Khoo, Z., An, J., Chua, C., Shen, Y., Kuo, C. and Liu, Y., 2018. Effect of Heat Treatment on Repetitively Scanned SLM NiTi Shape Memory Alloy. *Materials*, 12(1), p.77.

Kutjak, Z.; Rozic, B.; Pirc, R. Electrocaloric Effect: Theory, Measurements, and Applications; Wiley: Hoboken, New Jersey, USA, 2015.

Lagoudas C., 2007. Shape Memory Alloys, Modelling and Engineering Applications

Lagoudas, D. *Shape Memory Alloys*; Springer: New York, NY, USA, 2011.

Li, P., Wang, Y., Meng, F., Cao, L. and He, Z., 2019. Effect of Heat Treatment Temperature on Martensitic Transformation and Superelasticity of the Ti49Ni51 Shape Memory Alloy. *Materials*, 12(16), p.2539.

Li, Z.; Shen, J.; Li, K.; Gao, X.; Guo, X.; Dai, W. Assessment of three different gadolinium-based regenerators in a rotary-type magnetic refrigerator. *Appl. Therm. Eng.* 2019, *153*, 159–167.

Lines, M.E.; Glass, A.M. *Principles and Applications of Ferroelectrics and Related Materials*; Clarendon Press: Oxford, England, 1977.

Low GWP Alternative Refrigerants for New Systems Safety Considerations. RACHP Engineering Technicians Section Good Practice Guide 53 (Revised March 2022) - IOR

Lu, H., Liu, L., Yang, C., Luo, X., Song, C., Wang, Z., Wang, J., Su, Y., Ding, Y., Zhang, L. and Li, Y., 2022. Simultaneous enhancement of mechanical and shape memory properties by heat-treatment homogenization of Ti2Ni precipitates in TiNi shape memory alloy fabricated by selective laser melting. Journal of Materials Science & Technology, 101, pp.205-216.

Lu, S.; Li, J.; Cheng, M.; Li, Q.; Li, F.; Lv, Z.; Zhang, Y.; Lu, C.; Li, S. Joule heating-A significant factor in electrocaloric effect. *Ceram. Int.* 2019, *45*, 16992–16998.

Mark O. McLinden, Andrei F. Kazakov, J. Steven Brown, Riccardo Brignoli, Ian H. Bell, Piotr A. Domanski, 2019. Options for Low-GWP Refrigerants in Small Air-conditioning Systems. Institute of Refrigeration.

Moghadam, A., Goshayeshi, H., Chaer, I., Paurine, A., Zeinali Heris, S. and Pourpasha, H., 2022. Experimental investigation of multiwall carbon nanotubes/water nanofluid pool boiling on smooth and groove surfaces. *International Journal of Energy Research, vol, pp*.

Molin, C.; Peräntie, J.; Le Goupil, F.; Weyland, F.; Sanlialp, M.; Stingelin, N.; Novak, N.; Lupascu, D.C.; Gebhardt, S.E. 2017, Comparison of direct electrocaloric characterization methods exemplified by 0.92 Pb(Mg1/3 Nb2/3)O3 -0.08 PbTiO3 multilayer ceramics. *J. Am. Ceram. Soc.*, *100*, 2885–2892.

Moria, H.; Ahmed, M.; Alghanmi, A.; Mohamad, T.I.; Yaakob, Y. Experimental Study of Solar Based Refrigerator Using Thermoelectric Effect. *Energy Procedia* 2019, *158*, 198–203.

Mota-Babiloni, A., Navarro-Esbrí, J., Barragán-Cervera, Á., Molés, F. and Peris, B., 2015. Analysis based on EU Regulation No 517/2014 of new HFC/HFO mixtures as alternatives of high GWP refrigerants in refrigeration and HVAC systems. International Journal of Refrigeration, vol. 52, pp.21-31.

Mutlu, F., Anlaş, G. and Moumni, Z., 2020. Effect of loading rate on fracture mechanics of NiTi SMA. International Journal of Fracture, 224(2), pp.151-165. (Mutlu, Anlaş and Moumni, 2020).

Nathad, A.; Ahmed, F.; Khalid, M.O.; Kumar, R.; Hafeez, H. Experimental Analysis of an Economical Lab Demonstration Prototype of a Thermo Acoustic Refrigerator (TAR). *Energy Procedia* 2018, *157*, 343–354.

Navarro-Peris, E.; Corberan, J.M.; Ancik, Z. Evaluation of the potential recovery of compressor heat losses to enhance the efficiency of refrigeration systems by means of thermoelectric generation. *Appl. Therm. Eng.* 2015, *89*, 755–762.

Noye, S., Mulero Martinez, R., Carnieletto, L., De Carli, M. and Castelruiz Aguirre, A., 2022. A review of advanced ground source heat pump control: Artificial intelligence for autonomous and adaptive control. Renewable and Sustainable Energy Reviews, 153, p.111685.

Olsen, U.L.; Bahl, C.R.; Engelbrecht, K.; Nielsen, K.K.; Tasaki, Y.; Takahashi, H. 2014, Modeling of in-vehicle magnetic refrigeration. *Int. J. Refrig.*, *37*, 194–200.

Ons. 2022. UK Environmental Accounts - Office for National Statistics. [online] Available at: <https://www.ons.gov.uk/economy/environmentalaccounts/bulletins/ukenvironmentalaccounts/2021#:~:text=Greenhouse%20gas%20(GHG)%20emissions%20in,greenhouse%20gas%20emissions%20in%202019> [Accessed 14 March 2022].

Ossmer, H. Elastocaloric Microcooling. Ph.D. Thesis, Karlsruhe Institute of Technology (KIT), Karlsruhe, Germany, 2017.

Ossmer, H., Chluba, C., Krevet, B., Quandt, E., Rohde, M. and Kohl, M., 2013. Elastocaloric cooling using shape memory alloy films. *Journal of Physics: Conference Series*, 476, p.012138.

Ožbolt, M.; Kitanovski, A.; Tušek, J.; Poredoš, A. Electrocaloric vs. magnetocaloric energy conversion. *Int. J. Refrig.* 2014, *37*, 16–27.

Pérez-Cerrato, M., Maass, B., Nó, M. and San Juan, J., 2021. Ni–Ti-Hf high-temperature shape memory alloy: Measure of the Clausius-Clapeyron coefficient through mechanical spectroscopy. Journal of Alloys and Compounds, 856, p.157948. (Pérez-Cerrato, Maass, Nó and San Juan, 2021).

Peralta, D., Canizares, C. and Bhattacharya, K., 2022. Ground Source Heat Pump Modeling, Operation, and Participation in Electricity Markets. IEEE Transactions on Smart Grid, 13(2), pp.1126-1138.

Pietrzyk, K.; Ohara, B.; Watson, T.; Gee, M.; Avalos, D.; Lee, H. Thermoelectric module design strategy for solid-state refrigeration. *Energy* 2016, *114*, 823–832.

Plaznik, U.; Vrabelj, M.; Kutnjak, Z.; Malič, B.; Rožič, B.; Poredoš, A.; Kitanovski, A. Numerical modelling and experimental validation of a regenerative electrocaloric cooler. *Int. J. Refrig.* 2019, *98*, 139–149.

PROPOSAL FOR A RESTRICTION (2023). rep. ECHA. Available at: https://cdn.ca.emap.com/wp content/uploads/sites/11/2023/02/rest_pfas_axv_report_en.pdf (Accessed: April 3, 2023).

Qian, S.; Wang, Y.; Yuan, L.; Yu, J. A heat-driven elastocaloric cooling system. *Energy* 2019, *182*, 881–899.

Qian, S. Development of Thermoelastic Cooling Systems. Ph.D. Thesis, Maryland University, College Park, MD, USA, 2015.

Rao, Z., Wang, X., Leng, J., Yan, Z. and Yan, X., 2022. Design methodology of the Ni50Ti50 shape memory alloy beam actuator: Heat treatment, training and numerical simulation. Materials & Design, 217, p.110615.

Resnina, N., Palani, I., Belyaev, S., Singh, S., Liulchak, P., Karaseva, U., Mani Prabu, S., Jayachandran, S., Kalganov, V., Iaparova, E. and Demidova, E., 2021. Influence of heat treatment on the structure and martensitic transformation in NiTi alloy produced by wire arc additive manufacturing. Materialia, 20, p.101238.

Romero Gómez, J. *et al.* (2013) "Magnetocaloric effect: A review of the thermodynamic cycles in magnetic refrigeration," *Renewable and Sustainable Energy Reviews*, 17, pp. 74–82. Available at: https://doi.org/10.1016/j.rser.2012.09.027.

Saechan, P.; Jaworski, J.A. Thermoacoustic cooler to meet medical storage needs of rural communities in developing countries. *Therm. Sci. Eng. Process* 2018, *7*, 164–175.

Sanjay Kumar R. , Srilakshmi R., 2019. An Investigation of Thermal Behavior of the Selected Latent Heat Storage Materials for the Temperature Range of 40℃ to 80℃ of Solar Heating Applications. International Journal of Applied Engineering Research and Development, 9(1), pp.21-34.

Shen, J., Lu, N. and Chen, C., 2020. Mechanical and elastocaloric effect of aged Ni-rich TiNi shape memory alloy under load-controlled deformation. *Materials Science and Engineering: A*, 788, p.139554.

Shen, L.; Zhang, W.; Liu, G.; Tu, Z.; Lu, Q.; Chen, H.; Huang, Q. Performance enhancement investigation of the thermoelectric cooler with segmented configuration. *Appl. Therm. Eng.* 2020, *168*, 114852.

Shi, J.; Han, D.; Li, Z.; Yang, L.; Lu, S.-G.; Zhong, Z.; Chen, J.; Zhang, Q.; Qian, X. Electrocaloric Cooling Materials and Devices for Zero-Global-Warming-Potential, High-Efficiency Refrigeration. *Joule* 2019, *3*, 1200–1225.

Shi, J.; Zhu, R.; Liu, X.; Bi-Jun, F.; Yuan, N.; Ren, Y.; Luo, H. Large Electrocaloric Effect in Lead-Free (Ba0.85Ca0.15)(Zr0.1Ti0.9)O3 Ceramics Prepared via Citrate Route. *Materials* 2017, *10*, 1093.

Scied.ucar.edu. 2022. The Ozone Layer | Center for Science Education. [online] Available at: <https://scied.ucar.edu/learning-zone/atmosphere/ozone-layer> [Accessed 9 May 2022].

Tassou, S.A.; Lewis, J.; Ge, Y.; Hadawey, A.; Chaer, I. (2010), A review of emerging technologies for food refrigeration applications. *Appl. Therm. Eng.* 2010, *30*, 263–276.

Tian, X.-X.; Asaadi, S.; Moria, H.; Kaood, A.; Pourhedayat, S.; Jermsittiparsert, K. Proposing tube-bundle arrangement of tubular thermoelectric module as a novel air cooler. *Energy* 2020, *208*, 118428.

Theccc.org.uk. 2022. [online] Available at: <https://www.theccc.org.uk/wp-content/uploads/2020/12/Sector-summary-Buildings.pdf> [Accessed 18 March 2022].

Tušek, J.; Engelbrecht, K.; Pryds, N. Elastocaloric effect of a Ni-Ti plate to be applied in a regenerator-based cooling device. *Sci. Technol. Built Environ.* 2016, *22*, 489–499.

Verma, S.S. Thermo-acoustic refrigeration. *IOSR J. Mech. Civ. Eng.* 2014, 58–63.

Wang, X.; Wu, Z.; Zhang, L.; Hu, J.; Luo, E. Traveling-wave thermoacoustic refrigerator for room temperature application. *Int. J. Refrig.* 2020, *120*, 90–96.

Wang, H.; Yu, G.; Hu, J.; Wu, Z.; Hou, M.; Zhang, L.; Luo, E. A novel looped low-temperature heat-driven thermoacoustic refrigerator operating in room temperature range. *Energy Procedia* 2019, *158*, 1653–1659.

Xu, J.; Luo, E.; Hochgreb, S. Study on a heat-driven thermoacoustic refrigerator for low-grade heat recovery. *Appl. Energy* 2020, *271*, 115167.

Xu, W.; Liu, Y.; Marcelli, A.; Shang, P.; Liu, W. The complexity of thermoelectric materials: why we need powerful and brilliant synchrotron radiation sources? *Mater. Today Phys.* 2018, *6*, 68–82.

Yang M. Z., Wu C., Dai C., Tsai W. Energy harvesting thermoelectric generators manufactured using the complementary metal oxide semiconductor process. Sensors, 13 (2013), pp. 2359-2367.

Yang, S. and Dui, G., 2013. Temperature analysis of one-dimensional NiTi shape memory alloys under different loading rates and boundary conditions. *International Journal of Solids and Structures*, 50(20-21), pp.3254-3265.

Zaitouni, H.; Hajji, L.; Mezzane, D.; Choukri, E.; Alimoussa, A.; Ben Moumen, S.; Rožič, B.; El Marssi, M.; Kutnjak, Z. Direct electrocaloric, structural, dielectric, and electric properties of lead-free ferroelectric material Ba0.9Sr0.1Ti1-xSnxO3 synthesized by semi-wet method. *Phys. B Condens. Matter* 2019, *566*, 55–62.

Zhao, D.; Tan, G. A review of thermoelectric cooling: Materials, modeling and applications. *Appl. Therm. Eng.* 2014, *66*, 15–24.

Zhang, K., Kang, G. and Sun, Q. (2019) “High fatigue life and cooling efficiency of NITI shape memory alloy under cyclic compression,” *Scripta Materialia*, 159, pp. 62–67. Available at: https://doi.org/10.1016/j.scriptamat.2018.09.012.

Chapter 8 Appendices

8.1 Appendix (a): MATLAB Code

```
P.HEX.NodeCount; % Be careful the more nodes the smaller the timestep look for
stability criteria
P.HEX.K % Nitinol Thermal Conductivity
P.NiTi.Dens kg/m^3 Nitinol Density
P.NiTi.cp J/kg.K Nitinol Specific Heat Capacity
P.HEX.DQout %W Fluid Heating Power
P.HEX.LH; %kJ/kg Latent Heat
P.HEX.Cycle; %s Cycle Time
P.HEX.DT; %K Temperature Lift

P.HEX.PlateL; % mm Plate Lenght L
P.HEX.PlateW; %mm Plate Width
P.HEX.PlateCSA = (P.HEX.PlateL *P.HEX.PlateW)/10^6; %m^2
P.HEX.tmat; % mm Material Thickness
P.HEX.Volume = (P.HEX.PlateL * P.HEX.PlateW * P.HEX.tmat)/10^9; %m3 Material's
Volume
P.HEX.Mass = P.NiTi.Dens * P.HEX.Volume; %kg Mass
P.HEX.dx = (P.HEX.tmat/1000)/P.HEX.NodeCount;
P.HEX.dy = (P.HEX.PlateL)/P.HEX.NodeCount;


% Node Array Setup
% This is 1D so each line represents a point accross the thickness of the
% material. symmetry is assumed so only half the material is modelled
P.HEX.Tfluidave = 20+273.15;
P.HEX.Tm(1:P.HEX.NodeCount,1) = 20+273.15; % Previous Timestep Temperatures
P.HEX.Tn(1:P.HEX.NodeCount,1) = 20+273.15; %Current Timestep Temperatures



P.HEX.ThermDiffus = P.HEX.K/(P.NiTi.Dens * P.NiTi.cp);
P.HEX.t_step = ((P.HEX.dx^2)*0.5)/P.HEX.ThermDiffus;
P.HEX.HT = P.HEX.Cycle/4; %s heat rejection time

P.HEX.En_row = 1;

t = 0;

while t <= P.HEX.HT
    for h = 500

        P.HEX.h = h;
   %[P]=Nus(P) % Calculate Nusselt Number
   %P.CYC.h = min(12e3,(( P.CYC.Nuh * P.CYC.Kwat ) / ( P.CYC.HydDia /1000 ))); %
Convective Heat Transfer Coefficient
   [P]= HeatTransfer(P) % Calculate Wall Temps
%    if t > 3
%        P.HEX.Tn(P.HEX.NodeCount) =
(E*P.HEX.K/P.HEX.dx)*(P.HEX.Tm(P.HEX.NodeCount-1)-
P.HEX.Tm(P.HEX.NodeCount))+E*P.HEX.h*(P.HEX.Tfluidave-P.HEX.Tm(P.HEX.NodeCount))+
(Qi*E) + P.HEX.Tm(P.HEX.NodeCount);
%    end
   t = t+P.HEX.t_step; % Update Time
```

```
   %P.HEX.En_row = P.HEX.En_row +1; %Update Array Line
    end
end
P.HEX.T = t;
P.HEX.En_row = P.HEX.En_row +1;

%% Explicit Wall Function
function [P]= HeatTransfer(P)
% Constant parameters
B = (P.HEX.ThermDiffus * P.HEX.t_step)/(P.HEX.dx^2);
P.HEX.qkJ = P.HEX.LH * P.HEX.Mass; %kJ Heating Load
P.HEX.qkW = P.HEX.qkJ/P.HEX.HT; %kW Heating Load
P.HEX.qwm3 = (P.HEX.qkW * 1000)/ P.HEX.Volume; %W/m3 Heat Generation
Q = (P.HEX.qwm3 *(P.HEX.dx^2))/P.HEX.K;

%P.HEX.U = (P.HEX.qkW * 1000)/(P.HEX.PlateCSA*P.HEX.DT);
%R = 1/P.HEX.U;
%P.HEX.HT_C = 1/(R - ((P.HEX.tmat/1000)/P.HEX.K));

P.HEX.HT_C = 1/((P.HEX.PlateCSA*P.HEX.qkW*1000/P.HEX.DT) -
((P.HEX.tmat/1000)/P.HEX.K));
%Energy
E = (2*P.HEX.t_step)/(P.NiTi.Dens * P.NiTi.cp * P.HEX.dx );
Qcv =(P.HEX.DQout/2); %Convective [Can be changed if you like ]
Qi = P.HEX.qwm3 * (P.HEX.dx/2); % Heat generations
P.HEX.Kwat = 4e-8*P.HEX.Tfluidave^3-2e-
5*P.HEX.Tfluidave^2+0.0024*P.HEX.Tfluidave+0.5559;

P.HEX.Tn(1) = (B * (P.HEX.Tm(2) + P.HEX.Tm(2)))+((1 - (2*B))*P.HEX.Tm(1)) + (Q*B);

for m = 2:1:P.HEX.NodeCount-1

    P.HEX.Tn(m) = (B * (P.HEX.Tm(m+1) + P.HEX.Tm(m-1)))+((1 - (2*B))*P.HEX.Tm(m))
+ (Q*B);
end

%P.HEX.Tn(P.HEX.NodeCount) = (Qcv*E) +
((((P.HEX.Kwat+P.HEX.K)/2)/P.HEX.dx)*E*(P.HEX.Tm(P.HEX.NodeCount-1)-
P.HEX.Tm(P.HEX.NodeCount))) + (Qi*E) + P.HEX.Tm(P.HEX.NodeCount);

P.HEX.Tn(P.HEX.NodeCount) = (E*P.HEX.K/P.HEX.dx)*(P.HEX.Tm(P.HEX.NodeCount-1)-
P.HEX.Tm(P.HEX.NodeCount))+E*P.HEX.h*(P.HEX.Tfluidave-P.HEX.Tm(P.HEX.NodeCount))+
(Qi*E) + P.HEX.Tm(P.HEX.NodeCount);

P.HEX.Tm = P.HEX.Tn; % Update the current
P.HEX.Bi = ((P.HEX.h * (P.HEX.tmat)) / P.HEX.Kwat);
%P.RES.Bi(P.CYC.En_row,1)=P.CYC.Bi; % Biot Number

%Plotting
%This will plot every iteration so just comment out if needed
figure(5)
%h=figure;

plot(P.HEX.Tm-273.15)
xlabel('Nodes');
ylabel('Temperature degC');

%frame=getframe(h);
%im=frame2im(frame);
```

```
%[imind,cm]=rgb2ind(im,256);
%imwrite(imind,cm,HEX_DESIGN_TRANSIENT,'gif','loopcount',inf);
end
```

8.2 Appendix (b): Excel Calculations

See the attached excel spreadsheet.